Synthesis and Fluorescence of Opal & Air-Sphere Photonic Crystals

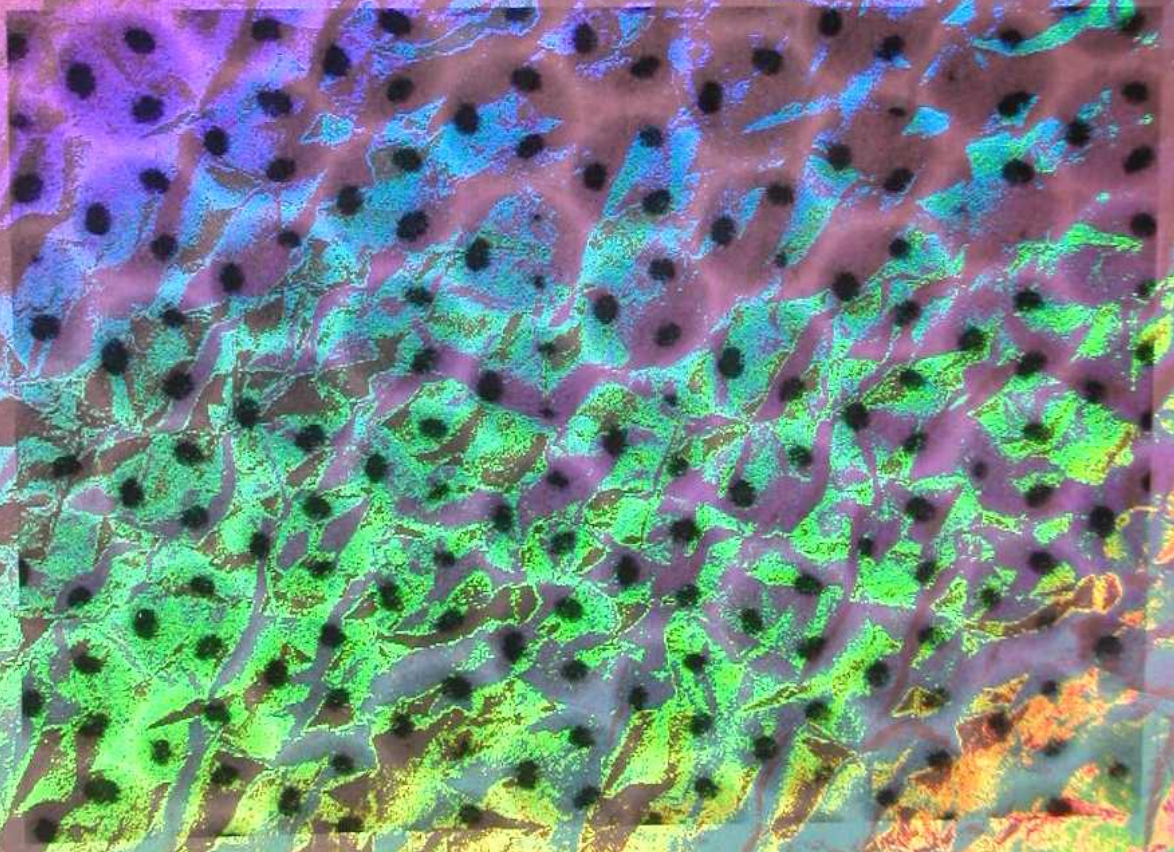

Lydia Bechger

Synthesis and Fluorescence of Opal & Air-Sphere Photonic Crystals

Lydia Bechger

Promotiecommissie:

Promotor	Prof. Dr. W. L. Vos
Overige leden	Dr. R. Balkenende (Philips Research Laboratories) Prof. Dr. W. L. Barnes (University of Exeter) Dr. ir. J. Huskens (University of Twente) Prof. Dr. A. Lagendijk (University of Twente) Prof. Dr. J. G. Vancso (University of Twente) Dr. G. H. Wegdam (University of Amsterdam)

The work described in this thesis is part of the research program of the "Stichting Fundamenteel Onderzoek der Materie (FOM)", which is financially supported by the "Nederlandse Organisatie voor Wetenschappelijk Onderzoek (NWO)".

It was initiated at the
Van der Waals-Zeeman Instituut, Valckenierstraat 65,
1018 XE Amsterdam, The Netherlands,

and was completed at
Complex Photonic Systems,
Faculty of Science and Technology,
and MESA+ Research Institute,
University of Twente, P.O. Box 217,
7500 AE Enschede, The Netherlands,

where a limited number of copies of this thesis is available.

Cover: Titania air-sphere crystal (403-31), by Lydia Bechger.

Printed by PrintPartners Ipskamp, Enschede, The Netherlands.

ISBN: 90-365-1991-8

SYNTHESIS AND FLUORESCENCE OF OPAL & AIR-SPHERE PHOTONIC CRYSTALS

PROEFSCHRIFT

ter verkrijging van
de graad van doctor aan de Universiteit Twente,
op gezag van de rector magnificus,
prof. dr. F.A. van Vught,
volgens besluit van het College voor Promoties
in het openbaar te verdedigen
op donderdag 18 december 2003 om 15.00 uur

door

Lydia Bechger

geboren op 18 oktober 1972

te Amsterdam

Dit proefschrift is goedgekeurd door:

Prof. Dr. W. L. Vos

Aan mijn ouders

Contents

Chapter 1

Introduction

1.1 Light and colors

Light is crucial to many biological, physical and chemical processes. An example of a chemical reaction that is induced by light is the photosynthesis in plants, where light energy is converted into chemical energy. Carbondioxide and water are converted into adenosine tri phosphate (ATP) and oxygen under influence of light [1]. All food we eat is a product of this photosynthesis. Another field where light plays an important role is in medical science. Laser light is used in many therapies [2]. Laser therapy is not only applied for cosmetic surgery or tattoo removal but also in skin wound healing, dentistry and many serious diseases as cancer and arteriosclerosis.

These examples demonstrate that not only light is essential for life on earth but also stresses the importance for humans to manipulate light. Mankind is continuously trying to imitate nature or in more friendly words "to use nature as a source of inspiration". Whereas nature is able to convert light into energy with a high efficiency, researchers are still trying to harvest solar energy in an efficient way by the use of the basic chemistry of photosynthesis. Aspects such as self-cleaning, utilization of the complete sunlight spectrum and lifetime of solar cells are nowadays high priority topics [3]. This example clearly illustrates that if light can manipulated, it would be interesting for a variety of research fields such as (photo)chemistry, biology, and physics.

Light is affected by objects that surround us by several means. Absorption, emission, reflection and scattering of light of certain distinct wavelengths occur,

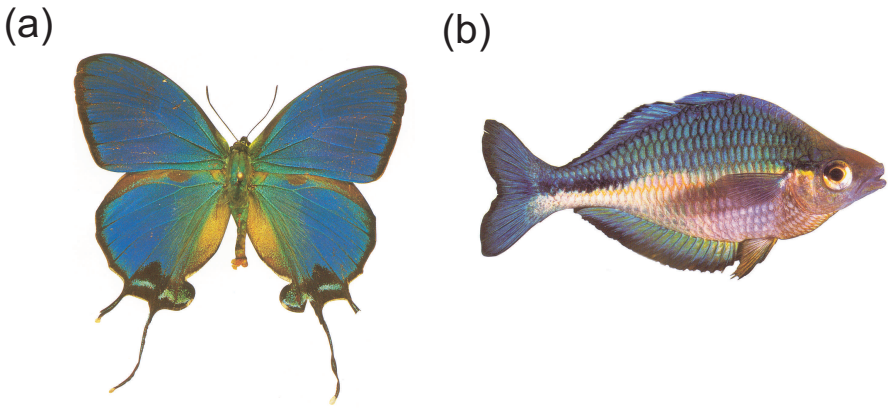

FIGURE 1.1: *Photographs of examples of iridescence caused by interference from multilayer structures with periodically varying refractive indices. (a) Butterfly Thecla Coronata, belongs to the family Lycaenid, commonly known as Ecuador hairstreak [4]. It owes its blue iridescence to a multilayer structure of air and cuticle. (b) Melanotaenia lacustris or Lake Kutubu Rainbow [5]. Due to a structure of periodically varying refractive index of air and chitine the incident light is Bragg diffracted and the reflected light appears in a rainbow of colors. Pictures reprinted with permission [6].*

and appear to the eye as a color appearance of an object.[1] If a color appearance of an object is created by absorbance of specific wavelengths, the wavelengths that are not absorbed determine the color of appearance; white materials do not absorb visible wavelengths whereas black material absorbs all visible wavelengths. Emission of light by substances such as pigments that are present in the material, can also cause the color appearance of an object. In nature and every day life many examples of absorption and emission are encountered; a Ferrari car is red since the pigment *perylene*, present in the finish, absorbs green light and emits red light [8, 9]; grass is green since the chlorophyll absorbs blue and red light and emits green light [10].

The appearance of a blue sky is explained by a completely different phenomenon: scattering. Particles that are smaller than the wavelength of light and present in the sky cause the blue part of the emitted spectrum of the sun to be scattered more than the red part of the spectrum, causing a blue appearance [11]. This phenomenon is also called Rayleigh scattering. Another example of scattering is present in the

[1] Although light of a certain distinct wavelength has a particular color, it can not be said vice versa that a color corresponds to one specific wavelength. The color vision is determined by a collection of physical, photochemical and psychological phenomena such as the intensity of the light and the sensitivity of the eye [7]. That's why we speak in this chapter of a color appearance and not about specific colors.

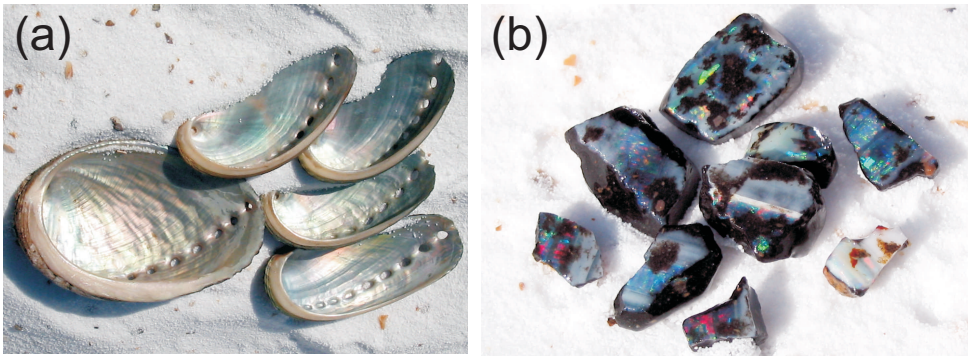

FIGURE 1.2: *Photographs of examples of natural opalescence. (a) Shells of the Haliotis asinina, or "sea ear", which are very common in the Indo-pacific Ocean. The mother-of-pearl consists of alternate layers of calcium carbonate and conchiolin, that are deposited during respectively the summer and the winter, and from which the light is reflected. (b) Mexican opal from the mines of Queretaro in Mexico [13]. Beautiful opalescence is apparent due to constructive interference from periodically arranged glass spheres.*

white appearance of milk and also clouds; since the light is multiply scattered in a random way the material appears white instead of transparent [12].

A color appearance can, however, also result from reflectance of specific colors from the physical structure of the material. Due to constructive interference from a plane, a thin layer, or a collection of ordered lattice planes in the material, light with a certain wavelength is reflected causing appearance of a color. If such a structure is illuminated with white light, the light is reflected under different angles and the incident white light is split up into its spectral colors. This phenomenon is also known as iridescence. A thin layer of oil on water is a beautiful example of this iridescence, the light is reflected from the frontside and the backside of the oil layer since there is a change in refractive index at both sides; from air to oil and from oil to water. The reflected waves interfere constructively and cause a rainbow-like color appearance. Other examples of iridescence in nature are butterfly wings [14] or fish-scales. In figure 1.1(a) the butterfly wings reflect blue-greenish colors due to the wing structure consisting of discrete multilayers of cuticle and air. Figure 1.1(b) displays a rainbowfish with a hue of colors. White light, for instance sunlight, hits the scales that consist of polygonal stacks of transparent chitinized plates, the light is split by diffraction and refraction causing a rainbow-like appearance. It should be noted that the color of appearance can additionally be caused by the presence of pigments. Both color expressions can occur simultaneously. Other examples of iridescence caused by constructive interference that occur in nature are the feathers of hummingbirds, reptiles, insects or minerals [15–17].

If in addition to iridescence also some random scattering takes place, due to for instance imperfections, the phenomenon of constructive interference is called opalescence. The iridescence has then a milky appearance. Opalescence in nature is widely known from mother-of-pearl or gemstone opal [18], and in figure 1.2 beautiful examples are shown of such natural opalescence. Figure 1.2(a) displays shells of the haliotidae family, also called "sea ear". The opalescent appearance is caused by alternating layers of anorganic, calcium carbonate, and organic, conchiolin, material. These materials are formed due to seasonal fluctuations, where the anorganic material is deposited during the summer and the organic material during the winter. In figure 1.2(b) a photograph of noble opal is shown. All colors of the rainbow are present. The microscopic structure of these opals consist of periodically arranged glass spheres, organized in a three-dimensional (3D) ordering.

Light can be described as a wavelength λ or as a frequency ω in electromagnetic oscillations per unit time and has typical length scales of λ = 400-1000 nm, corresponding to frequencies of ω = 3-7,5 THz (THz = 10^{12} s^{-1}). For comparison computers nowadays have processors that work at a clock speed of ω = 3.2 GHz (GHz = $10^{9}s^{-1}$) [19]. If the frequencies of light are considered to be the (maximum) speed with which light can be manipulated, it illustrates that studying light interaction and transport is an excited subject to investigate.

In this thesis we will discuss and investigate structures, so-called photonic crystals, that are engineered to show interference effects, while in addition scattering effects take place. Due to the strong interaction of these photonic crystals with light they exhibit characteristics that can influence the emission of light sources. We probe the possibility of these photonic structures to manipulate light emission by investigating the fluorescence from dye-doped photonic structures.

1.2 Bragg diffraction

In our research we are highly interested in reflection appearances caused by constructive interferences from a multilayer system. As will become clear in the next section, these interferences can lead to phenomena that influence light in an exceptional manner. Constructive interference of reflected waves was first described by Sir Lawrence Bragg and is illustrated in figure 1.3. The condition under which a light beam reflects from a crystal lattice is

$$x\lambda = 2d \sin\theta \tag{1.1}$$

known as Bragg's law or Bragg's condition [20], where x is an integer number (the order of the reflection), λ the wavelength of the waves, d the lattice spacing and θ the angle of incidence between the beam and the lattice plane. When the

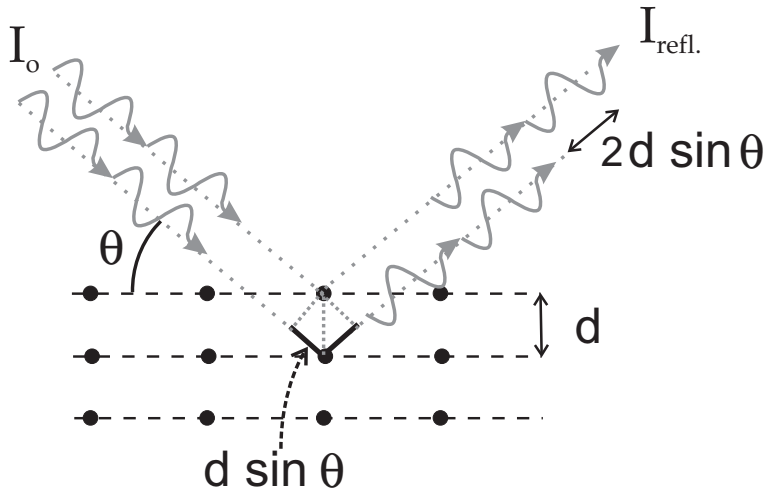

FIGURE 1.3: *The principle of Bragg diffraction from lattice planes. Incident waves are diffracted at the lattice planes and constructively interfere if the path length difference is exactly an integer number of 2d sinθ.*

path length difference of these reflected waves is equal to an integer number of wavelengths x, the waves constructively interfere and the wave with that certain wavelength is amplified. In figure 1.3 the scattered or reflected waves from the crystal planes have a path length difference of $2d \sin\theta$ and interfere constructively after they are reflected from the structure.

Bragg diffraction was first described for X-rays where atomic lattices caused these interference phenomena [20]. The technique of X-ray diffraction is based on this principle, where a crystalline material reflects X-rays under characteristic angles, appearing as intensity peaks as a function of 2θ.

For visible light this same principle of Bragg diffraction holds. Here the crystal lattice does not have lattice constants on the order of angstroms (10^{-10} m) but the lattice consists of a periodicity on 500 nanometer (10^{-9} m) length scales. Therefore no X-rays are reflected but wavelengths of visible light. Since white light contains all visible wavelengths, a beam of white light that is illuminating the crystal planes under different angles, will result in different reflected colors. This phenomenon is called iridescence and when scattering takes place simultaneously it is called opalescence. A natural opal, a crystal of periodically arranged glass spheres, is a beautiful example where this opalescence occurs [18]. The material of the spheres is transparent for optical wavelengths, but the spheres are arranged as a 3D grating, causing Bragg reflection to occur.

The nice colored photonic crystals are exactly accounted by this same phenomenon. The crystals do not absorb light, which is very important, but reflect light of a certain wavelength that is thus excluded from the crystal.

1.3 Photonic crystals: strongly interacting with light

Photonic crystals are 3D composites of dielectric materials with a periodicity in refractive index on length scales of the wavelength of light [21–24]. Due to this periodic variation in refractive index, the light is diffracted and interferes constructively. When a crystal is perfectly ordered, diffraction can occur for nearly 100 % of the incoming light, where all the light of a specific wavelength is reflected and not lost due to absorption or diffuse scattering. The reflectivity can for instance be measured by illuminating the photonic crystal with a white light source; the reflected wavelength will then manifest as a peak in the reflected spectrum. This light can not penetrate into the crystal, and is excluded from propagation in the crystal. Such a forbidden wavelength range in one direction is called a stop gap.[2] How such a stop gap develops can be explained with figure 1.4. For a one-dimensional photonic crystal consisting of alternately a layer of n_1 and n_2, the situation is depicted where an incident wave with a wavelength that is equal to the periodicity in refractive index in the crystal, illuminates the crystal. Since the incident wave has a wavelength that corresponds with the lattice spacing of the crystal as in Bragg's law, i.e., $\lambda = 2d$, the wave is reflected. The incident and reflected wave have identical wavelengths and interfere with each other while travelling in opposite directions, and they build up a so-called standing wave. Standing wave (1) has its antinodes in n_1 and nodes in n_2 and is predominantly in n_1 whereas in standing wave (2) predominantly is in the material with n_2. Both standing waves have identical wavelengths but mainly exist in a different medium, n_1 or n_2. Since the frequency of light ω is equal to

$$\omega = \frac{c}{n} \cdot k = \frac{c}{n} \cdot \frac{2\pi}{\lambda} \tag{1.2}$$

where c is the speed of light, n the refractive index and λ the wavelength, both standing waves have a different frequency. Wave vector k represents the number of periods per length along a certain direction. Generally it can be said that in a crystal with periodically varying refractive indices, there are two frequencies at a given wavelength at the Bragg condition.

It appears that due to these two different frequencies at the Bragg condition, a stop gap opens up as displayed in figure 1.5, where the higher frequency corresponds to the wave in n_{low} and the lower frequency to the wave in n_{high} (recall

[2] If this wavelength range is determined experimentally it is called a stop band.

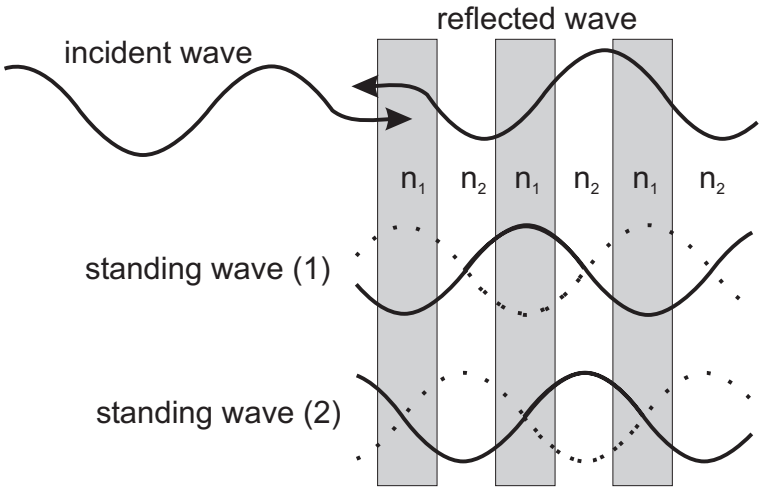

FIGURE 1.4: *A scheme demonstrating light propagation in one-dimensional crystals with periodically varying refractive indices. Since their is a incident and a reflected wave that interfere with each other, a standing wave is developed with antinodes in either material* n_1 *or in* n_2*. This illustrates that at one wavelength, two frequencies can exist.*

equation (1.2)). The wave vector on the x-axis is directed along the direction of the wave propagation and inversely proportional to the wavelength. At π/a, where a is the lattice constant, a "forbidden" frequency range is developed. In this frequency range, light with a wavelength corresponding to a/λ cannot exist in the crystal and is therefore excluded. When no periodicity in refractive index is present which is the case in free space or vacuum, the behavior of frequency with wavelength is linear, plotted in figure 1.5 as a gray dashed line. In the right panel of figure 1.5 a reflectivity peak from a photonic crystal is plotted. At the position of the stop gap a peak manifests; the light with this frequency and along this direction cannot enter the crystal and is reflected.

The width of the stop gap, i.e., the width of the reflectivity peak, denoted as $\Delta\omega$ is a very important measure for photonic crystals. This width is indicated in figure 1.5 with an arrow. To classify the interaction strength of photonic crystals with light, a parameter was invented; the photonic parameter Ψ. The photonic parameter or photonic strength describes the polarizability per volume and can be expressed as

$$\Psi = \frac{\Delta\omega}{\omega} \propto 3\phi\frac{m^2-1}{m^2+2} \tag{1.3}$$

where $\Delta\omega$, ω_0, ϕ and m are respectively the width and the center frequency of the stop gap, the volume fraction of the high index material and the refractive index

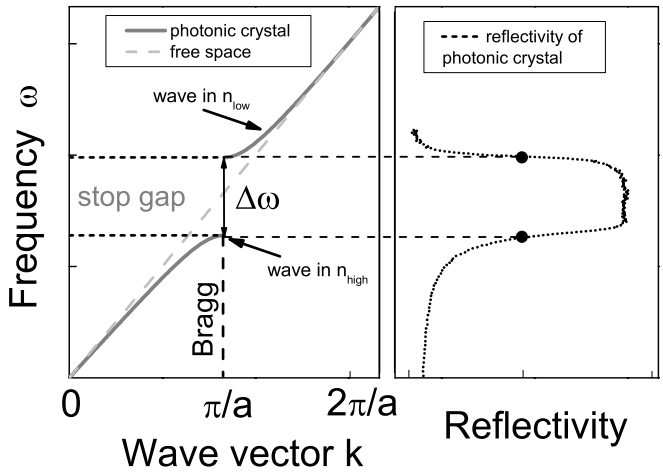

FIGURE 1.5: *At the Bragg condition there are two standing waves, one in n_{high}, and one in n_{low}. A stop gap is developed, a range where no frequency can exist. For comparison the frequency behavior of a homogeneous dielectric is plotted, where the relation with the wave vector is linear. In the right panel the reflectivity peak is plotted, i.e., the stop band, of a photonic polystyrene opal that is illuminated with white light. The reflected light appearing in the spectrum is excluded from the crystal and corresponds to the frequencies of the stop gap.*

contrast between the low and high index material. This photonic parameter was developed by Vos *et al.* in 1996 [25, 26]. As can be seen from equation (1.3), the photonic parameter is strongly influenced by the refractive index contrast m and the volume fraction of the high index material ϕ. A high refractive index contrast results in a wide stop gap and thus a large photonic strength. For small refractive index contrasts the stop gap is very small or will even vanish. Strongly photonic crystals are defined in this thesis as crystals with a photonic parameter that is large enough to have modifications in the density of states (see for density of states section 1.5), corresponding to $\Psi > 6$ %. For comparison atoms in a crystal lattice interact less strongly with X-rays and result in much lower values of $\Psi \sim 0.01\%$. In chapter 3 the photonic parameter will be discussed in more detail.

1.4 Photonic band gap

A stop gap is described for propagation of light along one direction; when a stop gap is present in all directions simultaneously, a photonic band gap is created; the light can not propagate in any direction for a certain frequency range. This phenomenon was first described in the eighties by Yablonovitch [21] and John [22]. In the left panel of figure 1.6 the situation of a photonic band gap is depicted. The schematic stop gaps are plotted for a two-dimensional (2D) square lattice, to simplify the graph. The forbidden frequencies along three different directions, (0,1), (1,0) and (1,1) are plotted as a function of propagation direction. At a specific frequency range all stop gaps overlap, in the figure plotted as a hatched horizontal bar, and this is called a photonic band gap. At this frequency range the light cannot propagate along *any* direction in the photonic crystal, and the light with this frequency cannot exist in the crystal. From figure 1.6 it is clear that if the width of the stop gaps are too small, they will not overlap at all angles, and no photonic band gap is developed. The importance of the relative width was already outlined in the previous section. When a photonic band gap is present in a 3D structure, very interesting phenomena will develop where emission of photons can be inhibited.

1.5 Photonic band gap and spontaneous emission

Spontaneous emission is a process in which an emission source, such as an excited atom or dye-molecule, loses energy under emission of a photon. The spontaneous emission or decay of a light source, depends strongly on the surrounding medium [27]. Fermi stated already in 1932 that the decay can be treated as a transition between two states that depends on the strength of the coupling between these two states. His theory is now well-known under the name of Fermi's Golden Rule where properties of the material and the position of the source are included [28]. The radiative decay rate γ_{rad} of a transition from an initial to a final state at position r is described by Fermi's golden rule as:

$$\gamma_{rad} = \frac{1}{\tau} = \frac{2\pi}{\hbar^2} \sum_f |\Psi_f H(\vec{r}) \Psi_i|^2 \, \delta(\omega_f - \omega_i) \tag{1.4}$$

where $\hbar$ is Planck's constant, Ψ_i and Ψ_f the wavefunctions of respectively the initial and the final state and, τ the excited state lifetime. H is a operator that contains the transition dipole moment $\vec{\mu}$ of the transition and the electric field $\vec{E}(\vec{r})$ of the surrounding medium at that position, $H = \vec{\mu} \cdot \vec{E}(\vec{r})$.[3]

[3]The electric field $\vec{E}(\vec{r})$ depends on frequency ω, dielectric contrast ϵ (= n^2) and volume V as $E \propto \sqrt{\frac{\hbar\omega}{\epsilon V}}$.

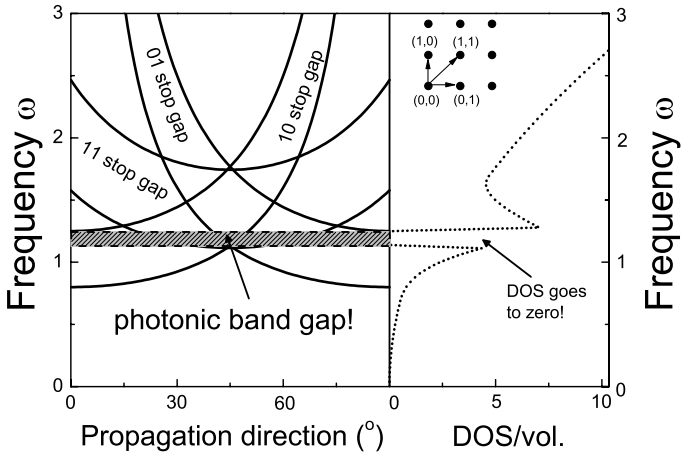

FIGURE 1.6: *Schematic stop gaps of a 2D square lattice; if the stopgap is present in three dimensions simultaneously, displayed in this figure with stop gaps in the (1,1), (1,0) and (0,1) directions in the small panel, a photonic band gap is developed. At this frequency range the stop gaps overlap and light is excluded along all directions. The stop gaps displayed here, are from a 2D square lattice. In the right panel the schematic DOS of a 3D photonic crystal is plotted. At the position of the photonic band gap the DOS vanishes and goes to zero. In this frequency range there are no modes for a light source to decay. It should be noted that such a strong modification of DOS only occurs for 3D photonic crystals and not for 2D.*

Fermi's golden rule sums over all available final states f [29]. The delta function $\delta(\omega_i - \omega_f)$ describes the conservation of energy; a photon can only be emitted if its energy agrees with the energy difference between the final and initial state.

If the coupling between the initial and final state is stronger, a transition will proceed more rapidly. This happens if there is more interaction between the dipole moment of the transition and the electric field of surrounding medium. In a material with a higher refractive index, i.e., a larger electric field, the interaction between final and initial state will therefore be stronger, resulting in a shorter lifetime. A beautiful example of influencing the coupling between the final and initial state is demonstrated in reference [30]; the decay of rare earth ions was clearly influenced by their surrounding medium that consisted of alcohols with different refractive indices. This clearly illustrates that the decay of a light source is strongly determined by the chemical environment. It should be noted that Fermi's golden rule is

not only applicable to fluorescence decay of light sources but also to for instance nuclear decay and many other physical transitions.

Equation (1.4) can be rewritten in a part related to the atom itself and a part related to the position dependent field as

$$\gamma_{\text{rad}} = \frac{1}{\tau} = \frac{2\pi}{\hbar^2}|\Psi_f H \Psi_i|^2 \, \rho(\omega, r) \tag{1.5}$$

where the part $|\Psi_f H \Psi_i|$ describes the coupling between the initial and final state (atom part) and $\rho(\omega, r)$ is the position dependent part also called local density of states (LDOS) [31]. Equation (1.5) describes that not only the chemical environment, included in $|\Psi_i H \Psi_f|$, determines the emission properties but also the spatial position of the light source plays an important role. In particular the *radiative* lifetime is strongly determined by the density of available light modes at that specific spatial position, the LDOS. If the LDOS is large compared to the vacuum, the emission is enhanced since there are more modes for the excited state to decay. In the case of a small LDOS the reverse occurs; the emission is inhibited. Modification of the LDOS is therefore a very interesting subject for research since the spontaneous emission can be influenced. Exactly this LDOS is strongly modified in photonic crystals.

The effect of a modified LDOS in photonic crystals was first described by Suzuki and Yu and by Sprik *et al.* [31, 32]. In photonic crystals the LDOS is changed in such a way that the emitted light from an embedded emission source is strongly modified; either enhanced or inhibited. In the case of a photonic band gap the LDOS is extremely modified and even goes to zero and spontaneous emission can be inhibited. Apart from inhibition or enhancement the light can also be localized. Localization of light occurs when the emission source is placed in a defect. In this way the light source can emit a photon but this photon cannot exit the defect.

Since performing LDOS calculations for a photonic crystal is quite complicated, often total density of states (DOS) calculations are done. The total DOS in free space is equal to

$$\rho(\omega) = \int dV \rho(\omega, r) = \omega^2/\pi^2 c^3. \tag{1.6}$$

where the LDOS is integrated over a volume V of an unit cell. A clear distinction should be made between LDOS and the (total) DOS. The total DOS is the averaged LDOS over one unit cell. Often the terms LDOS and DOS are randomly used but an unchanged total DOS is not necessarily an unaffected LDOS, so a crystal can still contain positions where the LDOS is going to zero, resulting in inhibited emission. As an example the schematic DOS of a photonic crystal as function of frequency is plotted in the right panel of figure 1.6. The DOS is plotted

per volume in units s/m^3. At the position of the photonic band gap the DOS goes to zero. It can also be seen that near the edges of the photonic band gap the DOS is increased.

The DOS for an emitting species in free space has an ω^2 behavior (see equation (1.6)), and is displayed in figure 1.7 as a black dotted line. The total available modes per volume are plotted as a function of a/λ where a is the lattice parameter of the photonic crystal. The DOS of free space displays an ω^2 behavior. Since the decay rate and therefore the lifetime is directly related to the DOS *and* Fermi's golden rule, an emitter in a homogeneous dielectric would show an ω^3 trend between lifetime and frequency. For comparison the calculated DOS are plotted for a photonic crystal consisting of air spheres in titania (TiO_2). The refractive index contrast is taken to be $n_{\text{titania}} = 2.55$ with a volume fraction of solid material of $\phi =$ 11 % v/v.[4] Right above 0.7 a/λ the first order stop gap is expected to appear. At this position a clear increase in DOS followed by a decrease is apparent. This is also referred to as the pseudo gap since it was demonstrated that the photonic band gap will not yet appear at this wavelength as was calculated by references [34, 35]. The second order stop gap develops just above 1.2 a/λ. Obviously larger deviations, decreases and increases, in the DOS are apparent. The photonic band gap is expected to appear at this wavelength. Since the refractive index contrast m for this face centered cubic (*fcc*) air-sphere crystal of titania is not large enough to create a photonic band gap, the DOS does not decrease to zero. For calculations done with a refractive index contrast of $m = 3.0$, resembling with for instance an air-sphere crystal of silicon, it was demonstrated that the DOS vanishes at this second order Bragg diffraction [33–35].

Modification of spontaneous emission was first observed by Drexhage and coworkers who measured emission rates from europium ions near a metallic surface [36]. Attenuation and enhancement of spontaneous emission was later intensively studied by the use of cavities, investigated in the field of cavity quantum electrodynamics (QED) [37]. The essence of cavity QED is that an atom or atoms are stored in an enclosure which has dimensions comparable to emission wavelength of atoms. Therefore, compared to atoms in free space, the atoms couple to either smaller or larger electric field modes. If emission exists at the resonant wavelength the emission is greatly enhanced while off-resonance emission would be inhibited. It was demonstrated that the DOS in optical microcavities [38] and near surfaces [39] shows large changes and several research groups already observed large effects in emission decay rates. To create a photonic band gap, however, a 3D photonic crystal is necessary.

[4] DOS calculations are performed by Femius Koenderink, see reference [33].

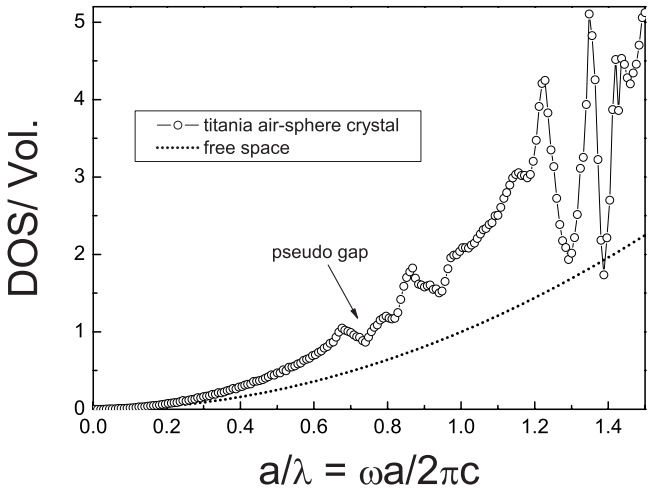

FIGURE 1.7: *The total DOS per volume of a titania air-sphere crystal as a function of a/λ. For the calculation a volume fraction ϕ and a refractive index contrast m of respectively ϕ = 11% v/v and m = 2.55 is assumed. At the first and second order Bragg, respectively at 0.7 and 1.2 a/λ, the DOS is clearly attenuated. As a comparison the DOS of free space is plotted which exhibits a ω^2 behavior.*

To observe the effect of the photonic band gap on spontaneous emission in photonic crystals, an emission source must be placed inside such a photonic crystal [40]. Recently more and more groups investigate the spontaneous emission of light sources in photonic crystals and this will be discussed in more detail in chapter 6. The control of spontaneous emission is a very interesting phenomenon. Enormous innovative advances can be made like thresholdless miniature lasers [21]; if the DOS can be manipulated to the point that there is only one mode to decay there would be no decay into other modes and lasing occurs into that one mode without loss.

Photonic crystals are also suggested in chemical applications such as solar cells and other fields of photochemistry. While the efficiency of dye-sensitized solar cells was already demonstrated by Grätzel and co-workers [41], very recently Nishimura *et al.* [42] demonstrated enhanced light harvesting efficiency by coupling a titania photonic crystal layer to a conventional film of titania nanoparticles. The titania photonic crystal acts as a dielectric mirror but also turned out to influence the dye absorbance.

The light used in photon-induced conversion reactions, will also be manipulated by photonic crystals, and therefore influence the reaction. If a reaction takes place in a macroporous photonic crystal, the light that induces this reaction is enhanced by an increased DOS (see figure 1.7) and reduced at a decreased DOS. Different DOS values at different frequencies could be used to create different changes in reaction rates or yields, depending on which reaction path is associated with which optical frequency.

From a material chemistry point of view photonic crystals made from semiconductors such as titania are an interesting subject for research [43]. From titania it is known it exhibits photocatalytic activity when irradiated by ultraviolet light, under which the titania can decompose organic products [44]. In combination with the macroporosity and the beautiful opalescence of titania air-sphere crystals, this can lead to interesting applications. In addition macroporous photonic crystals can effectively act as zeolites for large molecules; in this way separation chemistry can be combined with photochemistry or photocatalysis.

1.6 Air-sphere photonic crystals

Probably the most important quantity for photonic crystals is the refractive index contrast m between the two materials present, as is also illustrated by equation (1.3). A high refractive index contrast will result in a large photonic strength Ψ and this assures that the stop gaps in three directions will have a large overlap and the photonic band gap is wide. Usually photonic crystals are made with a combination of a high refractive index material and air. High refractive index materials can consist of semiconductors such as silicon, germanium, galliumarsenide and metaloxides and have refractive indices of $n > 2$, whereas air exhibits a low refractive index of $n = 1$. It should be considered however that a high refractive index usually is associated with a large energy gap. Since for photonic crystals absorption of light is not favorable the energy gap should be as low as possible. In figure 1.8 the relation between the refractive index and the energy gap is plotted. It can be seen that materials with high refractive indices, such as silicon, have a large energy gap and start already to absorb right below $\lambda \sim 1200$ nm. For applications with visible light these materials are therefore not suited. Materials that are interesting for optical applications have absorption edges below 450 nm. The relation between refractive index n and energy gap E_g is empirically described by Moss' rule [45] as

$$n^4 \cdot E_g = 77. \tag{1.7}$$

The behavior of Moss rule is plotted as a black line and is on the lower edge of the data points. From this figure it is also clear why materials as titania (TiO_2)

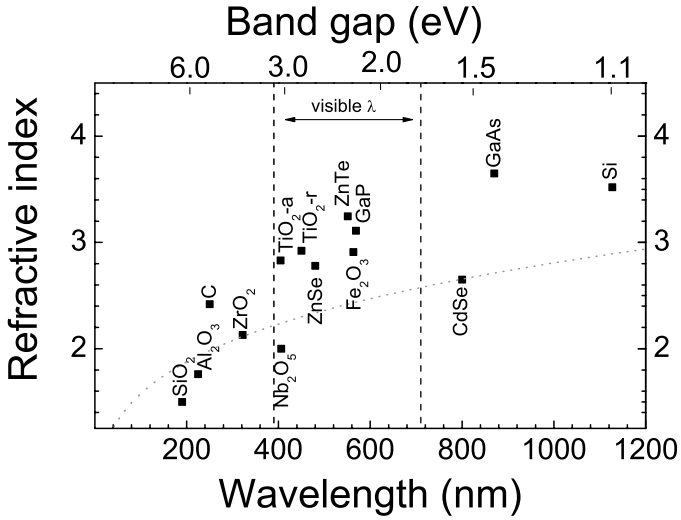

FIGURE 1.8: *The relation between the refractive index and the absorption edge of several semiconductors. A higher refractive index goes with a larger band gap. The metaloxides as TiO_2, ZrO_2 (zirconia) and SiO_2 (silica), used in our research have typical absorption edges below 450 nm. Data are taken from references [47, 48]*

and zinctelluride (ZnTe) are advantageous to use for photonic crystals. They have a relatively large refractive index and are partly transparent at optical wavelengths. In our research titania is used as backbone for photonic crystals, prepared via liquid precursors. Although zinctelluride turned out to be an attractive candidate, several attempts to fabricate zinctelluride photonic crystals via electrochemical deposition were unsuccessful [46] and will not further be discussed in this thesis.

In the past numerous photonic crystals were developed [23, 24]. Although 3D photonic crystals are necessary for creating a photonic band gap, many groups are also interested in 2D photonic crystals. These 2D structures do not confine light in all directions but can perfectly guide light into one certain direction. Examples are photonic crystal fibres [49]. A photonic crystal fiber consists of a hollow core enclosed in a photonic crystal structure. The wavelengths in the range of the stop gap of the enclosed structure are Bragg reflected and the light travels along the effectively infinite third dimension with very low losses. Other 2D structures, such as photonic crystal waveguides, can also guide light in one dimension. Visible light guidance in dielectric slabs with a lattice of air rods was previously investigated in near- and far-field [50], whereas waveguides consisting of regularly positioned pil-

lars of high index material, reported guidance of electromagnetic waves [51]. Even sharp bends around a 90° corner are reported [52, 53]. All these 2D structures manipulate light propagation strongly but will never be able to modify the spontaneous emission completely. Only a 3D structure can develop a photonic band gap and therefore the DOS and the spontaneous emission are strongly modified, provided that the refractive index contrast is large enough. For *fcc* close-packed structures it was calculated that the contrast $m = n_1/n_2$ should be at least $m = 2.8$ [35] whereas for a crystal with a diamond structure $m = 2.0$ will fulfill [54]. Until now, no one was ever able to make a diamond lattice for photonic crystal applications but the *fcc* crystal structure is widely used. For these *fcc* photonic crystals, artificial opals are usually applied as a template [55, 56]. Artificial opals consist of close packed nanometer sized particles of a high refractive index material. Since it is essential for developing a photonic band gap to have the high refractive index material in minority, an inverted structure is made which consists of interconnected air spheres in a solid backbone. These inverted opals are also called air-sphere crystals [57, 58] and already have proven to be very effective photonic crystals in which light is strongly modified. We note that besides ordered structures also disordered media experience a lot of attention for their optical phenomena, as already described by Anderson [59]. In these structures the light is randomly scattered and if the distance between scattering events becomes shorter than the wavelength of light, the light cannot propagate and is localized [59–61].

1.7 Outline of this thesis

In this thesis the fabrication and characterization of opal and air-sphere photonic crystals is described. Subsequently the fluorescence of light sources embedded in these photonic structures is investigated.

• Chapter 2 discusses the implementation of light sources on materials that are used as photonic crystal backbones. The materials that are investigated are polystyrene and metaloxides as titania and silica. The fluorescence behavior of the high efficiency light source rhodamine 6G (R6G) on these materials is characterized by means of fluorescence lifetime measurements, where the quantum efficiency of the light source turns out to be an important factor.

• Chapter 3 describes the preparation and characterization of air-sphere photonic crystals of several metaloxides. The synthesis of these air-sphere crystals is studied, where building blocks, template and other intermediate products are characterized in detail. Electron and optical microscopy, X-ray diffraction and absorption, and reflectivity measurements are performed to illustrate the high quality of the air-sphere crystals.

• Chapter 4 takes a closer look at the process of air-sphere crystal preparation and possible inhomogeneities that can arise during the preparation. Air-sphere crystals of hybrid oxides are fabricated and the spatial distribution of both materials is investigated with energy dispersive spectroscopy. The inhomogeneities are characterized from mm to 100 nm length scales.

• Chapter 5 presents fluorescence spectra of R6G dye embedded in polystyrene opals and alumina (Al_2O_3) inverse opals. The stop gap provides us information about the quality and the photonic strength of the crystal, these fluorescence measurements are very important. In this chapter the first experiments on fluorescence from photonic crystals with second order Bragg diffraction are described. Since in this second order range the photonic band gap will finally occur, this is of utmost importance. The results are explained and compared with previously performed reflectivity measurements and band structure calculations.

• Chapter 6 discusses measurements on fluorescence lifetimes of R6G dye embedded in the same photonic crystals as investigated in chapter 5. Especially the homogeneous linewidth of the dye and reabsorption probability of emitted light in photonic crystals are studied.

Chapter 2

Light Sources on Photonic Crystal Constituents

2.1 Introduction

Since the photonic band gap can strongly influence the spontaneous emission of light sources inside these photonic crystals we should consider the different source positions in the crystal. The emission properties of light sources strongly depend on their spatial position in a photonic crystal, as first described by Suzuki and Yu [32] and Sprik *et al.* [31]. In particular the radiative lifetime of a source is determined by the local density of states (LDOS), i.e., the density of available light modes at a spatial position in a narrow wavelength bandwidth. Possible ways to put a light source in an air-sphere photonic crystal are depicted in figure 2.1. One possibility is to place the light source in the center of the air sphere represented as position A. This can be achieved by the use of for instance an atomic vapor that can move freely through the air holes. The light sources can also be built in in the solid backbone, as position B displays. References [62] and [63] describe how to incorporate dye in a silica matrix. Such an incorporation of a light source should be done during the air-sphere crystal preparation. Another possibility is to deposit light sources on the inner surface of the air spheres, displayed as position C. This deposition can be achieved by simple adsorption of a light source from a solution after the air-sphere crystal synthesis is completed [64, 65].

Emission sources used to probe density of states (DOS) effects resulting from the photonic band gap, have to meet several requirements. First of all the emitter

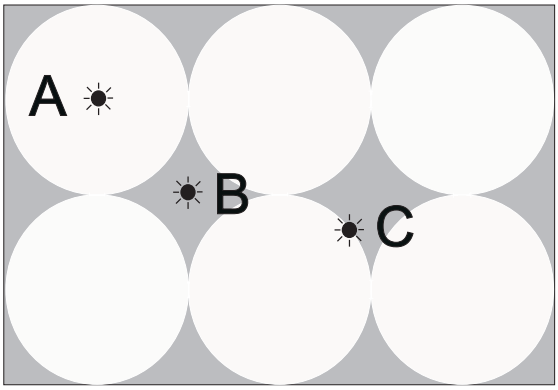

FIGURE 2.1: *Schematic drawing of possible positions for an emission source in an air-sphere crystal. A light source in the center of the air sphere, displayed as position A, is achievable by an atomic vapor. Position B displays the light source in the solid backbone and can be achieved by incorporation. Position C displays the light source on the inner surface of the air sphere and is achievable by adsorption.*

should be efficient, i.e., possess a high quantum efficiency, to investigate spontaneous emission dynamics [65]. Secondly, to ensure that emission from inside the photonic crystal is measured, the emission from the surface should be removed, also called "bleaching", so the emission source should be able to be bleached. Thirdly the excited state lifetime should not be too long, i.e., exhibit a large oscillator strength [66], to allow interesting interferences between sources and their emitted photons. Two other important quantities in lifetime measurements are the homogeneous and inhomogeneous linewidths, respectively Γ_{hom} and Γ_{inhom}. A broad inhomogeneous spectrum is desirable for photonic experiments since it can cover the whole band gap, a broad homogeneous linewidth, however, is not desirable for lifetime measurements. A small homogeneous linewidth is present if the energy distribution of the transition is small. In this way the (inhibited) emission can be probed exactly in this narrow band, in other words, the homogeneous linewidth should be smaller than the changes in the density of states.

Possible light sources to use in photonic experiments are organic dyes, rare earth ions, quantum dots or atoms. Due to the long lifetimes and the narrow inhomogeneous emission spectra of rare earth ions, and the inability of bleaching rare earth ions, quantum dots, and atoms, we have chosen to use dyes. Dyes usually have high quantum efficiencies, can easily be bleached and they possess broad inhomogeneous and narrow homogeneous emission spectra. Rhodamine 6G (R6G) dye, a very well-known laser dye, exhibits a very high quantum efficiency, values of > 95 % for R6G in ethanol are reported. Typical lifetimes of R6G dye are 3.6

ns [67]. The nanosecond regime allows to have interferences with the emitted photons of the light source. The homogeneous linewidth reported for R6G dye is Γ_{hom} ~ 4 nm [68], smaller than the bandwidth of the changes in the DOS, that usually has a value comparable to the stop band width (~ 40 nm). The inhomogeneous linewidth of organic dyes are generally very broad Γ_{inhom} ~ 150 nm [68, 69].

In this chapter we present measurements of fluorescence emission spectra and fluorescence lifetimes of R6G dye adsorbed on different materials, intended to use for photonic crystals. After adsorbing the dye on these different materials we measure the lifetimes and spectra of the dye to infer the fluorescence properties of the light sources. In this way we are able to determine the applicability of dye on high index materials, of which photonic crystals consist.

2.2 Laser dye R6G in ethanol

In order to check the natural emission properties of R6G, like lifetime behavior with concentration, we first investigate R6G dissolved in ethanol. From R6G in ethanol it is known it has a high quantum efficiency [67, 70].

The emission lifetimes of the dye were obtained using a time-correlated single-photon counting technique [71] described in more detail in chapter 6. The dye is excited with pulsed laser light of wavelength λ = 400, 440 or 520 nm, run by a picosecond Pulsed Diode Laser driver (PDL) from Picoquant. The fluorescence was detected via a Carl Leiss spectrometer over the whole emission spectrum, ranging from 560-645 nm, with a Hamamatsu R3809U Micro Channel Plate (MCP) detector, a time to amplitude converter (TAC) and a multi-channel analyzer (MCA). The time difference between the MCP signal and the excitation pulse from the PDL was recorded by the MCA. The time resolved fluorescence was recorded in 8192 channels covering a time frame of 22 ns. The beam hits the sample with an angle away from the (possible) Bragg angle to ensure penetration into the crystal planes. The emitted photons were collected from the sample in reflection with a detection angle $\alpha = 0°$, corresponding to the normal of the (111) surface. Darkcounts in the time-resolved fluorescence data were determined by averaging the counts before t = 0 and were subtracted. The data were plotted as histograms with an logarithmic y-axis for convenience (see for more details about the set up, figure 6.2 in chapter 6).

In figure 2.2(a) the decay curve of R6G in ethanol is displayed as measured with our set-up. The concentration of the solution was 10^{-5} molar (M) and was kept in a 400 μm thin capillary. The dye is excited at λ = 520 nm and the emission lifetime is measured at the peak fluorescence of R6G, i.e., λ = 560 nm. The decay of the R6G dissolved in ethanol displays a straight line over 2 decades and can be

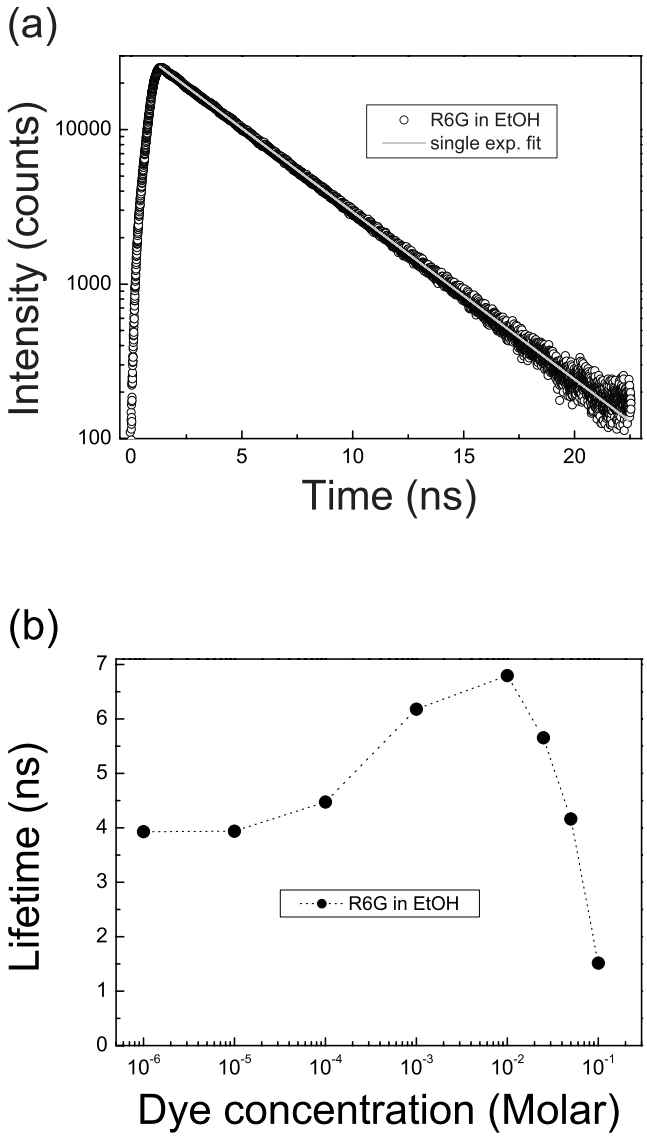

FIGURE 2.2: *(a) Lifetime of R6G in ethanol (10^{-5} M) measured at the peak fluorescence, pumped with λ = 520 nm. The decay curve is well fitted with a single exponential model resulting in a lifetime τ = 4.01 ± 0.01 ns (χ^2 = 1.5). (b) Measured lifetimes of R6G at different concentrations in a 400 μm thin capillary. The dye was pumped with λ = 400 nm. An increase in concentration causes an extension in lifetime due to reabsorption. Above a concentration of 10^{-2} M, self-quenching dominates, which shortens the lifetime considerably.*

fitted with a single exponential model,

$$f(t) = a \cdot e^{-t/\tau_0}, \tag{2.1}$$

where a is an amplitude correlated with the intensity and τ_0 is the lifetime. Fitting the data with this model results in a lifetime of $\tau = 4.01 \pm 0.01$ ns with a chi-squared (χ^2) of 1.5. The χ^2 test is performed to evaluate the goodness of the model applied to the experimental data. The theoretically predicted values were compared with the actual measured values and the deviations between these values were converted to a probability called the chi-squared:

$$\chi^2 = \sum_{i=1}^{n} \frac{(y_{\text{predicted}} - y_{\text{measured}})^2}{y_{\text{predicted}}} \tag{2.2}$$

where n is the number of data points, and y either the measured or the predicted value as a function of x. A large χ^2 is a result from a large deviation of the model from the actual data, and if χ^2 has a small value (~ 1) the model describes the data well. We can therefore conclude that a χ^2 of 1.5 shows the single exponential fit to be a good model for these data [72].

The measured lifetime of R6G in ethanol, $\tau = 4$ ns, as measured in Enschede, appears to be a longer lifetime as expected. The values for R6G lifetime found in literature vary a lot, but usually a value is found of ~ 3.6 ns [68, 73, 74]. This value for τ was also found for previous measurements on R6G in Amsterdam. We checked that the excitation wavelength does not influence the observed lifetime by measuring lifetimes of R6G in solution excited at various wavelengths, i.e., 400, 440 and 520 nm. We only observed a very small deviation in lifetimes for R6G solutions; excitation at $\lambda = 400$ nm results in a lifetime of 3.95 ± 0.03 ns, excitation at $\lambda = 440$ nm in a lifetime of 3.93 ± 0.01 ns and from excitation at $\lambda = 520$ nm we measured a lifetime of 4.01 ± 0.01 ns. A general possible explanation for longer observed lifetimes can be the presence of impurities. To our knowledge, however, this does not explain the observed discrepancies either, since all dye solutions, in Amsterdam as well as in Enschede, were made freshly. We can conclude from our experiments of R6G in ethanol that R6G laser dye is an excellent candidate for lifetime measurements in photonic crystals. R6G displays a decay that is well fitted with a single exponential model and the dye exhibits a high efficiency.

2.3 Reabsorption

To check the important effects of reabsorption of emitted light, we performed lifetime measurements on solutions with different concentrations. All measurements

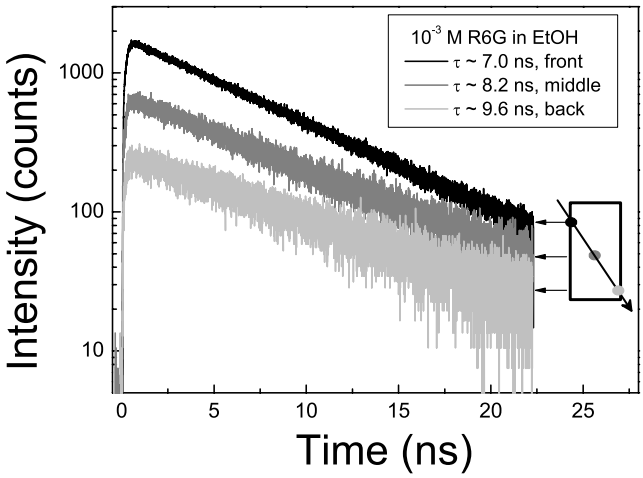

FIGURE 2.3: *Decay curves of the fluorescence from a 10^{-3} M R6G solution in a 1 cm cuvette. The dye is excited at λ = 440 nm. The fluorescence was taken from three different positions in the cuvette, as sketched on the right; from the front where the beam enters the cell, from the middle of the cell, and from the backside of the cell where the beam exits the cuvette. The black arrow indicates the excitation beam. The decay curves could all be well fitted with a single exponential model. The black line represents the surface position of the cell and displays a lifetime of 7.06 ± 0.01 ns (χ^2 = 1.04). The gray line displays a longer lifetime, i.e., τ = 8.23 ± 0.02 ns (χ^2 = 1.08). The light gray curve is the decay measured from the backside of the cuvette and displays a lifetime of almost 10 ns (9.57 ± 0.04 ns (χ^2 = 1.05)).*

were done with a λ = 400 nm pump and the solutions were in 400 μm thin capillaries. In figure 2.2(b) the relation between the lifetime and the dye concentration is plotted. The statistical error bars in the graph appear smaller than the symbols (for all data points less than 0.03 ns). As can be seen the trend in the lifetime is that with increasing concentration the lifetime is increased. Below 10^{-5} M the lifetime of R6G still displays the natural lifetime of ~ 4 ns but at 10^{-4} M the lifetime has already increased to ~ 4.5 ns. The maximum lifetime is observed at a concentration of 10^{-2} M, a value of almost 7 ns is measured. The longer lifetime at higher concentrations is attributed to reabsorption, also called self-absorption [73]. This radiative energy transfer happens when the emitted photon travels through the sample and is absorbed by another dye molecule, with a lower excitation energy,

before exiting the sample. If the amount of dye molecules is larger, the probability of reabsorption is enlarged and therefore the detected lifetime is increased. When the dye-concentration is increased further, above 10^{-2} M, the lifetime decreases as can be seen in figure 2.2. At 10^{-1} M the measured lifetime is even shorter than the natural lifetime of R6G, and was measured to be 1.5 ns. This decrease in lifetime is ascribed to self-quenching, also called Förster transfer. At very high dye concentrations the dye molecules are very close to each other. They interact and finally decay to the ground state without emitting a photon. Due to this dynamic quenching the fluorescent molecule exhibits a much smaller radiative efficiency causing a decrease in fluorescence intensity and quantum yield. Since this collisional quenching is a rate process that depopulates the excited state, the lifetime is also shortened.

A decrease in the count rate could be expected since quenching goes with an increase in non-radiative decay and therefore less intensity would be observed. We were, however, not able to compare differences in absolute count rates, since a lot of measurements were done with different settings.

The χ^2 of the decay of R6G in ethanol fitted with a single exponential model, did not exceed 1.5 for all measurements. Since all measured decay curves could be well fitted with a single exponential model, the question arises if this is understood when reabsorption and quenching is present. In the case of reabsorption a single-exponential could be expected, since the decay can be described as

$$f(t) = a \cdot e^{-t/\tau_{\text{meas}}} = a \cdot e^{-t/\frac{\tau_0}{(1-p)}}, \tag{2.3}$$

where the measured lifetime τ_{meas} is τ_0/(1-p) and p is the reabsorption probability. If the reabsorption probability p increases, the measured lifetime is also increased. For dye concentrations below 10^{-2} M this behavior is expected.

From self-quenching, however, non-single exponential behavior is expected. Both quenched and unquenched molecules are present. Therefore the decay exhibits the natural lifetime as well as quenched lifetimes, resulting in non-single exponential decay. For dye concentrations above 10^{-2} M we observed, however, also single exponential behavior. We are presently unaware of an explanation for this feature.

Hammond demonstrated in the late seventies already that at moderate dye-concentrations, 10^{-3} to 10^{-2} M, self-absorption is a considerable obstacle in accurate measurements of fluorescence decay times [73]. An important quantity is the thickness of the measuring cell where the dye-solution is positioned. He defined experimental conditions where the self-absorption is small and the lifetimes could be determined accurately. An example that clearly illustrates the hypothesis that reabsorption in our solutions is causing longer lifetimes, is shown in figure 2.3.

A thick cell, a 1 cm cuvette, is filled with a 10^{-3} M R6G solution and the dye is pumped with a 440 nm pulsed diode laser. Photons from different positions in the sample were detected as is displayed on the right in figure 2.3. The measurements were taken from three different positions of the cuvette; the front side of the cell, (where the beam enters the sample), the middle of the cell and the backside of the cell (where the beam exits the sample). The decay measured from the front position, the black curve, displays a lifetime of ~ 7.0 ns. When the detection position is moved to the center of the cuvette, displayed as the gray curve, the lifetime is increased to ~ 8.2 ns. The lifetime increases further if we detect the emission coming from the back of the cuvette. Since the light from the back of the cuvette has to travel all along the cuvette and meets a lot of R6G molecules, reabsorption is unavoidable, and the lifetime is extended. In our experiment we even measure a lifetime of 9.6 ns. An estimation on the absorption length l_a of R6G in a 10^{-3} M solution can be made with

$$l_a = \frac{1}{n \cdot \sigma} \tag{2.4}$$

where n is the molar concentration or the density of the absorbers, σ the molar absorptivity or the cross-section of the absorbers and l_a is the absorption length in cm. The molar absorptivity for R6G in ethanol is known from literature [75] and is $10.5 \cdot 10^4$ l/mol/cm. This results in an absorption length of ~ 0.01 cm, a very small value compared to the 1 cm cuvette that is used. Reabsorption has therefore a high probability to take place.

Reabsorption and quenching is illustrated in the Jablonski diagram [76] in figure 2.4. A schematic view of the fluorescence process is illustrated with two dye-molecules, S and A. First a photon of a certain energy $h\nu_1$ is absorbed by a R6G dye molecule (=absorption), creating the S_1 singlet electronic excited state (=excitation). The energy of the absorbed or emitted photons is schematically proportional to the lengths of the arrows. After excitation the dotted arrow downwards indicates the decay to a lower state of S_1, during which the molecule undergoes conformational changes and interacts with its environment (=relaxation). This relaxation is very fast, on the order of 10^{-12} sec, and results in the relaxed singlet excitation state, S_1. Subsequently a photon of a certain energy $h\nu_2$ is emitted (=fluorescence) and the ground state S_0 is reached. Reabsorption takes place when another dye molecule is nearby and absorbs the emitted energy $h\nu_2$ from the excited dye molecule. This process is radiative since a photon is involved, and increases the observed lifetime. Dipole-dipole interactions or Förster transfer, takes place when the dye molecules are close to each other. This transfer is non-radiative since the energy is directly converted from an excited state level of the donor molecule (S) to an excited state level of the acceptor molecule (A) without emitting a photon.

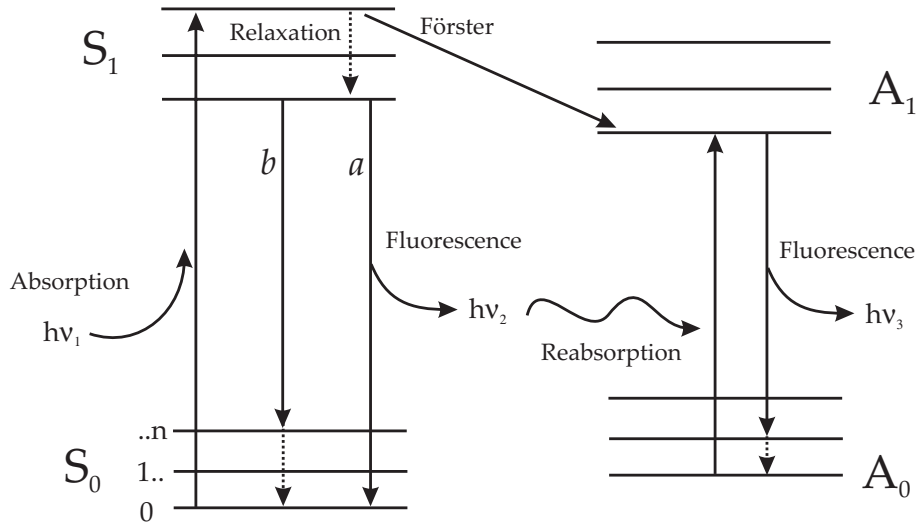

FIGURE 2.4: *Jablonksi diagram of two R6G dye molecules represented by S and A, illustrating the fluorescence process. After absorption of a photon the R6G molecule shifts to the excited state. Under transition back to the ground state a photon is emitted, which can be reabsorbed by another R6G molecule with lower energy. Non-radiative energy transfer (Förster transfer) takes place when the dye molecules are to close to each other; in this process no photon is involved.*

We clearly demonstrated with the experiments on R6G in ethanol that the lifetime of R6G increases with increasing dye concentration. We additionally observed that with increasing sample thickness the lifetime increases as well. These variations in lifetimes with different conditions and concentrations emphasizes the fact that it is very important to ascertain the concentration of the dye molecules in the photonic samples before comparing lifetimes with non-photonic samples.

2.4 Fluorescence of R6G on titania

We demonstrated that the R6G dye is a well chosen candidate for lifetime measurements, therefore the most likely next step is adsorption of R6G dye on the inner surfaces of the titania (TiO_2) backbone in the air-sphere crystal. In this strongly photonic crystal with a high refractive index the emission is strongly modified as was shown previously by Schriemer *et al.* [64] and Koenderink *et al.* [65]. Although in these experiments for the first time angle-independent modification of spontaneous emission was observed, the low fluorescence quantum-efficiency precluded a determination of the radiative decay rate that probes the photonic gaps.

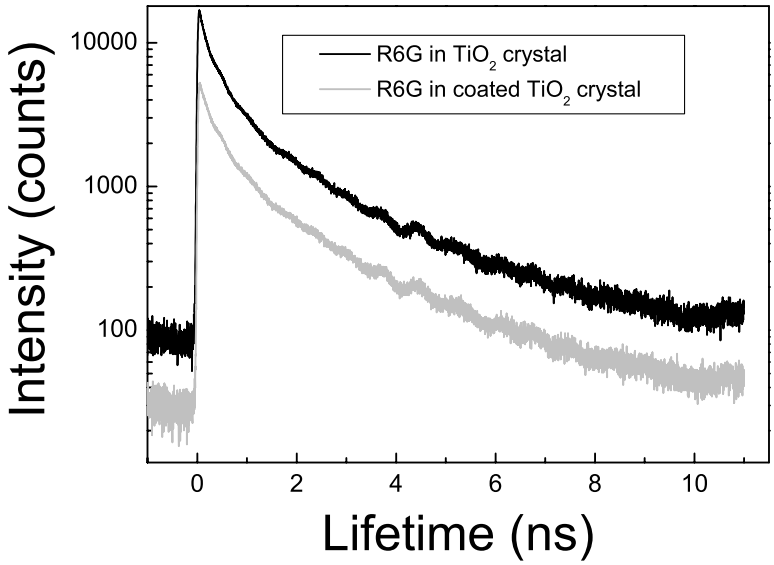

FIGURE 2.5: *Decay of R6G adsorbed in a titania air-sphere crystal (262-52-b) with sphere size r ~ 200 nm. The titania air-sphere crystal is doped with a 10^{-7} M R6G solution and R6G displays a τ_{mean} = 1.48 ± 0.01 ns . Decay from R6G on a silica coated titania air-sphere crystal is also displayed (241-53-a). The crystal is doped with same dye concentration. R6G adsorbed in this crystal displays a τ_{mean} = 1.68 ± 0.01 ns.*

An example of the decay of R6G dye in a titania air-sphere crystal is shown in figure 2.5. The dye is excited at $\lambda = 532$ nm with a set-up as discussed in section 2.5.2. The black curve shows a strong non-single exponential behavior compared to R6G dye in a non-reactive environment, see figure 2.2(a) for comparison. The R6G lifetime in the titania air-sphere crystal is very short with a τ_{mean} of 1.48 ± 0.01 ns. This non-single exponential behavior is ascribed to non-radiative decay γ_{nr}, since the measured lifetime τ_{tot} is a sum of radiative and non-radiative decays: $\tau_{tot} = 1/(\gamma_{rad} + \gamma_{nr})$.

It is known that many molecular species adsorbed on semiconductor surfaces show photochemical reactivity. These photosensitization processes attract a lot of attention from a practical point of view for uses such as solar energy conversion [41, 77, 78]. The organic molecule is excited by light and injects an electron into the conduction band of the semiconductor. This allows conversion from visible light to

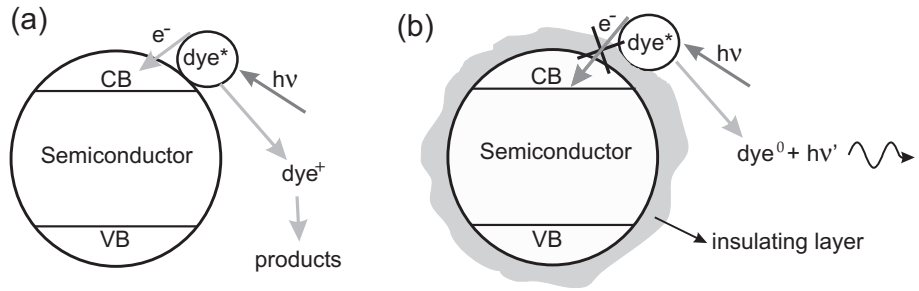

FIGURE 2.6: *(a) Electron transfer process where an electron of the excited state of an adsorbed dye molecule is injected into the conduction band (CB) of the semiconductor. VB represents the valence band. The remaining oxidized molecule undergoes transformation to yield a stable product. In figure (b) the surface of the semiconductor is shielded with a layer of insulating material, shielding the dye from the semiconductor surface and quenching is prevented. This way allows the dye to decay to the ground state and emit light.*

electric current. The inverse process, i.e. electrons at the semiconductor surface are scavenged by the ubiquitously present molecular oxygen, results in the degradation of the dye [79], see also figure 2.6(a). Since this non-radiative decay rate γ_{nr} is much faster than the radiative decay rate γ_{rad}, the fluorescence efficiency Q.E. for emission is strongly reduced to a few percent, since the $Q.E. = \gamma_{rad}/(\gamma_{rad} + \gamma_{nr})$. If a high fluorescence efficiency close to a semiconductor surface, in our case titania, is required, the dye or the host solid must be shielded, to decrease the non-radiative decay.

Titania is also used in the paint-industry, because of its white appearance. Due to its high refractive index and small grain size it scatters light strongly. A major concern is photodegradation of pigments adsorbed on titania, which takes place under ultraviolet and visible light illumination. To improve the weathering resistance of the pigments, the titania usually undergoes surface treatment. The particles are coated with an insulating layer like silica (SiO_2), alumina (Al_2O_3) or a polymer [80–82]. Van Dyk and Heyns [80] showed that treating titania powders with alumina and silica reduces the photo-activity and improves the dispersion stability. Kamat and coworkers [81] have investigated the coating of semiconductor powders with a polymer in order to prevent the electron transfer. Here it appeared that the dye dissolves into the polymer matrix and therefore comes close to the titania surface, where the tunnelling probability increases and electron transfer can easily take place after all.

The principle of shielding dye from semiconductor surfaces is shown in figure 2.6(b). The insulating layer, deposited on the semiconductor surface, shields the dye from this surface and thus reduces the electron tunnelling probability. This

insulating layer can consist of silica, alumina or a polymer, i.e., materials with a remote conduction band. The technique we apply to coat the titania is the use of tetraethoxysilane, a precursor that reacts with water under basic conditions to yield silica. Similar to this technique zirconia (ZrO_2), maghemite (Fe_2O_3) and gold colloids can be coated with silica [83–85]. Since coating titania air-sphere crystals, porous materials with a confined geometry, is a challenge to materials science and chemistry, we first study titania powders coated with silica. An interesting method to coat materials with silica in confined geometries has recently be demonstrated by Vossen and colleagues [86], where silicon pillars are coated with a silica layer of controllable thickness. In the following section we present measurements of fluorescence emission spectra and fluorescence lifetimes of R6G dye adsorbed on silica coated titania.

2.5 Dye-doped silica-coated titania powders

By coating titania with silica, we try to achieve highly efficient emission in an environment with a high refractive index. Titania powders were coated with various amounts of silica by the use of a hydrolysis of tetraethoxysilane. The dye was adsorbed on the coated powders and the fluorescence emission spectra and fluorescence lifetimes of the dye were measured. In this way the behavior of R6G dye, i.e., the presence of an electron transfer, adsorbed on titania powders coated with silica is investigated.

2.5.1 Sample preparation

Ethanol (99,5%) and ammonia-solution (31,5%) were obtained from Merck. Tetraethoxysilane (99%) was purchased from Fluka. Titania powder in the anatase crystal structure, with a mesh size of -325 was obtained from Aldrich.[1] R6G (99%) was obtained from Lambda Physik and the solutions in ethanol were made freshly each time. Silica powder, that was used as reference material, consists of 60 nm spheres prepared via a micro-emulsion technique [87]. The Scanning Electron Microscope (SEM) images were taken with an ISI DS-130 scanning electron microscope, after sputtering the samples with a thin layer of gold.

The coating-reaction was performed in plastic centrifuge tubes to prevent nucleation on a glass-wall. Titania (1 gram) was suspended in 10 ml ethanol. Ammonia (1.5 ml) was added and the suspension was stirred for 15 minutes. Three portions of 1.86 ml (8.3 mmol) tetraethoxysilane were added, with intervals of 20 minutes, under vigorous stirring and the suspension was stirred gently overnight.

[1] A mesh size of -325 corresponds to a particle size (diameter) smaller than 45 mm.

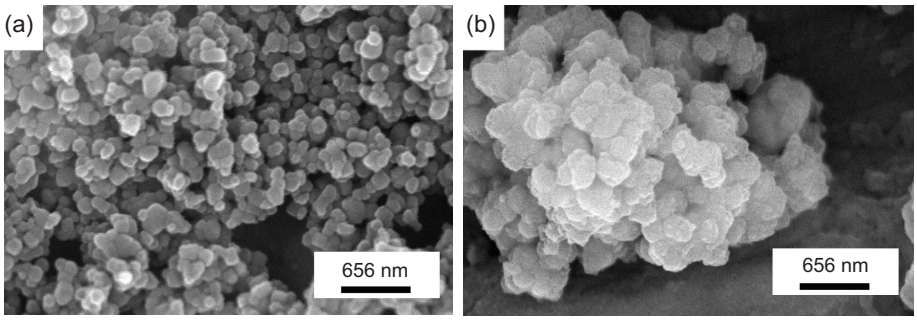

FIGURE 2.7: *SEM-images of (a) uncoated titania powder and (b) titania powder coated with 1 gram silica per gram titania. The particle size of the uncoated titania is about 100-250 nm in diameter. The diameter of the coated titania particles is about 200-400 nm and the particles seem more clustered together possibly caused by the silica.*

The amount of tetraethoxysilane was varied from 0 to 3.71 ml per 1 g titania. This corresponds to an amount of 0 to 1 g silica per 1 g titania. The next morning the suspension was firstly centrifuged and then decanted before the slurry was resuspended in fresh ethanol. This procedure was repeated four times and finally the powder was dried in an oven at 50°C for more than 10 hours.

Coated or uncoated (0.25 gram) titania powder or pure silica powder was suspended in 5 ml R6G solution (10^{-7} M in ethanol). The suspension was stirred for 30 minutes before it was centrifuged and resuspended in ethanol once. The dye doped titania powder was dried in an oven at 50°C for several hours.

Figures 2.7 shows SEM pictures of uncoated titania and titania coated with 1 gram silica per gram titania. The difference between both powders is clearly seen, since they are at the same scale. The particles of the uncoated titania are about 100-250 nm in diameter. The diameter of the coated titania particles is larger, about 200-400 nm. The coated titania particles appear to be clustered together. Possibly the silica coating encloses more than one titania particle and covers groups of particles.

2.5.2 Fluorescence of R6G

The samples were placed on a glass slide and all measurements were done at room temperature. Fluorescence spectra were obtained by exciting the dye with a $\lambda = 532$ nm laser beam obtained from a frequency-doubled pulse-compressed mode-locked Nd^{3+}:YAG (Spectra Physics) laser, emitting 3 ps pulses at 12.5 ns intervals. The excitation spot size is 0.3 mm in diameter. The spectra were collected via a Carl-Leiss prism spectrometer, the photo multiplier tube is protected against stray light by a Schott OG570 filter. The emission spectrum is recorded from 850 to 545 nm.

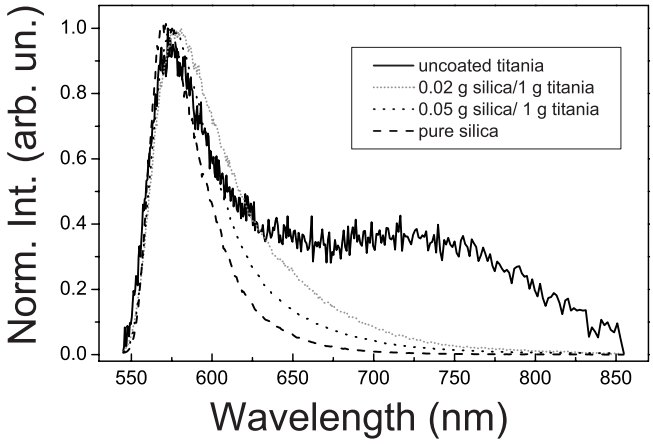

FIGURE 2.8: *Fluorescence spectra of R6G adsorbed on coated titania, uncoated titania and silica. Solid curve is uncoated titania, dashed is 0.02 g silica per 1 g titania, dotted is 0.5 g silica per 1 g titania and dash-dotted is pure silica. It can be seen that with decreasing amount of silica more intensity towards the red appears.*

The spectral resolution was ~ 4 nm. The emission lifetimes of the dye adsorbed on the powders were obtained using a time-correlated single-photon counting technique [71] (for more details see chapter 6). With this set-up a time-resolution of 55 ps is achieved.

The emission spectra of R6G are shown in figure 2.8. The spectra are normalized to the peak intensity. For comparison the spectra and lifetimes of R6G adsorbed on pure silica are measured, those resemble R6G in solution. It can be seen that with decreasing layer thickness, especially for the uncoated titania, there is relatively more fluorescence intensity in the red. Kay and Grätzel [88] ascribed such a shift to the interaction of the dye with the polar titania surface. We also considered that the red fluorescence band could be the result of a new emitting species.

The influence of the electron transfer from the excited state of the dye to the conduction band of titania can be probed by the excited state lifetime, since short lifetimes are expected if electron transfer is present. Lifetimes measured from doped titania powders with several layer thicknesses are displayed in figure 2.9. An arrow indicates increasing amounts of silica. The lifetime of R6G on pure silica, the upper curve, is obtained from a single exponential fit and is 3.50 ± 0.02 ns.

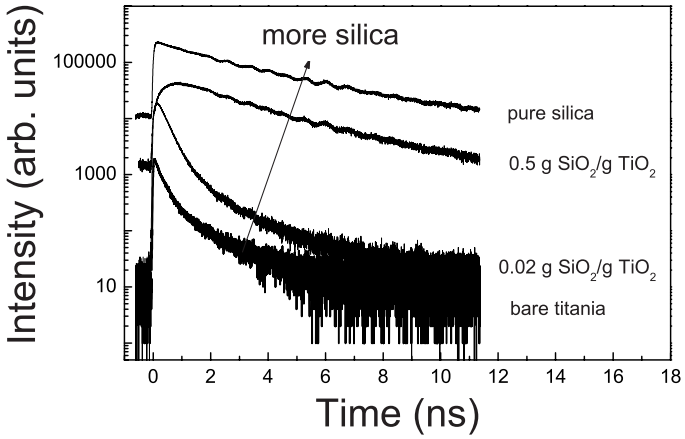

FIGURE 2.9: *Time resolved fluorescence of R6G adsorbed on uncoated titania, titania coated with 0.02 g silica/ 1 g, titania coated with 0.5 g silica/ 1 g and pure silica. An arrow indicates the increasing amount of silica. The lines are offset for clarity. It can be seen that the lifetime clearly decreases with decreasing amount of silica. A very short lifetime of 0.58 ns is obtained for R6G on bare titania.*

Comparing this value with a lifetime of 3.6 ns measured for R6G in ethanol, we conclude that R6G on silica has a high quantum efficiency (92%) as expected [67], since silica is considered to be an insulator [78]. The decay of R6G on bare titania is fast and not single exponential. The decay of R6G on the titania powders was modelled with a double exponential model

$$f(t) = \alpha_{\text{slow}} \cdot e^{-t/\tau_{\text{slow}}} + \alpha_{\text{fast}} \cdot e^{-t/\tau_{\text{fast}}} \tag{2.5}$$

where α_{slow} and α_{fast} are the amplitudes and τ_{slow} and τ_{fast} are the lifetimes. For the coated powders, τ_{slow} was taken to be 3.6 ns, the natural lifetime of R6G, as was measured with the set-up in Amsterdam for R6G in ethanol.[2] This model was adapted since it is expected that in coated powders besides fast decay due to possible electron transfer, also natural decay of R6G is present, in the form of R6G on silica. The fast decay, expeected to be caused by electron transfer, is represented in τ_{fast}. The mean lifetime τ_{mean} of R6G on coated and uncoated powders was calculated by averaging both decay times with their amplitudes.

[2]In Amsterdam lifetimes of 3.60 ± 0.05 ns were obtained for R6G in ethanol, whereas in Twente lifetimes of 3.97 ± 0.04 ns were obtained.

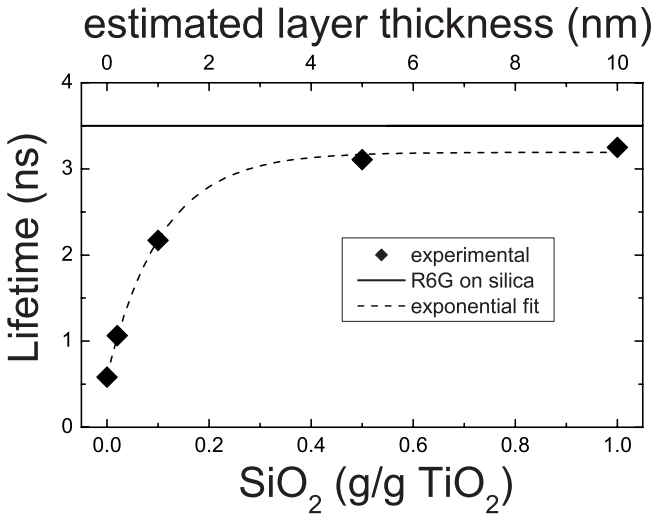

FIGURE 2.10: *Mean lifetime of R6G, obtained from figure 2.9, versus the amount of silica coating represented as diamonds. An exponential fit through the data points, with a 1/e value of ~ 2 nm, is indicated with a dashed curve. The straight line at 3.50 ns is the lifetime of R6G on pure silica. On the upper-axis the estimated layer thickness in nm is displayed.*

For the uncoated powder we obtain a mean lifetime for R6G of 0.58 ± 0.04 ns, which shows a clear non-single exponential decay. The curve for the sample that was coated with 0.02 g silica per 1 g titania still shows a fast decay component but the sample with 0.5 g silica per 1 g titania resembles the R6G on pure silica. Although there is a peculiar ingrowth in this curve that is not yet understood, the mean lifetime of 3.11 ± 0.01 ns almost matches the lifetime of R6G on pure silica which has a τ_{mean} of 3.50 ± 0.02 ns. Coating the titania with silica shows that the lifetime increases with increasing amount of silica.

In figure 2.10 the relation between the mean decay time and the amount of silica relative to titania is given. The error bars for the data points are comparable to the symbol size. The straight line at the top of the graph is the lifetime of R6G on pure silica. The dashed line is an exponential fit through the measured data points with a 1/e value of ~ 0.2 g silica/1 g titania. It is clear that the lifetime tends to the value of R6G on silica with increasing amount of silica. This exponential behavior is expected if we assume that the insulating silica layer acts as a barrier for the electrons and the tunnelling probability decays exponentially with the layer thick-

ness. On the upper axis the estimated layer thickness is shown. These values are calculated by assuming that the yield from the reaction of tetraethoxysilane to silica is 100% and all silica is deposited on the titania. We estimate the specific surface area, which manufacturers do not specify, to be 50 m^2/g [89]. If we suppose that the silica forms a homogeneous layer on the titania surface, we can calculate with these values the thickness of the silica layer. The 1/e value of the exponential fit corresponds to a thickness of $\sim$ 2 nm. Because the adsorption of R6G on titania is different from the adsorption of R6G on silica coated titania, the emitter concentration is different for each sample and therefore determining the rate constants from the fluorescence intensities is a challenge.

If we make the hypothesis that the radiative decay rate stays constant and the lifetime for R6G in ethanol corresponds with an efficiency of 95%, we can deduce the quantum efficiency for the different powders. This corresponds to quantum efficiencies of R6G on bare titania of 15%. For 5 and 10 nm coated titania powders quantum efficiencies of nearly 85% are obtained. The latter values are very close to the ideal case where there is no quenching. From these results we can conclude that a 5 nm layer (or 0.5 g silica/1 g titania) is thick enough to prevent electron transfer. Recently Tada *et al.* have observed that a monolayer of silica, $\sim$ 0.2 nm, has a promoting effect on photochemical reactions at titania surfaces of R6G in solution [90]. The thin silica layer significantly increases the adsorption of the organic species while the electron transfer is enhanced because the concentration of the dye near the titania sites is higher relative to the solution concentration. In dry condition, however, where there is no diffusion, they demonstrated that R6G on coated titania behaves similarly to the coated powders of our experiment.

We have shown that it is possible to shield a dye from a semiconductor surface by coating this surface with an insulating layer. By coating titania particles with an insulating silica layer we recover the quantum efficiency by suppressing the electron transfer from the excited state of R6G to the conduction band of titania. We were able to achieve a lifetime of 3.25 ns for R6G on silica coated titania, corresponding to a quantum efficiency of 85% that is approaching the 95% for R6G in ethanol. This result is of great advantage for engineering dynamic spontaneous emission in photonic crystals for which efficient light sources on high refractive index materials are required.

2.6 R6G emission from several non-quenching materials

2.6.1 Silica-coated titania crystals

Since we demonstrated that the R6G adsorbed on silica coated titania is an efficient emitter, we can now try to coat the inner-surface of our photonic titania air-sphere

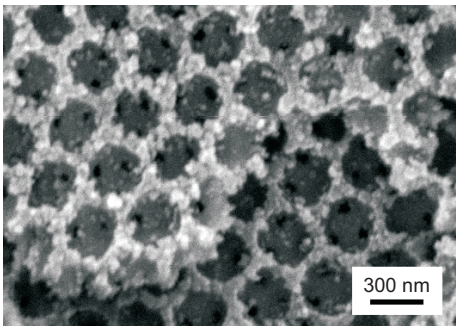

FIGURE 2.11: *SEM-image of a titania air-sphere crystal ($r \sim 200$ nm) treated with a silica-precursor in order to deposit a thin layer of silica. The silica tends to grow on the edges of the air spheres and does not form a homogeneous layer on the inner surface of the air spheres.*

crystals. After adsorption of the dye on the surface we are then in an excellent position to investigate inhibited emission lifetime effects.

The coating of the titania air-sphere crystals with silica was done in a similar way as for the powders, just the procedure was more gentle since vigorously stirring was not possible. Titania air-sphere crystals were treated with a reaction mixture containing silica precursor. The concentrations of the silica precursor TES and of ammonia present in the reaction mixture were chosen similar to those in the Stöber synthesis [91], a well-known sol-gel reaction to grow very monodisperse silica spheres. Concentrations of 0.35 mol/l TES and of 2 mol/l ammonia were low enough to avoid nucleation of colloids before the solution penetrated the air spheres and high enough to obtain a sufficiently thick silica layer of at least 2 nm [92]. We are certain that the reaction-mixture does penetrate the samples because a distinct color change was observed as is typical for infiltration. Furthermore tiny air-bubbles appeared around the sample.

Figure 2.11 is a SEM-picture of a titania air-sphere crystal treated with the silica precursor. This titania air-sphere crystal was made from a polystyrene template with sphere radii of $r \sim 262$ nm and has a similar long range order as crystals in for instance figure 3.7. The SEM-picture displays a (111) top view inside a small crack near the surface that was already present before the coating reaction. On the SEM-picture it can be seen that there are small silica spheres present, especially on the edges of the air spheres. In other SEM-pictures from the same sample (not shown here), there was also a bulk silica layer on top of the crystal consisting of small silica particles. It seems as if silica prefers to grow on sharp edges. Viewing in a crack made after the coating reaction, we observed that there was hardly any silica deposited on the inner air-sphere surfaces. Since the expected 2 nm thick layer would not be visible with electron microscopy we have doped a coated air-sphere crystal with R6G dye and measured the fluorescence lifetime. The decay of R6G in a coated air-sphere crystal of titania is displayed in figure 2.5, plotted as a gray curve. We observed a short $\tau_{\text{mean}} = 1.7$ ns, much shorter than the 3.6 ns

for R6G dye in ethanol and resembling almost the lifetime of R6G in the uncoated titania crystal. This indicates that the dye still transferred electrons to titania and therefore it is concluded that the inner air-sphere surfaces are incompletely covered with an insulating silica layer.

A possible explanation for this result, compared to what we have found with the silica coated titania powders, is a difference in geometry. The reaction conditions during the coating of the titania powder can be easily controlled by stirring. If the silica starts to grow as isolated islands on the surface of the titania powder, these islands can expand by the supply of silica precursor present in the reaction mixture and finally meet to cover the whole surface. In an air-sphere crystal, it is not possible to stir in each air sphere separately. If an air-sphere crystal is soaked into the reaction mixture and the silica starts to grow on the edges, it is possible that the remaining silica precursor on the outside of the sample has no chance to diffuse deep inside the crystal. In this way the silica precursor will stay outside the crystal and will nucleate on silica already present at the outer surface. Another possibility is that silica does not favorably grow on titania and prefers to grow on silica itself. This is consistent with the fact that silica is amorphous and titania is crystalline. Also, the acid/base behavior of the surface hydroxyl groups of titania (point of zero charge $\sim$ 6.0) are different from that of silica (point of zero charge $\sim$ 2.5) [93]. Treating the titania air-sphere crystal beforehand with an acid or base can make the surface less neutral and make the surface more attractive for the silica to nucleate.

It is clear that the technique of treating titania air-sphere crystals with a silica precursor, has not resulted in homogeneously coated inner surfaces. Coating a confined geometry, such as an air-sphere crystal, afterwards is complex. It is very difficult to control the reaction conditions inside the air spheres and therefore deposit a thin layer. In this way we will not be able to probe the photonic band gap with time-resolved emission measurements.

2.6.2 Fluoresence of R6G on zirconia, alumina and silica powders

Since the titania backbone displays electron transfer with adsorbed dyes and we were not able to make silica coated titania air-sphere crystals, we investigated the possibility of using pure insulating materials as alumina and silica as backbone for air-sphere crystals. These insulating materials would be perfect candidates for the control of dynamic spontaneous emission since they do not exhibit electron transfer. In this way efficient emission can be achieved which is necessary for observing lifetime changes. We are aware of the fact that these insulating materials exhibit a lower refractive index than the previously used titania (n_{silica} = 1.45 vs. n_{titania} = 2.7, at visible wavelengths) and therefore their interaction with light is less

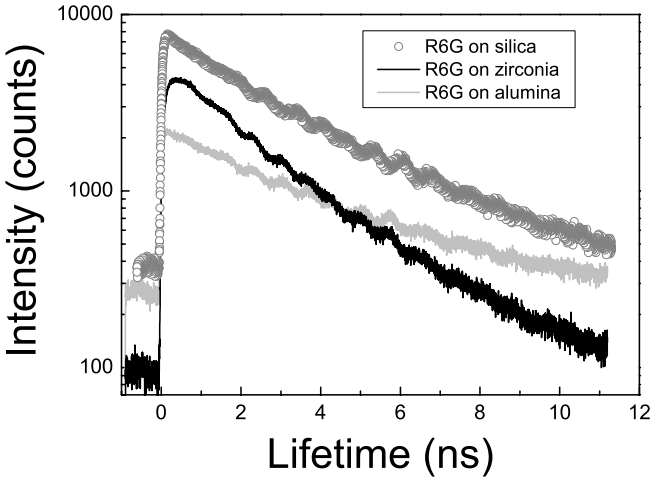

FIGURE 2.12: *Decay of R6G, adsorbed on different powders. The dye is excited at λ = 532 nm and the fluorescence is detected at the peak ($\lambda \sim 580$ nm). The decays could be fitted with a single exponential model resulting in lifetimes for R6G of $\tau_{mean} \sim 3.5$, 5.1 and 2.5 ns for respectively silica, alumina and zirconia. Oscillations in the decay curves are electronic.*

pronounced. Yet we still should be able to investigate emission lifetime changes in these pure insulating oxide crystals. Before performing emission experiments on dye doped air-sphere crystals of these insulating materials (see for preparation next chapter), we investigated the behavior of R6G dye on powders of these insulating materials.

In figure 2.12 the decay curves of R6G adsorbed on silica, zirconia and alumina is displayed. The decays were measured with the set-up used in section 2.5.2,[3] and were all fitted with a single exponential model. As was shown previously the behavior of R6G on silica is more or less comparable to R6G in ethanol with a lifetime of 3.50 ± 0.04 ns. Assuming the radiative decay to be constant, this lifetime corresponds to an efficiency of ~ 92 %.

R6G molecules on alumina display surprisingly a much longer lifetime, 5.09 ± 0.02 ns. It is not excluded that a different adsorption geometry of R6G on the alumina surface is causing this longer lifetime.

R6G adsorbed on zirconia displays a lifetime of 2.46 ± 0.05 ns. This shorter

[3]Excitation at λ = 532 nm, measurements were performed in Amsterdam.

lifetime is attributed by electron transfer. Although the zirconia exhibits a conduction band edge that is higher than that of titania [94], the excited state of R6G can still have electron transfer to the conduction band of titania as reported by several people [94, 95]. The lower lifetime can also be caused by the higher refractive index of zirconia compared to ethanol. The lifetime changes with the refractive index n of the medium the dye sits in, for this particular case resulting in a shorter lifetime ($n_{\text{ethanol}} = 1.36$, $n_{\text{zirconia}} = 2.13$).

From these results it can be concluded that silica and alumina are well chosen materials for the use of lifetime measurements in photonic crystals.

When the lifetime experiments were started up again in Twente different pumping wavelengths were used, $\lambda = 400$ and 440 nm. When repeating experiments on the alumina and silica powders it was found that excitation at these "blue" wavelengths, causes luminescence of the materials themselves, as can be seen in figure 2.13 for silica. The intensities are normalized for clarity. All spectra were measured with same pumping power. It can be seen that for powders doped with high dye-concentrations (10^{-4} M) the spectrum mainly consists of the R6G emission spectrum. With decreasing dye concentration, however, the spectrum becomes broader, as a result of a contribution of silica luminescence. At a doping concentration of 10^{-9} M the luminescence of silica dominates, and the spectrum resembles more or less the luminescence spectrum of bare silica.

From these results it is clear that insulating materials as silica are not good candidates for lifetime measurements in combination with pulsed 400 and 440 nm laser light. At high dye doping concentrations the fluorescence of the dye will dominate and the luminescence of the silica backbone will hardly influence the observed lifetime. At lower dye concentrations, however, the luminescence of the silica starts to contribute and can affect the measured lifetime. For alumina powders doped with low dye-concentrations similar luminescence phenomena were found. Luminescence of the backbone makes it hard to investigate lifetime effects in photonic crystals and therefore a different pumping source or a different backbone material should be used.

A readily available pulsed laser that could be used to excite R6G, and is not "too blue", is a pulsed LED emitting at $\lambda = 520$ nm. This light source excellently probes into the absorption spectrum of R6G and does not cause emission of the backbone since the power is very low. In this way insulating materials as alumina and silica can be used.

The advantage of polystyrene with respect to titania is that it, like silica and alumina, is an insulator and electron transfer from the excited state of the dye to polystyrene will not take place. Time-resolved measurements are in this way favorable for probing the lifetime. In the next section the behavior of R6G dye adsorbed on polystyrene will be discussed.

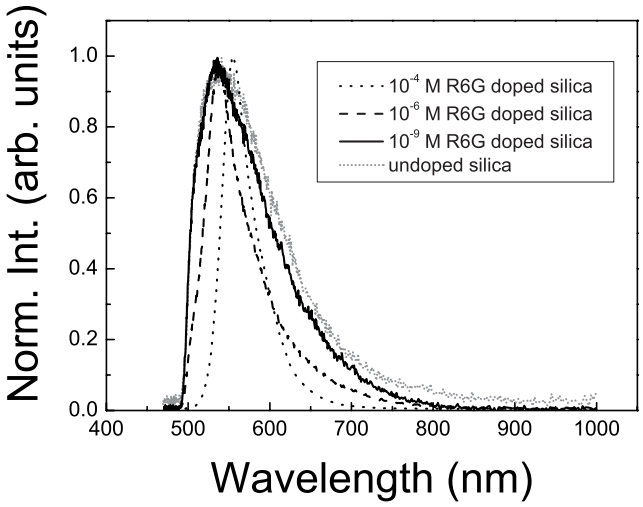

FIGURE 2.13: *Luminescence of bare and R6G doped silica powder pumped with a λ = 440 nm laser. At rather high dye doping concentrations (10^{-4} M) the spectrum mainly consists of the R6G emission spectrum. With decreasing dye concentration the spectrum becomes broader, expected to be caused by the luminescence of silica. Especially at a concentration of 10^{-9} M the luminescence of silica is very pronounced, and the spectrum resembles more or less the luminescence spectrum of bare silica.*

2.6.3 Fluorescence of R6G on polystyrene

To demonstrate inhibited emission in a photonic sample a comparison should be made with a carefully chosen non-photonic reference sample. Since the change in the lifetime can be small, comparing lifetime data is very delicate. In our experiments a polystyrene opal with a smaller lattice parameter was chosen as a reference sample for emission experiments as will be discussed in chapter 5 and 6. The first order Bragg diffraction of this sample appears at shorter wavelengths and therefore no photonic features show up in the emission range of R6G. Furthermore the polystyrene reference samples exhibit the same chemical properties, i.e., the R6G molecule is, like in the photonic samples, adsorbed on the polystyrene surface and "feels" the same chemical and electronic interactions. The DOS of these reference samples exhibits a constant ω^2 behavior without extreme variations, comparable to the DOS in vacuum. So no effects in the lifetime as a result of photonic band structures will be present.

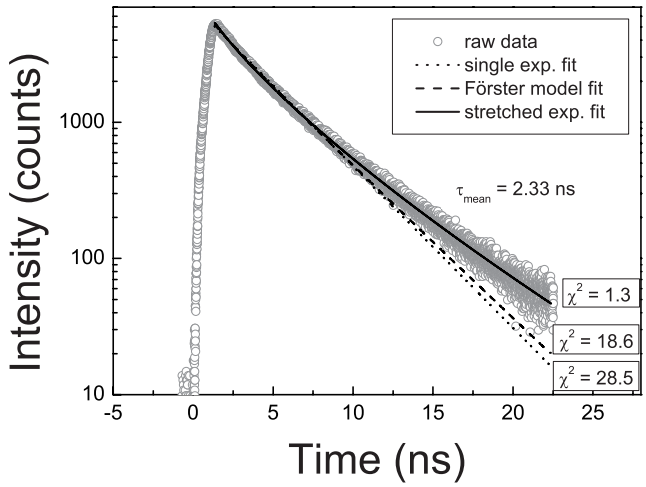

FIGURE 2.14: *The decay of R6G in a non-photonic polystyrene sample (111-1-c). The lifetime was measured at λ = 580 nm. The decay curve is fitted with three different models and from the χ^2 the goodness of the fit can be deduced. The single exponential model and the Förster model show a large χ^2. The stretched exponential model however fits well. The mean lifetime resulting from the stretched exponential model is τ_{mean} = 2.33 ns.*

The dye-concentrations were kept low to prevent dipole-dipole interactions. Dipole-dipole interactions occur when molecules are present next to each other. At these short distances the slightly positive part of one molecule interacts with the slightly negative part of another. This resonance energy transfer is also called Förster transfer as first described by Förster [96–98]. The Förster distance is the length between the molecules at which energy transfer is 50 % efficient. The values for the Förster distance of dyes are typically between 3 and 6 nm. In the experiments on lifetimes of R6G in ethanol we already demonstrated that at concentrations above 10^{-2} M these dipole-dipole interactions become a major issue. It is obvious that this non-radiative energy transfer reduces the quantum yield and hence are not desirable in lifetime measurements. Photonic and non-photonic samples in our research were typically doped with a 10^{-5} or 10^{-6} M dye solution.

From measurements of R6G emission adsorbed on polystyrene we observed that the peak fluorescence was slightly shifted compared to the fluorescence spectrum of R6G in ethanol; on polystyrene the peak appears at 590 nm, a shift of roughly 30 nm. This shift is possibly ascribed to a different geometry since the

R6G molecule is adsorbed on a surface compared to a "free" situation in solution.

We expected the concentration in our samples, non-photonic as well as photonic, to be below the Förster limit and therefore self-quenching to be no issue. We however did observe a non-single exponential behavior from R6G adsorbed on polystyrene and therefore we applied the Förster model to our data to confirm our hypothesis. This model is described by

$$f(t) = a \cdot e^{(-t/\tau_0)} \cdot e^{b(-t/\tau_0)^c} \tag{2.6}$$

where τ_0 is the natural lifetime of R6G, in the case where no interactions are present. The factor c is a value deduced from the dimension of the volume where R6G is located. Usually this value varies between $\frac{1}{3}$ to $\frac{1}{2}$ corresponding to respectively two or three-dimensionality. Parameter b is proportional to the local concentration and orientation of the quenchers. If b is zero, the decay is just single exponential and Förster transfer is not present [99, 100]. The natural lifetime of R6G as measured in ethanol is ~ 4 ns. Fitting the data with this model resulted in a value for c much smaller than $\frac{1}{3}$, implying an unphysical situation. Additionally we observed a very large χ^2, indicating this model does indeed not fit the experimental data. This confirms dipole-dipole interactions were not present.

Since the data could not be fitted with the single exponential and Förster model, a third model was applied to the data; a stretched exponential model that is written as

$$f(t) = a \cdot e^{(-t/\tau_0)^\beta} \tag{2.7}$$

where the lifetimes form a continuous distribution [101]. The parameter β can be described as a measure for the homogeneity of the dye molecules in the sample. If β is 1 the data could be described by a single exponential model and all dye molecules present in the crystal have the same lifetime. If the molecules have all different surroundings, i.e., there is a certain heterogeneity, the dye molecules exhibit all different lifetimes, and β decreases. In other words the smaller β, the broader the lifetime distribution.

The goodness of several fitting models is shown in figure 2.14 where the fit of three different models is displayed; a single exponential model, a Förster model and a stretched exponential model. The raw data were taken from a 111-1-c sample that had a sphere size of $r = 111$ nm, and was doped with a 10^{-6} M solution. As can be seen the single exponential model and the Förster model deviate slightly from the raw data. Especially in the long time tail, beyond 10 ns, the models do not fit the data. This is also expressed in the values of χ^2 that both exceed far beyond 10. The stretched exponential model however fits the data very well and displays a χ^2 of only 1.3. The average lifetime can be calculated from the parameters resulted from

the stretched exponential model. The mathematical average lifetime resulting from a stretched exponential model turns out to be different for the expression used in fluorescence lifetime experiments [102]. The average lifetime used for fluorescence lifetime experiments, as first proposed by Laherrère and Sornette [103] for stretched exponential models in general, is

$$\tau_{\text{mean}} = \frac{\tau_0}{\beta} \cdot \Gamma(\frac{1}{\beta}), \tag{2.8}$$

where the Γ-function is defined as

$$\Gamma(x) = \int_0^\infty t^{x-1} e^{-t} dt. \tag{2.9}$$

This model for lifetime calculation was previously used by several other people in fluorescence lifetime experiments [101, 104, 105]. In our research the stretched exponential is applied henceforth to all measured data, photonic as well as non-photonic samples. The mean lifetime for the polystyrene sample showed in figure 2.14 turns out to be $\tau_{\text{mean}} = 2.33$ ns. In this chapter we will not discuss the deviation of this lifetime from lifetimes observed of R6G in ethanol (see chapter 6).

With the results shown in this section, we demonstrated that the combination of R6G dye and polystyrene is well chosen, and can be used further on in emission experiments. The polystyrene opals are of high quality, do not display luminescence when illuminated at $\lambda = 520$ nm and do not exhibit electron transfer with adsorbed dye molecules.

2.7 Conclusion

In this chapter we have shown it is very important to chose a good combination of emission source and high refractive index material. A high efficiency source is very important and therefore non-radiative decay, i.e., electron transfer, should be excluded. High refractive index semiconducting materials such as titania can have electron transfer with the excited state of organic dyes and we have shown that preventing this electron transfer is possible by coating the titania surface with an insulating layer. The technique of coating titania powders worked well but applying this same coating procedure to air-sphere crystals of titania resulted in inhomogeneously coated crystals. To overcome the problem of electron transfer we explored the possibility of the use of other materials, that are insulating and exhibit no electron transfer with organic dyes. Although the refractive index of these materials is lower (see figure 1.8 and equation (1.7)), their crystals still have a strong interaction with light. The pumping light source used to excite the dye molecule should

be carefully chosen since high energy, corresponding to short wavelengths, and high powers can cause luminescence of the backbone, that considerably influences the observed lifetime. We investigated and concluded that R6G dye adsorbed on polystyrene does not show electron transfer. The decay of R6G on polystyrene could be fitted well with a stretched exponential model. With these results we are in an excellent position to investigate lifetime changes in photonic crystals, as will be performed in chapter 6.

Chapter 3

Synthesis and Characterization of Air-Sphere Crystals

3.1 Introduction

The development of porous materials is a subject of intensive research. Well-known structures like zeolites are widely used in every day life including desiccants, pet litter, and powdered laundry detergents [106, 107]. Many of these porous materials are prepared via a template assisted-growth. The basic principle of template-assisted growth is the formation of a template, usually by self-assembly, followed by infiltration of the voids in the template with a solid material and finally the removal of the template. Self-assembly can occur by bacteria [108], emulsions [109], block copolymers [110] and colloidal suspensions [58, 111–116]. Probably the most widely used technique for photonic applications are colloidal suspensions, since the sizes of the colloidal particles match well with the required range.

For the use of opal-based crystals in photonics, several important quantities should be met. First of all the sphere diameter should be adjusted between 300 nm and 1300 nm to work at optical wavelengths. This directly illustrates why colloidal particles are widely used in photonic crystal preparation, since these nanometer sized particles are readily available with a high monodispersity or can be synthesized in a controlled way.

Secondly the macroporous structure should be highly ordered in order to build up Bragg diffraction from the crystal lattice planes. The fact that second order Bragg diffraction, the wavelength range where the face centered cubic (*fcc*) pho-

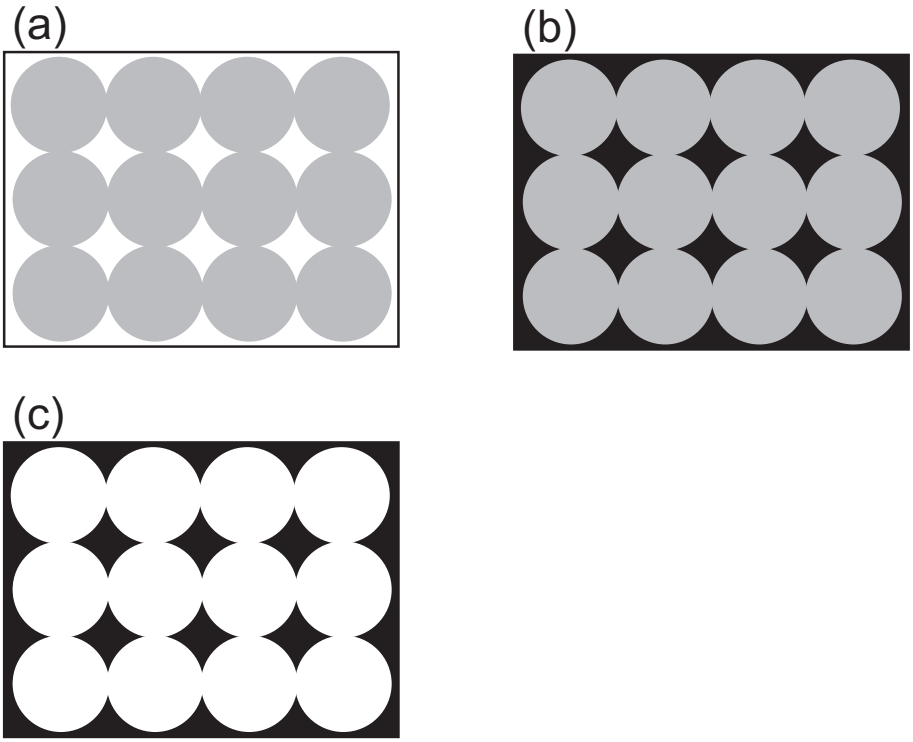

FIGURE 3.1: *General infiltration scheme for the preparation of fcc air-sphere crystals. (a) A colloidal crystal is grown from a colloidal suspension by self-organization of small spheres. After evaporation of the solvent an artificial opal is left with spheres in a fcc close-packed structure. The crystal consists of 74% v/v solid material and 26% v/v air. (b) The interstitial holes between the spheres is infilled with a solid material. This can be done by techniques as electrochemical deposition, chemical vapor deposition or liquid precursor infiltration. (c) The template is removed by heating (for polymer spheres), dissolving or by etching. When calcination is used, the backbone usually becomes crystalline at these high temperatures.*

tonic band gap will occur, is much more sensitive to disorder, stresses the importance of making highly ordered structures. Recently Li and Zhang calculated that photonic band gaps are only developed if the polydispersity of the spheres in the crystal is less than 5% [117]. The polystyrene spheres in our work never exceed a size dispersion of 2%.

Thirdly it is very important that the refractive index contrast should be as high as possible. For close-packed *fcc* crystals it turned out that the refractive index contrast should be at least 2.8 to create a photonic band gap [34, 35]. With different crystals structures, e.g., the diamond structure, a lower refractive index contrast of 2.0 will even suffice [54].

Finally the high index material should not absorb at optical wavelengths. Since usually high index materials have small energy gaps (see figure 1.8), the sphere size of the template should be chosen such, that the photonic Bragg diffraction appears above this wavelength. For instance galliumphosphide with a refractive index of n = 3.4 starts to absorb at $\lambda < 550$ nm.

As discussed in chapter 1 inverse opals are effective photonic crystals. The principle of the synthesis of these so-called air-sphere crystals, is displayed in figure 3.1. First a colloidal crystal is grown from a colloidal suspension, as displayed in figure 3.1(a), by self-organization of small nanometer sized particles. The particles arrange in a *fcc* crystal [118, 119], with a particle volume fraction $\phi \sim 50\%$ v/v. When the colloidal crystal is formed the solvent is evaporated and an artificial opal in a close packed structure is left, consisting of 74% v/v solid material and 26% v/v air.

Secondly the interstitial holes of the template, the artificial opal, can be infiltrated with a solid material, as illustrated in figure 3.1(b), by many means such as electrochemical deposition [120] or infiltration of solid particles [121]. The infiltration of the interstitial spaces can be repeated several times to increase the filling fraction.

In the final step the template is removed, displayed in figure 3.1(c). This can be done by heating, etching or dissolving. Heating or dissolving is usually applied for polymeric templates, while etching is applicable for oxide templates as silica (SiO_2).

In the past many groups have produced ordered macroporous structures consisting of a variety of materials via various techniques. Air-sphere crystals of elemental materials as germanium [122, 123], silicon [124, 125] and diamond/graphite [112], prepared via CVD, were already reported. Other materials prepared with CVD-techniques were antimony trisulfide [126], galliumarsenide [127] and zincsulfide [128].

Deposition of solid material between templates by means of electrochemistry resulted in macroporous structures of gold [129], germanium [130], nickel [131]

and very recently galliumarsenide [132]. Although in reference [132] the galliumarsenide formation was confirmed with electron dispersive X-ray spectroscopy (no details shown), experts in the field of electrochemistry doubt the possibility of synthesizing galliumarsenide this way [133].

Colloidal particles were not only used as templates but also were used to infiltrate the interstitial holes. Examples of nanometer sized solid particles that were used to make inverse opals are gold [134–136], titania (TiO_2) and silica [137, 138], and quantum dots [114].

The technique of liquid precursors is mostly applied for inverse opals of metaloxides such as titania, zirconia (ZrO_2), alumina (Al_2O_3) [58, 113, 115, 139, 140] and niobia (Nb_2O_5) [141, 142]. The liquid precursor infiltrates the interstitial holes and solidifies after hydrolysis.

In our research we concentrate on the synthesis of ordered macroporous structures of titania, that exhibits a refractive index of 2.7 [57] and is transparent at optical wavelengths (see also figure 1.8). Since titania turns out to be a semiconductor with electron transfer of dyes (see chapter 2), which is undesirable for emission experiments in photonic crystals, we fabricated alternative air-sphere crystals consisting of the insulators silica, alumina and zirconia. The air-sphere crystals are characterized with optical and electron microscopy, reflectivity, X-ray diffraction and X-ray absorption.

3.2 Colloids as building blocks for photonic crystals

For the synthesis of our air-sphere crystals colloidal particles are used. Colloidal particles are small objects with radii in the range of 1 nm to 1 μm and are widely used in foods, inks, paints, foams and many more [143]. For optical applications colloidal particles with dimensions less than 100 nm are too small, unless they are highly charged, therefore we concentrate on particles with radii larger than 100 nm.[1] Colloidal particles with these dimensions can be synthesized via many approaches. The most commonly used method is the emulsion polymerization for polymer latexes [144] and the controlled hydrolysis for inorganic oxides [91, 145, 146]. Polystyrene latex spheres are especially interesting for their use as templates in inverse opals made of metaloxides. For the use in inverse opals of high refractive index materials like galliumarsenide [127] and gold [129], silica spheres are more effective. In these syntheses high temperatures and reactive chemicals are used, to which polystyrene spheres are not resistant. Since latex spheres are commercially available in a whole range of diameters and with a very small size distribution, we

[1] The International Union of Pure and Applied Chemistry (IUPAC) defines micropores as pores with radii $r < 1$ nm, mesopores with $1 < r < 25$ nm, and macropores with $r > 25$ nm.

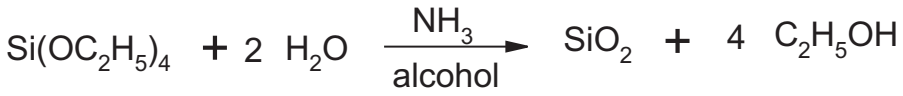

FIGURE 3.2: *Reaction of tetra ethoxy silane to yield silica. Under basic conditions a nucleophilic attack of the hydroxide ions of ammonia on the silicon atom takes place. The ethoxide-groups are replaced by these hydroxide ions and a hydroxysilane is generated. After release of water solid silica is yielded.*

concentrate here on the synthesis of silica spheres by the use of the hydrolysis of metal-alkoxides.

Already in the late sixties Stöber, Fink and Bohn described a base induced hydrolysis of tetraethoxysilane (TES) to yield monodisperse silica spheres in the micron-range [91]. By changing the concentration of the reactants the radius could be varied between 50 nm and 2 μm. The overall reaction of the Stöber synthesis is displayed in figure 3.2. The TES undergoes a nucleophilic substitution reaction where the hydroxide ion (OH^-) created by the ammonia attacks the electrophilic silicon atom and the ethoxide-groups are replaced by these hydroxy groups. The resulting tetrahydroxysilanes ($Si(OH)_4$) condensate with each other under the release of water to yield silica.

In the following section we describe the Stöber synthesis of silica spheres with four different sizes. Since the particles were synthesized for templates for air-sphere crystals of galliumarsenide and galliumphosphide, and galliumarsenide and galliumphosphide start to adsorb light below respectively $\lambda < 900$ nm and 550 nm, sphere radii for the template of such air-sphere crystals should be larger than respectively $r = 350$ and 225 nm. In this estimation a filling fraction of the high index material of 20% is assumed and it is taken into account that for *fcc* crystals the photonic band gap manifests in the range of second order Bragg diffraction.

3.2.1 Silica synthesis

All reactions were carried out in a so-called "Stöber-jar" placed in a thermostatic bath with a temperature of 20°C.[2] Glassware is cleaned with 8% hydrogenfluoride to remove possible nucleation sites (-OH groups) for the silica formation. Ethanol and ammonia (30%) are obtained from Merck. TES (99%, Fluka) is freshly distilled. The total TES concentration in the ethanol reaction mixture is 0.17 mol/l. The ammonia concentration is 2.25 mol/l for SL1 and SL2, and 1.70 mol/l for SL3 and SL4. SL1, 2, 3 and 4 correspond to the sample names (S=silica, L=Lydia,

[2]The synthesis of the silica spheres was performed at Van 't Hoff Laboratory at Utrecht University, at the colloid synthesis facility.

number 1 t/m 4 designates the batch). The reactions are on three liter scale. First the ammonia and ethanol are mixed thoroughly after which the TES is added in a constant stream and under vigorously stirring. Within 15 minutes the nucleation is already visible; the reaction mixture becomes turbid. The reaction mixture is stirred for two days and nights. During the first nucleation a maximum sphere size of $r \sim 250$ nm can be reached as described by Bogush *et al.* [147], and therefore a second growth step is necessary to increase the sphere size. This can easily be done by adding an additional amount of TES to the reaction mixture after the first growth step is completed. The amount of added TES can be predicted with the following equation

$$V_2 = V_1((\frac{r_2}{r_1})^3 - 1) \tag{3.1}$$

where r_1 and r_2 are respectively the radius of the spheres before and after the second growth step [147]. V_1 and V_2 are respectively the volume of TES in the first (nucleation) step and the volume necessary for the desired radius r_2. After the reaction is completed the spheres are collected by sedimentation and decantation. During the sedimentation, which took at least three weeks for the smaller spheres (r = 231 nm), the reaction mixtures were shielded from carbondioxide (CO_2) to prevent the formation of ammonia-salts and therefore decrease the aggregation. After decantation fresh ethanol is added to decrease the concentration of the ammonia.

We observed that the maximum sphere radius obtained after the first reaction step was larger than expected, about r = 300 nm instead of the expected r = 250 nm, based on reference [147]. A possible explanation for this discrepancy can be the low speed of stirring during the addition of TES. When stirring is not fast enough larger seeds are produced and therefore a larger final sphere size is obtained. This also influences the polydispersity in a negative manner since the nucleation is not homogeneous. Since the radii of SL1 and SL2 were larger than expected, we lowered the concentration of ammonia in the synthesis of SL3 and SL4. This indeed yielded a smaller sphere radius in the first reaction step.

In table 3.1 the radii and polydispersities are displayed of the four different samples, measured with both Transmission Electron Microscopy (TEM) and Dynamic Light Scattering (DLS). A polydispersity δ is defined as the standard deviation divided by its mean. It can be seen that SL1, SL2 and SL3 have smaller radii if measured with TEM. This difference between the TEM-radius and the DLS-radius is usually observed; the spheres shrink significantly under the high vacuum in the TEM, yielding a smaller sphere size [148]. This is apparent for three samples, SL1, SL2 and SL3. For SL4 however the same sphere size is observed with both TEM and DLS. We do not have an explanation for this deviation. It can be seen that the size dispersion of especially SL1 and SL2 is quite high. Usually large polydispersities can be decreased by applying a second growth step. Since the growth of SL1

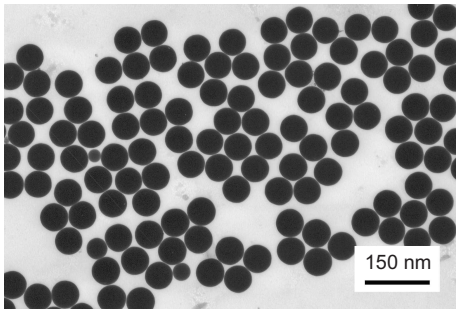

FIGURE 3.3: *Silica spheres (SL2) prepared via the Stöber synthesis. The radius of the spheres is r = 334 nm with a polydispersity δ = 6%. Some small spheres are also apparent, probably a result of a second nucleation during the second growth step.*

was done in one single step and the sphere size is larger than expected for a one-step synthesis (maximum $r \sim 250$ nm), the polydispersity could not be decreased. Differences in size distribution between the TEM and DLS radius can be explained by means of statistics. For the determination of the sphere size with TEM, 100 spheres are measured whereas with DLS more than 100000 spheres contribute. The polydispersities of SL3 and SL4 are both below 5%. It is known that this $\delta = 5\%$ is the boundary above which spontaneous colloidal crystallization becomes harder, i.e., more defects are present and the long-range order is much less. Pusey already demonstrated that if the polydispersity is larger than $\delta = 12\%$ a crystal will not be formed at all [149].

In figure 3.3 a TEM photograph is displayed, showing SL2 silica spheres with a radius of $r = 334$ nm. The spheres are monodisperse with a size distribution of $\delta = 6\%$. This polydispersity is partly caused by the presence of silica spheres with a deviant radius. In the photograph small particles are visible, probably formed by a second nucleation during the second growth step. Also dumbbells were found (not visible in photograph), a result of aggregation of two spheres, yielding larger sphere radii and therefore a larger polydispersity.

Sample name	Synthesis steps	R_{TEM} (nm)	δ TEM (%)	R_{DLS} (nm)	δ DLS (%)
$SL1$	one	302	9	322	11
$SL2$	two	334	6	343	6
$SL3$	two	275	5	301	1
$SL4$	one	231	4	231	2

TABLE 3.1: *Synthesized silica spheres with different sphere sizes. Sphere radii and polydispersities (δ) were measured with TEM and DLS. A deviation between TEM and DLS radius is usually observed and ascribed to the high vacuum of the TEM, due to which the spheres shrink significantly.*

Recently, a small number of silica colloidal systems have become available commercially from Duke Scientific. Nevertheless, synthesizing silica spheres ourselves is necessary to maintain sufficient flexibility in the fabrication of photonic crystals.

3.3 Artificial opals: templates for air-sphere crystals

The artificial opals are synthesized from a colloidal suspension of small particles by self-organization. To be able to work at optical wavelengths with photonic crystals, the particles should be on the order of the wavelength of light, i.e., several hundreds of nanometers. By sedimentation of these colloidal particles under gravity a *fcc* packed colloidal crystal is formed [118, 119]. The sedimentation can be induced by centrifugation. In this way the crystallization is forced and the process time is reduced. A disadvantage however is that smaller domain sizes are obtained, as will be discussed at figure 3.4 in this section. Once the colloidal crystal is formed, seen from the colorful Bragg reflections, the crystal is dried after which the artificial opal is formed. This artificial opal also exhibits beautiful reflections due to the refractive index contrast and the periodicity that is on the same order as the wavelength of light.

3.3.1 Experimental

For the growth of the templates, we have used 10% v/v colloidal suspensions of monodisperse polystyrene latex spheres in water with radii ranging from r = 63 to 426 nm, as obtained from the supplier (Duke Scientific). The crystal growth process was done in thin flat capillaries with a width of 4 mm, a thickness of 400 μm and a length of 7 cm. The growth took for the largest spheres (r = 426 nm) two months. Sometimes the growth of colloidal crystals was initiated by centrifuging the suspension for a couple of minutes. For the smallest sphere sizes (r < 213 nm) the colloidal crystals were completely grown in a centrifuge, since growing them by normal sedimentation would take more than six months. During the growth the top of the capillary is closed to prevent evaporation of the solvent. When the colloidal crystal was completely formed the top of the capillary was opened and the water was slowly evaporated over a time of 1-2 months. This should be done very carefully since the initial colloidal crystal consists of ϕ = 50-60% v/v polystyrene spheres and the final artificial opal of ϕ = 74% v/v, a relative densification of 50% [118]. The obtained artificial opal was 15-20 mm in length. The growth of silica opals was done similarly and further used in experiments of CVD of galliumarsenide [127]. The growth of these silica opals will not be discussed here.

The Scanning Electron Microscope (SEM) images were either taken with an ISI DS-130 scanning electron microscope (at the University of Amsterdam), after sputtering the samples with a thin layer of gold, or with a LEO Gemini 1550 FEG scanning electron microscope (at MESA+ institute at Twente University).

Optical microscope photos were taken with an Olympus SZ60 microscope, equipped with an Olympus SC35-12 camera.

3.3.2 Results and discussion

In figure 3.4 an optical micrograph is displayed of two artificial opals with measured sphere radii of r = 460 nm (sphere radius specified by the supplier is slightly smaller, r = 439 nm).[3] The opals were grown in flat capillaries by sedimentation. The beautiful blue and green colors are a result of optical Bragg diffraction. Different colors appear because the angle of incidence of the illuminating white source varies with the (111) crystal planes. Furthermore different colors can be caused by higher order Bragg diffraction. The first order Bragg diffraction for an opal with r = 460 nm, is λ_{111} = 2165 nm, far away from the wavelengths of visible light (λ = 400-750 nm). Second order Bragg diffraction, however, appears already at λ_{222} = 1080 nm, close to visible wavelengths. Different higher order diffraction conditions are easily met for slightly different angles of observation, causing a collection of reflected colors. The opals have a width of 3 mm and a length of about 1.5 cm.

In the bottom part of both opals many small crystallites are apparent compared to the large "elongated fingers" in the upper part. These small domains clearly illustrate the difference between slow and fast crystallization; the small crystallites are caused by fast crystallization in the centrifuge whereas the vertical long bands are slowly grown. The vertical crack in the middle, clearly seen in especially figure 3.4(a), is due to shrinking during the evaporation from colloidal crystal to opal.

In figure 3.5(a) and (b) several SEM-pictures are displayed. In figure 3.5(a) a well ordered *fcc* structure can be seen which consists of an area of 24 by 18 spheres corresponding to 20 by 15 μm. This area is part of an even larger domain. The radius of the particles is 460 ± 3 nm. The face that is seen is the (111) plane that preferentially grows parallel to the glass wall of the capillary [118, 119].

In figure 3.5(b) a large domain is seen from an opal with the same sphere size as in (a). It consists of 98 spheres by 127 spheres corresponding to an area of 86 by 112 μm. Several spheres have popped out probably during removal from the capillary where the spheres can be stuck to the glass wall. Although some line defects are seen they do not break up the large crystal domain. The fissure at the

[3]The measured sphere radius with SEM is applied henceforth. This also holds for particles with different radii further in this thesis; the measured SEM radius is applied. For more details see reference [57]

bottom right however, does interfere with the crystal domain and is probably caused during drying of the colloidal crystal as first mentioned by Park and Xia [150]. Although Jiang *et al.* ascribed such cracks to the vacuum applied in the SEM [148], we think that the cracks seen in our opals are caused by shrinkage during drying of the colloidal crystal.

3.4 Infiltration and calcination

After the opal is formed the interstitial holes between the spheres are filled with a solid material by the use of liquid precursor. The voids between the spheres are infiltrated via capillary forces through the opened bottom of the capillary. Since the precursors are usually quite viscous in pure form they are diluted with alcohol to make them less viscous. The infiltration can be followed by eye since the refractive index ratio changes, from $n_{\text{polystyrene}}/n_{\text{air}}$ to $n_{\text{polystyrene}}/n_{\text{liquid}}$, and the color changes from white opalescent to gray. After infiltration, the liquid precursor is hydrolyzed with water to yield a solid pre-stage of the metal oxide. Many hydroxyl groups are still present in this stage. The procedure of infilling and hydrolysis were performed up to six times, to get a maximum filling fraction of ϕ = 5 to 12% v/v.

After the infiltrations are completed the polystyrene is removed by heating to a temperature of 450°C. At this temperature the polystyrene is gasified and burned. During this heating also the remaining hydroxyl groups from the metal oxide and the remaining solvent is removed. With powder X-ray diffraction the crystalline structure of the material is determined, which can be either amorphous or crystalline. In the following section we describe the infiltration of opal templates with titania (TiO_2), zirconia (ZrO_2), alumina (Al_2O_3) and silica (SiO_2).

3.4.1 Experimental

To infiltrate the opals we have used liquid precursors consisting of an alkoxide diluted with an alcohol: ethanol or propanol. The precursors used for zirconia, alumina and titania were respectively zirconium(IV) propoxide TPZ (70% solution in 1-propanol), aluminum tri-sec butoxide TBAl (97%) and titanium (IV) propoxide TPT (98%) and were purchased from Aldrich. The silica precursor tetra ethoxy silane (99%) (TES) was obtained from Fluka. Ethanol (99.5%) was obtained from Merck and 2-propanol (99.5%, anhydrous) from Aldrich. The infiltrations were done in a glovebox under nitrogen to prevent premature hydrolysis before complete infiltration. An infiltration took typically about $\frac{1}{2}$ until 1 hour. Usually it was observed that the lower part is infiltrated best because the space between the spheres is blocked at a certain height and therefore the upper part is less infiltrated. To overcome this problem we also added precursor from the top. In this way both

FIGURE 3.4: *Optical micrograph of two opals (a) and (b), that both consist of polystyrene spheres with radius r = 460 nm. Colorful blue and green reflections are apparent, resulting from optical Bragg diffraction. At the bottom of the opals many small crystallites are present, caused by fast crystallization by centrifugation. The upper part of the samples consist of large crystals, due to slow crystallization. A long vertical crack is present in both opals, caused during drying from colloidal crystal to opal.*

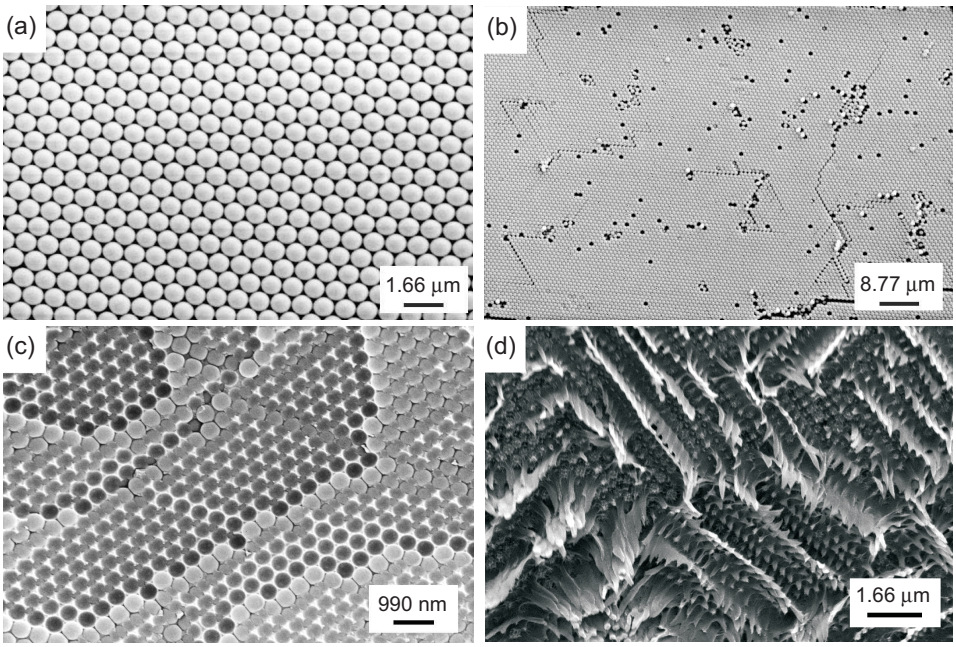

FIGURE 3.5: *SEM-images of several opal templates. (a) An image of an opal with particle radius r = 460 ± 3 nm. The spheres are well ordered in a hexagonal plane, i.e., the fcc (111) plane. (b) Zoomed out image of a different sample with the same sphere size. Vacancies are attributed to the removal of the opal from the capillary, and line defects are attributed to drying. (c) An image of an infiltrated opal where the polystyrene spheres are still present. The template consists of spheres with a radius of r = 238 ± 2 nm and is infiltrated one time with the precursor of titania. (d) Side view of a cleavage plane of a r = 225 ± 2 nm polystyrene opal infiltrated with the precursor of silica. It can be seen that there is still some ordered nanostructure present but the polystyrene spheres are totally disappeared. The sample is optically transparent.*

the top part and the bottom part are infiltrated. After the opal was infiltrated with the precursor it was first placed in a nitrogen flow for several hours to evaporate the remaining solvent ethanol or propanol. After the solvent was evaporated the infiltrated opal was placed in a water-rich environment to hydrolyze. During the reaction with water the alkoxy-groups are replaced by hydroxy-groups yielding a solid pre-stage of the metaloxide ($M(OH)_4$).

Silica inverse opals were made with small colloidal silica-particles with a radius of r = 10-13 nm and were made by Judith Wijnhoven at Utrecht University. The particles were suspended in ethanol. After each infiltration the sample was left to dry overnight. Nine or ten infiltrations were necessary to obtain a maximum

volume fraction $\phi \sim 10\%$ v/v for a robust structure. In some cases a last infiltration with TES was done to get smoother silica walls.

To remove the polystyrene template the samples were heated to $T = 450°C$ in the following way: 0.33°C/min to 80°C, one hour at 80°C, 1°C/min to 450°C, 6 hours at 450°C, cooling down with 10°C/min. During this heating procedure the remaining hydroxyl groups of the pre-stage of the metaloxide are also removed and the oxide is crystallized.

To determine the crystallinity of the metaloxide material (the backbone), wide-angle X-ray Diffraction (XRD) was done on a Nonius PDS120 powder diffractometer equipped with a CPS120 detector and using a Cu K_α generator at a wavelength of $\lambda = 0.154$ nm.

3.4.2 Results and discussion

A SEM-image of an infiltrated opal is seen in figure 3.5(c). This opal with a sphere size of $r = 238 \pm 2$ nm was infiltrated one time with the titania precursor TPT. The TPT reacted with an excess of water but the polystyrene was not yet calcined. A clear difference can be seen between the infiltrated opal and the bare opal in figure 3.5(a). The white material is the hydrolyzed titania precursor. Since this plane is a cleavage plane also areas are present where the spheres have left a circular imprint. Moreover parts are visible with triangular traces, the original interstitial holes. This SEM-image clearly illustrates that the well-ordered *fcc* arrangement of the polystyrene spheres is not affected during the infiltration and the hydrolysis of the precursor. Since often SEM-images of bare templates or completely formed air-sphere crystals are shown, this SEM-image is one-of-a-kind since it displays both materials: the template as well as the final air-sphere crystal backbone.

The result of infiltrating an opal with TES, the precursor of silica, is displayed in figure 3.5(d). This precursor reacts with water in the same way as the other alkoxide precursors, although much slower. Different from our usual experiences the opal became optically transparent during the first infiltration. From the SEM-picture it can be seen that there is still some ordered structure present but the polystyrene spheres have totally disappeared. It appears that the TES is reactive towards polystyrene and dissolves the polystyrene. Since the speed of hydrolysis and subsequent condensation of TES is lower compared to other oxide precursors [146], it is possible that TES interacts with the polystyrene surface before it deposits as silica. It is remarkable that other groups were able to fabricate silica inverse opals with TES [115, 151, 152] even without diluting the precursor with alcohol. Possible differences between their and our experiment is the surface of the polystyrene spheres. Most groups synthesize the polystyrene particles themselves and therefore the surface characteristics are in principle known. It is believed that

the presence of charged groups, like sulfate groups or carboxylate groups, act as the catalysts for silica polymerization. Duke Scientific did not specify the surface of their polystyrene particles and therefore the surface characteristics are unknown to us. Another factor can be an unknown surfactant, not specified by the supplier, present in the colloidal suspension. After drying of the colloidal crystal the surfactant remains on the polystyrene surface and can influence the polymerization. We have also investigated the possibility of infiltrating the opals first with hexadecyltrimethylammoniumbromide (HTAB), a surfactant that induces the silica polymerization [153, 154]. However, after infiltrating these pretreated samples with TES, the opals also became optically transparent. The HTAB therefore did not noticeably influence the silica polymerization.

The infiltrated opal is heated to remove the polystyrene spheres and to complete the reaction of the alkoxides to solid titania. After infiltration and reaction with water it is assumed that the solid is a complex conglomerate that contains still many hydroxy and alkoxy-groups. This was also analyzed with Raman spectroscopy where an TPT infiltrated and not yet calcined opal, revealed complicated spectra that are very different from any known polymorph of titania [58]. The removal of remained hydroxyl and alcohol groups will consequently bring shrinkage about as will be discussed in section 3.5.1.

In order to check the crystallinity of the material backbone in the air-sphere crystals, and therefore the completion of the reaction to solid crystalline material, powder X-ray diffraction was done. For these experiments we did not use the air-sphere crystals themselves but powder that was prepared the same way. In figure 3.6(a), (b) and (c) the XRD-patterns of respectively titania, zirconia and alumina are displayed that have been heated to different temperatures. The curves are offset for clarity.

Figure 3.6(a) shows a sequence of XRD-patterns, taken from the precursor of titania TPT, which has reacted with water and was heated to three final temperatures T. After 10 hours at $T = 250°C$, no diffraction peaks are apparent at all. Heating for 10 hours at $T = 350°C$ gives one weak peak suggesting that crystallization of titania has started. Heating to a temperature of 450°C finally yields a diffraction pattern with many diffraction peaks, that agrees very well with the anatase form of titania [155]. From the width of the X-ray Bragg peaks the grain size of the crystallites can be calculated with Scherrer's formula [156]. The averaged grain size of the particles is found to be 15.2 ± 1.2 nm. The fact that the titania and zirconia backbone consist of 10-20 nm crystallite grains causes optical Rayleigh scattering, i.e., scattering from particles smaller than the wavelength of the light. Exactly this Rayleigh scattering causes the white appearance of the crystal that occurs besides iridescence, causing a opalescent appearance.

The XRD patterns displayed in figure 3.6(b) are taken from zirconia powder

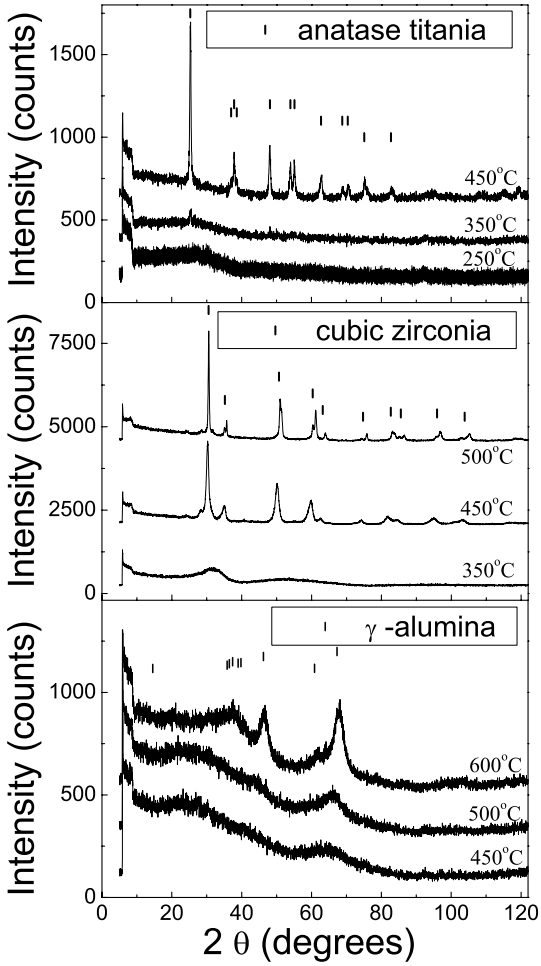

FIGURE 3.6: *XRD-patterns of several metaloxide powders reacted from liquid precursors. (a) Diffraction patterns of titania. At T = 350 °C the diffraction pattern shows a weak peak at the position of the strongest anatase diffraction peak (2θ = 25.3 °). The upper diffraction pattern (T = 450 °C) is in excellent agreement with the anatase diffraction pattern displayed as vertical ticks. (b) Diffraction patterns for zirconia calcined at various temperatures. Zirconia starts to crystallize from T = 350 °C and is completely crystalline at T = 500 °C. (c) Diffraction patterns of alumina. Broad humps are apparent, typical for amorphous materials. Heating to T = 600 °C establishes two Bragg peaks, indicating that crystallization has initiated.*

made from TPZr. The patterns show that at T = 300°C zirconia reveals no X-ray reflections. A broad hump is apparent, suggesting that the crystallization process has started, i.e., hydroxyl groups are eliminated and Zr-O-Zr bonds begin to form. At a temperature of 450°C the reflections are clearly visible and at T = 500°C the peaks are even narrower and zirconia has become crystalline in the metastable cubic form [157]. After heating until a temperature of 450°C the powder was white and the averaged grain size was found to be 7.5 ± 0.4 nm. Tick marks display the literature values for the expected Bragg peaks for the cubic form of zirconia and agree well with the observed peaks. The powder heated until T = 500°C was black and the averaged grain size turned out to be ∼ 20 nm. Although the peaks at T = 500°C are more pronounced we heated the air-sphere crystals of zirconia only until a temperature 450°C to prevent the black color. A black color causes absorption of visible light, which is disastrous for photonic crystals. Different from our results Holland *et al.* found zirconia in the baddeleyite phase (monoclinic) after heating for 7-12 hours at T = 575°C [115, 139]. It is known from zirconia that it transforms in the monoclinic phase by heating to higher temperatures. Probably this transformation has happened above T = 500°C and therefore is not present in our samples.

Alumina does not completely crystallize below a temperature 600°C as was measured with powder X-ray diffraction. In figure 3.6(c) it can be seen that after heating the alumina powder to T = 600°C broad peaks are formed indicating that the alumina starts to crystallize. The positions of the appearing peaks resemble those of the γ-alumina [158]. This γ-alumina is indeed the first crystalline form in the transformation sequence upon heating [159, 160]. Since the widths of the peaks are very broad and reflections at other angles are missing we can conclude that the alumina has not crystallized completely. We were not able to heat at higher temperatures due to oven limitations. We also expect that heating to higher temperatures can destroy the macroporous structure, as also seen with titania [57]. Vaudreuil *et al.* heated alumina air-sphere crystals to several temperatures and checked the crystallinity of the material with powder XRD [142]. Below T = 900°C only very weak were reflections present and the material was still amorphous. Heating to a temperature 1200°C resulted in crystalline α-alumina but the structure was totally collapsed and even globular particles were formed.

From silica it is known that it is amorphous below T = 800°C. Consequently we did not perform X-ray diffraction experiments on our silica material.

Thermogravimetric analysis experiments by Yan *et al.* have revealed that all polystyrene is removed at a temperature of 350°C [161]. Thus, the temperature of 450°C used to complete the reaction to titania, zirconia and alumina, is certainly sufficient to remove the template and obtain air-sphere crystals. The observation of fully crystallized anatase titania at T = 450°C agrees well with the thermogravimet-

ric experiments that reveal an exothermic peak at $T = 404°C$ [162]. For zirconia, reference [163] observed a strong exothermic peak at $T = 430°C$ [163], corresponding well with our observation of crystalline metastable cubic zirconia at a temperature of 450°C.

As an alternative to heating, we have also extracted the polystyrene with an organic solvent, tetrahydrofuran. This yielded a disordered inverse structure without long-range order and the sample broke into small pieces. These results are attributed to a swelling of the polystyrene particles before their dissolution. By dissolving the polystyrene, the sample is not heated, therefore the reaction to crystalline titania, zirconia and alumina is not completed.

Powder X-ray diffraction is a powerful tool to characterize the crystallinity of a material and we have shown that for materials applied in our air-sphere crystals, higher temperatures result in a crystalline material of the backbone. The observation of crystalline material is first of all important because the materials in crystalline form are transparent at optical wavelengths. Secondly, the refractive index increases with increasing calcination temperature, due to evaporation of the volatiles and breakdown of the molecular units leading to the formation of oxides with higher density. Thirdly a crystalline material is inextricably bound with a high purity of the material which is beneficial for materials science or chemical applications. For optical experiments the high purity is even more important since low optical absorption, associated with material purity, is indispensable for photonic crystal experiments.

3.5 Inverse opals of inorganic oxides

After the removal of the template by calcination a macroporous structure is produced, also called an air-sphere crystal. The structures consist for 90% v/v of air and therefore are very brittle. Caution is required during handling of these small pieces of air-sphere crystal. Typical sizes of the crystal are 1-2 mm in cross-section. The quality of the air-sphere crystals are usually investigated with scanning electron microscopy but recently more and more groups are aware of the importance of optical characterization of these air-sphere crystals. The technique to investigate photonic crystals with small angle X-ray scattering (SAXS) was first described by Wijnhoven *et al.* [57] and turned out to be an excellent probe for bulk long-range order, air-sphere surface roughness and size polydispersity, and will not be discussed here due to its complexity. In the following sections we describe the characterization of inverse opals with SEM, optical microscopy, reflectivity experiments and X-ray absorption.

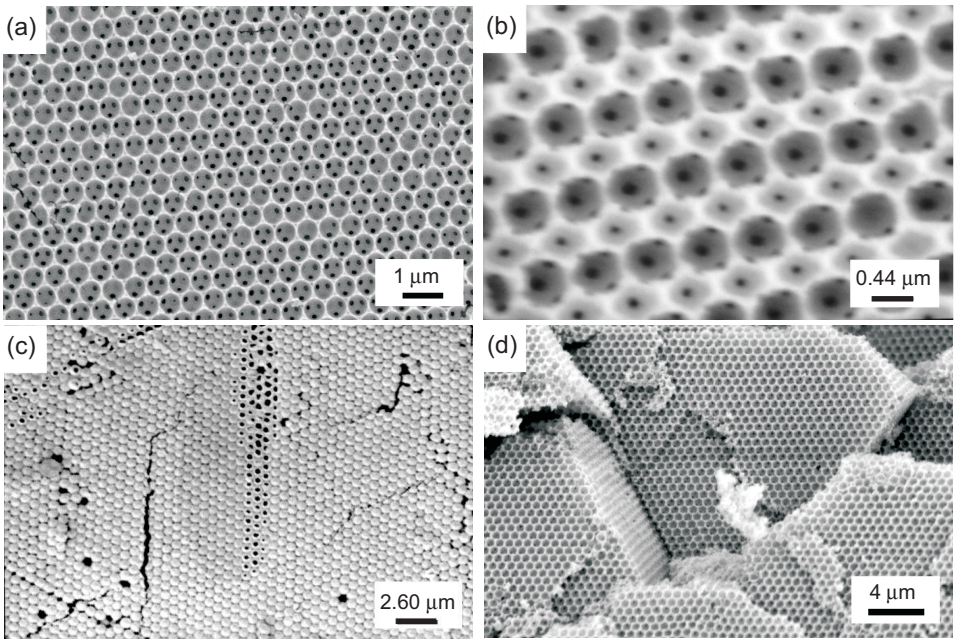

FIGURE 3.7: *SEM-images of inverse opals made of titania. (a) A fcc surface plane of an air-sphere crystal with sphere radii of r = 321 ± 4 nm. The air spheres are arranged in a nearly perfect hexagonal pattern. The windows, i.e., the black spots, connect the neighboring air spheres lying one layer beneath. (b) A (110) cleavage plane of a different sample, made from a r = 460 ± 2 nm. The macropores are arranged in a rectangular pattern. (c) A (111) plane of an inverse opal with sphere radii of 322 ± 3 nm (same sample as figure (b)). The spheres are closed, in contrast with what is usually seen, probably due to the space between the capillary and opal itself. (d) An image of the same crystal as displayed in (b) and (c). This picture clearly illustrates the 3D character of the air-sphere crystals.*

3.5.1 Characterization with scanning electron microscopy

SEM is a widely used technique to characterize inverse opals, especially their surface characteristics. In figure 3.7(a)-(d) SEM-images of several inverse opals made of titania are displayed. Figure 3.7(a) shows the surface of a sample with sphere radii of r = 321 ± 4 nm. The surface is a nearly perfect hexagonal arrangement of 22 by 17 spheres corresponding to an area of 14 by 11 μm. This hexagonal arrangement corresponds to a (111) crystal plane. The sample results from a r = 403 ± 2 nm polystyrene template and had a shrinkage of 20% compared to the template. In our experience, the flat surfaces of the crystals are invariably the (111) planes, because upon crystallizing the template, the colloids prefer to order parallel to the

capillary wall [118, 119]. The highly-ordered structure of macropores confirms that inverse opals are authentic replicas of the original opal templates (compare with figure 3.5(a)). The dark spots in figure 3.7(a) are remnants of the contact points between nearest-neighbor spheres in the template that have developed into windows between the pores. At these positions the precursor did not deposit and therefore these positions remain as air holes.

It is common for air-sphere crystals synthesized from metal-alkoxides to shrink, since the precipitated material in the opal still contains a lot of hydroxy and alkoxy-groups and is not yet the solid titania. We usually observed a shrinkage between 25-30% (see in more detail section 3.5.2). As a result not only the air spheres but also the domain size in inverse opals is commonly smaller compared to the domain size in polystyrene opals. This shrinkage is possibly a restriction for certain applications as will be discussed section 3.9.

Figure 3.7(b) shows a rectangular arrangement of a single domain of macropores of a different sample, made from a template of $r = 460 \pm 2$ nm. The spheres have a radius of $r = 322 \pm 3$ nm, a shrinkage of 30% compared to the template. The rectangles have an edge ratio 1 to $\sqrt{2}$, and are thus a (110) cleavage plane. The smaller pores are from a layer at a more elevated height (towards the viewer), whereas the large pores are in a next layer deeper down. The observation of this (110) plane is important crystallographic information since it confirms the existence of a *fcc* crystal and rules out other close-packed hexagonal structures, such as random and hexagonal close packed (*hcp*). Previously such random and *hcp* stacks of hexagonal planes were often reported for colloidal crystals of other groups [164].

Figure 3.7(c) shows an interesting feature that occurs on a surface of a macroporous crystal: nearly all the pores are totally covered with a shell of titania instead of being open, as in figure 3.7(a), and as usually reported in literature. A few macropores near the center of the SEM have partially open surfaces. Since such "closed" pores have not been reported elsewhere, it is attributed to a characteristic of our sample synthesis, in particular the growth inside glass capillaries. We propose that closed macropores are related to incomplete wetting of the alkoxide on the glass wall of the capillary during the synthesis: if the opal spheres are close to the glass wall, the opal surface can not be completely covered, resulting in surfaces as in figure 3.7(a). If there is some space between the opal and the glass wall due to shrinkage of the opal upon drying, the latex can be completely covered with the precursor/ethanol mixture, resulting in covered surfaces as in figure 3.7(c). We note that there is optically no noticeable difference between macropores with "closed" or "open" surfaces: both kind reveal the same beautiful colored iridescence. Therefore, we do not consider closed air spheres as a defect. The surface in figure 3.7(c) also reveals a small line defect (lower left), that we attribute to strain as a result of the shrinkage that occurs during the calcination. Nevertheless, the fissure is much

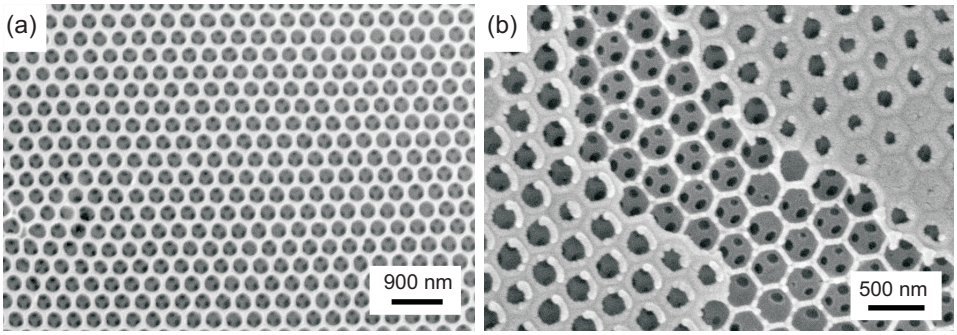

FIGURE 3.8: *SEM-image of an inverse opal made of zirconia. (a) A nearly perfect hexagonal arrangement of macropores in zirconia that forms a fcc (111) surface plane. The domain without any defects is quite large, about 20 by 25 spheres and is part of an even larger domain consisting of 100 by 80 spheres. The mean domain size is about 40 by 30 μm. The sphere size of the air-spheres is r = 181 ± 1 nm. This is a shrinkage of 24% compared to the template which consisted of r = 238 ± 2 nm spheres. (b) An image from the same sample as in (a), also on the surface. The open air spheres are like a path in a domain of closed air spheres. The closed spheres diffract as well as the open spheres.*

smaller than the whole crystal domain. Thus, this SEM picture shows a large single domain of 35 by 57 spheres, corresponding to 22 by 35 μm.

Figure 3.7(d) displays a SEM-image from the same crystal as in (b) and (c). From this picture the three-dimensional (3D) character is clearly visible. It can be seen that both materials are connected structures as the windows are present in air-spheres of all the displayed layers. From theory it is well-known that a 3D connectivity of both high- and low-index material in a photonic crystal is favorable [23]. Figure 3.7(d) clearly illustrates that the structure inside, so not only the surface, exhibits the same long range order.

In figure 3.8 SEM-pictures of a zirconia air-sphere crystal are displayed. Figure 3.8(a) is a (111) surface plane of an air-sphere crystal made of pure zirconia. The domain without any defects is quite large, about 20 by 25 spheres and is part of an even larger domain consisting of 100 by 80 spheres. The mean domain size is about 40 by 30 μm. The sphere size of the air-spheres is $r = 181 \pm 1$ nm. This size is a shrinkage of 24% compared to the template which consisted of $r = 238 \pm 2$ nm spheres. We found shrinkages comparable to those of the titania air-sphere crystals. Figure 3.8(b), a picture from the same sample, shows air spheres with both open and closed surfaces. The open air-spheres are as a connected line between the closed air spheres. We have also seen similar closed air spheres in titania crystals. These closed air spheres diffract as well as the open spheres as was observed with

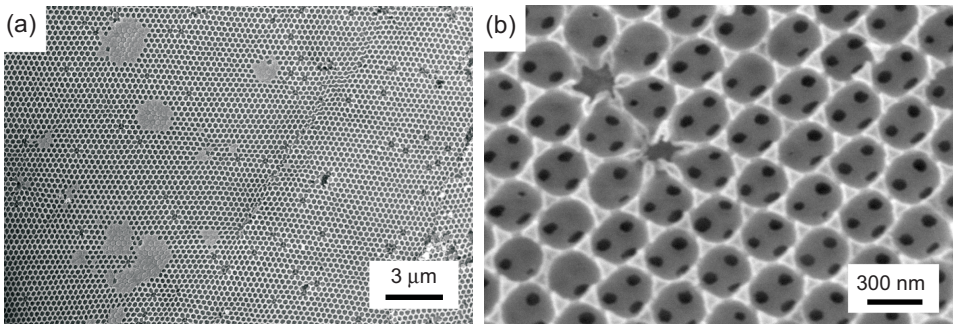

FIGURE 3.9: *(a) a (111) top view of a large domain in a alumina inverse opal with an average air-sphere radius of r = 161 ± 3 nm. The domain is as large as 90 by 65 spheres. (b) A close-up from the same picture. The windows in this picture are clearly visible and also the interstitial space between three spheres. There are two peculiar features in the upper left corner; a kind of collapsed air sphere in the shape of a flower.*

optical microscopy.

Figure 3.9(a) shows a (111) top view of an inverse opal of pure alumina. The picture displays a large domain of ~ 90 by 65 spheres corresponding to an area of ~ 30 by 20 μm. The mean air-sphere radius of this crystal is r = 161 ± 3 nm, that is a shrinkage of 29% compared to the template with r = 225 ± 2 nm spheres. This value agrees well with the values observed in titania and zirconia inverse opals. In figure 3.9(b) a close-up of this same picture is shown. The windows in this picture are clearly visible and also the interstitial space between the three spheres. In the upper left corner of this picture there are two peculiar features; a kind of collapsed air spheres in the shape of a flower. It is an open question if these are formed because of a missing polystyrene sphere in the template before the infiltration or that the air sphere is cracked afterwards, for instance during the calcination.

Since infiltrating our polystyrene opals with TES did not result in air-sphere crystals of silica, we used instead small nanometer sized silica particles, that are not reactive towards polystyrene. The silica nanoparticles used in our research had sphere radii of ~ 10 nm. In some samples a last infiltration with TES was done to get smoother silica walls. The TES nucleates on the silica already present and therefore "glues" the silica particles together. Because there is already a lot of silica present we believed the precursor would not react with the polystyrene like we observed in figure 3.5(d).

The result of infiltrating a polystyrene opal eight times with a silica suspension followed by an infiltration with TES is shown in figure 3.10(a). A nicely ordered air-sphere crystal is apparent. The air-sphere size is about 370 ± 2 nm in radius, a shrinkage of ~ 13% compared to the template. The typical domain size is 18.5

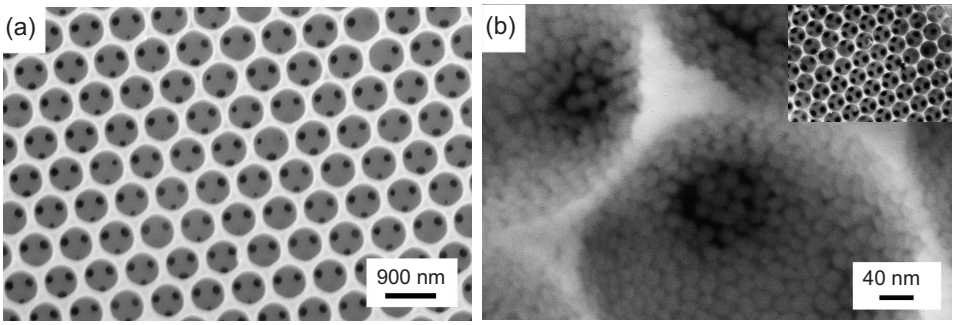

FIGURE 3.10: *SEM-images of two inverse opals made of silica. (a) A (111) top surface of an inverse opal of silica. The template was a r = 426 ± 4 nm polystyrene opal and was infiltrated eight times with a 10 nm silica sol and one time with TES. The final air-sphere size is 370 ± 2 nm in radius. (b) (111) arrangement of macropores in silica obtained from a template with r = 238 ± 2 nm after nine infiltrations with the 10 nm silica sol. A granular texture of the silica is apparent and the separate silica spheres are visible. These spheres are actually the silica spheres from the suspension and have indeed a size of r ∼ 10 nm. The air spheres have a radius of r = 221 ± 1 nm.*

by 15 μm (25 by 20 spheres), in good correspondence with values found for titania, zirconia and alumina. The determining factor for the domain size in the final air-sphere crystal is the quality of the polystyrene template. Since for the infiltration with solid particles similar templates are used compared to the preparation via liquid precursors, the domain sizes are similar.

Meng *et al.* and Subramania *et al.* already demonstrated that it was possible to make inverse opals in this way. Meng *et al.* used ultrafine particles of silica ($r \sim$ 7 nm) and infilled the voids of polystyrene opals by capillary forces [137]. Subramania *et al.* mixed a slurry of small silica nanoparticles with polystyrene spheres in advance, and used this mixture to grow the crystal [138]. After calcination high quality inverse opals were obtained with both techniques.

We also infiltrated the polystyrene opal with the silica nanoparticles suspension without an infiltration of TES afterwards. The result is shown in figure 3.10(b) where three air spheres are visible that are part of a larger domain as displayed in the inset. This picture is made with a high magnification and we expected to see silica nanoparticles from the suspension used for the infiltration. Indeed in the zoomed-in picture separate silica particles were visible with a particle size of r = 10-13 nm; the nanospheres used for the infiltration. The air-sphere radius is r = 221 ± 1 nm, a shrinkage of 12% compared to the template. This shrinkage perfectly matches with the result in figure 3.10(a).

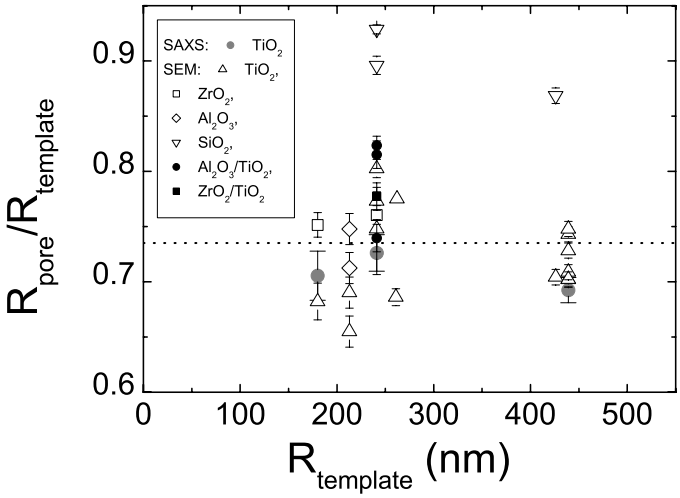

FIGURE 3.11: *Ratio of radii of macropores in air-sphere crystals R_{pore} compared to their opal templates R_{template} as a function of R_{template}. The radii are measured from SEM-pictures of air-sphere crystals of several oxides. Additional radii for macropores in titania are obtained from SAXS measurements done previously. It can be clearly seen that the silica inverse opals (down triangles) show less shrinkage compared to other oxides.*

We have shown with SEM-pictures that the formation of metal-oxide air-sphere crystals via sphere-templating results in well-ordered macroporous structures. Several deviations from most commonly observed structures, as closed spheres and different crystal planes, were discussed. These features do not influence the long-range order of the crystals adversely.

3.5.2 Shrinkage of air-sphere crystals compared to their template

After the repeated infiltrations of the precursor, the solid material between the polystyrene spheres is not yet the metaloxide (M_xO_y) itself, but a hydrolyzed species with still many hydroxyl groups present. The metal oxides itself, TiO_2, ZrO_2 and Al_2O_3, are formed during the heating cycle to 450°C where the remaining hydroxyl groups are evaporated and M-O-M bonds are formed. TiO_2 and ZrO_2 become crystalline during this heating cycle. It is not unlikely to observe shrinkage during this heating cycle since the hydrolyzed species between the polystyrene spheres is not yet in its final stage. Shrinkage does not happen if the filling material is already in its final form before the template is removed, as is illustrated previously with

rocksalt [57], gold [129] and germanium [130].

In figure 3.11 the radii of macropores in several oxides R_{pore} normalized to the radii of the template $R_{template}$ are plotted as a function of $R_{template}$. Ratios obtained from previously performed SAXS measurements are also displayed. The ratio is clearly smaller than 1 as is expected from the density change during heating. The average shrinkage for air-sphere crystals of all oxides (except SiO_2) was found to be 0.735 ± 0.046, and is plotted as a horizontal dotted line. It can be seen that the observed shrinkages vary around this value, without any size-dependent trend. Our inverse opals experience a linear shrinkage of 26.5%, which is in agreement with results reported elsewhere on air-sphere crystals (26-34%) [115] and ceramics (∼ 25%) [146]. The mixed oxide air-sphere crystals (ZrO_2/TiO_2 and Al_2O_3/TiO_2) display an average shrinkage that is somewhat smaller than for the pure oxides. Especially the Al_2O_3/TiO_2 crystals show a reduced shrinkage, only 21% compared to the template. This still agrees with the values found in literature.

The shrinkage observed for the silica inverse opals is much less, ∼ 10%, compared to crystals made of other oxides. This is caused by the fact that the silica is already in its final form during the infiltration and only shrinkage occurs due to the filling of the empty spaces between the nanoparticles. Other groups have noted that shrinkage of air-sphere crystals of metaloxides prepared via liquid precursors was less if the polystyrene template was removed upon extraction instead of heating [115].

3.5.3 Volume fraction determined by X-ray absorption

The volume fraction of the high index material is a very important quantity to interpret optical data on photonic crystals, thus it should be determined carefully. Previously the volume fraction was estimated from the average refractive index obtained from optical reflectivity measurements and the lattice spacing determined with SEM [58]. If the tilt correction for the SEM-micrograph is taken into account, this is a reliable technique to determine the volume fraction and will be discussed in section 3.6.2. Many other groups, however, rarely report measurements on the volume fraction and assume it to be the maximum possible value of ϕ = 26% v/v [124]. Also, the use of average refractive indices from Bragg diffraction [165, 166] may suffer from systematic errors, due to, e.g., neglecting of multiple Bragg effects [25, 167].

A technique that is independent from optical and SEM measurements is X-ray absorption. In this section we will discuss X-ray absorption experiments to determine the volume fraction of the solid material in an air-sphere crystal. The transmission of X-rays through a titania air-sphere crystal was measured at the beamline

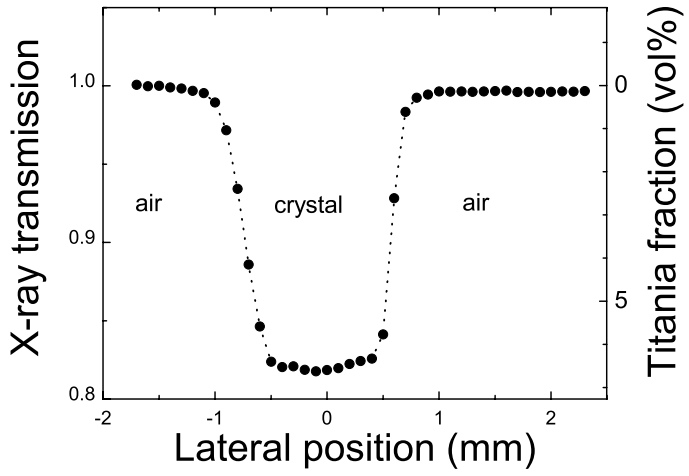

FIGURE 3.12: *X-ray transmission through an inverse opal of titania as a function of sample position. The X-ray beam probes a width of 0.3 mm, the width of the sample is 1.3 mm. At lateral position 1 and -1 mm the sample is outside the beam, at 0 mm the sample is in the middle of the beam.*

4/ID2 of the European Synchrotron Radiation Facility.[4] The monochromatic beam had a wavelength of 0.0989506 nm and could be focused on the sample to a narrow spot of about 0.3 x 0.6 mm. The absorbed X-rays account for the amount of material in the sample. In figure 3.12 the transmission of an air-sphere crystal of titania is measured as a function of position. The titania crystal consists of macropores of r = 149 nm. At lateral position x = 1 and -1 mm the sample is outside the beam, at x = 0 mm the sample is in the middle of the beam. When the sample is outside the beam, at position x = 1 and -1 mm, the transmission is 1, no X-rays are absorbed. If the sample is positioned in the beam, the transmission turns out to be 0.82. With a known absorption coefficient (α),[5] the thickness of the sample (L) and the intensities of the incident (I_0) and transmitted beam (I_t), the density of the absorbing material (ρ) can be calculated with the use of Lambert-Beer's law

$$I_t = I_0 \cdot e^{-\alpha L \rho}. \tag{3.2}$$

The corresponding volume fraction for this particular sample is plotted on the

[4]X-ray measurements were performed by J. E. G. J. Wijnhoven, M. Megens, M. S. Thijssen, T. Narayan and W. L. Vos.

[5]Taken from *International Tables for X-ray Crystallography*, Kynoch Press, Birmingham, 1962.

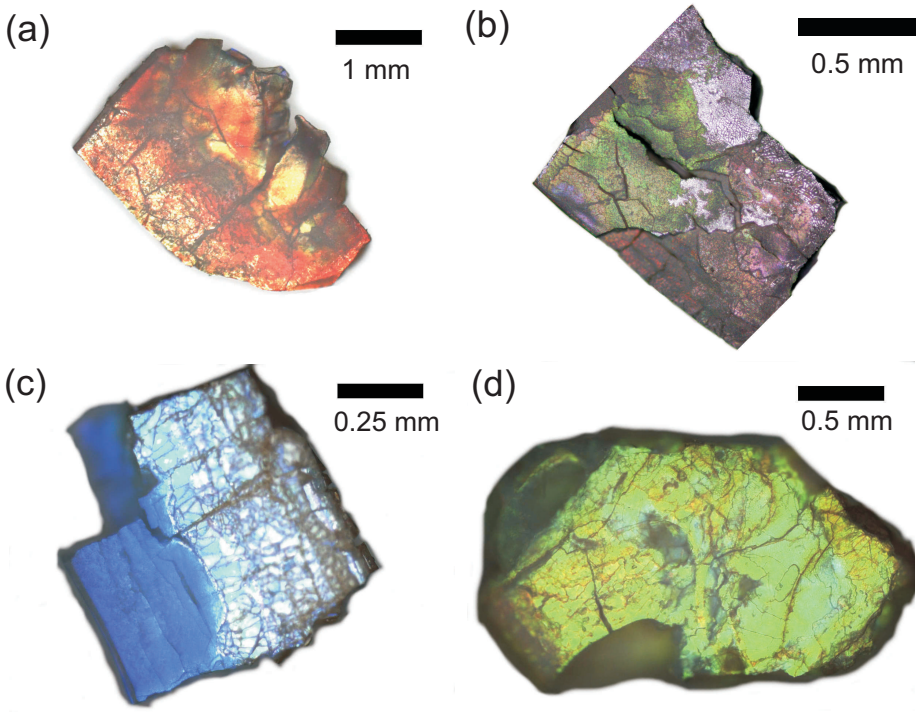

FIGURE 3.13: *Optical microscope images of air-sphere crystals made of several oxides. (a) An inverse opal alumina made from a r = 225 nm template (213-43). The lattice parameter is ~ 510 nm and the (estimated) average refractive index n_{avg} is 1.076 resulting in first order optical Bragg diffraction of λ ~ 630 nm, apparent as a orange-red color. (b) A crystal of air-spheres in titania with lattice parameter a ~ 1400 nm. A palette of colors is apparent, probably due to high-order multiple Bragg diffraction. (c) An air-sphere crystal made of zirconia with lattice parameter a ~ 370 nm (sample 180-41). Optical Bragg reflections appear as blue colors. (d) A silica air-sphere crystal (180-54) that was made from the same template as the zirconia air-sphere crystal in (c). Due to less shrinkage, the optical Bragg reflections are greener.*

right-hand axis of figure 3.12. The maximum volume fraction, i.e., the minimum transmission is found to be 6.5% for this particular sample. Additional measurements were done on titania inverse opals with several sphere sizes ranging from r = 120 to 1000 nm, yielding in volume fractions varying from ϕ = 5 to 12% v/v [57]. The trend in the observed volume fractions is that inverse opals with smaller sphere sizes have relatively less material than inverse opals with larger pores (r > 300 nm). This difference resembles the observations in SEM-pictures where the windows in small-pore samples are often relatively larger. We can not exclude, however, that incomplete infiltration of the small-pore samples studied may play a role.

No X-ray transmission experiments were done on inverse opals consisting of zirconia, alumina and mixed oxides. We expect nevertheless their behavior in volume fraction to be the same as for titania inverse opals since the same dilution ratios for the precursor and the same number of infiltrations were performed. For silica inverse opals we expect the volume fraction to be slightly larger, since more infiltrations are performed and the infiltration is done with a solid material.

It is obvious that all measured volume fractions are lower than the maximum ϕ = 26% v/v at complete infiltration of the interstitial holes. This is mainly caused by the presence of windows and incomplete infiltration. An infiltration with the precursor of an metaloxide is done with a diluted precursor since the precursor itself is too viscous and will always lead to incomplete infiltration. The maximum volume fraction after 6-8 infiltrations with diluted precursor (1:1 v/v with alcohol) can be calculated and turned out to be ϕ = 5-7% v/v. This is on the lower edge compared to the observed values in X-ray experiments (ϕ = 5-12% v/v). These larger volume fractions observed with X-ray absorption can be explained with inhomogeneous infiltration (see chapter 4). Also different dilution ratios that are sometimes used (3:1, 2:1 v/v precursor/alcohol), can result in larger volume fractions.

The volume fraction can also be determined with reflectivity experiments. With the center position of the reflectivity peak and the sphere size obtained independently from SEM-images, the average refractive index can be estimated. From the average refractive index the amount of solid material can be calculated as is also done in section 3.6.2 and equation (3.3). From these estimations values for ϕ of 10% are found, in agreement with the results found with X-ray absorption. An alternative way to estimate the amount of high index material in an inverse opal is to weigh the samples before and after infiltration [115]. With this method, however, infiltrated and non-infiltrated parts are averaged.

3.6 Optical reflectivity of inverse opals

The photonic air-sphere crystals synthesized in this chapter are excellent candidates to investigate spontaneous emission lifetime effects. Since the density of states in these crystals are strongly modified it is expected that the spontaneous emission will be controlled. The quality of the air-sphere crystals is then of utmost importance. An essential tool to determine the quality of photonic crystals is by means of optical characterization, from which the photonic parameter Ψ can be deduced. Air-sphere crystals already display by eye bright colors that are a result of optical Bragg diffraction, indicating a strong interaction with light. The wavelength of this diffraction is determined by the average refractive index and the lattice spacing of the crystal. The interaction of the crystal with light can also be measured with reflectivity, one of the oldest ways to study Bragg diffraction of crystals [20].

3.6.1 Optical microscopy

In figure 3.13 optical micrographs of several pieces of air-sphere crystals are displayed. The samples are illuminated with diffuse white light from above. Beautiful iridescence is apparent which is the result of constructive interference of waves reflected by successive (111) crystal planes present in the air-sphere crystal, see also equation (1.1). Both the average refractive index of the material and the spacing between the air spheres influence the color appearance. Next to iridescence optical Rayleigh scattering occurs, since the air-sphere crystal backbones consist of nm-sized grains, causing an opalescent color appearance. In the following paragraph we will demonstrate that the calculated wavelength of the reflected light agrees with the observed color appearance. Figure 3.13(a) displays an air-sphere crystal of pure alumina with a lattice parameter $a \sim 510$ nm, which can be calculated from the measured SEM-radius r, by $a = 2\sqrt{2} \cdot r$. From the lattice parameter a, the first order lattice spacing is calculated with $d_{111} = a/\sqrt{3}$. By assuming a filling fraction of $\phi = 10\%$ v/v high index material, as was determined previously by the use of X-ray absorption in titania air-sphere crystals (see previous section), the average refractive index is estimated from:

$$n_{\text{avg}} = (1 - \phi) \cdot n_{\text{air}} + (\phi) \cdot n_{\text{solidmaterial}}. \tag{3.3}$$

With the values of the average refractive index n_{avg} and the (111) lattice spacing d_{111}, the first order optical Bragg reflection λ_{111} can be calculated with Bragg's law

$$\lambda_{111} = 2 \cdot d_{111} \cdot n_{\text{avg}}. \tag{3.4}$$

The value for λ_{111} turned out to be for this air-sphere crystal 630 nm, appearing in a yellow-orange reflectance as seen in photograph 3.13(a).

Appearance of several colors simultaneously is due to higher order Bragg diffraction which turns out to be a complex multiple diffraction phenomenon [167, 168]. This higher order Bragg diffraction was also seen in opals, see figure 3.4. In figure 3.13(b) a beautiful example of this multiple Bragg diffraction for an air-sphere crystal is apparent. The lattice constant of this air-sphere crystal of titania is $a \sim 1400$ nm. The value for λ_{111} and λ_{222} of this crystal appear respectively above 1800 and 900 nm. The sample displays green as well as red colors.

Figure 3.13(c) displays an air-sphere crystal made of pure zirconia. The template used for this air-sphere crystal consisted of polystyrene spheres of $r = 180$ nm. This resulted in an air-sphere size of $r = 130 \pm 2$ nm (measured from SEM-pictures and not shown here), and a lattice parameter $a \sim 370$ nm. Because of the smaller air-spheres compared to figures 3.13(a) and (b), the optical Bragg reflections appear at shorter wavelengths. The calculated first order optical Bragg reflection is at $\lambda \sim 470$ nm which manifests in a blue color as can be seen in the photograph.

In figure 3.13(a) silica air-sphere crystal is displayed that was made from a template with the same sphere size as the zirconia air-sphere crystal in figure 3.13(c) (template $r = 180$ nm). The silica sample shows optical Bragg reflections more towards the green compared to the blue reflections of the zirconia sample. This is caused by a larger lattice parameter of the silica sample; the silica samples do not shrink as much as the samples made with the liquid precursors. The radii of the air spheres are larger, estimated to be $r \sim 155$ nm,[6] compared to $r = 130$ nm for the zirconia sample. These larger air spheres cause the optical Bragg diffractions to appear at longer wavelengths, appearing in the photograph of figure 3.13(d) as green reflections.

It is clear from this collection of optical images that the color changes with change in average refractive index and lattice spacing. The air-sphere crystals prepared from different materials show brilliant opalescence, indicating a strong interaction with light. A more detailed study of light interacting with crystals is shown in the next section, where reflectivity measurements are described.

3.6.2 Reflectivity measurement of inverse opals

Previously in our research group reflectivity measurements were done on titania inverse opals with several sphere radii. Since white light is used, the stop gap will manifest as a peak in the reflected spectrum; a reflectivity peak [167–169]. Galisteo-Lòpez and Vos also measured reflectivity as a function of angle of incidence with a monochromatic light source [170]. In their experiment single domains are probed and reflectivities are found up to 94%.

[6]The air-sphere radius is estimated from a shrinkage of $\sim 15\%$, since no SEM-pictures were available of this particular sample.

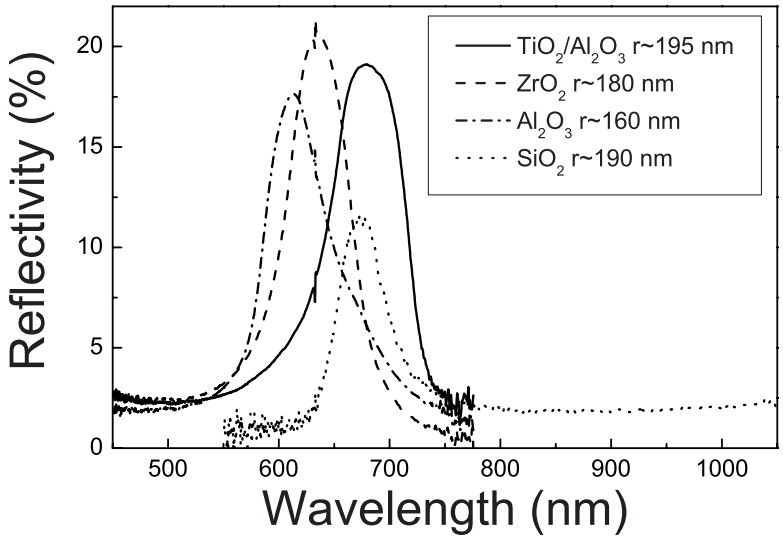

FIGURE 3.14: *Reflectivity spectra from air-sphere crystals of different oxides as a function of wavelength. Intense peaks are apparent resulting from optical Bragg diffraction. The titania/alumina peak, plotted as a solid line, is slightly asymmetric, probably caused by disorder. The zirconia peak, the dashed line, displays the highest reflectivity and exhibits the highest refractive index contrast m. The alumina and silica, displayed as a dashed-dotted and dotted line, show respectively a reflectivity of 17.5 and 12%.*

Several other research groups investigated the optical properties of self-assembled photonic crystals. Synthetic opals were investigated by Vlasov *et al.* [125, 164], where a reflectivity of 96% was found. How they calibrated the reflectivity, however, was not mentioned. Titania inverse opals were previously measured by several groups [165–171]. Subramania *et al.* report intense diffraction peaks on titania inverse opals but do not mention the absolute reflectance [165, 171]. Schroden *et al.* measured diffuse reflectance from photonic crystal powders of zirconia with different air-sphere radii spanning all colors of the visible spectrum [172]. The first results on higher order Bragg diffraction were reported by Vos and Van Driel [167, 168].

Optical reflectivity experiments were done with a Biorad FTS-60A Fourier Transform spectrometer with a broadband xenon lamp. The light beam is focused to a 0.6 mm diameter spot on the sample. The sample is aligned with the face of

the crystal to the incident beam. The spectra were referenced to those of a silver mirror with > 95% reflectivity [167, 169].

Figure 3.14 shows reflectivity spectra of several oxide air-sphere crystals as a function of wavelength λ. Intense peaks are apparent resulting from optical Bragg diffraction. The (111) Bragg reflections taken at normal incidence probe the stop gap in the [111] or Γ-L direction.[7] The small spikes at λ = 632 nm are from a co-propagating He-Ne laser beam in the spectrometer. Reflectivities were measured on crystals of pure oxides as well as on an air-sphere crystal consisting of two oxides (see chapter 4). Although the Bragg reflections of the crystals are intense and can easily be seen with the naked eye (see figures 3.13(a)-(d)) the maximum reflectivities are less than 100% for several reasons. An ideal diffraction peak has a flat top with 100% reflectivity as predicted with dynamical diffraction theory [20]. Experimental curves are usually rounded and have maxima less than 100%. One reason for this reduction is that light can be scattered diffusively by defects present at the (111) sample surface. This light will not be detected with our setup and decrease the reflectivity. Secondly the spot size of the beam, 0.6 mm, is larger than one crystal domain, that is usually around 30 μm in cross-section, resulting in illuminating more than 400 domains simultaneously. Illuminating several domains at the same time can give non-specularly reflections because the domains may be misaligned to each other. This is indeed confirmed by experiments that probe with a beam size of 10 μm and report reflectivity up to 94% [170]. We can exclude absorption in our experiments, since the oxides used in our air-sphere crystals are transparent at optical wavelengths.

We observed that for several reflectivity peaks the baseline was quite high, probably due to miss alignment. Usually baseline values below 3% are observed, in agreement with Fresnel reflection and the values of n_{avg} [173]. For clarity we therefore subtracted the titania/alumina, zirconia and alumina spectra with respectively 5, 2 and 3%. The silica-sample did not display a high baseline. The mixed oxide alumina/titania shows a maximum reflectivity as high as 19%. An optical micrograph of this sample is displayed in figure 4.5(a). The peak appears at a wavelength of 680 nm, in good resemblance with figure 4.5(a), where a picture of the same sample is shown and nice red reflections are apparent. The reflectivity of the pure zirconia sample is 20.5% and appears at λ_{111} = 640 nm. This zirconia sample was also investigated with optical microscopy (not shown here) and the main Bragg diffracted light was in the range of orange-red, resembling the measured value. The maximum reflectivity of the pure alumina sample is 17.5%. The peak is not symmetric probably caused by disorder (discussed below). The center position of the peak is at λ_{111} = 610 nm. The silica inverse opal displays a reflectivity of 12%

[7] The $\Gamma - L$ denotation results from the Brillioun zone, where Γ and L correspond respectively to symmetry points (0,0,0) and $(\frac{1}{2}, \frac{1}{2}, \frac{1}{2})$.

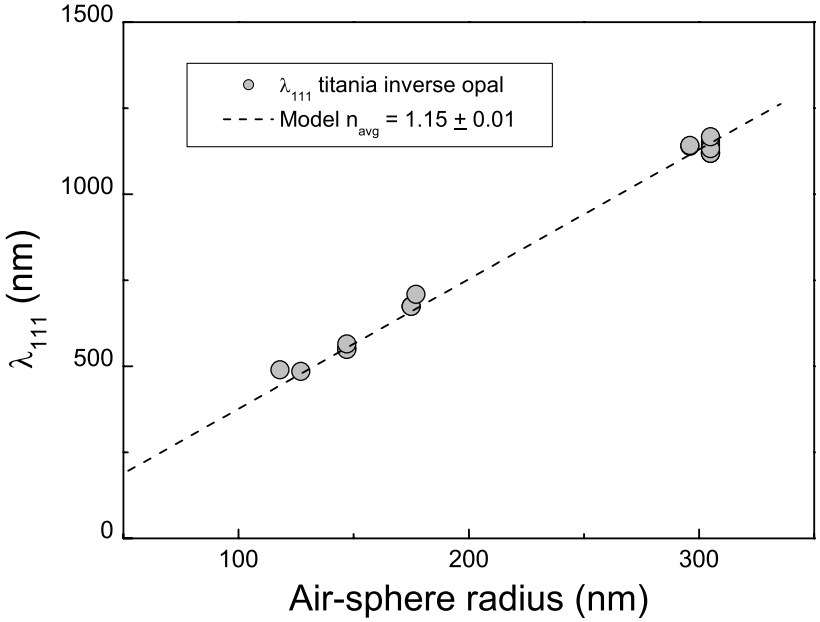

FIGURE 3.15: *The center wavelength λ_{111} for titania air-sphere crystals with different sphere radii. The error bars are smaller than the symbol size. A linear fit is applied through the data points and the origin, resulting in Bragg's law with an average refractive index n_{avg} of 1.15. By assuming a refractive index of titania $n_{titania} = 2.55$, a volume fraction $\phi = 9\%$ is obtained.*

and the maximum intensity appears at $\lambda_{111} = 675$ nm.

Although the reflectivities were not as high as 100%, we could clearly observe the Bragg peak for air-sphere crystals of different oxides. The peak position resembled the color that was observed by eye. A maximum reflectivity less than 100% could easily be explained by misaligned domains that give non-specularly reflections since the beam size is considerably larger than the domain size.

3.7 Optical reflectivity and refractive index

The observed trend in the measured diffraction peaks is that the maximum reflectivity decreases with decreasing refractive index contrast m. This is expected since a higher refractive index contrast has a larger photonic strength (see also equation (1.3) and next section). If we assume to probe for all air-sphere crystals the

same number of layers, the structure with the highest refractive index contrast will reflect more light per layer and therefore will display a higher reflectivity. Silica displays the lowest reflectivity whereas zirconia has the highest reflectivity. The refractive index contrasts of silica and zirconia air-sphere crystals are respectively m = 1.45 and 2.13. Further on in this chapter we concentrate on position and relative width of the reflectivity peaks which are together with the intensity of the reflectivity peak, important quantities for photonic crystals.

From the center wavelength λ_0 it is possible to make a estimate about the filling fraction ϕ. With the radius of the air-spheres, measured with SEM, the lattice spacing d_{111} can be calculated. With equation (3.4) the average refractive index n_{avg} can be deduced, which consists of two refractive indices, n_{air} and $n_{\text{solid material}}$. The filling fraction ϕ can then be estimated with equation (3.3). Here we assume that the average refractive index has a linear relationship with the filling fraction. An example of applying Bragg's law to several data points together is shown in figure 3.15. The measured center wavelengths λ_{111} from titania air-sphere crystals are plotted as a function of their sphere radius (measured from SEM-photographs). A linear fit without offset, i.e., Bragg's law, is applied through the data points and the origin, resulting in an average refractive index n_{avg} of 1.15 ± 0.01. If we assume the refractive index of titania to be n_{titania} = 2.7, a volume fraction of the solid backbone ϕ = 8.8 ± 0.6% v/v is obtained [33, 57].

By applying Bragg's law to the zirconia crystals it turned out that the filling fraction is about ϕ = 6.6 ± 0.1% v/v.[8] This value agrees well with values for volume fractions of titania air-sphere crystals that were previously measured with X-ray absorption [57]. With X-ray absorption values were found of ϕ = 5-12% v/v. This resemblance is expected since we observed with electron and optical microscopy already a lot of resemblance with the titania air-sphere crystals. For alumina air-sphere crystals values for the filling fraction of ϕ = 15 ± 2% v/v were found. This value exceeds the expected range and can be explained by a mismatch in estimated sphere radius. The the sphere radius was not measured on exactly the same sample but on a sample from the same template. For the air-sphere crystal made from pure silica the filling fraction is larger, about 17% v/v. This can be explained by the fact that the opal template is infiltrated with the silica itself, not a precursor. So no reaction has to take place and therefore no density change from liquid to solid material occurs.

For the mixed oxide titania/alumina sample, the refractive index of the solid material consists of two components, titania and alumina. The average refractive index of the solid material is calculated by assuming a filling ratio of 77%/23% v/v titania/alumina (see chapter 4). The filling fraction found this way is ϕ = 5% v/v,

[8] For these crystals we only measured on one sample so no curve is plotted as figure 3.15.

at the lower boundary of the values found with X-ray absorption on titania inverse opals. In the situation of a measured reflectivity from an area were alumina is the main component,[9] however, a volume fraction of $\phi = 8\%$ v/v can be estimated.

In general we can conclude that the obtained volume fractions from reflectivity experiments agree well with the volume fractions measured with X-ray absorption. An average volume fraction of $\phi = 10\%$ v/v, that is usually assumed, is well-founded.

3.8 Relative widths of reflectivity peaks

The relative width of a reflectivity peak is a good measure for the photonic strength, i.e., the light interaction of the crystal, of a photonic crystal. From the full width at half-maximum (FWHM) of the reflectivity peaks, also denoted as $\Delta\lambda$, we can deduce this relative width, expressed as $\Delta\lambda/\lambda_0$, where λ_0 is the center frequency. We must realize that the measured relative width is the sum of the width caused by photonic strength and disorder

$$\left(\frac{\Delta\lambda}{\lambda_0}\right)_{\text{measured}} = f\left(\left(\frac{\Delta\lambda}{\lambda_0}\right)_{\text{photonic}}, \left(\frac{\Delta\lambda}{\lambda_0}\right)_{\text{disorder}}\right). \tag{3.5}$$

In a perfect crystal without any defects the measured relative width would only result from the photonic strength of the air-sphere crystal. Since fabricated photonic crystals are never free from defects, we have a contribution of disorder causing broadening of the reflectivity peak. This broadening of the measured diffraction peaks may be caused by a finite crystal size and other imperfections, as grain boundaries between simultaneously illuminated crystal domains that scatter light diffusively, non-crystalline features that sometimes occur on the surfaces of air-sphere crystals, like bulk pieces of pure oxide material, or strain caused by a variation in radii (polydispersity).

We propose to describe the relative width of diffraction peaks in the finite size broadening as the dominant disorder contribution:

$$\left(\frac{\Delta\lambda}{\lambda_0}\right)_{\text{measured}} = \sqrt{\left(\frac{\Delta\lambda}{\lambda_0}\right)^2_{\text{photonic}} + \left(\frac{\Delta\lambda}{\lambda_0}\right)^2_{\text{finite size}}}. \tag{3.6}$$

The finite size broadening $(\Delta\lambda/\lambda_0)_{\text{finite size}}$ is taken to be the Scherrer formula known from X-ray diffraction [156]. This term is inversely proportional to the

[9] As a result of inhomogeneous infiltration (see chapter 4, for instance figure 4.4), areas of pure alumina and pure titania were present in this sample.

number of lattice planes that diffract light. Equation (3.6) appears to hold for one-dimensional stacks of dielectric layers [174] and is assumed here to describe three-dimensional crystals. Bertone *et al.* demonstrated for photonic silica crystals that a finite crystal size clearly influences the relative width of diffraction peaks of visible wavelengths [175]. Their data points clearly match with equation (3.6): for a thin photonic crystal of only 9 layers consisting of silica spheres, a relative width is found that is much broader than the diffraction peak of a 50 layer photonic crystal. The consequence of equation (3.6) is that the measured width $(\Delta\lambda/\lambda_0)_{\text{measured}}$ is always an upper bound to the photonic width $(\Delta\lambda/\lambda_0)_{\text{photonic}}$. To obtain $(\Delta\lambda/\lambda_0)_{\text{photonic}}$ as good as possible, we only perform optical experiments on well-characterized samples (e.g. SEM), we search for minimum linewidths and high reflectivity in reflectivity spectra, and we search for samples whose first order reflectivity peaks do not show specious shoulders or extra peaks. In this way we found for titania air-sphere crystals values of the relative width of around 13% [58], one of the strongest interacting photonic crystals in the visible range.

It is possible to experimentally measure the interaction strength between light and photonic crystals by measuring the relative width of the (111) Bragg reflection peaks. The expression for the photonic parameter Ψ, also called the photonic strength, is

$$\Psi = 3 \cdot \phi \cdot \frac{(m^2-1)}{(m^2+2)} \cdot g(K,r) \approx \left(\frac{\Delta\lambda}{\lambda_0}\right)_{photonic}, \tag{3.7}$$

where $g(K,r)$ is the form factor of the scatterers, generally a function of sphere radius r and diffraction vector K. In this form factor geometric features like window size and surface roughness can be included. The refractive index contrast is defined as the ratio $m = n_{\text{solid material}}/n_{\text{air}}$. Spry and Kosan described already in the eighties a relation between refractive index contrast and optical bandwidth for colloidal crystals [176]. They assumed smooth spheres, so no features like window size and surface roughness were included. The form factor could in this way be described as $g = 3/u^3 \cdot (\sin u - u\cos u)$, where $u = kr$, with $k = 2\pi/d$. We applied this model to our data. In figure 3.16 the relative widths are displayed as a function of m. The drawn curve in the graph is the relation between $(m^2-1)/(m^2+2)$ and the relative width as written in equation (3.7). Based on previously measured values for relative widths of optical diffraction peaks of titania air-sphere crystals, we draw the curve through the value of titania, where a value of $\phi = 10\%$ v/v is assumed. In this way the form factor $g(K,r)$ is fixed. To compare the measured relative width for the different oxides we assume that form factor and the volume fraction is the same for all samples measured here. One other curve is plotted where $\phi = 20\%$ v/v is assumed.

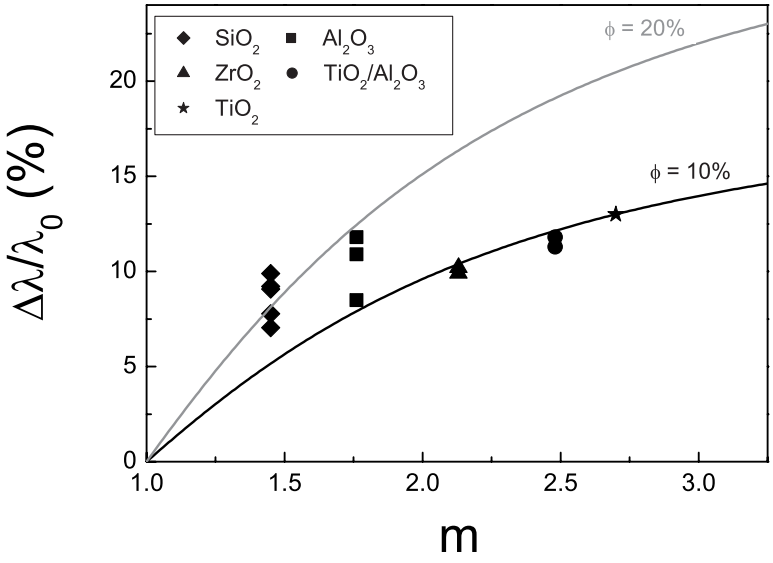

FIGURE 3.16: *Relative widths displayed as a function of m, the refractive index contrast ($n_{\text{solid material}}/n_{\text{air}}$). The drawn curve in the graph is the relation as described in equation (3.7). The assumed volume fraction (ϕ = 10%) and form factor are based on results from previous reflectivity experiments on titania air-sphere crystals. With increasing refractive index contrast the photonic strength is increased. The data are presented as follows: silica by diamonds, alumina by squares, zirconia by triangles, titania/alumina by dots and titania by an asterisk. As a comparison the relation is plotted where ϕ = 20% is assumed.*

In figure 3.16 the relative widths for the different samples are displayed. Since reflectivity was done at several spots on the same sample, there is more than one data point that corresponds to a specific value of m (reflectivity peaks of these extra data points are not shown in figure 3.14). As can be seen from the plot, especially the values for zirconia and alumina/titania perfectly follow the trend of the curve. The measured value for zirconia has a value slightly lower than the curve. This can be caused by the fact that the filling fraction is lower than the assumed ϕ = 10% v/v. Indeed the calculated value of the filling fraction for zirconia, shown in the previous paragraph, turned out to be ϕ = 9% v/v. The measured value for the mixed oxide sample is also shifted downwards. As was also seen at the zirconia sample the filling fraction of the solid material is lower than the assumed ϕ = 10%

v/v. The average refractive index is difficult to predict for this mixed oxide. The materials are not homogenously distributed so the refractive index ratio m can vary with different spots on the sample (see also chapter 4). We obtained a volume fraction for these mixed oxide samples between ϕ = 5-8% v/v.

The values for pure alumina and pure silica show a slightly larger value than the curve. We expect the larger values for the relative width of alumina to be caused by disorder. The predicted relative width is slightly below 8% (see figure 3.16). Although the average relative width, measured from three reflectivity peaks, is 10%, the lowest value for the relative width is 8.5%, almost matching the predicted value.

Not only disorder is expected to cause the larger value of the relative width for silica. Since we obtained from the reflection of silica a volume fraction of ϕ = 17% v/v, much larger than the values calculated for the crystals made with the liquid precursor, this can be an explanation for the larger relative width of silica. As a comparison the relation between m and the relative width of the reflectivity peak where a volume fraction of ϕ = 20% v/v is assumed, is plotted. This curve resembles well with the largest relative width of silica. The three lower values are from reflectivity data not shown here, are taken from a sample with a similar sphere size. From these reflectivity peaks volume fractions between ϕ = 17-23% in one sample were obtained. It is not unlikely that this variation in volume fraction is caused by different air-sphere radii present in one sample. It is observed that different parts in one sample can exhibit different sphere radii, caused by different shrinkages. In this way the lattice parameter is over or underestimated and therefore the volume fraction can be larger or lower.

The form factor $g(K, r)$ can also influence the larger value of the relative width for the silica reflectivity peak. It is clear that the structure of the silica inverse opals is different from the inverse opals made with liquid precursors. The silica backbone consists of small spherical particles clustered together, as can be seen in figure 3.10(b), whereas the backbone of the inverse opals made via liquid precursors consists of very densely packed asymmetric grains. Both cases can result in different form factors and consequently in a smaller or broader relative width of the reflectivity peak.

The alumina air-sphere crystal shows in the reflectivity graph quite a broad and asymmetric peak probably caused by disorder such as a variation in air-sphere radii. Due to this broadening of the reflectivity peak, the value in relative width as displayed in figure 3.16 is likely larger than the predicted one.

When a photonic crystal is of good quality the relative width of a diffraction peak is a robust measure of the width of a stopgap. Since we measured from all our air-sphere crystals broad diffraction peaks, we can say that our air-sphere crystals are strongly photonic. We observed relative widths of the reflectivity peaks between 8 and 13% for respectively silica, alumina, zirconia, alumina/titania and

titania air-sphere crystals. The results agree resemble well with the predicted values. The relative widths, i.e., the photonic strength, is increasing with refractive index contrast as predicted by the curve in figure 3.16. The slight deviation of measured relative widths from the predicted value for the relative width is caused by the finite size of the photonic crystal and differences in assumed volume fractions and sphere sizes. The lowest photonic strength is observed for silica air-sphere crystals ($\Psi = 8\%$) whereas the titania inverse opals displayed the highest photonic strength ($\Psi = 13\%$). In chapter 5 we determine the relative widths of the stop gaps, by means of emission experiments.

3.9 Conclusion

We have described the preparation of well-ordered air-sphere crystals by the use of self-organizing systems. Air-sphere crystals of several oxides were prepared and characterized by several means.

The template is grown from colloidal polystyrene particles by slow crystallization. A well-ordered *fcc* structure is formed as was observed with SEM and previously confirmed with SAXS [118, 119]. The template structures are easily inverted with the use of liquid precursors of oxides that are readily available. To create a high refractive index contrast titania and zirconia were used whereas to create air-sphere crystals of insulating materials silica and alumina were applied. The excellent matching replica structure of the air-sphere crystals compared to the template was determined with SEM. The macropores in the air-sphere crystal are interconnected via windows, caused by touching spheres in the template.

The presence of interstitial holes, observed in air-sphere crystals of metal-oxides titania, zirconia and alumina, confirm that the formation of the metal-oxide is surface templating. Jiang *et al.* [177] first demonstrated that infiltration and reaction of metalalkoxides on polystyrene substrates is surface templating, a term first used by Zakhidov *et al.* [112]. Although these interstitial holes cause a decrease in volume fraction of high index material and one might expect this to decrease the photonic strength, band structure calculations demonstrated that these interstitial holes enhance the widths of the photonic stop bands of a crystal [35, 168]. The presence of windows, that are in fact necessary for the removal of polystyrene, also increase the photonic strength. Experimental observations with titania inverse opals consisting of spheres with and without windows have respectively a relative stop band width of 13% and 10% [178].

Powder XRD and X-ray absorption were used to determine respectively the crystallinity and the volume fraction of the backbone material. The alumina and silica air-sphere crystals consists of an amorphous backbone whereas titania and zirconia become crystalline during the heating process. With X-ray absorption

volume fractions where found that were similar to volume fractions estimated via the measured SEM-picture and the measured reflectivity peak. For silica a larger value for the volume fraction was found and this could be explained by the larger number of infiltrations and no conversion from liquid precursor (or the hydrolyzed species of this precursor) to solid material.

The well-ordered arrangement of the macropores, as determined with SEM and reflectivity, is important to be able to create a photonic band gap. Since the photonic band gap is expected to develop at second order Bragg diffraction which is much more sensitive to disorder, a high quality photonic crystal is of utmost importance. With the measurement of relative widths of reflectivity peaks, we demonstrated that our air-sphere crystals exhibit only very little disorder as they are almost matching the predicted value, where no disorder is encountered.

Although our oxide inverse opals are effective photonic crystals they will probably not reveal a photonic band gap, since their refractive index contrasts are too low. Also the preparation technique used for the oxide air-sphere crystals has its limitations since it will never be possible to fabricate large single crystals due to shrinkage during the calcination process. Since the domain size of air-sphere crystals prepared this way is commonly found to be maximal 50 by 50 μm, this limits applications in IC-technology, where domains on e.g. wafers usually have sizes of at least 20 mm in cross-section.

For uses of air-sphere crystals in catalysis and paints this small crystal size is unimportant. The most important quantities for catalysis are a high surface area, chemical stability, and an uniform sphere size to separate molecules on the basis of their size [106, 107]. Our air-sphere crystals do clearly meet these requirements.

Air-sphere crystals are very interesting subjects for optical research in order to understand the behavior of light in these photonic air-sphere crystals. In the last years the properties of the first order stop gap was intensely investigated by determining the stop gap position, width, and depth, and density of states effects were observed [65]. Recently the progress is made to explore second order stop gaps. First measurements on stop gaps in reflectivity are already reported [167, 168]. Second order stop gaps measured by means of emission experiments will be discussed in chapter 5 and are to our knowledge the first investigations of second order Bragg diffraction with light probed from inside.

Nowadays more and more effort is put in developing macropores in different crystal structures, e.g., diamond lattices, where lower refractive indices are sufficient to create a band gap [54]. It is beyond dispute that macroporous materials are the future for creating photonic band gap crystals.

Chapter 4

Homogeneity of Air-Sphere Crystals from Hybrid Oxides on mm to 100 nm Length Scales: The Process of Air-Sphere Crystal Formation

4.1 Introduction

Electron microscopy is probably the most widely used technique to characterize the backbone of (oxide) air-sphere crystals. It is a reliable technique since it visualizes the macroporous structure, clearly illustrating the discrete air spheres. From the arrangement of the air spheres the crystal pattern can be deduced. This technique, however, determines only the surface characteristics. Optical techniques, e.g., reflectivity and transmission experiments, probe larger areas of the crystal. Long-range order, over a wide extent, can be investigated this way. Recently more and more people have become aware of the importance of optical characterization (see also section 3.6.2). Wijnhoven *et al.* were the first to explore air-sphere crystals with X-ray experiments [57]. With X-ray absorption volume fractions were determined and small angle X-ray scattering was used to examine long-range order in three dimensions. Although all these techniques are very important for studying the backbone of air-sphere crystals, they cannot be used for homogeneity character-

istics. Inhomogeneities especially need attention when air-spheres crystals consist of two different materials. The spatial distribution of these two materials is then of high importance. Conversely the study of possible inhomogeneities will also yield new information on the formation of large macroporous assemblies.

On mesoporous (1 nm $< r <$ 25 nm) and microporous ($r <$ 1 nm) scales, Raman *et al.* have already explored the formation of metaloxides on template surfaces at a molecular level [153]. They have investigated the formation of mesoporous silicas where the pore morphology is dependent on preparation circumstances like concentration of the reactants, aging conditions and molecular interactions between template and reactant. To the best of our knowledge, however, nobody has ever taken such a close look at the process of macroporous ($r >$ 25 nm) structure formation. We are the first to explore the process of air-sphere crystal formation, by studying inhomogeneities.

Previously we have already observed inhomogeneities with the naked eye during liquid precursor infiltration, i.e., some parts of the crystal change color from white to grayish during the infiltration while other parts remain white. Usually these white parts were visible in the upper part of the crystal and if precursor was added from the top the remaining white parts could be infiltrated after all. These differences in infiltration already indicate that the infiltration is not always uniform on mm scale, the typical length scales of opals. When applying only one material, this inhomogeneity seems to be no issue since it averages out. When applying two or more different materials however, this inhomogeneity can be a serious point.

To investigate the homogeneity of inverse opals we have prepared samples consisting of two oxides. The principle of this sample preparation is illustrated in figure 4.1. The starting material is the same as for the pure titania (TiO_2) air-sphere crystal; an artificial opal consisting of monodisperse polystyrene spheres. The first step is the infiltration of the opal with the precursor of one oxide, in this particular example alumina (Al_2O_3) or zirconia (ZrO_2). Since Jiang *et al.* already demonstrated that infiltration and reaction of alkoxides on polystyrene substrates is surface templating, a term first used by Zakhidov *et al.* [112], this is expected to result in a layer covering the polystyrene spheres [177]. The second step is the infiltration of the remaining air voids with another oxide, in this case titania, which deposits on the already present insulating oxide layer. The third and final step is the removal of the template by calcination during which the polystyrene is burned away and an air-sphere crystal with a spherically layered structure is expected. Studying the composition of this expected structure will provide information about the inhomogeneity.

Electron Dispersive Spectroscopy (EDS) is a good technique for investigating inhomogeneities in air-sphere crystals made of mixed oxides. A high energy electron beam hits a certain sample area and the present elements radiate charac-

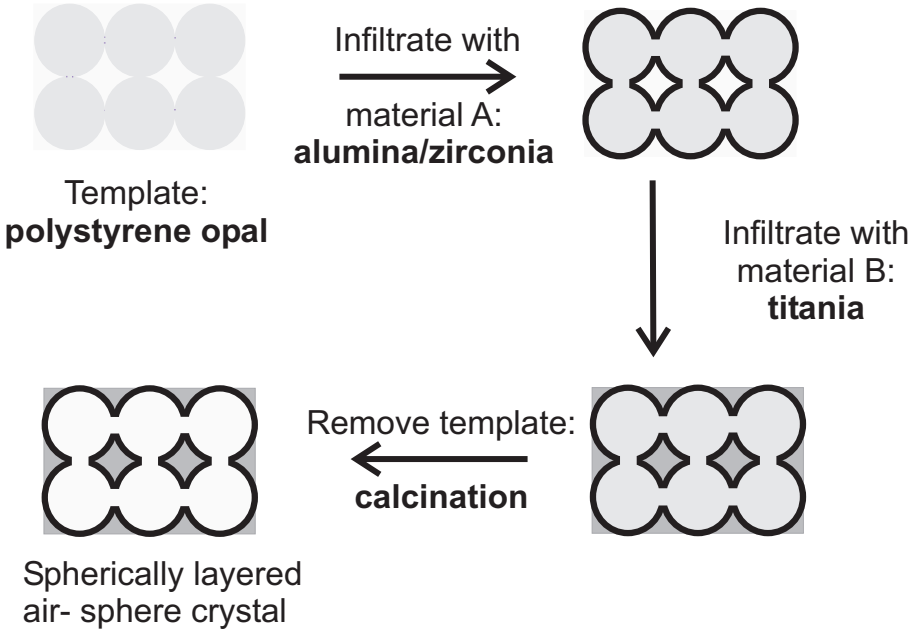

FIGURE 4.1: *Schematic drawing of the principle of the preparation of spherically layered mixed oxide air-sphere crystals. The artificial opal is first infiltrated with a precursor of one oxide, e.g., alumina, silica or zirconia, before it is infiltrated with another oxide, e.g., titania. After calcination an air-sphere crystal is expected consisting of two materials with a spherically layered shell structure.*

teristic X-rays. Applying this technique in combination with Scanning Electron Microscopy (SEM), areas can be probed with several hundreds μm in cross section. EDS in combination with Transmission Electron Microscopy (TEM) can even probe on single air-sphere level, i.e., about 100 nm.

Although the technique of spherically layered mixed oxide air-sphere crystals appears to be very good to investigate the homogeneity of inverse opals, it was originally developed to create efficient emission from light sources in air-sphere crystals. If first an infiltration is done with an insulating material followed by an infiltration with a high index material, in our case titania, a spherically layered air-sphere crystal with an insulating oxide layer on the inner surface and a high refractive index contrast is generated. This thin insulating layer prevents the electron transfer from the excited state of the dye to the conduction band of high index material titania. In previous experiments (see section 2.5), it has been shown that coating titania powder with a silica layer indeed prevents electron transfer [92]. Above a certain layer thickness the electron transfer is precluded, resulting in effi-

cient emission and a long lifetime of laser dye compared to a short lifetime and a low quantum efficiency on bare titania.

Several studies of macroporous materials consisting of more than one oxide have previously been presented. Holland *et al.* have prepared yttria(Y_2O_3)-stabilized zirconia by mixing both precursors in advance [115]. After infiltration and calcination it was shown with EDS that the yttrium was distributed evenly throughout the sample. Gu *et al.* have demonstrated tuning of the refractive index of inverse opals by mixing silica and titania nanoparticles before infiltrating the opal with this mixture [179]. The spatial distribution of both oxides was undetermined. Mixing the precursors in advance will, however, not contribute to an insight into inhomogeneous infiltration and therefore are not useful for tracer experiments. Yin and Wang have made cobalt doped titania by treating porous titania with a solution of cobalt carbonyl in heptane [113]. EDS was used to study if the cobalt species had penetrated into the pores, and indeed the presence of the cobalt was confirmed. Since the relative intensity of cobalt and titanium varied between different regions in the sample, Yin and Wang suggested that the cobalt may have formed a compound with titanium. Although Yin and Wang apply the materials separately it differs from our technique since they apply the second material after the formation of the air-sphere crystal. We applied two different materials in such a way that inhomogeneities in the formation of the air-sphere crystal are easily recognized. We infiltrate the opal one time with material A followed by 4 or 5 times with material B. In this way the ratio between the two materials is as large as possible and differences in distribution are simply determined.

4.2 Preparation of hybrid oxide air-sphere crystals

The first step of the preparation of mixed oxide air-sphere crystals is the infiltration of the artificial opal.[1] To infiltrate the opals, i.e., fill the interstitial space between the spheres with a solid material, we have used liquid precursors consisting of an alkoxide diluted with an alcohol: ethanol or propanol. The precursors titanium(IV) propoxide (98%) (TPT), zirconium(IV) propoxide (70% solution in 1-propanol) (TPZ) and aluminum tri-sec butoxide (97%) (TBAl) were purchased from Aldrich and used without further purification. Ethanol (99.5%) was obtained from Merck and 2-propanol (99.5%, anhydrous) from Aldrich. The infiltrations were done in a glovebox under nitrogen and took typically about $\frac{1}{2}$ till 1 hour. After infiltration the opal is placed in a nitrogen flow for several hours before it is placed in a water-rich environment to react with water. The infiltrations were performed once (for zirconia) or twice (for alumina) with the precursor of the insulator, respectively

[1] See for template growth chapter 3.

TPZ and TBAl, followed by four or four infiltrations with the precursor of titania (TPT).

To remove the polystyrene template and to crystallize the oxides, the samples were heated to 450°C in the following way: 0.33°C/min to 80°C, one hour at 80°C, 1°C/min to 450°C, 6 hours at 450°C and cooling down with 10°C/min.

The SEM-images were taken with an ISI DS-130 scanning electron microscope, after sputtering the samples with a thin layer of gold. The spatial measurements done with the micrographs were corrected for tilt. TEM-images were taken with a Philips CM30 Twin STEM.

EDS-SEM was done with a Jeol JXA-8621 Superprobe at Leiden University. The superprobe was equipped with a single crystal detector. The characteristic K_α and L_α lines were detected with either a pentaerythritol (PET) or a thalliumacidphtalate (TAP) single crystal. All EDS-SEM measurements were done with a 20 kV electron beam. A typical scan of the emission lines of one element took about 10 minutes. EDS-TEM was done with a Philips CM30 TEM, fitted with a Kevex Delta-Plus EDX detector and based at the Central Materials Analysis Lab at the MESA+ Research Institute. Measurements were done with a 300 kV electron beam. A typical measurement took about 200 seconds. The X-ray lines were detected through a boron nitride (BN) window on a silicon lithium (SiLi) detector.

Optical microscope photos were taken with an Olympus SZ60 microscope, equipped with an Olympus SC35-12 camera.

4.3 Structural characterization

The infiltration of the liquid precursors into the opal can be followed by eye. Air-sphere crystals reveal optical Rayleigh scattering because of the presence of small crystallites. Due to multiple scattering of light from these small grains the air-sphere crystals appear white. When infiltrating the opal with liquid precursor the refractive index contrast changes (from solid material/air to solid material/liquid), and as a result a different color, gray, is apparent.

Already in the synthesis of pure oxide air-sphere crystals it was noticed that the bottom part was usually infiltrated best during the infiltration (see chapter 3). Although this problem was overcome by adding precursor from the top, areas were still present where no color change was observed. This illustrates that even on mm scale differences in infiltrations are observed, and therefore inhomogeneous distributions of materials are obvious if applying more than one oxide in several infiltration steps.

In the synthesis of mixed oxide air-sphere crystals, where two materials were applied separately the same inhomogeneities were observed. Some areas in the opal turned grayish whereas other parts remain white opalescent.

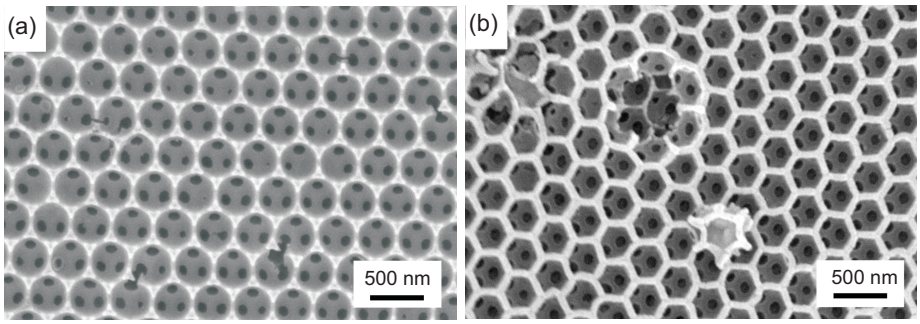

FIGURE 4.2: *SEM images of two inverse opals consisting of two different materials, respectively alumina/titania (a) and zirconia/titania (b). The air spheres are well-ordered in the fcc (111) plane. In both images the connecting windows are clearly visible as dark spots. In (a) also the interstitial holes can be seen between each triplet of air spheres, which indicate that surface templating has taken place. The air spheres of (b) look more hexagonal than what we usually observe [57, 58]. One air sphere has popped out probably caused by heating or handling.*

4.3.1 Scanning electron microscopy

Figure 4.2 shows SEM-pictures of air-sphere crystals made from two different mixed oxides. Both pictures show well ordered air spheres. Figure 4.2(a) is a top view of the (111) surface plane of an alumina/titania sample made from an $r = 238 \pm 2$ nm polystyrene template. The radius of the air spheres is 196 ± 2 nm, a shrinkage of ~ 18% compared to the template, on the lower boundary compared to values observed in pure titania air-sphere crystals. The largest single domain observed in this sample is about 16 by 24 μm, which corresponds to an area of 40 by 60 spheres, comparable to the pure titania air-sphere crystals that were previously made from similar substrates [58]. Connecting windows, clearly seen as black spots in the figure, indicate that the air spheres are connected with the layers beneath. Interstitial holes between the air spheres are also clearly visible, confirming that the infiltration and reaction are surface templating and not volume templating [58]. Figure 4.2(b) is a (111) plane of a zirconia/titania air-sphere crystal also made from a polystyrene template with sphere radii of 238 nm. After calcination, a shrinkage of 22% is obtained resulting in an air-sphere radius of 185 ± 2 nm. The largest domain observed in this sample is about 30 by 30 μm, which corresponds to an area of 80 by 80 spheres. This domain size is similar to sizes found in pure oxide air-sphere crystals. In this SEM-picture the windows are also clearly visible. There is a peculiar defect on the surface; one air sphere has popped out of the plane and fits with its shape exactly in the remaining hole. This defect is probably due to heating

or handling. The air spheres in this micrograph look more rectangular than round compared to SEM-pictures of other air-sphere crystals. We are presently unaware of an explanation for this feature. This morphology was observed previously by several other groups. Holland *et al.* [115] also noticed this rod-like structure with pure zirconia inverse opals but did not have a clarification for it. Yan *et al.* [161] detected a similar skeleton in an iron metal air-sphere crystal prepared by reduction of an iron-oxide (F_2O_3) crystal. They assigned the rod-shaped morphology to enhanced sintering since the process takes place under hydrogen instead of nitrogen. Recently Dong *et al.* [180] described a method to synthesize such rod-like skeletons in titania. They observed that after one infiltration cycle with the precursor of titania (TPT) in a high concentration (80% v/v in ethanol), the obtained inverse opal shows a rod-like skeleton in the inner part of the sample. At the surface of the sample however, a normal shell structure was found. They ascribed the deviating behavior in the particular sample regions to different drying and reaction conditions. The photographed area in SEM-image 4.2(b) is most probably an external surface and therefore we do not think that this deviation is caused by similar phenomena. Since with small angle X-ray scattering no evidence was observed for such structural deviations [57], we believe the rod-like skeleton is rather an incidental feature than an usual phenomenon. From the micrographs it can be seen that successive infiltrations with different oxide-precursors results in air-sphere crystals of high quality, comparable to the quality of the pure titania air-sphere crystals [58].

4.3.2 Energy dispersive spectroscopy with SEM

With EDS it is possible to detect the density of atoms in a sample by the use of characteristic X-rays generated with an electron beam. The intensity of the X-rays is a gauge for the amount of atoms present at a certain area. In this way the distributions of both oxides can be mapped in the air-sphere crystals. In the experiment, we have detected the K_α radiation of aluminum and titanium, at energies of 1.4870 keV (corresponding to a wavelength of 8.34013 Å) and 4.5090 keV (corresponding to a wavelength of 2.74973 Å) respectively. The L_α radiation of zirconium was detected at 2.0420 keV (corresponding to a wavelength of 6.07050 Å). Calibrating the atomic densities of the elements from the emitted intensity is difficult because of the sensitivity of the detector and absorption processes: different elements have different emission wavelengths, and therefore they are absorbed differently by the elements present in the sample. For example, the K_α radiation of aluminum is not absorbed in the same way by titanium as the L_α radiation of zirconium. Measurements on the pure elements zirconium, aluminum, and titanium indicated that the detector was less sensitive for the zirconium radiation by roughly a factor of ten. Consequently we use the measured intensities only as a qualitative gauge.

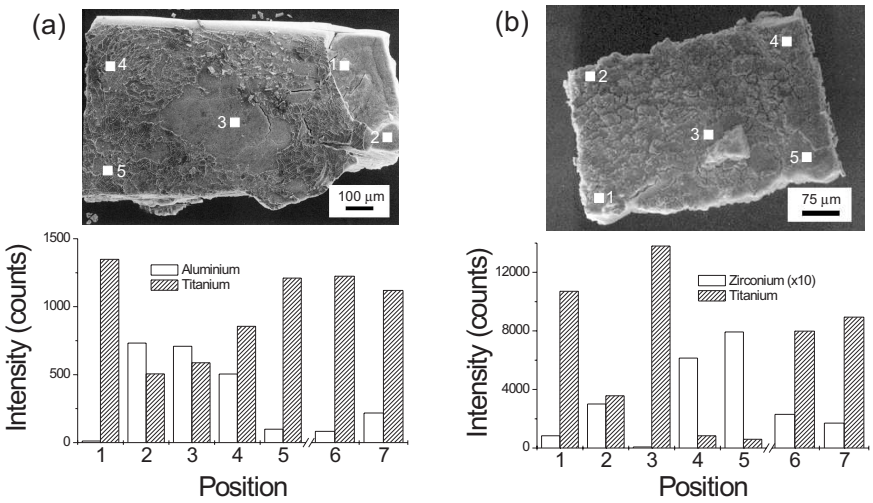

FIGURE 4.3: *Bar diagrams (left and right/a and b) of the measured intensities for the specific X-ray radiations of different elements present in the sample. The measurements were done at several positions on the sample, corresponding to the numbers in the SEM picture (insets). Positions 6 and 7 are from different samples. (a) Data for alumina/titania samples, open bars for Al, hatched bars for Ti. (b) Data for zirconia/titania samples. Open bars are intensities for Zr multiplied by 10 because of the tenfold lower detector efficiency. Hatched bars are for Ti.*

The excitation volume depends on the porosity and chemical composition of the sample, and on the voltage used. The penetration depth can be calculated with the use of a Monte Carlo simulation [181].[2] A porosity of 90% was assumed, based on earlier results [58], and the chemical composition of the backbone was estimated from the infiltration ratio, which was 23% v/v alumina for the alumina/titania sample and 24% v/v zirconia for the zirconia/titania sample. The excitation volume had roughly the shape of a liquid drop, with a depth between 8 and 10 μm and a width between 6.5 and 7.5 μm, where the widths decrease exponentially with depth. The probe volume is much larger than a single air sphere, since we are probing about 20 layers in depth. On the other hand the probe volume is small enough to distinguish different areas in the samples, that have typical lateral sizes between 500 μm and 1 mm.

The upper panels of figure 4.3(a) and (b) are SEM-pictures of respectively alumina/titania and zirconia/titania samples. These pictures show the whole samples

[2]The Monte Carlo simulation was kindly performed by mr. Ton Gortenmulder of Leiden University.

and the numbers on each piece show the positions where the EDS measurements were done. Initially, each area was examined with SEM to judge the nature of the area, i.e., open or closed air spheres, the presence of bulk material, order or disorder. Next the EDS measurements were done at that same position. Figure 4.3(a) and (b) are bar diagrams of the intensities measured at five different positions on each sample and two additional points obtained on other samples. Figure 4.3(a) displays data measured on alumina/titania samples. Positions 2, 3, and 4 show a distribution with both materials present. Although the intensities vary a little throughout the sample, the general trend appears to be rather an even distribution of materials. With SEM we determined that these positions revealed open air-sphere structures as in figure 4.2(a). Positions 1 and 5 consist of areas where the structure did not contain open air-sphere structures but areas covered with bulk material. As can be seen from the bar diagram, the intensity of titanium at these positions is very high compared to the intensity of aluminum so we can conclude that the bulk material at these positions mainly consists of titania. Position 6 and 7 are measured on a different sample, made in the same preparation batch. Position 7 was an open air-sphere structure with a lot of disorder. There is some signal of aluminum in addition to the main component titanium. Position 6 was an area covered mainly with bulk material. The main component of this area is titanium.

In figure 4.3(b) the measured intensities on zirconia/titania samples are shown. Since the sensitivity of the detector for zirconium was much less, we have multiplied all the intensities of zirconium with a factor of ten. Positions 1, 2, 4 and 5 were determined with SEM to be open air-sphere structures. In the bar diagram it can be seen that both materials show a signal, an indication that titanium as well as zirconium are present in these areas. There is variation in the distribution: at position 1 and 2 titania appears to be the main element present, as expected from the calculated chemical composition of 76%/24% v/v titanium/zirconium. On the other hand, at position 4 and 5 the zirconium signal is much stronger, suggesting that here zirconia is the majority. Position 3 was determined with SEM to be a closed area covered with bulk material. Indeed there is at this position hardly any signal from zirconium indicating that this area consists mostly of titania. Considering there is beneath this bulk titania layer a porous structure which can consist of both titania and zirconia one might expect to see a zirconium signal. Since the excitation depth in bulk material is substantially lower than in a porous structure, we are probably only exciting the bulk layer on top and do not reach the porous structure at all, resulting in no signal from zirconium. Position 6 and 7 are measured on a different sample made in the same preparation batch. Both areas consist of open air-sphere structures. Titanium as well as zirconium are present, with the titanium signal stronger as expected.

Generally in the EDS-SEM experiments we find both infiltrated elements present

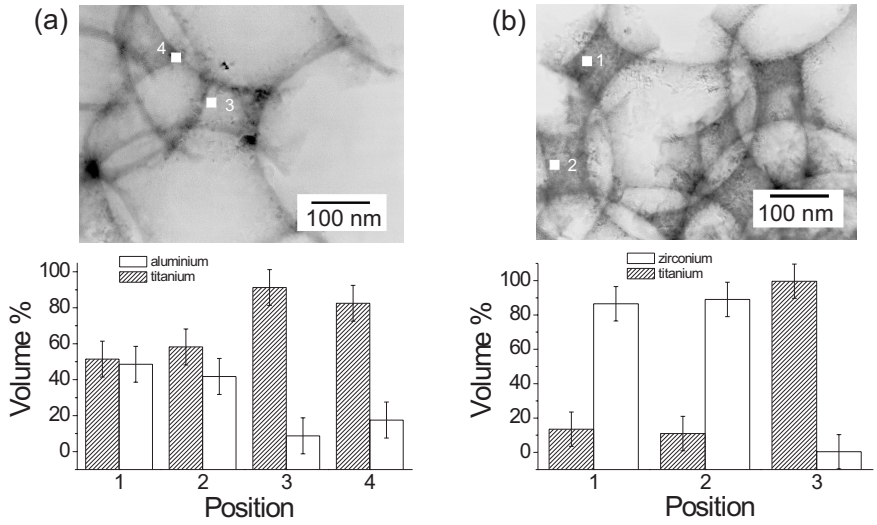

FIGURE 4.4: *Bar diagrams of the measured atom percentages for the specific X-ray radiations of Al and Ti in an alumina/titania air-sphere crystal (a) and Zr and Ti in a zirconia/titania air-sphere crystal (b). The measurements were done at several positions on the sample, corresponding to the numbers in the TEM picture (insets). Position 1 and 2 in (b) and position 3 in (a) are outside the range of the photograph. Open bars represent Al or Zr, hatched bars Ti.*

in the air-sphere structures. Usually titanium appears to be present in excess, as expected since titania is the main component in our samples ($\sim$ 75% v/v). In some areas we found aluminum or zirconium in excess. These results demonstrate the inhomogeneity of the infilling procedure. The observation that possible bulk material on the surface of the samples is mainly titania can be explained by the fact that the last infiltrations are done with the titania precursor. In this way the titania precursor had more chance to settle on the outside.

4.3.3 Energy dispersive spectroscopy with TEM

Since the EDS measurements done with SEM only investigates the homogeneity on a lenghtscale of $\sim$ 100-500 μm, we also performed EDS via TEM. With EDS-TEM it is possible to probe within single air-spheres. In figure 4.4(a) and (b) two typical TEM-pictures of an alumina/titania and a zirconia/titania sample are displayed. The samples were prepared by crushing an air-sphere crystal from the same preparation batch as used in the EDS-SEM experiment. We have performed measurements at different positions in an area with a maximum cross-section of 500 nm. The bar-

diagram shows the volume fractions of the present elements at different positions in this 500 nm area (not all positions are visible on the image). The absorption properties are in these samples less important since only X-ray emission from one or two layers is detected. Therefore we used the measured intensities to calculate the volume percentages (with the program Quantex+ 1.6). A correction is done for different detection sensitivities of the different elements. All positions were interstitials like position 3 in figure 4.4(a) and position 1 and 2 in figure 4.4(b), except position 4 in figure 4.4(a) which represents an edge in between two adjacent air-spheres. From the displayed volume percentages in figure 4.4(a) and (b) it is obvious that there is a large variation in the ratio of the elements. In figure 4.4(a) aluminum and titanium at position 1 and 2 show a rather evenly distributed volume fraction. These positions are however less than 300 nm away from position 3 and 4 where the ratios are significantly different. At these positions the titanium is the main component, which is expected on basis of calculations on chemical compositions. In figure 4.4(b) on position 1 and 2 the ratios of zirconium and titanium hardly varies. Surprisingly zirconium is found as the main component at these positions. At position 3 however, an interstitial that is only 200 nm away from position 2 (not shown in the TEM-picture), titanium is the major element. These results demonstrate that even within single air-spheres, i.e., on $\sim$ 100 nm lengths, the materials are not homogeneously distributed. To check whether this result was representative we did measurements at more positions at different pieces of crushed material. In these experiments we observed similar inhomogeneity. Although the technique of successive infiltrations with different oxide precursors results in well-ordered mixed oxide air-sphere crystals, the distributions of the oxides is clearly not even throughout one sample.

We additionally observed that the titania present in the alumina/titania and the zirconia/titania sample was crystalline. This could be seen from crystallographic patterns that are caused by interference of the lattice planes. These patterns are visible in TEM-pictures with a higher magnification and were also observed for zirconia, indicating crystallinity of both metaloxides.

4.3.4 Optical microscopy

Figure 4.5(a) and (b) displays respectively an alumina/titania and a zirconia/titania air-sphere sample. The samples are illuminated with diffuse white light from above. Beautiful opalescence is apparent that is the result of constructive interference of waves reflected by successive (111) crystal planes present in the air-sphere crystal. Both the average refractive index of the sample and the spacing between the air spheres influence the reflection wavelength. For the alumina/titania air-sphere

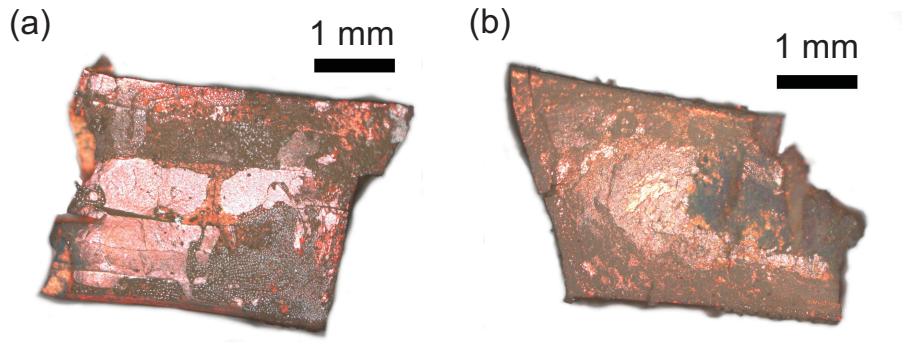

FIGURE 4.5: *Optical micrographs showing opalescence of polycrystalline air-sphere crystals made from mixed oxide air-sphere crystals. (a) An alumina/titania air-sphere crystal with a lattice parameter a ~ 550 nm. Intense red reflections are apparent. (b) A zirconia/titania air-sphere crystal made from a template with the same sphere size (r = 238 ± 2 nm). Due to more shrinkage the lattice parameter is smaller (a ~ 520 nm) and reflections are shifted towards shorter wavelengths and appear as orange-red reflections.*

crystal in figure 4.5(a), the first order Bragg reflection is at $\lambda_{111} \sim 735$ nm appearing as a red reflectance. To estimate this exact wavelength we assumed a volume fraction of $\phi = 10\%$ v/v (porosity of 90%) and a refractive index of the backbone material based on a chemical composition of about 77%/23% v/v titania/alumina. Although the average refractive index of the zirconia/titania sample in figure 4.5(b) is higher since zirconia has a higher refractive index than alumina, and therefore the Bragg peak would shift more to the red, this sample shows a more red-yellow appearance. This is caused by the fact that the air-sphere size of this sample was ~ 6% smaller than the air-sphere size of the alumina/titania sample, resulting in a blue-shift, consistent with an orange-red color. Since the template for both samples were $r = 238$ nm polystyrene opals, we conclude that the alumina/titania sample shrinks less than the zirconia/titania sample. The optical micrographs of these air-sphere crystals show shiny and colorful reflections demonstrating that the quality of the mixed oxide air-sphere crystals is comparable to the air-sphere crystals made from pure titania [57]. From the micrographs can also be seen that they do not reflect one specific color but a range of colors, i.e., orange-red-yellow. We do not expect this to be caused by the inhomogeneity in the material distribution, i.e., the spatial variation of the average refractive index. In pure oxide air-sphere crystals variations in diffracted colors were also seen (see chapter 3). So even when crystals consist of only one material alteration is apparent. These were due to multiple Bragg diffraction for large lattice parameters and different crystal orientations. We

ascribe the color variations in these samples to the same phenomena.

4.4 Discussion and conclusion

We were able to produce highly ordered composites consisting of macropores in a solid backbone made of mixed oxides. We have characterized the quality of the samples with scanning electron and optical microscopy, from which we conclude that the long-range order of these mixed oxide air-sphere crystals is of high quality.

We are the first to report on spatial distributions in air-sphere crystals. We observed an extreme spatial inhomogeneity in air-sphere crystals prepared via successive infiltrations, as measured with EDS. With the naked eye inhomogeneities on mm scale were observed, whereas with EDS-SEM inhomogeneities on $\sim$ 100 μm scale were surveyed. Even on single air-sphere level, i.e., $\sim$ 100 nm, inhomogeneity in material distribution was measured with EDS-TEM. The ratio between the two present materials was varying from pure material A, via a mixed ratio A/B, to a pure material B in several positions in the crystal, apparent on all three length scales.

Differences in spatial distribution on mm and 100 μm scale can indicate that the oxide precursor does not infiltrate homogeneously in the opal template. During each infiltration parts of the template may be infiltrated completely and other parts may not be infiltrated at all, as was also observed by eye. Let us consider the infilling process; the liquid is infiltrated via capillary forces into the opal. Since an opal experiences shrinkage during drying from the colloidal crystal, it displays cracks often in vertical direction (see chapter 3). Exactly these vertical cracks are infilled first via capillary forces. As time moves on, a matter of seconds, other parts of the opal are infiltrated as well, also via capillary forces. Some parts however stay empty, and the precursor solution does not wet the polystyrene surfaces over here. Since our samples are infiltrated at least five times to get a reasonable filling fraction, it is not surprising that such inhomogeneous infiltration may result in compositional variations throughout one sample. Additionally parts of the opal that are already infiltrated and have reacted once, can block these areas for following infiltrations.

Since the precursor and the diluting solvent, i.e., ethanol or propanol, are already mixed in advance no diffusion of the precursor in the solvent is expected. During the infiltration process the mixture is diffusing with a constant flow between the spheres and the composition of the mixture is not expected to change.

With EDS-TEM inhomogeneities on an even shorter length scale were observed. Differences in the ratio between the two present materials were seen within single air spheres, corresponding to length scales of $\sim$ 100 nm. These inhomogeneities cannot likely be ascribed to inhomogeneous infiltration, therefore we

should consider other possibilities of inhomogeneity, namely a redistribution of the materials during the evaporation, reaction or calcination processes.

Evaporation process: After each infiltration process the redundant solvent (ethanol or propanol), that is used for diluting the precursor, is evaporated in a constant nitrogen flow. During this evaporation water is not yet present and the precursor gets more concentrated. Since the precursor solution wets the surface and the formation of air-spheres is surface templating, the remaining pure precursor is expected to stick to the polystyrene. We should however consider diffusion of the precursor during the evaporation of ethanol. The molecules nearby the sample surface will probably evaporate first and therefore the amount of precursor will increase relatively. In this way a concentration gradient can develop and diffusion of precursor to lower concentration areas, i.e., the inner part of the crystal, can take place. We think, however, it is very unlikely that at this stage inhomogeneities will occur.

Reaction process: The sample from which all the alcohol has evaporated, is next exposed to water and the precursor hydrolyzes. During this hydrolysis the alkoxy-groups are replaced by hydroxyl-groups and the precursor condensates. The material solidifies on the surface of the polystyrene spheres. This reaction step is a nucleation step, the material changes from a fluid to a solid, and a redistribution can take place. During this density change inhomogeneities are likely to originate since the nucleation takes place at several different positions separately. Once the material is nucleated it is a solid and diffusion will not take place anymore.

Calcination process: During the calcination process the polystyrene is gasified and simultaneously the metaloxide is crystallized. First the infiltrated opal is heated slowly to 80°C. At this temperature the remaining alcohol, produced by the hydrolysis, is evaporated. Following the sample is heated with 1°C/min to a higher temperature, usually 450°C. Above 100°C remaining water starts to evaporate and the hydrolyzed precursor of the metaloxide, i.e., the solid pre-stage, starts to dehydrate. Above 300°C the polystyrene starts to decompose, and above 350°C all the polystyrene is removed, see Yan *et al.* [161]. At these higher temperatures also the metaloxide is densified: hydroxyl groups are eliminated and metal-oxygen-metal bonds begin to form. The metaloxide crystallizes in crystallites with a maximum cross section of 50 nm. This densification leads to a redistribution of the material and causes further inhomogeneities in material composition. For samples consisting of one oxide this can only lead to differences in volume fraction from point to point. These inhomogeneities however are much smaller than the optical wavelength.

Since our samples consist of two materials, redistribution of the material during the crystallization process is of major importance. If crystallization processes occur it is not unlikely that the materials are redistributed from one position to

another in order to form a denser composition. In the alumina/titania sample the alumina stays amorphous and the titania becomes crystalline. The alumina present between domains of titania may disturb the crystallization process and the materials are preferably redistributed. This also holds for the zirconia/titania sample. Both materials crystallize during the heating, likely at different temperatures and therefore may also be separated.[3]

Our investigation is a first step to get an insight into the homogeneity of air-sphere crystals prepared via infiltration of artificial opals with liquid precursors. Awareness of inhomogeneities in such infiltration processes is very important when control in distribution of material is desirable.

An important consequence of the inhomogeneous distribution of the oxides can be the spatial variation of the average refractive index since both alumina and zirconia have lower refractive indices than titania. Calculating the variation in average refractive index by comparing a composition of 100% titania and a composition of 100% alumina, we obtain a variation of the average refractive index, and thus the Bragg diffraction wavelength, that is at the most 7% based on a porosity of 90%. Such an extreme variation is of the order or less than the width of the photonic stop bands. Therefore an inhomogeneous distribution of oxides appears to be a minor issue for many photonic applications. When applying materials with a more distinct refractive index however larger variations can be present and should be considered.

Since the technique of successive infiltrations does not result in titania air-sphere crystals with a homogeneous shell of insulating material on the inner spheres, they are not good candidates for dynamic spontaneous emission experiments. Due to the possible inhomogeneity of the layered mixed oxide air-sphere crystals, infiltrated dye molecules may experience different environments, varying from unshielded to shielded semiconductor surface. As a result, time-resolved measurements may reveal a distribution of lifetimes from both quenched and shielded molecules. This will impede the interpretation of lifetimes related to photonic band gap effects [65]. For photonic crystals consisting of pure elemental materials, this electron transfer can be prevented by other, more accessible, means. For instance air-sphere crystals consisting of Si [124] or Ge [130]. Here an oxidation of the inner surface can result in respectively an insulating SiO_2 and GeO_2 layer [130].

All discussed inhomogeneities in our investigation were observed in air-sphere crystals prepared via a liquid precursor infiltration. For crystals prepared via gas phase infiltration, e.g., chemical vapor deposition [127], the diffusion process would be different. Nevertheless inhomogeneities can occur and is an interesting subject for further investigation.

[3] For titania the exothermic peak is observed at 404°C [162], while for zirconia a strong exothermic peak is observed at 430°C for metastable cubic zirconia [163].

Chapter 5

Directional Fluorescence Spectra of Laser Dye in Photonic Crystals

5.1 Introduction

The spontaneous emission of light sources embedded in photonic crystals can be strongly modified in either an angle-dependent or an angle-independent manner. Angle-dependent features appear as stop bands in emission spectra, where the modified spectra change with angle. When a stop band is present in all directions simultaneously, a photonic band gap is created, which is angle-independent. Angle-independent effects result in a modification of the total emission. This angle-independent modification is caused by the modified density of states (DOS) and can result in a change in lifetime and total emitted power of the emission source. Angle-independent modification will be discussed in the chapter 6.

Angle-dependent modification results from Bragg diffraction of the emitted light by the lattice planes in the photonic crystal and appears as a stop band in the emission spectrum. Since the stop gaps are the building blocks of the photonic band gap, their optical properties are essential. Stop gaps can be investigated experimentally by means of reflectivity, transmission and emission. In this chapter we will concentrate on measuring stop bands with emission measurements on dye-doped polystyrene opals.

The spectral position, i.e., the center wavelength where the stop band appears, is very well characterized, since it is determined by the lattice spacing and the average refractive index. Several groups reported modified emission in the form of

stop bands and determined the spectral position of the stop band. Light sources like dye molecules, quantum dots and rare earth ions were embedded in artificial and inverse opals where the emission sources were either incorporated in the spheres or present in a solution between the spheres [40, 64, 65, 182–189].

Another important quantity is the spectral width of the stop band, i.e., the full width at half minimum/maximum (FWHM) [169, 190]. The relative width, i.e., the FWHM ($\Delta\lambda$) divided by the center wavelength λ_0, is directly proportional to the photonic strength Ψ, as also stated in equations (3.7) and (1.3). The width of the stop band was first explored by Vos *et al.* [26]. They measured transmission and diffraction of photonic colloidal crystals and investigated the relative width in relation with the volume fraction of the high index material. An optimum of the relative width, and therefore Ψ, was found as a function of the density of scatterers. The relative width is not only determined by photonic strength, also disorder can contribute to broadening of the peak as already discussed in section 3.8. This stresses the importance of investigating this quantity.

Recently the depth of the stop band, i.e., the amount of attenuation, was explored. Especially the analysis of this attenuation has attracted our attention since it is a strong additional measure of the photonic strength of the photonic crystal. The attenuation A can be described as

$$A = 1 - \frac{l_{\text{Bragg}}}{l}, \tag{5.1}$$

where l_{Bragg} is the Bragg length and l the mean free path of light in the photonic crystal [191]. The Bragg length, determined by $l_{\text{Bragg}} = 2d_{111}/\pi\Psi$, is the length or number of crystal planes, that the light penetrates from outside into a photonic crystal [176]. A short Bragg length is apparent for strongly photonic crystals since the light is intensely excluded. For less photonic crystals this length is much longer since the light penetrates more deeply into the crystal. The mean free path in a crystal is defined as the average distance between scattering events. The mean free path is inversely proportional to the concentration of scatterers and their cross-section. With a constant mean free path it can be assumed that stronger photonic crystals show more attenuation, since in stronger photonic crystals the Bragg length is shorter. Typical values of l_{Bragg}/l are between 0.2 and 0.5 corresponding to attenuations in the stop band of 80 to 50% as observed by Megens *et al.* [40, 192], Schriemer *et al.* [64] and Koenderink *et al.* [33]. In all these experiments strong angle-dependent attenuations were observed, Megens *et al.* probed colloidal crystals, whereas Schriemer *et al.* [64] demonstrated modified emission of laser dye in inverse opals of titania. Inhibition of total emission, which is angle-independent, was first reported by Koenderink *et al.* [65]. Titania inverse opals doped with laser dye showed a broadband fivefold reduction of vacuum fluctua-

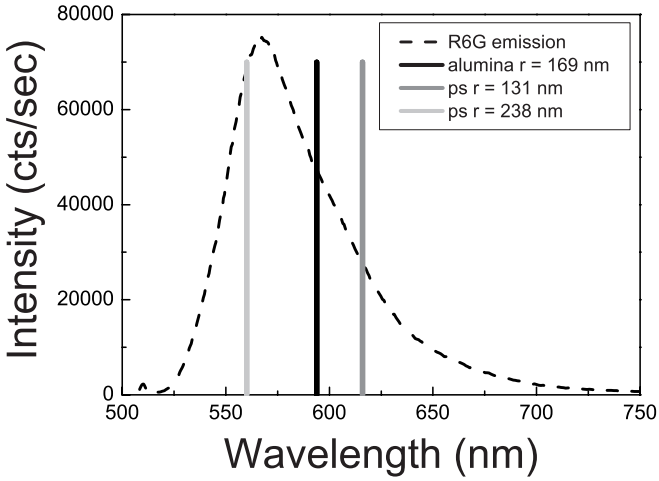

FIGURE 5.1: *Emission of R6G compared with the center position of the stop gaps of the doped photonic crystals used in our experiments. The center positions of the stop gaps are calculated with Bragg's law. Alumina inverse opal with r = 169 nm is displayed as a black bar, polystyrene opal first order with = 131 nm as a gray bar and polystyrene opal second order with a = 238 nm presented as a light-gray bar.*

tions. Beyond a strong inhibition Koenderink *et al.* also observed a slight enhancement at the (blue) side of the stop band of dye-doped titania inverse opals.

Galstyan *et al.* [193] predicted enhancements near the wavelengths of the stop bands. They proposed a model where standing wave effects determine enhancements either at the red part or at the blue part of the stop band. This can also be explained with figure 1.4 in chapter 1. At one particular wavelength there are two frequencies; the light can either be in the high index material or in the low index material (air). When the light wave is mainly in the high index material, as can be expected for artificial opals (that consist for 74% v/v of solid material), there will be more intensity at the blue side of the stop band. For inverse opals on the other hand, the light wave will mainly be in the low index material air since the inverse opal consists for almost 90% v/v of air. This would cause an enhancement at the red part of the stop band.

In the experiments discussed in this chapter, we investigate angle-dependent emission of Rhodamine 6G (R6G) in opal as well as inverse opal structures. The measured stop bands are characterized by determining the width, center position

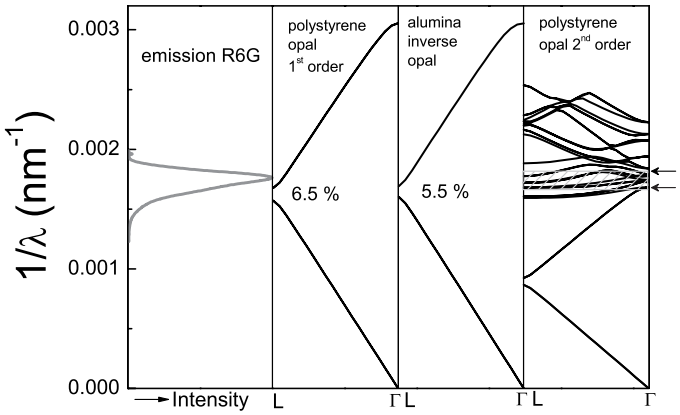

FIGURE 5.2: *Emission of R6G compared with the frequencies of the stop gaps of the doped photonic crystals used in the experiments. The positions of the first and second order stop gaps in the Γ-L direction are calculated with bandstructure calculations. Polystyrene opal with r = 131 nm has a stop gap of 6.5%; alumina inverse opal with r = 169 nm a stop gap of 5.5%. Polystyrene opal with r = 238 nm, has a first order stop gap outside the emission of R6G. The second order shows a complex band structure and not a clear stop gap can be appointed. The stop gap is expected to appear in the arced area.*

and amount of attenuation. By comparing the direct and indirect structures we can investigate standing wave effects. We are the first to explore photonic crystals with second order Bragg diffraction using emission experiments. Since the photonic band gap for face centered cubic (*fcc*) structures is expected to occur at this second order Bragg, this research is of utmost importance.

The crystals, opals as well as inverse opals,[1] were doped with a laser dye, Rhodamine 6G, that is either absorbed on the surface of the polystyrene spheres or on the inner surface of the backbone of the air-spheres. The polystyrene opals consist of nominally $r = 129$ nm spheres (denoted as first order photonic sample) or $r = 241$ nm spheres (denoted as second order photonic sample). The actual sphere sizes of both samples turned out to be $r = 131 \pm 3$ nm and $r = 238 \pm 2$ nm respectively, as was measured with SEM. These radii will be used further in this chapter as the radius although the sample denotation is different. The alumina inverse opal consists of air-spheres with $r = 169 \pm 3$ nm and was made from a $r = 213$ nm polystyrene template. In figure 5.1 the center positions of the expected [111] stop gap at $\alpha = 0°$

[1] See for preparation and characterization chapter 3 and especially section 3.3.

for several samples are plotted together with the emission spectrum of R6G. From this plot it is clear that the first order stop gap of the alumina inverse opal and the polystyrene opal with r = 131 nm as well as the second order stop gap of the polystyrene opal with r = 238 nm are chosen to occur in the red part of the R6G emission spectrum.

The frequencies of the stop gaps in the [111] or Γ-L direction as calculated with band structure calculations are plotted in figure 5.2,[2] in comparison with the emission of R6G. From this graph it is clear that the first order stop gap of the polystyrene opal with r = 131 nm and the alumina inverse opal with r = 169 nm, occur in the red part of the R6G emission spectrum. The expected stop gap widths are respectively 6.5 and 5.5%. The first order stop gap of the polystyrene opal with r = 238 nm appears in the infrared but the second order bands coincide well with the R6G emission spectrum. The second order stop gap is quite complex [168] and is placed between the fifth and sixteenth band, as is marked with two arrows. It is difficult to appoint the spectral width of this second order stop gap. The R6G spectrum displayed in this plot is taken from R6G dye adsorbed on a polystyrene opal with no Bragg attenuation in the emission range of R6G.

5.2 Experimental setup

The set-up used to measure the emission spectra is displayed in figure 5.3. The dye inside the crystal is excited with a continuous wave (cw) laser beam (λ = 514 nm, from a Lexel Argon laser) with low power, i.e., less than 0.1 mW, to prevent bleaching of the dye and luminescence of polystyrene. The amount of bleaching at this power was negligible since there was no intensity drop after illuminating a particular spot for more than four hours. The pump beam is focussed with lens L_3 to a spot size of approximately 50 μm in cross-section and hits the sample with an angle away from the Bragg angle, to establish penetration of the laser light into the crystal. The emitted photons are collected with a detection angle α with respect to the normal of the (111) planes of the sample. If $\alpha = 0^\circ$ the surface of the crystal is perpendicular to the detection angle. The light is detected from the sample in reflection; lens L_1 collimates and L_2 focuses the light on the spectrometer slit. The aperture A_1 determines the angular spread of the emitted light. The photons are detected by a photomultiplier tube (PMT) that is protected against direct reflected laser light by an OG530 filter placed in front of the Carl Leiss spectrometer. The OG530 filter cuts off the light below λ = 530 nm. The emission spectrum is

[2] Band structure calculations were done by Femius Koenderink with the use of a model where a volume fraction of 74% and 11% of the high index material and a refractive index of 1.59 and 1.76 for polystyrene opals and alumina inverse opals was assumed respectively [33].

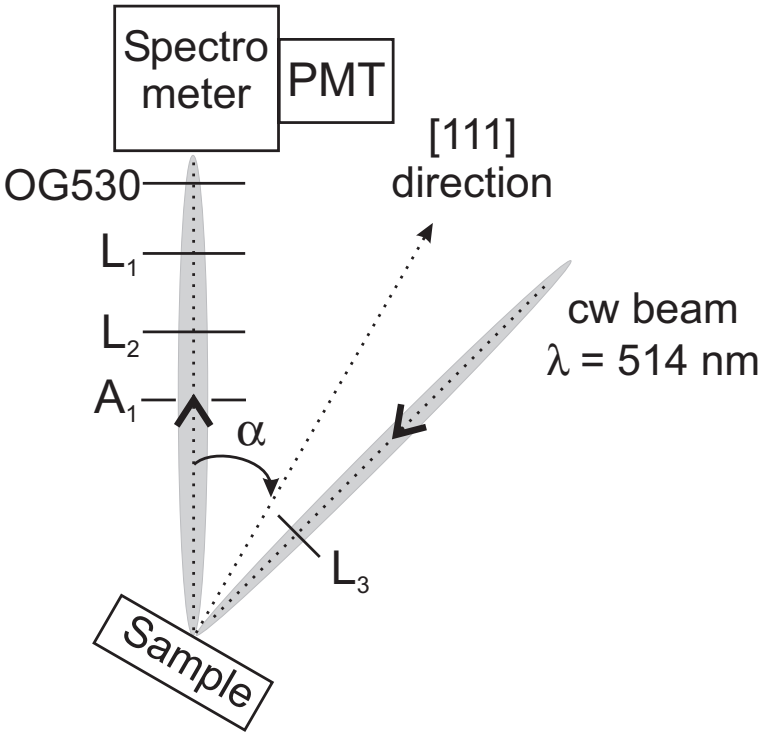

FIGURE 5.3: *Schematic of optical set-up. The pump beam of an Argon laser (λ = 514 nm), is focussed on the (111) surface of the sample. The fluorescence of the excited light is collected in reflection with an angle α away from the surface normal. Lens L_3 focuses the laser beam before it hits the sample, L_1 collimates and L_2 focuses the emitted light before it reaches the spectrometer. With aperture A_1 the angular spread of the emitted light can be adjusted. The photons are detected with a photomultiplier tube (PMT) via a prism spectrometer. The PMT is protected against direct reflected laser light by an OG530 cut-off filter.*

recorded from 503 to 815 nm. The slit widths of the spectrometer were set to 0.1 mm. With these settings a spectral resolution of ~ 4 nm was achieved.

To ensure only emission from internal sources, the dye molecules on the outer surface are selectively bleached by illumination with an intense laser beam under the Bragg angle [40]. The Bragg angle is determined by rotating the sample till the position where the reflection is the strongest. During bleaching the laser beam is not focussed and roughly illuminates the whole sample. The power of the unfocussed beam is 50 mW, yielding an intensity drop of a factor of 2 in half an hour.

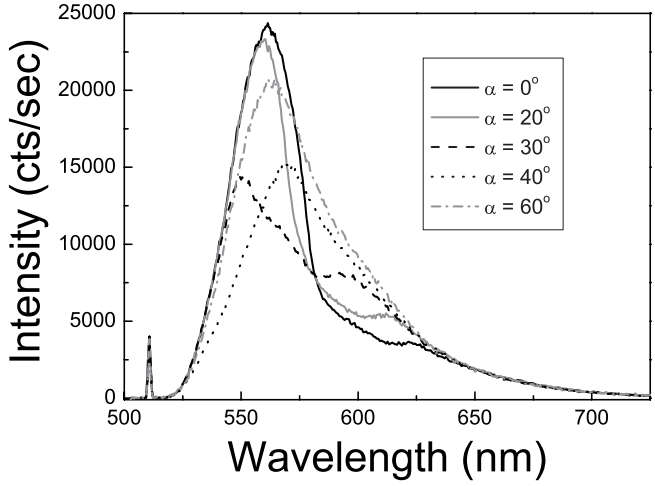

FIGURE 5.4: *Emission spectra of R6G adsorbed in a polystyrene opal with sphere size r = 131 nm (129-16-e). The first order Bragg diffraction of this sample coincides with the emission range of R6G. Strongly modified spectra are apparent. Black solid line represents $\alpha = 0°$; gray solid line $\alpha = 20°$; black dashed line, $\alpha = 30°$; black dotted line, $\alpha = 40°$; and the gray dashed-dotted line, $\alpha = 60°$. The $\alpha = 60°$ spectrum is unaffected by the stopgap since the first order Bragg diffraction is moved out of the emission spectrum of R6G. The sharp peak at $\lambda = 514$ nm results from the Argon laser excitation line.*

The crystals were doped with a 10^{-5} or 10^{-6} Molar R6G dye solution. The concentration of the dye solution was kept low to prevent self-absorption and non-radiative transfer.

5.3 Emission of R6G in opals with first order Bragg diffraction

Emission spectra of R6G adsorbed in a polystyrene opal with $r = 131 \pm 3$ nm are displayed in figure 5.4. The spectra were collected at different detection angles and were overlapped in the long wavelength limit, at 650 nm, the range were no crystal effects are apparent. This is done in order to correct for the variations in detection efficiency at different angles. Correction factors for overlapping were never larger than 2, where the $\alpha = 0°$ spectrum is not scaled. Dark counts from detector and stray light were subtracted. The dark counts were determined by averaging the

counts observed outside the emission range of R6G for each spectrum separately. The sharp peak appearing at $\lambda = 514$ nm is the Argon laser excitation line.

From the spectra it is clear that the emission of R6G is suppressed over a wide spectral range. Especially the $\alpha = 0°$ spectrum shows a strongly modified spectrum, with a suppressed domain ranging from 575 to 625 nm. At a wavelength of 600 nm there is a clear attenuation. This wavelength is exactly at the position where the stop gap is expected to be, based on calculations with Bragg's law [25]. With increasing angle the center position of the first order Bragg diffraction shifts to shorter wavelengths, manifesting in a shift of the inhibition. At $\alpha = 30°$ the attenuation has moved towards $\lambda = 575$ nm and the emission starts to recover at the red part of the fluorescence spectrum. The $\alpha = 40°$ spectrum is strongly modified at the blue part, and at the emission maximum of R6G, at $\lambda = 550$ nm, the emission is intensely reduced. Since the first order Bragg diffraction moves with angle with $\cos\alpha$, at $\alpha = 60°$ the attenuation has moved past $\lambda = 500$ nm. This results in an unaffected R6G spectrum at $\alpha = 60°$ as can be clearly seen in figure 5.4.

To visualize the present stop bands, the measured spectra should be normalized to a carefully chosen reference sample. The reference sample for these measurements was chosen to be a polystyrene opal with a smaller lattice parameter. The stop band of this sample is at shorter wavelengths, where R6G does not emit. Additionally this sample exhibits the same chemical properties as the photonic sample. The reference sample used for the normalization consists of spheres of $r = 63$ nm and was doped with a similar dye concentration. The spectrum of this sample was measured with a low power excitation source (a pulsed LED, see for more details chapter 6), and therefore scaling by a factor 8 was necessary.

To study the emission properties in relation with the direction of emission we have divided the spectra of figure 5.4 by the 0° spectrum of a $r = 63$ reference sample. In figure 5.5 the resulting intensity ratios of the spectra are displayed, which are scaled to unity in the long wavelength limit above 650 nm. The spectral position and width of the stop bands, are clearly seen and shift towards the blue with increasing angle. At $\alpha = 0°$ the center wavelength of the attenuation is at 600 nm, marked in the graph with a circle and a vertically dropped line. The observed center position of this stop band attenuation can be compared with reflectivity measurements. Reflectivity experiments were done with externally incident plane waves and are a complementary measure for the position and widths of stop bands. The reflectivity peak of a similar polystyrene opal, i.e., the same sphere size and same high quality, is plotted in figure 5.5 as a gray short-dotted line. The reflectivity is as high as 50%.[3] The center position of the reflectivity peak appears at $\lambda = 598$ nm, in excellent agreement with the position of the observed stop band measured with

[3]The reflectivity is referenced to a silver mirror with > 95% reflectivity.

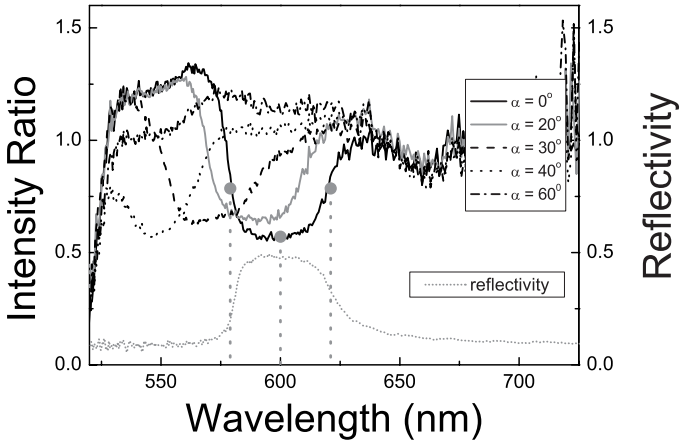

FIGURE 5.5: *Intensity ratios of the emission of R6G in a polystyrene opal with sphere size r = 131 nm (129-16-e). Raw spectra, as plotted in figure 5.4, are divided by the 0 ° spectrum of a r = 63 nm reference sample. Black solid line; α = 0 °, gray solid line; α = 20 °, black dashed line; α = 30 °, black dotted line; α = 40 °, black dash-dotted line; α = 60 °. The width and depth of the attenuation at α = 0 ° are marked with gray circles. The reflectivity peak measured at α = 0 °, the gray short-dotted line, shows the excellent matching shape and position.*

emission experiments. It is clear that not only the position but also the shape of the stop band and the reflectivity peak match excellently.

The decrease in emission clearly illustrates the photonic character of the polystyrene opals. As displayed in equation (5.1), the mean free path and the Bragg length determine the amount of attenuation, here defined as (1-Intensity Ratio). With a long mean free path, i.e., long range order, and a small Bragg length, i.e., a strong photonic character, the attenuation is large. The maximum attenuation, observed in figure 5.5 is 43%. Emission spectra taken at higher angles, α = 20, 30 and 40°, also show a strong inhibition, with attenuations varying between 38 and 43%. Although the attenuations are intense, the emission does not completely disappear in the stop band. This will be discussed in more detail in section 5.6.

It is remarkable that there is an increase at the blue side of the spectrum in the plotted intensity ratios in figure 5.5, i.e., there is enhanced emission observed that is above unity. For the α = 0° spectrum the intensity ratio reaches a value of 1.3 below λ = 575 nm. Similar results are observed for α = 20 and 30°. The normalized spectrum taken at α = 40° does not show this enhancement since the

stop band has moved below $\lambda = 530$ nm where the color-filter cuts off the light. The $\alpha = 60°$ spectrum shows a more or less featureless behavior. The intensity ratio, however, is larger than unity in the range 625-575 nm and reaches a value of 1.2. On photonic titania inverse opals [65] large decreases in intensity were observed for dye emission at $\alpha = 60°$. This directly illustrates the difference in source efficiency; dye on titania emits with a low efficiency, and therefore the emitted power is directly proportional to the radiative decay rate (see section 6.1). The strong enhancement at the blue side of the stop band investigated in our experiments are observed for the first time with emission measurements, and can be related to the diffuse propagation and internal refraction of the emitted light. This will be discussed further in section 5.6.

The relative widths of the stop bands are an indication for the photonic strength of the crystal and can be deduced from figure 5.5 by measuring the full width at half minimum and divide this FWHM by the center position [190]. Two circles at $\lambda =$ 578 and 621 nm, mark the width in the $\alpha = 0°$ spectrum in figure 5.5. The half minimum is taken to be 0.79 at both sides.[4] The relative width of the $\alpha = 0°$ spectrum, turned out to be 7.2%. The relative widths of the stop bands at higher angles have comparable values and vary between 7.1 and 7.2%. The relative width of the reflectivity peak is measured to be 6.9% and in good agreement with the values observed in the emission experiments. This resemblance in relative widths is expected since the stop band in both experiments, reflectivity and emission, is determined by the outer crystal planes near the surface. In transmission experiments usually broader widths are observed since the peak is determined by the whole probed volume and therefore is more sensitive to slightly different crystal orientations [40]. With band structure calculations values for the relative width of the stop gap of 6.5% were found. This value is slightly lower than the observed values in our experiments, and can be caused by the presence of unavoidable defects, that are not taken into account in the calculations. Nevertheless the calculated and measured value agree very well each other.

The half minima and the center positions of the stop bands are plotted as a function of detection angle in figure 5.6. The data are connected with lines. The relative width as calculated with band structure calculations (6.5%) is displayed as a vertical gray bar at $\alpha = -7°$. This value holds for $\alpha = 0°$ and agrees nicely with the measured relative width. As a comparison the center position of the stop gap, as it develops with first order Bragg diffraction is plotted [190], represented as a gray curve without symbols. The average refractive index used is 1.44, calculated from the known filling fraction and the refractive index of polystyrene, respectively, ϕ

[4] Although the half minimum at the blue side can also be interpreted as 0.94. Since with reflectivity experiments the reflectivity is never less than 0 we use 0.79 as the half minimum.

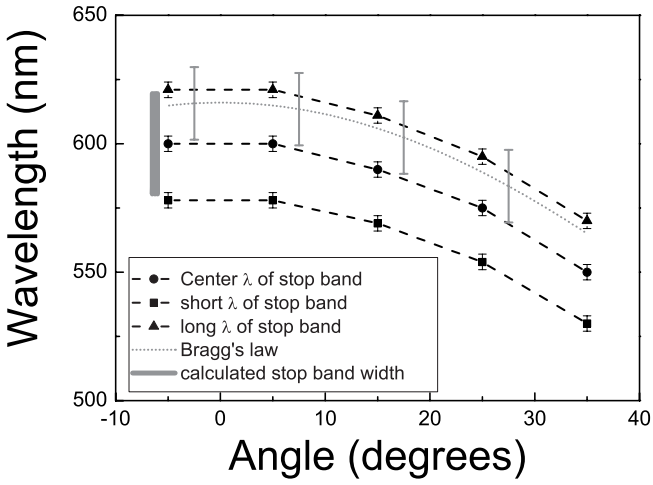

FIGURE 5.6: *The wavelengths of the measured stop bands in a R6G doped polystyrene opal with r = 131 nm (129-16-e) as a function of detection angle. The center, upper and lower edges of the stop band are denoted by respectively circles, triangles and squares. A comparison is made with Bragg's law where* n_{avg} *= 1.44 is used as average refractive index and internal refraction is taken into account. An excellent match is apparent between observed and calculated values.*

= 74% v/v and $n_{polystyrene}$ = 1.59.[5] The assumed sphere size is the one that is measured with SEM, r = 131 nm. Refraction, which takes place when the light exits the sample near the sample surface, has been taken into account.[6]

Since $\alpha = 0°$ in the experiment is not determined with high accuracy, we checked the real angle with a linear fit of the measured center positions. This resulted in an external angle that is shifted with 5° compared to the assumed $\alpha = 0°$. It can be seen that the trend of the predicted center wavelength as a function of angle matches nicely with the observed values in the experiment. The measured center position at $\alpha = 0°$ is slightly lower than the predicted value with first order Bragg diffraction. This deviation can be caused by a small difference in sphere size. Since the sphere radius is measured within an error of ± 3 nm, the center position can shift 14 nm up or down. The error bars for this deviation are plotted in figure 5.6 as vertical gray error bars, from where it is clear that they do agree with

[5] n_{avg} = 0.74 x $n_{polystyrene}$ + 0.26 x n_{air}

[6] The angle under which the light is exiting the crystal is calculated by the use of Snell's law.

measured stop band centers.

We have shown strongly modified emission spectra of R6G embedded in polystyrene opals, appearing in clear stop bands. The attenuations are strong; the emission is inhibited with ~ 43 %. Comparing the relative width of the calculated stop gap with the measured data it turns out that there is only a slight deviation, suggesting a minor contribution of disorder. The dye in the polystyrene opal behaves as an efficient emitter and therefore this sample is very well-suited for time-resolved measurements.

5.4 Emission of R6G in inverse opals with first order Bragg diffraction

The alumina inverse opal exhibits a higher refractive index contrast than the polystyrene opals, $m = 1.76$ for alumina inverse opals versus 1.59 for polystyrene opals. Secondly the alumina inverse opal has the high index material in minority since it is an inverse structure. These characteristics are some of the requirements for a photonic band gap and as a consequence these crystals should interact more strongly with light compared to polystyrene opals. The filling fraction of the alumina inverse opals is, on the contrary, lower, i.e., $\phi \sim 10\%$ v/v. As a result the relative width of the stop gap, or the photonic strength, as predicted with band structure calculations is less. This can also be seen in figure 5.2 where the the stop gap of an alumina inverse opal has a calculated width of 5.5%, compared with the polystyrene opal that has a calculated width of 6.5%. Nevertheless these inverse structures of alumina are interesting for emission experiments since this gives us the opportunity to compare direct and indirect structures. In this section we will perform and discuss similar measurements as done with the polystyrene opals in the previous section.

Figure 5.7 displays the emission spectra of R6G in an alumina inverse opal with air-sphere size $r = 169 \pm 3$ nm. The R6G dye is adsorbed on the inner surface of the backbone of the air spheres and excited at $\lambda = 514$ nm. The spectra are collected, after bleaching of the outer surface, at different detection angles and are overlapped in the long wavelength limit, at 700 nm. The $\alpha = 30^\circ$ spectrum is not scaled and shows the actual measured counts. The emission of R6G is clearly reduced over a large extent, especially the $\alpha = 0^\circ$ spectrum is suppressed over a wide spectral range, reaching from 570 to 650 nm. The attenuation in the $\alpha = 0^\circ$ spectrum is most pronounced since it happens in the center of the R6G dye spectrum, at $\lambda = 610$ nm. With increasing angle the stop band shifts to shorter wavelengths, appearing in a shift in attenuation. At $\alpha = 30^\circ$ the decrease in emission has moved towards $\lambda = 550$ nm and the red part of the R6G emission spectrum starts to recover. At $\alpha = 60^\circ$ the stop band has completely moved outside the emission region of R6G

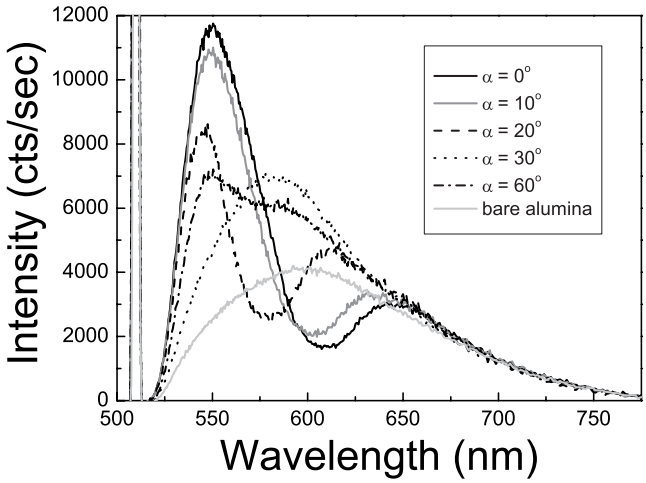

FIGURE 5.7: *Emission spectra of R6G adsorbed on the inner surfaces of an inverse opal of alumina. The air-sphere size is r = 169 nm (213-43-b). Attenuations in the emission of R6G are clearly seen over a wide range. The black solid line displays α = 0 °; gray solid line α = 10 °; black dashed line, α = 20 °; black dotted line, α = 30 °; and black dashed-dotted line displays α = 60 °. The luminescence of bare alumina, measured from a non-photonic air-sphere crystal, is represented by the light-gray line and covers the whole emission range of R6G. At λ = 514 nm the Ar laser excitation line is clearly visible.*

and results in an unaffected spectrum. The $\alpha = 60°$ spectrum plotted in figure 5.7, however, displays an extra hump at λ = 590 nm. This extra emission is probably caused by alumina. The luminescence of the pure alumina backbone, measured on an undoped sample with same pump power, is also displayed in figure 5.7. The luminescence spectrum covers the whole emission range of R6G spreading from 520-750 nm. The luminescence observed at long wavelengths (beyond 700 nm), seen in all the spectra, can also be a contribution of luminescence of alumina. This alumina luminescence has however no influence on the clearly present modification of the R6G emission by Bragg diffraction.

The alumina inverse opals clearly show more intense attenuations in the stop bands compared to the polystyrene opals. This can also be seen in figure 5.8 where the intensity ratios of the spectra are displayed. The spectra are divided by the 60° spectrum to visualize the present stop bands. Since a spectrum of a sample with a smaller lattice parameter was not available, the $\alpha = 60°$ spectrum serves as a refer-

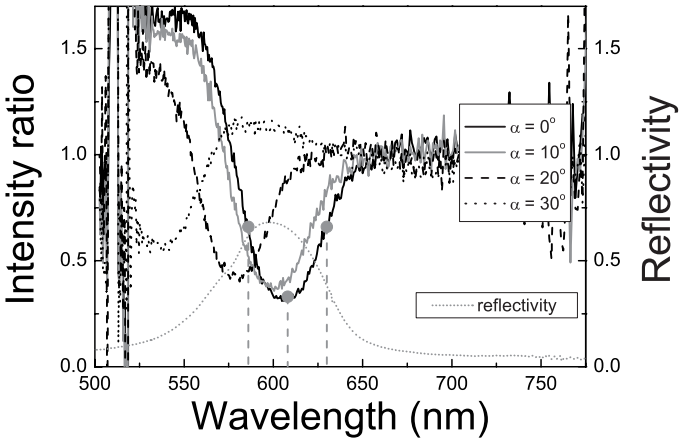

FIGURE 5.8: *Intensity ratios of the emission of R6G in an inverse alumina opal with sphere size r = 169 nm (213-43-b). Raw spectra, as plotted in figure 5.7, are divided by the 60 ° spectrum. The black solid line represents α = 0 °; gray solid line, α = 10 °; black dashed line, α = 20 °; and the black dotted line α = 30 °. The reflectivity peak measured at α = 0 °, the short-dotted gray line, matches well with the position of the stop band.*

ence. One might consider the $\alpha = 60°$ spectrum of the photonic sample even to be the proper reference for observing stop bands. This is indeed correct for determining the position and width of stop bands. For comparing DOS and enhancement effects, however, the $\alpha = 60°$ spectrum does not fulfill. Although the stop band in the $\alpha = 60°$ spectrum is moved out of the emission spectrum of R6G, the spectra are still modified by internal Bragg diffraction and modified DOS. The attenuations resulting from normalizing to the $\alpha = 60°$ spectrum, are easily recognized and shift towards the blue with increasing angle. The maximum suppression for the $\alpha = 0°$ spectrum is 67%, compared to 43 % for the polystyrene opals. The polystyrene opals are more strongly photonic (see also their widths in figure 5.2) and therefore the Bragg attenuation length l_{Bragg} is less than for the alumina opals. The larger attenuation seen in the alumina opals therefore suggests that the mean free path is larger in the alumina inverse opals, based on equation (5.1). The mean free path for polystyrene opals was measured to be $l \sim 15\ \mu$m [191]. The mean free path of inverse opals was measured for titania and turned out to be $l \sim 15\ \mu$m [191]. The alumina inverse opal exhibits the same structure factor as the titania inverse opal since it is also an air-sphere structure. Therefore we can estimate l for alumina with

the model of Koenderink *et al.* [194], where $l \propto 1/(m-1)^2$. This yields a value of $l \sim 60$ μm for alumina compared to $l \sim 15$ μm for titania. Since $l_{\mathrm{Bragg}} \propto 1/\Psi$, and Ψ ($= \Delta\lambda/\lambda_0$) can be deduced from figure 3.16, the Bragg attenuation length can be estimated, resulting in a $l_{\mathrm{Bragg}} = 13$ μm. Taken together this results in an attenuation $A = 1 - \frac{13}{60} = 75\%$, in good agreement with the observed attenuation of $\sim 67\%$. This resemblance confirms our assumptions and demonstrates the simple models of l_{Bragg} and equation (5.1) to be accurate.

The maximum suppression in figure 5.8 appears at $\lambda = 608$ nm, marked in the graph with a circle, and this position can be compared with reflectivity data taken from a similar sample made from a template with the same sphere size and of the same high quality. The reflectivity peak of an inverse alumina opal with $r = 169$ nm is plotted in figure 5.8. The center position of the peak is at $\lambda = 598$ nm and slightly shifted, 10 nm, compared to the value observed in the emission measurements. As was seen with reflectivity measurements in chapter 3, this is not uncommon for the alumina inverse opals, where on similar samples center positions were found varying from 558 to 613 nm. This variance is expected to be caused by a difference in shrinkage resulting in smaller of larger air-spheres, even present in crystals made from the same template (see figure 3.11).

A remarkable feature in figure 5.8 is that the attenuations decrease strongly with increasing angle. The $\alpha = 0°$ spectrum shows an attenuation of 67%, where at $\alpha = 30°$ this value is already decreased to 43%. The amount of attenuation as a function of angle will be discussed further in detail in section 5.6.

Another intriguing feature is the enhancement at the blue side of the stop band. This increase is even larger than the one observed in the polystyrene opals and exceeds an intensity ratio of 1.5. It is interesting to remark that the enhancement is present in direct as well as in indirect structures. This enhancement will be discussed in section 5.6.

The relative widths of the stop bands are directly proportional to the photonic strength of the crystal. The FWHM is marked in figure 5.8, with two circles at wavelengths of 586 nm and 630 nm. The half maximum is taken to be at 0.66 at both sides.[7] The relative widths of the attenuations in the inverse alumina opals, vary between 6.1 and 7.2%. These widths can be compared with the predicted value of 5.5%. This is a deviation from the measured value and is attributed to the presence of unavoidable defects, since the relative width is a measure of both the photonic strength and the disorder. The disorder can not taken into account in the band structure calculations. In the polystyrene opals the disorder is expected to be less pronounced than in the alumina inverse opals since its preparation process is two process steps less. Although the deviation of the measured relative width from

[7] For the same reason as with the polystyrene opals the half maximum at the blue side is interpreted as 0.66 and not as 1.00.

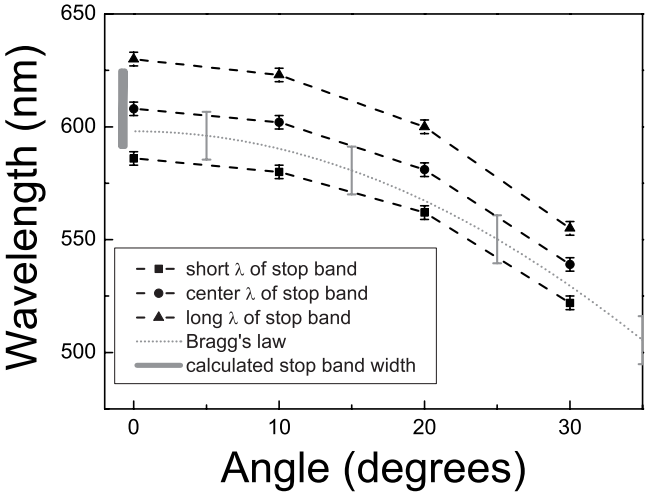

FIGURE 5.9: *Angular dependence of the measured stop bands in a R6G doped inverse alumina opal with r = 169 nm (213-43-b). The positions of the center, upper and lower wavelengths of the FWHM are plotted as a function of detection angle with respectively circles, triangles and squares. A comparison is made with the center wavelength assuming single (111) Bragg diffraction, where n_{avg} = 1.084 is taken as average refractive index. Correction for internal refraction is done.*

the predicted relative width of stop gaps in polystyrene opals is less than for the alumina inverse opals, the alumina crystals are still of outstanding quality as also demonstrated in chapter 3.

The relative width as measured with reflectivity measurements, gives a value of 10.4%. The difference in width is clearly seen in figure 5.8, where the reflectivity peak appears to be much broader. This deviation in width is attributed to the presence of disorder caused by different shrinkages. The shrinkage during the calcination is ~ 25% and can vary throughout one sample, creating different sphere sizes in different areas. Since with reflectivity a larger focus is used and therefore more areas are averaged, these differences in sphere sizes can cause broadening. On similar alumina samples, with similar sphere sizes, relative widths of 8.5% were found, coming close to the values observed in emission experiments.

In figure 5.9 the angular dependency of the stop bands is displayed. The center, upper and lower wavelength at half height are plotted as a function of detection angle. The gray curve without symbols is the calculated center position assuming

single (111) Bragg diffraction, the width of this calculated stop gap is plotted as a vertical gray bar just below $\alpha = 0°$. The average refractive index is estimated as $n_{avg} = 1.084$, from an estimated filling fraction of $\phi \sim 11\%$ and the refractive index of alumina, $n_{alumina} = 1.76$.[8] The curve of the calculated stop gap starts at a slightly lower value, at $\lambda = 598$ nm compared to 608 nm for the measured wavelength. This can be caused by a difference in sphere size, since the sphere size is determined by measuring air spheres on an electron micrograph. Usually in SEM-measurements an uniform sphere size is found with an uncertainty of maximum ± 8 nm. For the alumina air spheres that were measured on a similar sample as the sample used for the emission measurements, a deviation in sphere size of ± 3 nm was calculated. Such a variation can cause a shift in center wavelength of ± 10 nm, that agrees well with the measured value. This variation is indicated in figure 5.9 as error bars on the curve of Bragg's law and matches very well with the measured value.

The alumina inverse opals are excellent candidates for emission experiments. Clear stop bands were observed and the position and the relative widths of these stop bands agreed well with theory as well as with earlier performed reflectivity measurements. The strong attenuations observed for the alumina inverse opals compared to the polystyrene opals are explained with a longer mean free path l as estimated with a model. We are the first to compare attenuations in direct and indirect structures.

5.5 Emission of R6G in opals with second order Bragg diffraction

Since we expect the DOS in the second order Bragg diffraction range to vary much more than on the first sample, it is interesting to investigate emission from crystals with higher order Bragg diffraction. The interaction between light and matter in these samples increases as light will diffract from more than one lattice plane. This results in not one clear single stop gap, as is the case with first order photonic crystals, but a complex combination of several diffractions. Previously second order reflectivity was observed from inverse titania opals [167], [168] but emission from samples with second order Bragg diffraction was never investigated. Therefore it would be a complementary research to measure emission of dye in a photonic sample with second order Bragg diffraction. We have investigated a sample with a lattice parameter that has its second order Bragg diffraction in the emission range of R6G. The samples have a sphere size of $r = 238 \pm 2$ nm and the first order Bragg appears above $\lambda_{111} = 1100$ nm, as was measured with reflectivity and calculated with single (111) Bragg diffraction. The second order Bragg diffraction

[8] $n_{avg} = 0.11$ x $n_{alumina} + 0.89$ x n_{air}

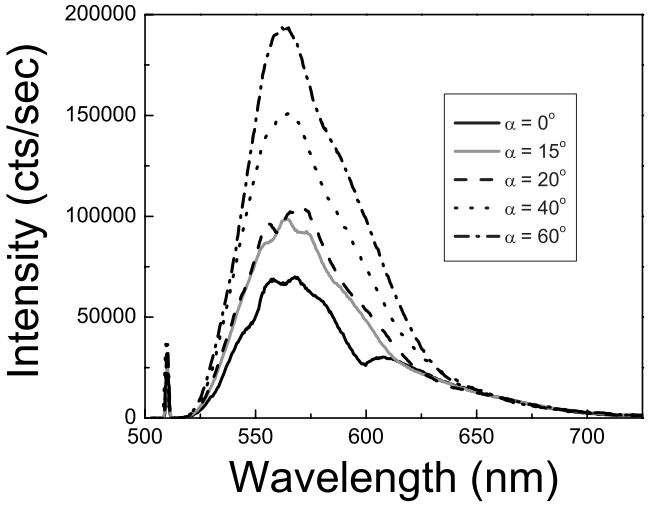

FIGURE 5.10: *Emission spectra of R6G adsorbed in a polystyrene opal with sphere size r = 238 nm (241-33-a). The second order Bragg diffraction of this sample corresponds with the emission range of R6G. A strong suppression is apparent. Black solid line displays α = 0 °; gray solid line α = 20 °; black dashed line, α = 30 °; black dotted line, α = 40 °; and light gray line α = 60 °.*

is at shorter wavelengths, $\lambda_{222} \sim 590$ nm, and manifests in the emission region of R6G, as also seen in figure 5.1. In figure 5.10 the emission spectra of R6G in a polystyrene opal with $r = 238 \pm 2$ nm are displayed. Correction for background is done by averaging and subtracting the dark counts below 520 nm. The spectra are overlapped at $\lambda = 660$ nm (the $\alpha = 20°$ spectrum is not scaled), although this is not the long wavelength limit. From calculations we learned, however, that at this wavelength the DOS resembles the free space value and thus we expect photonic effects to be reduced.

It can be seen in figure 5.10 that the emission of R6G is modified over a wide range, reaching from 625 to 570 nm. This coincides with almost the complete emission range of R6G. Particularly the $\alpha = 0°$ spectrum shows a strongly altered emission, with a large decrease in emission at $\lambda = 598$ nm. Also at the peak emission, at a wavelength of 562 nm, a clear suppression in emission is observed. At the blue side of the emission spectrum, around $\lambda = 550$ nm, the intensity is reduced as well. This is clearly different from the first order samples where no decrease in emission was observed below wavelengths of 560 nm. With increasing angle

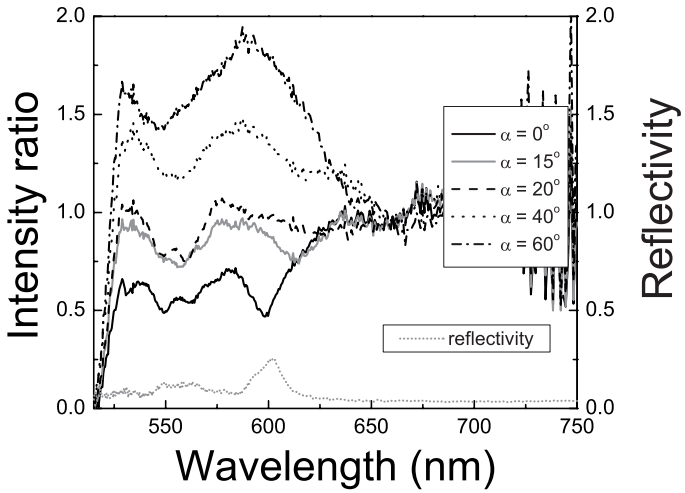

FIGURE 5.11: *Intensity ratios of the emission of R6G in a polystyrene opal with sphere size r = 238 nm (241-33-a). The spectra, as plotted in figure 5.10, are referenced to a polystyrene opal with a smaller lattice parameter (a = 296 nm). The black solid line represents α = 0 °; gray solid line, α = 20 °; black dashed line, α = 30 °; the black dotted line α = 40 ° and the black dash-dotted line α = 60 °. The reflectivity peak, courtesy of E. Flück, shows the same variations and is displayed by the short dotted gray line. The position as well as the shape of the attenuations in the α = 0° spectrum match excellently with the reflectivity data.*

the inhibition of emission becomes less, resulting in an increase in intensity at all wavelengths compared to the $\alpha = 0°$ spectrum. In the $\alpha = 15°$ spectrum it appears that the attenuations that are seen in the $\alpha = 0°$ spectrum are slightly moved, ~ 7 nm, towards the blue. The attenuations appear respectively at wavelengths of 586, 569 and 556 nm, compared to 598, 562 and 550 nm in the $\alpha = 0°$ spectrum. At $\alpha = 20°$ the emission at the red part of the R6G spectrum partly recovers. A narrow attenuation is observed here at $\lambda = 560$ nm. Beyond $\alpha = 20°$ the sharp attenuations are not visible anymore. Since the suppression does not consist of one single feature it cannot easily be concluded that the observed features shift with angle. Obviously the attenuations do not simply shift with $\cos \alpha_{\text{internal}}$) which is seen in experiments with first order samples.

To highlight the stop band features in the spectra, we divide the spectra of figure 5.10 by the spectrum of a reference sample with a sphere size of r = 63 nm. The Bragg diffraction of this samples appears far below λ = 300 nm and therefore will not influence the R6G emission spectrum. The normalized spectra are scaled to unity in the wavelength region above 660 nm. The resulting intensity ratios, as plotted in figure 5.11, show strong attenuations over the whole emission range of R6G. The intensity ratio of the $\alpha = 0°$ spectrum shows a strong suppression from 625 to 525 nm. At λ = 598 nm the emission is even reduced with 53%. This attenuation in the $\alpha = 0°$ spectrum of the second order has a sharp triangular shape at λ = 600 nm. Two less intense attenuations are observed at a wavelength of 562 and 550 nm; here the emission is decreased with respectively 52 and 46%. The $\alpha = 40°$ and 60° spectra do not show an attenuation: it seems rather to be an enhancement. The $\alpha = 40°$ spectrum has a maximum value of 1.45 at λ = 585 nm whereas the $\alpha = 60°$ spectrum even shows an intensity ratio of 1.9 at this wavelength. The features in the $\alpha = 40°$ and 60° spectra are very similar, at λ = 585 nm an intense enhancement and at λ = 550 nm a strong attenuation.

As a comparison the reflectivity ratio of a similar sample with same sphere size is plotted in figure 5.11. The reflectivity ratio is scaled with a factor 3 for clarity. It can be seen that the center position of the main reflectivity peak coincides perfectly, within 3 nm, with the position of the sharp triangular attenuation in the 0° spectrum. The reflectivity signal observed between 570 and 545 nm is not distinguishable in separate peaks but the position matches well with the observed attenuations in the emission spectrum.

With reflectivity experiments the entry to second order Bragg diffraction was already made by Vos and Van Driel [167, 168]. They described higher order Bragg diffraction of titania inverse opals measured with angle-resolved reflectivity. Their results were compared with bandstructure calculations and agreed well. As opposed to simple Bragg diffraction [20, 25], at higher order Bragg the light can diffract from many lattice plane simultaneously. This results in spectral positions of stop gaps that hardly vary with increasing angle. In our emission experiments indeed the spectral position of the measured stop bands do almost not change; from $\alpha = 0°$ to $\alpha = 40°$ it modifies nearly the complete emission spectrum of R6G, ranging from 525 to 625 nm. This angle-independent width is supplementary evidence for the strong photonic character of these second order polystyrene opals.

It is clear that the shape of the modified emission spectra of R6G is completely different from the modified emission spectra of R6G in polystyrene opals with first order Bragg diffraction. The second order Bragg diffraction is less characterized than the first order. Not a clear single gap is observed but a contribution of suppressions at several wavelengths. This difference between the first and second order Bragg diffraction can already be seen in the photonic band structure calculations

where the first order gap of the r = 238 nm sample in the Γ-L direction shows one clear stop gap, see figure 5.2. The second order Bragg diffraction, however, that appears at shorter wavelengths, is a complex sum of band structures. No single gap can be appointed. We expect the stop gap to be between the fifth and sixteenth band since these bands have slopes close to the average refractive index. In figure 5.2 this area is arced and marked with two arrows.

The attenuation observed in these second order Bragg samples is larger (53%) than the attenuation found in the first order samples where the maximum attenuation was found to be 43%. If we consider the mean free path in opals to be the same for first and second order opals [191], we can assume that the Bragg length is shorter for the second order opal (see also equation (5.1)). This is consistent with the width of the attenuated emission, which is much broader for the second order Bragg diffraction, and thus indicating a larger photonic strength.

It can be speculated whether the features at λ = 600, 562 and 550 nm are a result of surface grating modes as was first explored in 2D photonic crystals by Labilloy *et al.* [195]. These grating modes can influence the optical properties of the photonic crystal and should therefore be examined before excluding them. For our *fcc*-packed crystals the longest grating spacing d can be calculated with

$$d = \sqrt{\frac{3}{8}} \cdot a_{fcc}, \tag{5.2}$$

where a_{fcc} is the known lattice parameter. For the polystyrene opals with radius 238 nm the first order grating mode appears at maximum 412 nm. This is far to the blue compared to the emission range we explored and can therefore be excluded.

We observe that the shape and position of the attenuations change with increasing detection angle and cannot be explained with simple Bragg diffraction. Since the band structure calculations already showed a complex collection of bands and not a distinct stop gap it is very difficult to address the observed features. It is clear that further theoretical interpretation in this area is necessary and an important subject for additional research. Further experimental research will be performed in the following chapter where lifetime measurements on similar samples are explored. Our experiments on emission from photonic crystals with second order Bragg diffraction are advanced, since for *fcc* crystals the photonic band gap will appear at this second order Bragg. This again illustrates the importance of investigating higher order Bragg diffraction.

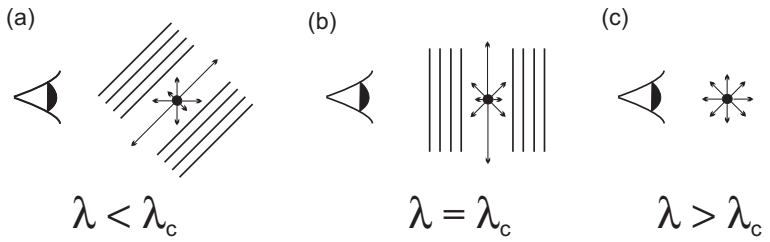

FIGURE 5.12: *Cartoon of a light source emitting at λ in a photonic crystal with one set of crystal planes. The detection is performed at $\alpha = 0°$. (a) Light is emitted at a wavelength λ below the stop band wavelength (λ_c). The light can be diffracted from the lattice planes and light can be inhibited and enhanced in certain directions. (b) The emission is in the stop band wavelength, $\lambda = \lambda_c$. Inhibition takes place and therefore enhancement can occur. (c) If light is emitted with a wavelength longer than λ_c the light will not experience Bragg diffraction and no enhancement and attenuation are observed.*

5.6 Enhanced and attenuated fluorescence

A remarkable feature in the observed intensity ratios is the increase in emission at the blue side of the spectrum, i.e., there is more emission at shorter wavelengths than is expected on basis of the emission properties of R6G. This increase in intensity is seen in both first order samples; the polystyrene opal with r = 131 nm and the alumina inverse opal with r = 169 nm. For the polystyrene opal the enhancement can be seen in the $\alpha = 0°$ spectrum in figure 5.5. The wavelength region over which the emission is attenuated ranges from 575 to 625 nm. Below λ = 575 nm however, the intensity ratio exceeds unity and reaches a value of 1.3. In the alumina inverse opals, see figure 5.8, an enhancement of even 1.6 is observed. These enhancements can be explained with the so-called escape function of diffuse light, a model developed by Koenderink and Vos [196]. In essence, if emission in certain directions is limited due to internal Bragg diffraction, the chance of escaping in the other existing angles is enhanced. In references [196] and [194] angle-resolved transmission on titania inverse opals is described. They observed enhancement at wavelengths outside the stop gap which cannot only explained by internal reflection. While the titania inverse opals are known to be very effective photonic crystals, light is multiply scattered in a random way due to unavoidable disorder. Exactly this additional *diffuse* light transport can theoretically explain the enhancement. Inevitably our opals also exhibit disorder which cause similar phenomena. Since the emission of R6G in certain directions is suppressed due to internal Bragg diffraction, in the $\alpha = 0°$ spectrum from 575 to 625 nm, the R6G emission in other directions is increased. In our experiments the enhancement is seen in both direct opal and

indirect inverse opal structures, at the blue side of the stop band.

Why the enhancement is only present at the blue side of the stop gap can be schematically illustrated with figure 5.12. In this figure a light source in a photonic crystal is emitting and the light is detected at $\alpha = 0°$. Note that the light is diffuse in the bulk of the sample. When light is emitted at a wavelength in the stop band wavelength ($\lambda = \lambda_c$) it is diffracted from lattice planes and the diffracted light has a probability to escape at other angles causing enhancement at certain wavelengths. Light emitted with a wavelength below the stop band ($\lambda < \lambda_c$) is not Bragg diffracted from lattice planes at $\alpha = 0°$ but it can encounter Bragg diffraction at higher angles. For such oblique angles, more light will be detected for $\lambda = \lambda_c$ ("enhancement"), because light cannot exit perpendicularly to the crystal planes. When light is emitted at a wavelength above the stop band wavelength ($\lambda > \lambda_c$), however, it will not experience internal diffraction, also not at higher angles, and no enhancement will be observed.

Since the enhancements at the blue side are both present for the direct as well as the indirect structure, the explanation of the enhancement with standing wave effects can be ruled out. As discussed in section 5.1, this model describes that the enhancement at wavelengths near the stop band are caused by the standing wave that is either in the high index material or in the low index material [193]. This explanation is not in agreement with our experimental situation.

To explain the difference in enhancement between the alumina inverse opals and the polystyrene opals we compared the amount of attenuation and enhancement as a function of angle, see figures 5.13 and 5.14. From both figures it can be seen that an increase in attenuation corresponds to an increase in enhancement. The internal angles are displayed at the top x-axis. In figure 5.13 the intensity ratios of the first order polystyrene opal are displayed. The attenuations are slightly above 0.50 and the enhancements are at ~ 1.25. The attenuations and enhancements show a small trend where an increase in attenuation, i.e., a lower value for the intensity ratio, corresponds to an increase in enhancement, i.e., a higher value for the intensity ratio. For instance at $\alpha = 10°$ a slight increase of the attenuation is observed compared to $\alpha = 0°$, and the enhancement also is somewhat increased.

In figure 5.14, where the intensity ratios of the inverse alumina sample are displayed, the trend between enhancement and amount of suppression is more pronounced. In the $\alpha = 0°$ spectrum of the alumina inverse opal the intensity ratio is below 0.40 and the enhancement is at 1.6. The attenuation as well as the enhancement are stronger than the values found for polystyrene, where values of respectively 0.5 and 1.25 are found. This suggests that a stronger attenuation results in an stronger enhancement. A larger variation is seen in the attenuations and enhancements as a function of angle. Here it is clearly seen that with increasing angle the attenuation decreases and also the enhancement lowers. The stronger trend with

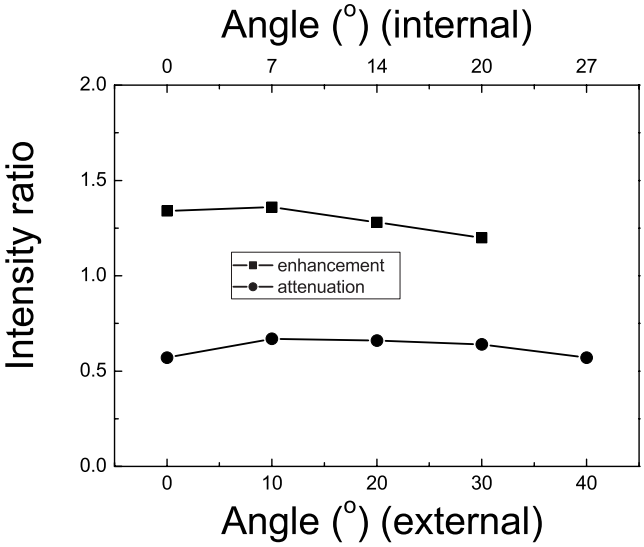

FIGURE 5.13: *The intensity ratios of the attenuations and enhancements of the first order polystyrene opal plotted as a function of angle. The lines are guides to the eye. At $\alpha = 40°$ the data point for enhancement is missing since here the light is cut-off by the filter. Error bars are comparable to the symbol size.*

angle for alumina samples compared to the polystyrene samples can be explained with the fact that the internal angle deviates less from the external angle for the alumina sample. The difference between the internal and external angle for the polystyrene sample is larger, a shift of 10° in external angle results in only a shift of 7° for the internal angle and therefore less change with external angle, whereas for alumina these values are respectively 10° and 9°.

It can be seen from figures 5.13 and 5.14 that the observed enhancement is angle-dependent. This was also obtained in the theoretical model proposed by Koenderink and Vos [196].

Although the attenuations in emission stop bands are very pronounced, the emission is not completely attenuated to 0, even though the light sources are deep inside the samples. This is different from what is seen in conventional transmission experiments, where the transmission of external plane wave entirely vanishes in the expected stop gap. This difference between the transmission and emission experiments was first observed by Megens *et al.* [40], and explained by scattering from defects near the surface. In emission experiments the embedded light source emits

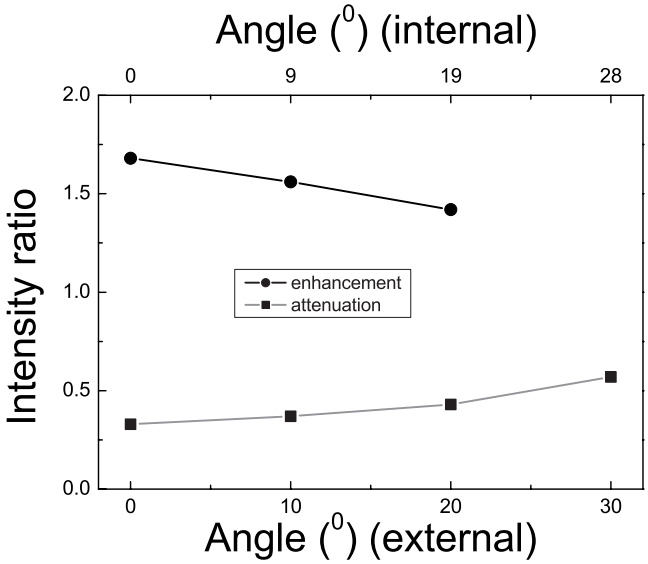

FIGURE 5.14: *The intensity ratios of observed attenuations and enhancements in an alumina inverse opal. Strong angle-dependent behavior is apparent where with increasing angle a decrease in attenuation goes with an decrease in enhancement. An intensity ratio for the enhancement at $\alpha = 30^\circ$ is lacking since the light is cut off by a color filter.*

photons and does not emit in the direction of the stop band. When the light comes near the sample surface, it may scatter off some defects. These defects cause diffuse scattering of the light in all directions, also in the direction of the original stop band, and emission at the wavelength of the stop band is observed. In transmission experiments these phenomena do not occur since the light that travels through the crystal to the detector is well collimated and the randomly scattered light is not detected.

5.7 Conclusions

We have shown the polystyrene opals and alumina inverse opals to be very effective photonic crystals. The attenuations seen in the direct and indirect structures could be well explained with different mean free paths and Bragg attenuation lengths. We are the first to explore emission experiments with second order photonic crystals and demonstrated strongly modified emission from these crystals. The first order

samples, opals as well as inverse opals also showed strong attenuated emission and displayed an increase at the blue side of the stop band. This enhancement was explained with the escape model of diffuse light by Koenderink *et al.* [194]. The enhancement observed and explained in our experiments was the first measured with internal sources. The widths of the measured stop bands show values that compared well to widths observed in reflectivity measurements and theory. Slight deviations from the predicted values were attributed to unavoidable defects present in the crystal that can not be included in (band structure) calculations. Since no electron transfer is present in these samples, and therefore the quantum efficiency remains high, the photonic systems investigated here are very promising to use in time-resolved measurements. In the following chapter lifetime measurements on these, in this chapter investigated, photonic crystals will be discussed.

Chapter 6

Lifetime Measurements of Laser Dye Embedded in Photonic Crystals

6.1 Introduction

Spontaneous emission can strongly be modified by its surrounding medium as discussed in chapter 1 and 5. Angle-dependent effects were investigated in terms of stop gaps in the previous chapter. In this chapter we will concentrate on angle-independent modifications, that include lifetime effects and modifications on total emission.

The spontaneous emission of a light source in a photonic crystal, is proportional to the density of states (DOS) in the crystal. Since the DOS in photonic crystals is subject to intense variations compared to the DOS in vacuum, the spontaneous emission can be enhanced or inhibited.

Several groups have investigated spontaneous emission of light sources in photonic crystals. Martorell and Lawandy claimed already in the early nineties to have inhibited radiative decay of dye molecules dissolved in an ordered aqueous suspension of polystyrene spheres [197]. The fluorescence lifetime of the dye in this photonic structure was 1.75 times longer than the observed lifetime in a disordered reference sample. They ascribed the observed inhibition to the periodic dielectric medium; a real photonic effect. In 1993 Tong *et al.* described lifetime changes of Kiton Red S in monodispersed polystyrene colloids compared to dye dissolved in water [198]. They clarified that the origin of the processes causing the change in lifetime are not all associated with the photonic band structure. Also the electronic

interaction of the emission source with the surrounding medium can influence the lifetime effect. Li and Zhang performed several calculations on the modification of atomic spontaneous emission [199]. They calculated for the photonic system used by Martorell and Lawandy a maximum lifetime change induced by the photonic band structure of 5%. This is far below the observed variation of 1.75 times.

Petrov *et al.* observed non-exponential spontaneous decay containing both accelerated and inhibited components compared to the dye fluorescence in a homogeneous reference sample [187]. Their photonic sample consisted of porous spherical silica globules arranged in a face centered cubic (*fcc*) lattice, filled with a dye containing polymer film. The reference sample is just a freestanding dye containing polymer film. They explained the observed acceleration and inhibition with a change in the photon DOS in the photonic crystal compared to the reference. Megens *et al.* criticized their interpretation explaining that the modification of the fluorescence decay times are not a result of photonic effects, as was demonstrated theoretically as well as experimentally [200]. They calculated the largest effect of inhibition to be $\sim$ 10% but only at the blue edge of the stop band. Petrov *et al.*, however, measured at the red side, the edge where no inhibition should be present. Li and Zhang also calculated on the system used by Petrov *et al.*. A maximum photonic effect was calculated to be below 5%, by no means explaining the results of Petrov. Most probably the large accelerations and inhibitions seen by Petrov are caused by chemical interactions since the photonic and reference sample are not chemically identical. More calculations on lifetime modification in photonic crystals were performed by Wang *et al.* [201]. They calculated on photonic crystals similar to those of Petrov and reported a wide lifetime distribution for emission sources in these crystals, concluding that the observations by Petrov *et al.* are plausible. Finally we mention, as was recently observed with fluorescence measurements described in chapter 2, that luminescence of the backbone of the crystal should be considered. Since Petrov *et al.* excite their dye at λ = 337.1 nm, far into the ultraviolet, we currently think the luminescence of the silica backbone has a major contribution to their observed lifetime behavior.

Time-resolved measurements were also performed by Megens *et al.* on systems where dye was incorporated in photonic colloidal crystals [192]. To minimize chemical interactions and adsorption of the dye on the sphere surfaces, the dye in these crystals is incorporated and shielded inside the colloidal spheres. Although they observed in the photonic and reference samples identical stop gaps, by comparing the observed fluorescence lifetimes in the photonic samples with the colloidal liquids, they observed a small decrease of at most $\sim$ 2% in relation to the reference system. They explained the longer lifetime observed in the colloidal suspensions, i.e., the reference samples, in terms of multiple scattering that is more pronounced in random media. The pathlength of the emitted light to the detector is considerable

increased and causes a lengthening in detected lifetime. Li and Zhang performed calculations on this sample system of Megens *et al.* as well. A maximum lifetime change of 4% was estimated, in good agreement with the experimental results of Megens *et al.*

Modified emission of phosphorescent sources has also been reported [202]. The lifetime of ZnS:Mn infilled in a polymer photonic crystal showed a strong dependence on emission wavelength. No stop gaps, however, were apparent in the spectra, and therefore it is unclear to what the lifetime change is related.

Recently de Dood *et al.* studied the spontaneous emission of erbium embedded in silicon photonic crystals [203]. These crystals consist of a layer-by-layer lattice of silicon bars and is only five layers (< 3 unit cells) thick. The modification of the emission is explained in terms of the change in the local density of states (LDOS), but also internal Bragg scattering and the internal quantum efficiency is taken into account. Besides spectral changes, lifetime changes are measured and after a careful analysis an inhibition of 25% ± 10% is observed.

Since it seems like in all previous discussed experiments no large lifetime changes were measured, the question arises whether the observations of lifetime changes in the past are really a result of the photonic band structure. Clearly chemical interactions of the light source with the surrounding structure play an important role and are systematically underestimated. Since the photonic crystals are either weakly photonic or exist of only a few unit cells, the stop bands are narrow (∼ 5%). Also DOS calculations do not predict that large lifetime changes and therefore the observed modifications are not expected to be photonic. This illustrates the importance of continuing the research on light sources in photonic crystals in order to understand the influence of the DOS on spontaneous emission. Until now only calculations on total DOS are performed but the urge arises for a careful LDOS analysis since the LDOS really probes the position of the light source in a photonic crystal and determines the final radiative decay rate.

In order to investigate the photonic band gap with time-resolved spontaneous emission, several essential conditions should be taken into account. A change in lifetime is only large if the quantum efficiency is high. Dyes adsorbed on semiconductors can have electron transfer which drastically reduces the quantum efficiency as discussed in chapter 2. Continuous wave (cw) total emission experiments are preferably done with low efficiency sources as was done in reference [65]. To observe a time-resolved change in the decay rate, however, an efficient emitter should be created. This can be illustrated with the following argumentation; if γ_{tot}, γ_{rad}, γ_{nonrad} are respectively the total, radiative and non-radiative decay rates, at a certain pump rate P, the population of the excited state is equal to P/γ_{tot}. The emitted power W is then proportional to $W = P(\gamma_{\mathrm{rad}}/\gamma_{\mathrm{tot}})$. In the situation of a low efficiency, e.g., when electron transfer is present, γ_{tot} is nearly independent of the

radiative decay since the non-radiative decay is dominating. A change in the radiative decay will therefore result in a modification of the total emitted power and consequently the measured emission rate. In the situation of high efficiency, however, the emitted power W as measured with cw, is equal to the pump rate P, since $\gamma_{rad}/\gamma_{tot}$ equals unity. The total emitted power will therefore not provide information about the radiative decay rate. To observe a change in the decay rate, i.e., a lifetime change, time-resolved measurements should be done.

A second requirement for investigating time-resolved spontaneous emission is a highly ordered crystal to influence the DOS. Disorder drastically reduces the extreme variations in the DOS and therefore destroys the possibility for observing a lifetime change.

Additionally the surrounding material should not be luminescent from itself since this obstructs the lifetime analysis.

Two other important quantities in lifetime measurements are the homogeneous and inhomogeneous linewidths, resp. Γ_{hom} and Γ_{inhom} (see also chapter 2). A broad Γ_{inhom} (broader than the stop band) and a narrow Γ_{hom} (smaller than the bandwidth of the changes in the DOS) are desirable for photonic experiments [192].

In chapter 5 we have shown cw emission measurements of Rhodamine 6 G (R6G) dye embedded in polystyrene opals and we have demonstrated that these opals are very effective photonic crystals, with relative stop gap widths of $\sim 7\%$. The high structural quality of the polystyrene opals and the high quantum efficiency of the emission source established strongly modified emission spectra and seem to be a well chosen combination for the lifetime measurements as well. The quantum efficiency of R6G dye in ethanol is $> 95\%$ and the linewidths of the R6G dye appear to be $\Gamma_{hom} \sim 4$ nm [68] and $\Gamma_{inhom} \sim 150$ nm [68, 69] respectively, compared to measured stop band widths of ~ 40 nm. Changes in DOS are usually comparable to the width of the stop gap and therefore clearly larger than the Γ_{hom}. The R6G doped polystyrene opals consequently appear to be good candidates for time-resolved fluorescence experiments.

The calculated DOS (denoted as $\rho(\lambda)$) for several polystyrene opals is plotted in figure 6.1.[1] The plot is deduced from figure 1.7; with a known lattice parameter a of a polystyrene opal, the curves obtain a wavelength axis as is displayed in figure 6.1. The $\rho(\lambda)$ is multiplied with an extra factor $1/\lambda$ (ω) resulting from the $H(\vec{r})$ term in Fermi's golden rule to estimate emission rates. Opals with $a = 370$ and 675 nm were chosen since their, respectively, first and second order Bragg diffraction coincides with the emission spectrum of R6G. From the polystyrene opal with the smaller lattice parameter, $a = 370$ nm and represented with black squares, it is clear that there is a broad decrease of $\rho(\lambda)/\lambda$, that starts at $\lambda = 570$

[1] See for a detailed description of the calculation of DOS reference [33].

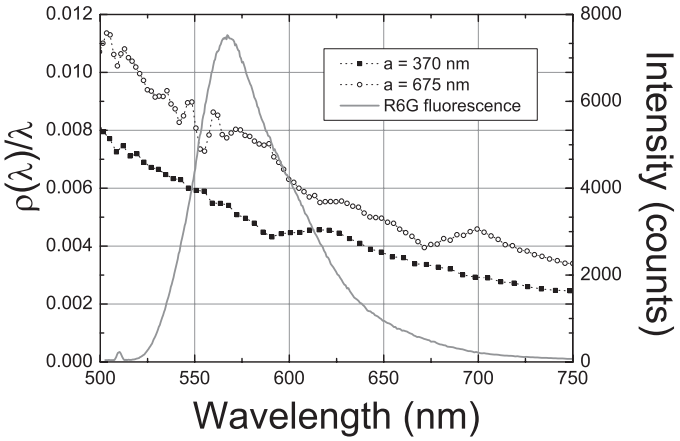

FIGURE 6.1: *Emission spectrum of R6G compared with the DOS ($\rho(\lambda)$) of several polystyrene opals. The $\rho(\lambda)$ is multiplied with a factor 1/λ. The $\rho(\lambda)/\lambda$ of a polystyrene opal with a = 370 nm is displayed with black squares and the $\rho(\lambda)/\lambda$ of a polystyrene opal with a = 675 nm as open circles. The $\rho(\lambda)/\lambda$ of a = 370 nm is multiplied with an extra factor 2.5 for clarity, the lines are plotted as a guide to the eye. The emission spectrum of R6G on polystyrene is plotted as a gray curve. It can be seen that the $\rho(\lambda)/\lambda$ of the opal with a = 370 nm decreases in the red part of the R6G emission. The $\rho(\lambda)/\lambda$ of the opal with a = 675 nm has a decrease right above 550 nm but a larger reduction starts above 590 nm.*

nm and is as wide as 30 to 40 nm. This is the range of the well-known pseudogap of *fcc* crystals [34, 35]. For the opal with the larger sphere size, a = 675 nm and displayed as open circles, the $\rho(\lambda)/\lambda$ shows a sharp and narrow decrease at λ = 555 nm which can be numerical noise since the calculation was done with less data points. At a wavelength of 590 nm, a sharp increase sets in, directly followed by a broader decrease. This wide decrease ranges from 590 to 700 nm and is as large as 20%. This is exactly the wavelength range of second order Bragg diffraction where the band gap is expected for *fcc* crystals [34, 35]. Since the variations in $\rho(\lambda)/\lambda$ coincide well with the emission of R6G, also plotted in figure 6.1, it appears that the combination of R6G dye and these particular polystyrene opals is well chosen to investigate lifetime modifications. Since the changes in the $\rho(\lambda)/\lambda$ are directly proportional to the lifetime at that particular wavelength, they should manifest in our measured lifetimes.

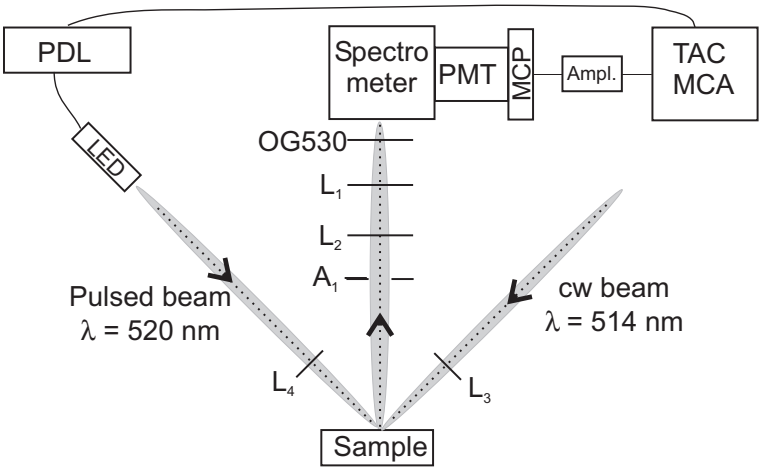

FIGURE 6.2: *Schematic of optical set-up used for lifetime measurements. The pump beam, a pulsed LED (λ = 520 nm), is focussed via L_4 on the (111) surface of the sample. The cw beam is needed for bleaching the surface before performing lifetime measurements. The fluorescence of the excited light is collected in reflection. The photons are detected with a MCP via a PMT which is protected against direct reflected light with a Schott OG530 cut-off filter. The MCP signal is amplified and together with PDL signal fed to a TAC and MCA, which records the time difference between the signal and the excitation pulse.*

6.2 Experimental

The emission lifetimes of the R6G dye in polystyrene opals were obtained using a time-correlated single-photon counting technique [71]. This technique is a statistical method to measure the time profile of a light source after excitation with a light pulse. In this way the time difference is traced between the "start" time, i.e., a moment related with the excitation pulse, and the "stop" time, i.e., the moment the emitted photon arrives at the detector. By recording a collection of these events and plotting it as a histogram the probability of the delay is measured. The set-up used for the time-resolved measurements is displayed in figure 6.2. The dye in the polystyrene opals was excited with a pulsed light emitting diode (LED) from Picoquant run by a picosecond pulsed diode laser driver (PDL), emitting 600 ps duration pulses at 50 ns intervals. The fluorescence was detected over the whole emission spectrum, ranging from 560-645 nm, with a Hamamatsu R3809U Micro Channel Plate (MCP) detector (the "stop") via a spectrometer. The signal from the MCP detector is amplified and fed to a constant fraction discriminator, time to amplitude converter (TAC). The time difference between the MCP signal and the excitation pulse from the PDL ("start") was recorded by the multi channel analyzer

(MCA). The first ns was not taken into account since in this time the pulse of the LED (FWHM ~ 900 ps) is still present. With this set-up a time-resolution of ~ 55 ps is achieved. The fluorescence was recorded in 8192 channels covering a time frame of ~ 22 ns.

To ensure emission from inside the crystal a cw Argon beam, focussed with L_3, is used to bleach the outer surface of the sample. The incident pulsed beam was focussed with lens L_4 to an excitation spot size that is less than 1 mm in diameter. The emitted light is collimated with L_2 and focussed with L_1 on the spectrometer slit where an OG530 filter cuts off the light below 530 nm. Since the fluorescence signal was very low the spectrometer slits were adjusted between 0.6 mm and 1 mm,[2] resulting in a resolving power $\Delta\lambda$ between 5 nm and 10 nm. The events were accumulated for various times, depending on the count rate. For high count rates of more than 10000 counts/s, the events were recorded for 500 s. Low count rates of less than 10000 counts/s, were recorded between 5000 and 50000 s. The beam hits the sample at an angle away from the Bragg angle to ensure penetration into the crystal planes. The emitted photons were collected from the sample in reflection with a detection angle $\alpha = 0°$, corresponding to the normal of the (111) surface. Dark counts in the time-resolved fluorescence data were determined by averaging the counts before $t = 0$ and were subtracted. The data were plotted as histograms with an logarithmic y-axis for convenience. In this way the noise is averaged out and the difference between measured lifetimes, i.e., the slope of the curve, can easily be recognized.

The luminescence of the polystyrene backbone was investigated and found to

[2]For comparison, in experiments with higher power lasers a slit width of 0.1 mm is common.

Sample	a (nm)	Doping (Molar)	N molecules (per 100 nm^2)	Conc. in sample (Molar)
$63-2-b$	180	10^{-5}	~ 5	$0.26 \cdot 10^{-5}$
$63-1-a$	180	10^{-5}	~ 5	$0.26 \cdot 10^{-5}$
$111-1-c$	315	10^{-6}	~ 0.75	$0.26 \cdot 10^{-6}$
$111-1-a$	315	10^{-5}	~ 7.5	$0.26 \cdot 10^{-5}$
$129-22-a$	370	10^{-6}	~ 1	$0.26 \cdot 10^{-6}$
$129-17-a$	370	10^{-5}	~ 10	$0.26 \cdot 10^{-5}$
$241-33-a$	675	10^{-6}	~ 1.5	$0.26 \cdot 10^{-6}$

TABLE 6.1: *Relation between doping concentration, lattice parameter a, amount of adsorbed molecules N per surface area and overall dye concentration per volume in several polystyrene opals. The assumption is made that all dye molecules present in the interstitial holes during the doping are adsorbed.*

be negligible. The count rate of the polystyrene fluorescence was a factor 1000 lower compared to the count rate of the R6G fluorescence. Therefore, we can exclude that the luminescence of polystyrene is contributing to the signal.

Samples were doped with R6G solutions of 10^{-5} Molar (M) or of 10^{-6} M in ethanol. We already demonstrated in chapter 2 that these concentrations are below the Förster limit, since the decay of R6G on polystyrene could not be fitted with a Förster model. In table 6.1 the different dye concentrations are listed, expressed in concentration per surface area and per volume. The number of molecules per surface area and the concentration per volume are calculated for several sphere sizes and dye concentrations. The numbers are estimated by assuming that all dye molecules present in the interstitial holes during doping are adsorbed. Since the ratio between volume and surface is larger for the larger spheres, the general trend is that with increasing sphere size and constant doping concentration the number of molecules per surface area increases. Additionally it is observed that with a constant sphere size the number of molecules increases with increasing doping concentration. From the values listed in table 6.1 it can directly be concluded that the number of molecules per 100 nm^2 never exceeds 10 (for 10^{-5} M) and therefore indeed do not come in the range of the Förster energy transfer for dye molecules ($\sim$ 6 nm) [204] as was also demonstrated in chapter 2.

6.3 Lifetimes of R6G in photonic polystyrene opals

Before performing lifetime measurements on the photonic polystyrene opals their photonic properties were checked with emission spectra measurements. When a clear stop band was present the samples could be used for lifetime measurements since this indicates the photonic quality of the crystal. The lifetime measurements were done at several wavelengths to probe the whole spectrum of R6G. An example of a typical decay curve of R6G in a photonic sample is shown in figure 6.3. The sample is a polystyrene opal with a = 370 nm and doped with 10^{-5} M R6G. The curve could be fitted well with a stretched exponential model that is consistent with a distribution of lifetimes and was applied henceforth to all data. The assumption of a distribution of lifetimes is reasonable because of the different positions of the molecules in the crystal or by the geometrically different possibilities for adsorption on the surface of the spheres. The resulting τ_{mean} was calculated with the fitting parameters of the stretched exponential model via equation (2.8) and resulted in a value of 3.55 $\pm$ 0.02 ns. The χ^2 resulting from this stretched exponential fit was always less than 2, in this particular case even 1.27, indicating the stretched exponential model is appropriate. In figure 6.4 the observed lifetimes for two photonic polystyrene opals with a = 370 nm (exact sphere size r = 131 $\pm$ 2 nm, denoted as 129-samples), are displayed as a function of wavelength. The displayed

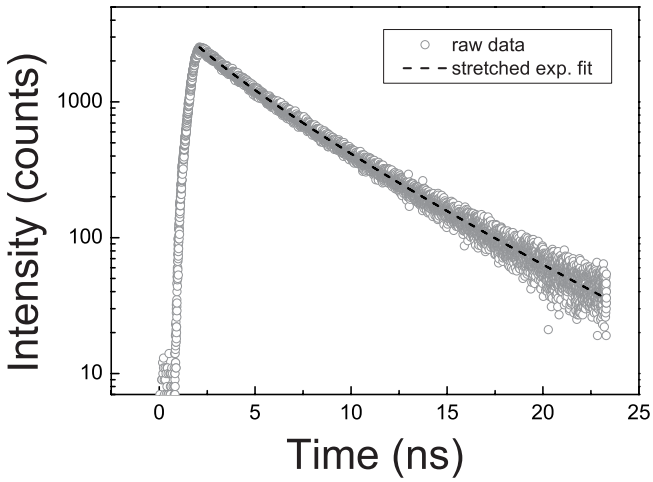

FIGURE 6.3: *An example of a typical decay of R6G in a photonic polystyrene sample (129-17-a) doped with a 10^{-5} M solution. The fluorescence was detected at λ = 580 nm. The decay curve is fitted with a stretched exponential model resulting in a mean lifetime τ_{mean} of 3.55 ± 0.02 ns and a χ^2 of 1.27.*

lifetimes are the τ_{mean} and the error bars resulted from the fit. It can be seen that both photonic samples, doped with various dye concentrations, display different lifetimes. The sample doped with a higher dye concentration displays nearly constant lifetimes around $\tau_{\text{mean}} \sim 3.5$ ns compared to a nearly constant $\tau_{\text{mean}} \sim 3.1$ ns for the sample with the lower concentration. The shorter mean lifetime of 3.15 ns at λ = 560 nm is attributed to reduced vibrational thermalization in the upper excited electronic state, since this emitting wavelength is very close to the excitation wavelength. As a result the estimated error bar is slightly larger.

As a comparison the calculated $1/\rho(\lambda)$ is plotted with an extra factor λ resulting from Fermi's golden rule [29]. The $\lambda/\rho(\lambda)$ is expected to coincide with the trend in the lifetimes as we expect the $\rho(\lambda)$ to influence the decay rate. Initial inspection of figure 6.4 shows that the trend in the $\rho(\lambda)$ does not agree with the measured lifetimes of the photonic samples, especially for low dye concentrations. We will discuss this discrepancy in further detail in section 6.6.

Since the DOS at the second order Bragg diffraction is expected to vary much more, opals with second order Bragg diffraction were also investigated. The sample that was investigated had a lattice parameter of a = 675 nm and was doped with a

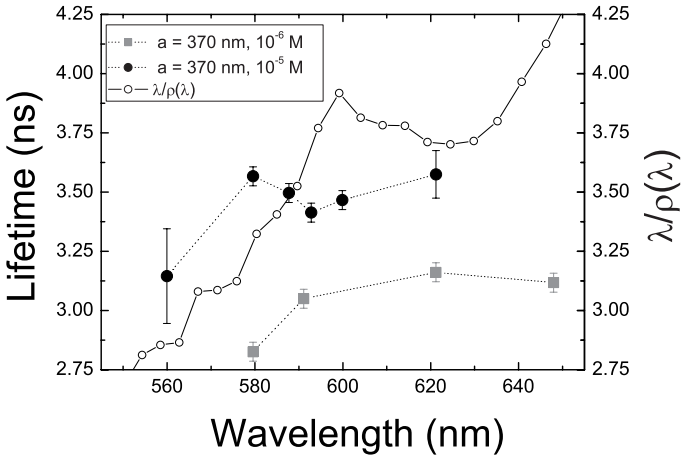

FIGURE 6.4: *Lifetimes of R6G in different photonic samples doped with different dye concentrations. Samples that were measured are 129-22-a (a = 370 nm), squares, doped with a 10^{-6} M R6G solution and 129-17-a (a = 370 nm), triangles, doped with 10^{-5} M R6G solution. Connecting lines are plotted as a guide to the eye. As a comparison $\lambda/\rho(\lambda)$ is plotted divided by a factor $15 \cdot 10^{10}$. It can be seen that the trend in the $\rho(\lambda)$ does not coincide with the observed lifetimes.*

10^{-6} M dye concentration (actual sphere size $r = 238 \pm 2$ nm, denoted as 241-33-a). This sample appears to be strongly photonic as was checked with cw emission and reflectivity measurements (see chapter 5). Second order Bragg diffraction of this sample appears at $\lambda \sim 560$ nm. Decay curves are again fitted with a stretched exponential. The measured lifetimes are plotted in figure 6.5. The mean lifetime of R6G measured from this sample varies between $\tau_{\text{mean}} = 3.9$ and 4.1 ns. It is seen that these lifetimes are systematically longer compared to the first order photonic samples. Furthermore, the data do not agree with the theoretical estimates obtained from the DOS, but display a constant behavior.

This experiment of time-resolved measurements on samples with second order Bragg is the first ever reported in the range of the expected band gap of *fcc* crystals and an important subject for further research.

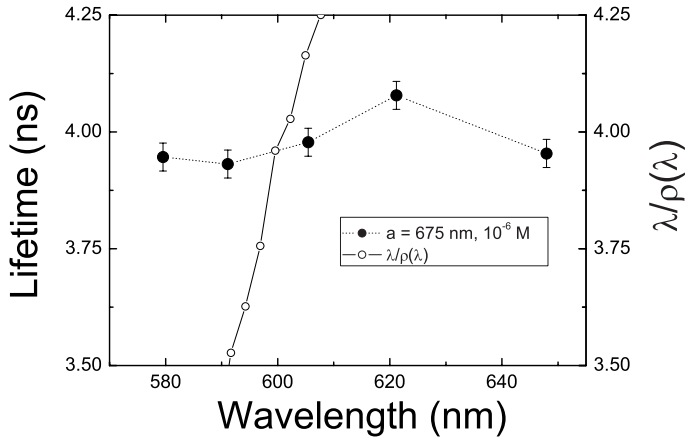

FIGURE 6.5: *Lifetimes of R6G in a photonic sample, 241-33-a (a = 675 nm), with second order Bragg. The sample is doped with a 10^{-6} M R6G solution. The connecting line is plotted as a guide to the eye. As a comparison $\lambda/\rho(\lambda)$ is plotted divided by a factor 4 · 10^{10}. It can be seen that the trend in the $\rho(\lambda)$ does not coincide with the observed lifetimes and it increases much more strongly with increasing wavelength.*

6.4 Lifetimes of R6G in non-photonic polystyrene opals

To analyze the measured lifetimes in the photonic samples in terms of photonic effects, a comparison should be made with carefully chosen "non-photonic" reference samples, i.e., a polystyrene opal with a smaller lattice parameter. These reference samples exhibit the same chemical properties, and the Bragg diffraction appears far into the blue, where the decay of R6G is not affected. The DOS of these reference samples is smooth and resembles the ω^2 dependency of the DOS in vacuum, so no changes in the lifetime as a result of photonic band structures are present.

Four different non-photonic samples were investigated with two different lattice parameters, a = 180 nm (actual sphere size r = 63 ± 1 nm, denoted as 63-samples) and a = 315 nm (actual sphere size r = 111 ± 2 nm, denoted as 111-samples). The samples were doped with either a 10^{-5} M or a 10^{-6} M R6G solution. The first order Bragg appears at $\lambda_{111} \sim 260$ nm and $\lambda_{111} \sim 520$ nm for a = 180 and 315 nm respectively. In figure 6.6 the lifetimes are plotted as a function of wavelength. The plotted lifetimes are the τ_{mean} obtained from fitting the data with a stretched exponential model. The connected lines are guides to the eye. As can be seen in

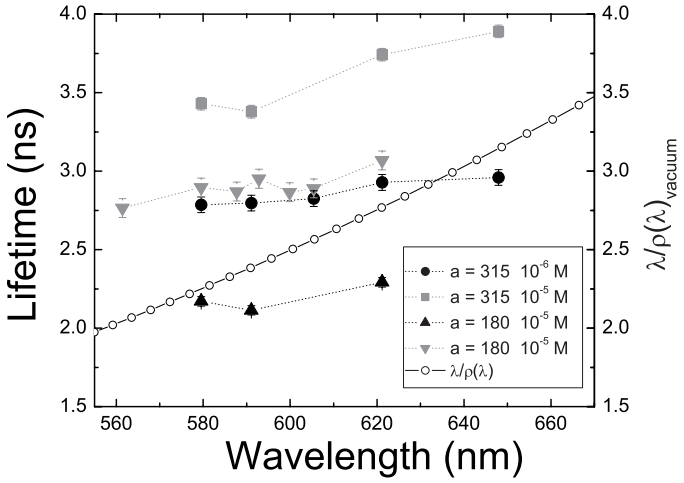

FIGURE 6.6: *Lifetimes of R6G in different reference samples doped with different dye concentrations. Samples that were measured are 111-1-a (a = 315 nm), squares, and 63-1-a (a = 180 nm), down triangles, both doped with 10^{-5} M and 111-1-c (a = 315 nm), circles, and 63-2-b (a = 180 nm), up triangles, both doped with 10^{-6} M. Connecting lines are plotted as a guide to the eye. Error bars are very small, sometimes even smaller than the data points. It appears that samples with a higher dye concentration display a longer τ_{mean}. As a comparison $\lambda/\rho(\lambda)_{\text{vacuum}}$ is plotted, divided by a factor $6.5 \cdot 10^{11}$ to have comparable y-axes. An increase in $\lambda/\rho(\lambda)_{\text{vacuum}}$, i.e., a decrease in $\rho(\lambda)_{\text{vacuum}}$, should result in a lengthening of the lifetime. This trend is not apparent in the lifetime data.*

figure 6.6 the observed lifetimes in the references samples vary between 2.1 and 3.9 ns and are nearly constant for each sphere size during the whole measured wavelength range.

All the measured lifetimes on the polystyrene opals are shorter than the lifetime of R6G in ethanol, which is $\tau_{\text{mean}} \sim 4$ ns. This is expected to be mainly caused by the different refractive indices of polystyrene and ethanol. Although we are not sure if R6G is only on the surface of polystyrene or is also penetrated into the polymer, we assume that R6G feels overall a polystyrene environment. The lifetime of R6G in the higher index polystyrene changes by the ratio $n_{\text{ethanol}}/n_{\text{polystyrene}}$ compared to R6G in ethanol and therefore a lifetime of ~ 3.4 ns is then expected.[3]

The observed trends in figure 6.6 are that higher dye concentrations show longer

[3] $n_{\text{ethanol}} = 1.36$, $n_{\text{polystyrene}} = 1.59$

lifetimes and larger spheres show longer lifetimes. The sample with a = 315 nm and doped with the highest dye concentration of 10^{-5} M exhibits the longest τ_{mean} = 3.4 ns, while the a = 315 nm 10^{-6} M sample has a τ_{mean} of 2.8 ns. The a = 180 nm samples show a shorter τ_{mean} than the a = 315 nm samples, namely between 2.1 ns and 2.9 ns. It is remarkable that the samples with a = 180 nm, that both were doped with a 10^{-5} M dye solution display a different τ_{mean}. One of these samples (63-1-a) was not prepared via the normal procedure but resulted from a dried bottle of suspension. At this moment we are unable to explain if the difference in lifetime is caused by this different preparation method.

Different sphere sizes that were doped with same dye concentrations also display a different τ_{mean}. For instance the a = 180 nm sample and the a = 315 nm that were both doped with a 10^{-5} M R6G solution exhibit respectively a τ_{mean} of 2.1 and 3.4 ns. These large variations in τ_{mean} in reference samples illustrates the difficulty of an absolute comparison between reference and photonic samples.

Last but not least we observed that the surprising trend in τ_{mean} does not resemble $\lambda/\rho(\lambda)_{\text{vacuum}}$, that is plotted as a comparison in figure 6.6. The $\lambda/\rho(\lambda)$ of free space increases with λ^3 and this trend is clearly not apparent in our lifetime data, but will be resolved in the next paragraphs.

6.5 Reabsorption of dye in photonic crystals

Since the lifetime measurements on R6G dye molecules in both photonic and non-photonic environments resulted in a wide variation in τ_{mean}, we take a closer look at differences in τ_{mean} for systematically varied parameters starting with the dye concentration.

The general trend we observe is that in samples with a higher dye concentration, see also table 6.1, a longer τ_{mean} is observed. Two different non-photonic reference samples were measured and they displayed a pronounced difference in τ_{mean}. Both samples had a lattice parameter of a = 315 nm and were doped with either a 10^{-5} M or a 10^{-6} M dye solution. They respectively display a τ_{mean} of $\sim$ 3.6 and $\sim$ 2.9 ns, as can also be seen in figure 6.6.

In the experiment with photonic samples, a = 350 nm, also a variation in τ_{mean} was observed. Two samples with the same sphere size were doped with a different dye concentration, 10^{-5} M and 10^{-6} M. The sample that was doped with the 10^{-5} M dye solution displayed a τ_{mean} of 3.5 ns whereas the sample doped with 10^{-6} M displayed a shorter τ_{mean} of 3.1 ns (see figure 6.4).

The differences observed in τ_{mean} can be explained with reabsorption, similar to the experiments with R6G in ethanol (see figure 2.3), where higher concentrations caused a longer τ_{mean}. In a sample with more dye molecules per volume, the probability for reabsorption is higher since the emitted light meets more dye molecules

during its path to the surface. For reabsorption the dye concentration per volume is important. The concentrations per volume area are listed in figure 6.1. The concentration per volume is the same for samples doped with similar dye concentrations since the interstitials in a *fcc* crystal always consist of $\phi = 26\%$ v/v. With equation (2.4) the absorption length for 10^{-5} M and 10^{-6} M doped polystyrene opals can be calculated. This results in absorption lengths of respectively $l_a \sim 3.7$ and $\sim$ 37 cm. Although the sample thickness L is only between 150 - 300 μm, the light path in a photonic crystal is much longer due to multiple scattering. The pathlength s covered by a photon in a photonic crystal is equal to

$$s = \frac{3 \cdot L^2}{l}, \tag{6.1}$$

where l is the mean free path [192]. A typical mean free path of $l \sim 15$ μm, as found in reference [191], results in path lengths between 0.45 and 1.8 cm. Consequently a photon travels at least for 0.45 to 1.8 cm in the crystal before it exits the sample. This distance is clearly much longer than the sample thickness. For the samples doped with 10^{-5} M, the absorption length l_a is on the same order of this path length, i.e., 3.7 cm, so reabsorption seems likely (see equation (2.4)). For samples doped with 10^{-6} M, l_a is much larger, i.e., 37 cm versus a path length s of ~ 1 cm and reabsorption is not likely to occur. Therefore we explain the longer lifetimes observed for samples doped with 10^{-5} M with reabsorption compared to samples doped with 10^{-6} M, where reabsorption is absent. If the probability for reabsorption can be approximated by s/l_a, samples doped with 10^{-6} M have a probability for reabsorption that is less than 5%. The measured τ_{mean} will, therefore, constitute of 95% of the natural lifetime, since $\tau_{\text{mean}} = \tau_0/(1 - p)$, see equation (2.3). When the samples are doped with 10^{-5} M, however, this probability is increased to almost 50% and the τ_{mean} is strongly increased.

Although multiple scattering is more pronounced in photonic samples than in reference samples, the emitted light in reference samples is also multiply scattered due to polydispersity of the spheres and the displacement from their position in the crystal [33]. The value for the mean free path l used in the calculation of the path length s holds for photonic samples with first order Bragg. Photonic samples with a second order Bragg have shorter mean free paths and the covered path length s will even be longer than ~ 1 cm, and reabsorption is actually more an issue.

We conclude from the observed phenomena that lifetime data in photonic crystals can be very sensitive to reabsorption. This is even more the case since light paths are strongly "folded up" in such materials, most extremely near edges of band gaps. We are the first to consider this reabsorption phenomenon in photonic crystals and we recommend that great care has to be taken concerning the concentration of light sources in a photonic crystal.

6.6 Homogeneous linewidths of dye in photonic crystals

To investigate possible "photonic" effects on the lifetime data taken with the lowest dye concentration, we compare $\lambda/\rho(\lambda)$ as is done in figures 6.4, 6.5 and 6.6. The $\lambda/\rho(\lambda)$ behavior should simulate the lifetime behavior since the decay rate γ_{rad} is determined by the available DOS and therefore the measured lifetime that is equal to $1/(\gamma_{rad} + \gamma_{nr})$ is related to the inverse DOS.

In figure 6.4, where the lifetimes of the photonic samples with a = 370 nm are plotted, it can be seen that τ_{mean} of the sample doped with 10^{-6} M, does not follow the trend of the $\lambda/\rho(\lambda)$. The $\lambda/\rho(\lambda)$ increases strongly whereas the photonic sample displays an almost constant behavior within $\sim$ 0.3 ns.

The τ_{mean} of the photonic sample with a = 675 nm is, together with the $\lambda/\rho(\lambda)$, plotted in figure 6.5. Here the trend in the $\lambda/\rho(\lambda)$ is even more pronounced as can be seen from the sharp increasing behavior. Although the $\lambda/\rho(\lambda)$ is very steep, the measured lifetimes do not coincide with this trend, and show a nearly flat behavior within $\sim$ 0.2 ns.

For non-photonic samples τ_{mean} can be compared with the $\lambda/\rho(\lambda)_{\text{vacuum}}$, as demonstrated in figure 6.6. Although the samples are not photonic and the DOS should exhibit a featureless behavior, a frequency dependence is still expected. The behavior of the DOS in vacuum is cubic with λ and increases from 2 to 3.5 ns in a wavelength range of less than 120 nm. The lifetimes of the non-photonic sample doped with 10^{-6} M, the black circles, however, display a behavior that is practically flat. The lifetimes only fluctuate within 0.17 ns, illustrating no noticeable influence from the DOS.

Additionally we mention that in previous research on photonic colloidal crystals also constant lifetimes were observed [192]. Dye molecules embedded in silica spheres that are arranged in a photonic colloidal *fcc* structure, display a constant lifetime behavior as a function of wavelength.

It is remarkable that in all samples the measured τ_{mean} is almost constant with wavelength. An explanation why this wavelength independent behavior is observed, for photonic as well as non-photonic samples, is the possibly much broader homogeneous linewidth Γ_{hom} of the dye. Initially it was assumed that the homogeneous width was small, $\Gamma_{\text{hom}} \sim 4$ nm, based on results by M. D. Barnes [68] in 1992. The results observed in our research, however, imply that Γ_{hom} is as broad as the emission spectrum. If Γ_{hom} is broad, the dye molecule possesses a large number of vibrational ground levels, mainly caused by interaction with the environment. If a molecule can not emit from the lowest vibrational level of the excited state directly to one of the zero levels of the ground state due to inhibition caused by the photonic DOS, it will emit with a different energy, i.e., a different wavelength, to a different level of the ground state. This can also be illustrated with the Jablonski diagram in

figure 2.4. If transition *a* can not take place since it is inhibited, transition *b* occurs, followed by vibrational relaxation to a lower vibrational level. This vibrational relaxation is very fast, on the order of 10^{-12} sec and will not influence the measured lifetime. Of course this model only holds if the Γ_{hom} is broader than the typical bandwidths of changes in the DOS, that are roughly equal to stop gap widths $\Delta\lambda$. Relative bandwidths of stop gaps in polystyrene opals are observed and calculated to be 6 to 7% ($\sim$ 40 nm). The spectral width $\Delta\lambda/\lambda_0$ of organic dye molecules is usually $\sim$ 10%, as also seen in figure 6.1, and indeed larger than the width of the stop gap. Due to this broad Γ_{hom} a change in lifetime will not be observed.

The homogeneous linewidth of R6G that initially was assumed to be $\Gamma_{\text{hom}} \sim$ 4 nm, was previously determined in experiments [68] with R6G molecules in micrometer sized droplets of glycerol. In these experiments narrow morphology dependent resonances enhanced the emission, probably promoting one particular transition. Of course this physical situation differs from our experiments where the dye is distributed in a photonic polystyrene opal and a lot of vibrational ground state levels are probed due to interaction with the environment.

Recently, Astilean and Barnes reported a lifetime modification of organic dyes in the solid state near a silver mirror [205]. They obtained a very good model for their data by assuming that the homogeneous linewidth is equal to the width of the emission spectra of organic dyes. This supports our proposition.

Compared to organic dyes, an advantage of quantum dots in photonic crystals is that quantum dots do not exhibit broad inhomogeneous and homogeneous linewidths. The broadening of the spectrum is mainly caused by the polydispersity of the quantum dots. Therefore quantum dots are in the future certainly promising candidates for lifetime measurements in photonic structures.

We conclude from our observations in lifetime changes, that the homogeneous linewidth Γ_{hom} of dye molecules on polystyrene is very broad. Therefore it will only be possible to observe lifetime changes of dye molecules in photonic band gap materials if the bandwidths of the DOS changes are broader than the complete emission spectra.

6.7 Radius dependent lifetimes

The lifetimes of R6G were measured from opals with different sphere radii. While on the basis of photonic crystal DOS no radius dependent lifetime change is expected, it appears that R6G molecules adsorbed in opals with smaller sphere radii display a shorter τ_{mean} compared to R6G molecules in opals with larger sphere radii. In figure 6.7 the τ_{mean} of R6G in all samples is plotted as a function of the sphere radius. The lifetime is the average of the lifetimes measured from wavelength range 560 to 650 nm. It can be seen that especially the samples doped with

10^{-6} M, the black circles, display a trend where a decrease in sphere size causes a decrease in lifetime. The difference between the smallest and largest sphere size is even larger than 1 ns. Samples doped with 10^{-5} M display a similar trend. Since the samples doped with 10^{-5} M are very close to the reabsorption regime, more discrepancies are observed in the lifetimes as for instance a longer τ_{mean} for sample r = 111 nm compared to r = 131 nm. The values found for the 10^{-5} M doped samples are, however, upper boundaries. If these same samples are doped with a lower dye concentration the τ_{mean} will even be shorter since the probability for reabsorption is decreased.

A hypothesis is proposed to describe the trend between lifetime and sphere radius in terms of the LDOS of single spheres. We propose that the LDOS at the surface of single spheres is possibly affecting the measured lifetime. In figure 6.7 the curve of the $1/\rho(\lambda, r)$ (= 1/LDOS) is plotted as a function of sphere radius. The LDOS for single silica spheres, was calculated by De Dood *et al.* [206]. The values of LDOS plotted in figure 6.7 are for positions just outside the surfaces and displayed with triangular symbols. The curve, that is plotted as a guide to the eye, demonstrates that a decrease in sphere radius causes an increase in the calculated LDOS. An increase in LDOS will consequently lead to a decrease in τ_{mean}, which is comparable to the trend seen in our opals where a smaller sphere radius causes a shorter lifetime of R6G.

We realize that the comparison with reference [206] is tentative since these calculations are done on isolated spheres and our opals consist of bulk crystals with touching spheres. This will affect the calculated LDOS without any doubt. Nevertheless, we propose that there are remnants of single sphere behavior in many sphere systems, in this case in the LDOS. Earlier, such effects have been seen on widths of stop gaps [190], whose behavior with increasing particle density was found to be determined by single-sphere form factors. A provocative conclusion from our observations is that dyes on the surface of tiny spheres are excellent light sources since the emission rates are considerably increased. [4]

With these results on varying τ_{mean} we are able to estimate the quantum efficiency of the dye in the opals. The fact that large differences are observed in measured lifetimes, directly illustrates that the quantum efficiency must be rather high. As was also demonstrated by Astilean and Barnes, a low quantum efficiency leads to poor control on spontaneous emission [205]. In the case of high quantum efficiency, however, lifetime changes of a factor of 2.5 were observed. In our measurements lifetime changes of a factor of almost 2 are obtained (compare the sample r = 238 nm (10^{-6} M) with sample r = 63 nm (10^{-5} M)). With a simple argument the

[4] Currently new lifetime measurements are being performed on R6G in opals with different sphere radii by I. Nikolaev. While some of these measurements might differ in detail, the main hypothesis that the local density of states is responsible for the observed lifetime changes, remains unaffected.

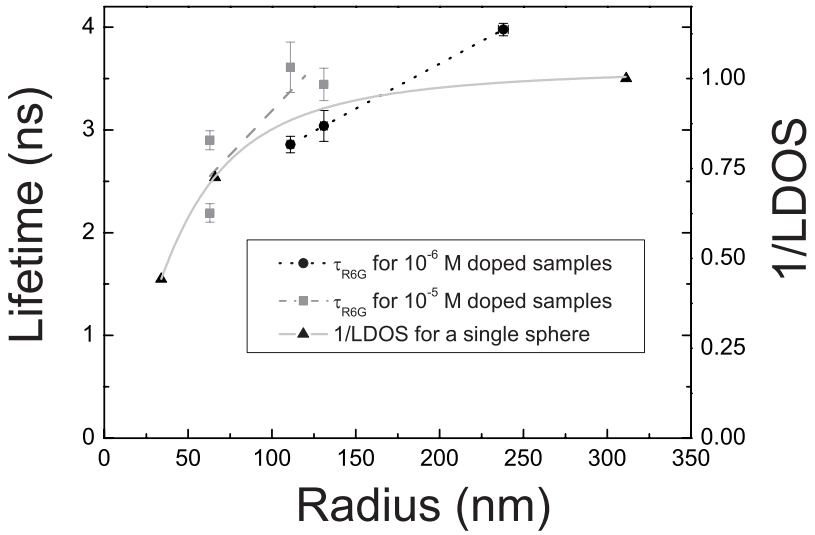

FIGURE 6.7: *The lifetime of R6G in polystyrene opals as a function of the radius of the polystyrene spheres. Data are plotted for 10^{-6} M, black circles, and 10^{-5} M, gray cubes, doped samples. The plotted lifetimes are averaged from λ = 560 to 650 nm. As a comparison 1/LDOS is plotted as calculated for single silica spheres with different sphere radii [206]. A dotted line is plotted as a guide to the eye.*

quantum efficiency of R6G in the polystyrene opals can be estimated. If we assume the non-radiative decay to be constant, the difference in observed lifetime is only caused by a difference in radiative decay rates, since $1/\tau = \gamma_{rad}/(\gamma_{rad}+\gamma_{nr})$. In this way the quantum efficiency is at least 50% if a factor 2 in lifetime change is observed. We can therefore conclude that R6G dye in polystyrene opals are efficient emitters.

6.8 Conclusion

In this chapter we have shown that several effects are very determinative for measurements of lifetime changes. First of all in the future it should be considered whether dye molecules are the right candidates for observing lifetime changes in photonic systems, since their Γ_{hom} is broader than the usual stop band width in opals. For stronger photonic crystals with broader gaps they may be suited.

We are the first to consider that the combination of concentration of dye molecules and multiple scattering of emitted light in photonic crystals, can strongly influence the detected lifetime, caused by reabsorption processes. This will be of utmost importance since many groups try to probe the band gap with dyes in photonic crystals.

By making the comparison between LDOS calculations on single spheres [206] and the trend in lifetime behavior of R6G dye on photonic and non-photonic samples, we are the first to explore single sphere effects in many-sphere systems. These interesting results imply that further research is needed.

References

[1] A. L. B. M. Biemans, A. A. F. Jochems, and A. J. A. M. C. Weyers, *Fudamentele Biologie* (Bohn, Scheltema & Holkema, Utrecht, 1987), pp. 76–116.

[2] J. Tunér and L. Hode, *Laser Therapy: Clinical Practice and Scientific Background* (Prisma Books AB, Grängesberg, Sweden, 2002).

[3] Workshop "Grensverleggende Ideeën voor Fotovoltaïsche Conversie", maart 2002, ECN, Petten.

[4] W. Landman, *Vlinder Encyclopedie* (Rebo International, Lisse, 1999).

[5] G. Sandford, *Tropische Zoetwatervissen* (Van Reemst, Houten, 1999).

[6] MP & C Piednoir, www. aquapress.com.

[7] R. P. Feynman, *The Feynman Lectures on Physics* (Addison-Wesley Pub. Co., Reading, 1970), Vol. 11, p. 35.

[8] W. A. Fischer, *Pigment Handbook Volume I: Properties and Economics* (John Wiley & Sons, New York, 1973), pp. 653–662.

[9] G. Seybold and G. Wagenblast, *New Perylene and Violanthrone Dyestuffs for Fluorescent Collectors*, Dyes Pigm. **11**, 303 (1989).

[10] H. H. Strain, *Spectral Absorption Properties of Ordinary an Fully Deuterated Chlorophylss a and b*, Biochim. Biophys. Acta. **75**, 306 (1963).

[11] C. F. Bohren, *Clouds in a Glass of Beer: Simple Experiments in Atmospheric Physics* (Jon Wiley & Sons, New York, 1987).

[12] H. C. Van de Hulst, *Light Scattering by Small Particles* (Dover Publications, Inc., New York, 1981).

[13] The stones were kindly provided by Dr. Y. Nahmad Molinari, University of San Luis Potosi, Mexico.

[14] P. Vukusic, J. R. Sambles, C. R. Lawrence, and R. J. Wootton, *Limited-view Iridescence in the Butterfly Ancyluris Meliboeus*, Proc. R Soc. Lond. B Biol. Sci. **269**, 7 (2002).

[15] C. H. Greenwalt, W. Brandt, and D. D. Friel, *Irisdescent Colors of Hummingbird Feathers*, J. Opt. Soc. Am. **50**, 1005 (1960).

[16] A. R. Parker, *Light Reflection Strategies*, Am. Sci. **87**, 248 (1999).

[17] P. Vukusic, J. R. Sambles, C. R. Lawrence, and R. J. Wootton, *Now You See It - Now You Don't*, Nature **410**, 36 (2001).

[18] J. V. Sanders and P. J. Darragh, *The Microstructure of Precious Opal*, Mineral. Rec. **2**, 261 (1971).

[19] Intel Press Release, 23 june 2003, Santa Clara, California.

[20] R. W. James, *The Optical Principles of the Diffraction of X-Rays* (Ox Bow Press, Woodbridge, Connecticut, 1962).

[21] E. Yablonovitch, *Inhibited spontaneous emission in solid-state physics and electronics*, Phys. Rev. Lett. **58**, 2059 (1987).

[22] S. John, *Strong localization of photons in certain disordered dielectric superlattices*, Phys. Rev. Lett. **58**, 2486 (1987).

[23] *Photonic Band Gap Materials*, edited by C. M. Soukoulis (Kluwer Academic Press, Dordrecht, 1996).

[24] *Photonic Crystals and Light Localization in the 21st Century*, edited by C. M. Soukoulis (Kluwer Academic Press, Dordrecht, 2001).

[25] W. L. Vos, R. Sprik, A. van Blaaderen, A. Imhof, A. Lagendijk, and G. H. Wegdam, *Strong Effects of Photonic Band Structures on the Diffraction of Colloidal Crystals*, Phys. Rev. B **53**, 16231 (1996).

[26] W. L. Vos, M. Megens, C. M. van Kats, and P. Bösecke, *Transmission and Diffraction by Photonic Colloidal Crystals*, J. Phys.-Condens. Matter **8**, 9503 (1996).

[27] E. M. Purcell, *Spontaneous Emission Probabilities at Radio Frequencies*, Phys. Rev. **69**, 681 (1946).

[28] E. Fermi, *Quantum Theory of Radiation*, Rev. Mod. Phys. **4**, 87 (1932).

[29] R. Loudon, *The Quantum Theory of Light* (Claredon Press, Oxford, 1983).

[30] F. J. P. Schuurmans, *Light in Complex Dielectrics*, Ph.D. thesis, University of Amsterdam, 1999.

[31] R. Sprik, B. A. van Tiggelen, and A. Lagendijk, *Optical Emission in Periodic Dielectrics*, Europhys. Lett. **35**, 265 (1996).

[32] T. Suzuki and P. K. L. Yu, *Emission Power of an Electric Dipole in the Photonic Band Structure of the Fcc Lattice*, J. Opt. Soc. Am. B **12**, 570

(1995).

[33] A. F. Koenderink, *Emission and Transport of Light in Photonic Crystals*, Ph.D. thesis, University of Amsterdam, 2003.

[34] H. S. Sözüer, J. W. Haus, and R. Inguva, *Photonic Bands: Convergence Problems with the Plane-Wave Method*, Phys. Rev. B **45**, 13962 (1992).

[35] K. Busch and S. John, *Photonic Band Gap Formation in Certain Self-Organizing Systems*, Phys. Rev. E **58**, 3896 (1998).

[36] K. H. Drexhage, H. Kuhn, and F. P. Schäfer, *Variation of the Fluorescence Decay Time of a Molecule in Front of a Mirror*, Ber. Bunsenges. Phys. Chem. **72**, 329 (1968).

[37] D. J. Heinzen, J. J. Childs, J. E. Thomas, and M. S. Feld, *Enhanced and Inhibited Visible Spontaneous Emission by Atoms in a Confocal Resonator*, Phys. Rev. Let. **58**, 1320 (1987).

[38] K. J. Vahala, *Optical Microcavities*, Nature **424**, 839 (2003).

[39] W. L. Barnes, *Fluorescence Near Interfaces: the Role of Photonic Mode Density*, J. Mod. Opt. **45**, 661 (1998).

[40] M. Megens, J. E. G. J. Wijnhoven, A. Lagendijk, and W. L. Vos, *Light Sources Inside Photonic Crystals*, J. Opt. Soc. Am. B **16**, 1403 (1999).

[41] B. O'Regan and M. Grätzel, *A Low-cost, High-efficiency Solar Cell based on Dye-sensitized Colloidal TiO_2 Films*, Nature **353**, 737 (1991).

[42] S. Nishimura, N. Abrams, B. A. Lewis, L. I. Halaoui, T. E. Mallouk, K. D. Benkstein, J. van de Lagemaat, and A. J. Frank, *Standing Wave Enhancement of Red Absorbance and Photocurrent in Dye-Sensitized Titanium Dioxide Photoelectrodes Coupled to Photonic Crystals*, J. Am. Chem. Soc. **125**, 6306 (2003).

[43] A. Mills, N. Elliott, I. P. Parkin, S. A. O'Neil, and R. J. Clark, *Novel TiO_2 CVD Films for Semiconductor Photocatalysis*, J. Photochem. Photobiol. A **151**, 171 (2002).

[44] K. Vinodgopal, D. E. Wynkoop, and P. V. Kamat, *Environmental Photochemistry on Semiconductor Surfaces: Photosensitized Degradation of a Textile Azo Dye, Acid Orange 7, on TiO_2 Particles Using Visible Light*, Environ. Sci. Technol. **30**, 1660 (1996).

[45] T. S. Moss, *Optical Properties of Semiconductors* (Butterworth, Oxford, 1959), p. 48.

[46] Private communication from Dr. R. W. Tjerkstra, University of Twente.

[47] J. Pankove, *Optical Processes in Semiconductors* (Dover Publications, Inc., New York, 1971), pp. 412–413.

[48] D. R. Lide, *Handbook of Chemistry and Physics* (CRC Press, Inc., New York, 1997), pp. 12–101.

[49] P. S. J. Russell, *Photonic Crystal Fibers*, Science **299**, 358 (2003).

[50] E. Flück, *Local Interaction of Light with Periodic Photonic Structures*, Ph.D. thesis, University of Twente, 2003.

[51] S. Y. Lin, E. Chow, V. Hietala, P. R. Villeneuve, and J. D. Joannopoulos, *Experimental Demonstration of Guiding and Bending of Electromagnetic Waves in a Photonic Crystal*, Science **282**, 274 (1998).

[52] Y. Fink, D. J. Ripin, S. H. Fan, J. D. Chen, J. D. Joannopoulos, and E. L. Thomas, *Guiding Optical Light in Air using an All-Dielectric Structure*, J. Lightw. Techn. **17**, 2039 (1999).

[53] Y. G. Roh, S. Yoon, S. Kim, H. Jeon, S. H. Han, Q. H. Park, and I. Park, *Photonic Crystal Waveguides with Multiple 90 Degrees Bends*, Appl. Phys. Lett. **83**, 231 (2003).

[54] K. M. Ho, C. T. Chan, C. M. Soukoulis, R. Biswas, and M. Sigalas, *Photonic Band Gaps in Three Dimensions: New Layer-by-Layer Periodic Structures*, Sol. Stat. Comm. **89**, 413 (1994).

[55] D. J. Norris and Y. A. Vlasov, *Chemical approaches to three-dimensional semiconductor photonic crystals*, Adv. Mater. **13**, 371 (2001).

[56] C. F. Blanford, H. Yan, R. Schroden, M. Al-Daous, and A. Stein, *Gems of Chemistry and Physics: Macroporous Metal Oxides with 3D Order*, Adv. Mater. **13**, 401 (2001).

[57] J. E. G. J. Wijnhoven, L. Bechger, and W. L. Vos, *Fabrication and Characterization of Large Macroporous Photonic Crystals in Titania*, Chem. Mater. **13**, 4486 (2001).

[58] J. E. G. J. Wijnhoven and W. L. Vos, *Preparation of Photonic Crystals Made of Air Spheres in Titania*, Science **281**, 802 (1998).

[59] P. W. Anderson, *Absence of Diffusion in Certain Random Lattices*, Phys. Rev. **109**, 1492 (1958).

[60] F. J. P. Schuurmans, D. Vanmaekelbergh, J. van de Lagemaat, and A. Lagendijk, *Strongly Photonic Macroporous GaP Networks*, Science **284**, 141 (1999).

[61] J. Gómez Rivas, *Light in Strongly Scattering Semiconductors: Diffuse Transport and Anderson Localization*, Ph.D. thesis, University of Amsterdam, 2002.

[62] A. Van Blaaderen and A. Vrij, *Synthesis and Characterization of Colloidal Dispersions of Fluorescent, Monodisperse Silica Spheres*, Langmuir **8**, 2921 (1992).

[63] A. Imhof, M. Megens, J. J. Engelberts, D. T. N. de Lang, R. Sprik, and W. L. Vos, *Spectroscopy of Fluorescein (FITC) Dyed Colloidal Silica Spheres*, J. Phys. Chem. B **103**, 1408 (1999).

[64] H. P. Schriemer, H. M. van Driel, A. F. Koenderink, and W. L. Vos, *Modified Spontaneous Emission Spectra of Laser Dye in Inverse Opal Photonic Crystals*, Phys. Rev. A **63**, 011801 (2000).

[65] A. F. Koenderink, L. Bechger, H. P. Schriemer, A. Lagendijk, and W. L. Vos, *Broadband Fivefold Reduction of Vacuum Fluctuations Probed by Dyes in Photonic Crystals*, Phys. Rev. Lett. **88**, 143903 (2002).

[66] W. T. Silfvast, *Laser Fundamentals* (Cambridge University Press, New York, 1996), chapter 2.

[67] R. F. Kubin and A. N. Fletcher, *Fluorescence Quantum Yields of Some Rhodamine Dyes*, J. Lumin. **27**, 455 (1982).

[68] M. D. Barnes, W. B. Whitten, S. Arnold, and J. M. Ramsey, *Homogeneous Linewidths of Rhodamine 6G at Room Temperature from Cavity-Enhanced Spontaneous Emission Rates*, J. Chem. Phys. **97**, 7842 (1992).

[69] P. C. Becker, H. L. Fragnito, J. Y. Bigot, C. H. Brito Cruz, R. L. Fork, and C. V. Shank, *Femtosecond Photon Echoes from Molecules in Solution*, Phys. Rev. Lett. **63**, 505 (1989).

[70] K. H. Drexhage, *Fluorescence Efficiency of Laser Dyes*, J. Res. NBS. **80(A)**, 421 (1976).

[71] D. Bebelaar, *Time Response of Various Types of Photomultipliers and its Wavelength Dependence in Time-Correlated Single-Photon Counting with an Ultimate Resolution of 47 ps*, Rev. Sci. Instrum. **57**, 1116 (1986).

[72] E. Kreyszig, *Introductory Mathematical Statistics* (John Wiley & Sons, Singapore, 1970), pp. 248–254.

[73] P. R. Hammond, *Self-absorption of Molecular Fluorescence, the Design of Equipment for Measurement of Fluorescence Decay, and the Decay Times of Some Laser Dyes*, J. Chem. Phys. **70**, 3884 (1975).

[74] K. A. Selanger, J. Falnes, and T. Sikkeland, *Fluorescence Lifetime Studies of Rhodamine 6G in Methanol*, J. Phys. Chem. **81**, 1960 (1977).

[75] U. Brakman, *Lambdachrome Laser Dyes* (Lambda Physik GmbH, Göttingen, 1994), pp. 150–153.

[76] J. R. Lakowicz, *Principle of Fluorescence Spectroscopy* (Kluwer Academic & Plenum Publishers, New York, Boston, Dordrecht, London, Moscow, 1999).

[77] A. Hagfeldt and M. Grätzel, *Molecular Photovoltaics*, Acc. Chem. Res. **33**, 269 (2000).

[78] P. V. Kamat, *Photochemistry on Nonreactive and Reactive (Semiconductor) Surfaces*, Chem. Rev. **93**, 267 (1993).

[79] T. Wu, G. Liu, J. Zhao, H. Hidaka, and N. Serpone, *Photo-assisted Degradation of Dye Pollutants: Self-photosensitized Oxidative Transformation of Rhodamine B under Visible Light Irradiation in Aqueous TiO_2 Dispersions*, J. Phys. Chem. B **102**, 5845 (1998).

[80] A. C. van Dyk and A. M. Heyns, *Dispersion Stability and Photo-activity of Rutile (TiO_2) powders*, J. Colloid Interface Sci. **206**, 381 (1998).

[81] L. Ziolkowski, K. Vinodgopal, and P. V. Kamat, *Photostabilization of Organic Dyes on Poly(styrenesulfonate)-Capped TiO_2 Nanoparticles*, Langmuir **13**, 3124 (1997).

[82] J. D. Bolt, *Titanium Dioxide Particles Having Substantially Discrete Inorganic Particles Dispersed On Their Surfaces*, U.S. patent **5886069**, (1999).

[83] J. N. Ryan, M. Elimelech, J. L. Baeseman, and R. D. Magelky, *Silica-coated Titania and Zirconia Colloids for Subsurface Transport Field Experiments*, Environ. Sci. Technol. **34**, 2000 (2000).

[84] L. M. Liz-Marzán, M. Giersig, and P. Mulvaney, *Synthesis of Nanosized Gold-Silica Core-Shell Particles*, Langmuir **12**, 4329 (1996).

[85] Q. Liu, Z. Xu, J. A. Finch, and R. Egerton, *A Novel Two-step Silica coating Process fro Engineering Magnetic Nanocomposites*, Chem. Mater. **10**, 3936 (1998).

[86] D. L. J. Vossen, M. J. A. de Dood, T. van Dillen, T. Zijlstra, E. van der Drift, A. Polman, and A. van Blaaderen, *Novel Method for Solution Growth of Thin Silica Films from Tetraethoxysilane*, Adv. Mater. **12**, 1434 (2000).

[87] K. Osseo-Asare and F. J. Arriagada, *Preparation of SiO_2 Nanoparticles in a Nonionic Reverse Micellar System*, J. Colloid Interface Sci. **50**, 321 (1990).

[88] A. Kay and M. Grätzel, *Photosensitization if TiO_2 Solar-cells with Chlorophyll Derivatives and Related Natural Porphyrins*, J. Phys. Chem. **97**, 6272 (1993).

[89] K. M. S. Khalil and M. Zaki, *Synthesis of High Surface Area Titania Powders via Basic Hydrolysis of Titanium(IV)Isopropoxide*, Powder Technol. **92**, 233 (1997).

[90] H. Tada, M. Akazawa, Y. Kubo, and S. Ito, *Enhancing Effect of SiO_x Monolayer Coverage of TiO_2 on the Photoinduced Oxidation of Rhodamine 6G in Aqueous Media*, J. Phys. Chem. B **102**, 6360 (1998).

[91] W. Stöber, A. Fink, and E. J. Bohn, *Controlled Growth of Monodisperse Silica Spheres in the Micron Size Range*, Colloid Interface Sci. **26**, 62 (1968).

[92] L. Bechger, A. F. Koenderink, and W. L. Vos, *Emission Spectra and Life-*

times of R6G Dye on Silica-Coated Titania Powder, Langmuir **18**, 2444 (2002).

[93] R. J. Hunter, *Zeta Potential in Colloid Science* (Academic Press, New York, 1981).

[94] K. Hashimoto, M. Hiramoto, and T. Sakata, *Photo-Induced Electron Transfer from Adsorbed Rhodamine B to Oxide Semiconductors Substrates in Vacuo: Semiconductor Dependence*, Chem. Phys. Lett. **148**, 215 (1988).

[95] J. E. Moser, M. Wolf, F. Lenzmann, and M. Grätzel, *Photo-Induced Charge Injection from Vibronically Hot Excited Molecules of a Dye Sensitizer into Acceptor States of Wide-Bandgap Oxide Semiconductors*, Zeitschr. Phys. Chem. **212**, 85 (1999).

[96] T. Förster, *Zwischenmolekulare Energiewanderung und Fluoreszenz*, Ann. Phys. **6**, 55 (1948).

[97] T. Förster, in *Comparative Effects of Radiation*, edited by M. Burton, J. S. Kirby-Smith, and J. L. Magee (Wiley, New York, 1960), pp. 300–341.

[98] T. Förster, in *Modern Quantum Chemistry*, edited by O. Sinanoglu (Academic Press, New York, 1965), pp. 93–137, part III, Action of Light and Organic Crystals.

[99] M. Tomita, K. Totsuka, and H. Ikari, *Resonance Energy Transfer in Dye Molecules Adsorbed Two Dimensionally upon Aqeous Suspensions of Polystyrene Spheres*, J. Opt. Soc. Am. B **16**, 1951 (1999).

[100] J. P. S. Farinha, M. T. Charreyre, J. M. G. Martinho, M. A. Winnik, and C. Pichot, *Picosecond Fluorescence Studies of the Surface Morphology of Charged Polystyrene Latex Particles*, Langmuir **17**, 2617 (2001).

[101] K. C. B. Lee, J. Siegel, S. E. D. Webb, S. Leveque-Fort, M. J. Cole, R. Jones, K. Dowling, M. J. Lever, and M. W. French, *Application of the Stretched Exponential Function to Fluorescence Lifetime Imaging*, Biophys. J. **81**, 1265 (2001).

[102] Private communication from Dr. C. M. Wubs, University of Twente.

[103] J. Laherrere and D. Sornette, *Stretched Exponential Distributions in Nature and Economy: "Fat Tails" with Characteristic Scales*, Eur. Phys. J. B **2**, 525 (1998).

[104] L. Deschenes and D. A. Vanden Bout, *Single-Molecule Studies of Heterogeneous Dynamics in Polymer Melts Near the Glass Transition*, Science **292**, 255 (2001).

[105] G. Schlegel, J. Bohnenberger, I. Potapova, and A. Mews, *Fluorescence Decay Time of Single Semiconductor Nanocrystals*, Phys. Rev. Lett. **88**, 137401 (2002).

[106] M. E. Davis, *Ordered Porous Materials for Emerging Applications*, Nature **417**, 813 (2002).

[107] A. Corma, *From Microporous to Mesoporous Molecular Sieve Materials and their Use in Catalysis*, Chem. Rev. **97**, 2373 (1997).

[108] S. A. Davis, S. L. Burkett, N. H. Mendelson, and S. Mann, *Bacterial Templating of Ordered Macrostructures in Silica and Silica-surfactant Mesophases*, Nature **385**, 420 (1997).

[109] A. Imhof and D. J. Pine, *Ordered Macroporous Materials by Emulsion Templating*, Nature **389**, 948 (1997).

[110] S. A. Jenekhe and X. L. Chen, *Self-Assembly of Ordered Macroporous Materials from Rod-Coil Block Copolymers*, Science **283**, 372 (1999).

[111] O. D. Velev, T. A. Jede, R. F. Lobo, and R. F. Lenhoff, *Porous Silica via Colloidal Crystallization*, Nature **389**, 447 (1997).

[112] A. A. Zakhidov, R. H. Baughman, Z. Iqbal, C. X. Cui, I. Khayrullin, S. O. Dantas, I. Marti, and V. G. Ralchenko, *Carbon structures with three-dimensional periodicity at optical wavelengths*, Science **282**, 897 (1998).

[113] J. S. Yin and Z. L. Wang, *Template-assisted Self-assembly and Cobalt Doping of Ordered Mesoporous Titania Nanostructures*, Adv. Mater. **11**, 469 (1999).

[114] Y. A. Vlasov, N. Yao, and D. J. Norris, *Synthesis of Photonic Crystals for Optical Wavelengths from Semiconductor Quantum Dots*, Adv. Mater. **11**, 165 (1999).

[115] B. T. Holland, C. F. Blanford, T. Do, and A. Stein, *Synthesis of Highly Ordered, Three-Dimensional, Macroporous Structures of Amorphous or Crystalline Inorganic Oxides, Phosphates, and Hybrid Composites*, Chem. Mater. **11**, 795 (1999).

[116] Y. Xia, B. Gates, Y. Yin, and Y. Lu, *Monodispersed Colloidal Spheres: Old Materials with New Applications*, Adv. Mater. **12**, 693 (2000).

[117] Z. Y. Li and Z. Q. Zhang, *Fragility of Photonic Band Gaps in Inverse-Opal Photonic Crystals*, Phys. Rev. B **62**, 1516 (2000).

[118] W. L. Vos, M. Megens, C. M. van Kats, and P. Bösecke, *X-Ray Diffraction of Photonic Colloidal Single Crystals*, Langmuir **13**, 6004 (1997).

[119] M. Megens, C. M. van Kats, P. Bösecke, and W. L. Vos, *Synchrotron Small-Angle X-ray Scattering of Colloids and Photonic Colloidal Crystals*, J. Appl. Crystallogr. **30**, 637 (1997).

[120] P. V. Braun and P. Wiltzius, *Macroporous Materials-Electrochemically Grown Photonic Crystals*, Curr. Op. Coll. Interf. Sc. **7**, 116 (2002).

[121] O. D. Velev and E. W. Kaler, *Structured Porous Materials via Colloidal*

Crystal Templating: From Inorganic Oxides to Metals, Adv. Mater. **12**, 531 (2000).

[122] H. Míguez, F. Meseguer, C. López, M. Holgado, G. Andreasen, A. Mifsud, and V. Fornes, *Germanium FCC Structure from a Colloidal Crystal Template*, Langmuir **16**, 4405 (2000).

[123] H. Míguez, E. Chomski, F. Garca-Santamara, M. Ibisate, S. John, C. Lpez, F. Meseguer, J. P. Mondia, G. A. Ozin, O. Toader, and H. M. van Driel, *Photonic Bandgap Engineering in Germanium Inverse Opals by Chemical Vapor Deposition*, Adv. Mater. **13**, 1634 (2001).

[124] A. Blanco, E. Chomski, S. Grabtchak, M. Ibisate, S. John, L. S. W., C. Lopez, F. Meseguer, H. Míguez, J. P. Mondia, G. A. Ozin, O. Toader, and H. M. van Driel, *Large-Scale Synthesis of a Silicon Photonic Crystal with a Complete Three-Dimensional Bandgap near 1.5 Micrometres*, Nature **405**, 437 (2000).

[125] Y. A. Vlasov, X. Z. Bo, J. C. Sturm, and D. J. Norris, *On-chip Natural Assembly of Silicon Photonic Bandgap Crystals*, Nature **414**, 289 (2001).

[126] B. H. Juárez, S. Rubio, J. Sánchez-Dehesa, and C. López, *Antimony Trisulfide Inverted opals: Growth, Characterization, and Photonic Properties*, Adv. Mater. **14**, 1486 (2002).

[127] J. S. Farthing, W. E. Buhro, L. Bechger, W. Vos, and J. E. G. J. Wijnhoven, *Air-sphere Crystals Composed of Gallium Arsenide and Gallium Phosphide*, Abstr. Am. Chem. Soc. **221**, 388 (2001).

[128] M. Müller, R. Zentel, T. Maka, S. G. Romanov, and C. M. S. Torres, *Photonic Crystal Films with High Refractive Index Contrast*, Adv. Mater. **12**, 1499 (2000).

[129] J. E. G. J. Wijnhoven, S. J. M. Zevenhuizen, M. A. Hendriks, D. Vanmaekelbergh, J. J. Kelly, and W. L. Vos, *Electrochemical Assembly of Ordered Macropores in Gold*, Adv. Mater. **12**, 888 (2000).

[130] L. K. Van Vught, A. F. Van Driel, R. W. Tjerkstra, L. Bechger, W. L. Vos, D. Vanmaekelbergh, and J. J. Kelly, *Macroporous Germanium by Electrochemical Deposition*, Chem. Comm. , 2054 (2002).

[131] T. Sumida, Y. Wada, T. Kitamura, and S. Yanagida, *Construction of Stacked Opaline Films and Electrochemical Deposition of Ordered Macroporous Nickel*, Langmuir **18**, 3886 (2002).

[132] Y. C. Lee, T. J. Kuo, C. J. Hsu, Y. W. Su, and C. C. Chen, *Fabrication of 3D Macroporous Structures of II-VI and III-V Semiconductors using Electrochemical Deposition*, Langmuir **18**, 9942 (2002).

[133] Private communication from Prof. Dr. D. Vanmaekelbergh and Prof. Dr. J. J.

Kelly, Utrecht University.

[134] O. D. Velev, P. M. Tessier, A. M. Lenhoff, and E. W. Kaler, *A Class of Porous Metallic Nanostructures*, Nature **401**, 548 (1999).

[135] P. M. Tessier, O. D. Velev, A. T. Kalambur, J. F. Rabolt, A. M. Lenhoff, and E. W. Kaler, *Assembly of Gold Nanostrucutred Films Templated by Colloidal Crystals and Use in Surface-Enhanced Raman Spectroscopy*, J. Am. Chem. Soc. **122**, 9554 (2000).

[136] K. M. Kulinowski, P. Jiang, H. Vaswani, and V. L. Colvin, *Porous Metals from Colloidal Templates*, Adv. Mater. **12**, 833 (2000).

[137] Q. B. Meng, Z. Z. Gu, O. Sato, and A. Fujishima, *Fabrication of Highly Ordered Porous Structures*, Appl. Phys. Lett. **77**, 4313 (2000).

[138] G. Subramania, V. N. Manoharan, J. D. Thorne, and D. J. Pine, *Ordered Macroporous Materials by Colloidal Assembly: A Possible Route to Photonic Bandgap Materials*, Adv. Mater. **11**, 1261 (1999).

[139] B. T. Holland, C. F. Blanford, and A. Stein, *Synthesis of Macroporous Minerals with Highly Ordered Three-Dimensional Arrays of Spheroidal Voids*, Science **281**, 538 (1998).

[140] B. T. Holland, L. Abrams, and A. Stein, *Dual Templating of Macroporous Silicates with Zeolitic Microporous Frameworks*, J. Am. Chem. Soc. **121**, 4308 (1999).

[141] P. Yang, T. Deng, D. Zhao, P. Feng, D. Pine, B. F. Chmelka, G. M. Whitesides, and G. D. Stucky, *Hierarchically Ordered Oxides*, Science **282**, 2244 (1998).

[142] S. Vaudreuil, M. Bousmina, S. Kaliaguine, and L. Bonneviot, *Preparation of Macrostructured Metal Oxides by Sedimentation-Aggregation*, Micropor. Mesopor. Mater. **44-45**, 249 (2001).

[143] R. Hunter, *Foundations of colloid science Vol. I* (Oxford University Press, Oxford, 1993).

[144] C. Larpent and T. F. Tadros, *Preparation of Microlatex Dispersions using Oil-In-Water Microemulsions*, Coll. Pol. Sci. **269**, 1171 (1991).

[145] V. K. LaMer and R. H. Dinegar, *Theory, Production, and Mechanism of Formation of Monodispersed Hydrosols*, J. Am. Chem. Soc. **72**, 4847 (1950).

[146] C. J. Brinker and G. W. Scherer, *Sol-Gel Science: The Physics and Chemistry of Sol-Gel Processing* (Academic Press, San Diego, 1990).

[147] G. H. Bogush, M. A. Tracy, and C. F. Zukoski, *Preparation of Monodisperse Silica Particles: Control of Size and Mass Fraction*, J. Non-Cryst. Sol. **104**, 95 (1988).

[148] P. Jiang, J. F. Bertone, K. S. Hwang, and V. L. Colvin, *Single-Crystal Col-*

loidal Multilayers of Controlled Thickness, Chem. Mater. **11**, 2132 (1999).

[149] P. N. Pusey, *The Effect of Polydispersity on the Crystallization of Hard Spherical Colloids*, J. de Phys. (Paris) **48**, 709 (1987).

[150] S. H. Park and Y. Xia, *Assembly of Mesoscale Particles over Large Areas and Its Application in Fabricating Tunable Optical Filters*, Langmuir **15**, 266 (1999).

[151] K. Velez, J. F. Quinson, and B. Fenet, *Modification Study of Aluminum Sec-butoxide by Acrylic Acid*, J. Sol-Gel Sci. Techn. **16**, 201 (1999).

[152] S. Vaudreuil, M. Bousmina, S. Kaliaguine, and L. Bonneviot, *Synthesis of Macrostructured Silica by Sedimentation-Aggregation*, Adv. Mater. **13**, 1310 (2001).

[153] N. K. Raman, M. T. Anderson, and C. J. Brinker, *Template-Based Approaches to the Preparation of Amorphous, Nanoporous Silicas*, Chem. Mater. **8**, 1682 (1996).

[154] O. D. Velev, T. A. Jede, R. F. Lobo, and R. F. Lenhoff, *Microstructured Porous Silica Obtained via Colloidal Crystal Templates*, Chem. Mater. **10**, 3597 (1998).

[155] M. L. Huggins, *The Crystal Structure of Anatase and Rutile, the tetragonal forms of TiO_2*, Phys. Rev. **27**, 638 (1926).

[156] B. E. Warren, *X-Ray diffraction* (Dover Publications, New York, 1990), pp. 251–254.

[157] G. Katz, *X-ray Diffraction Powder Pattern of Metastable Cubic ZrO_2*, J. Am. Ceram. Soc. **54**, 531 (1971).

[158] R. Zakharchenya, T. Vasilevskaya, and J. Russ, *Effect of Temperature on the Phase Composition and Properties of the Products of Hydrolysis of Alumina Alkoxides*, Russ. J. Appl. Chem. **65**, 2249 (1993).

[159] C. H. Shek, J. K. L. Lai, T. S. Gu, and G. M. Lin, *Transformation Evolution and Infrared Absorption Spectra of Amorphous and Crystalline Nano-Al_2O_3 Powders*, Nanostr. Mater. **8**, 605 (1997).

[160] M. Kumagai and G. L. J. Messing, *Controlled Transformation and Sintering of a Boehmite Sol-Gel by α-Alumina Seeding*, J. Am. Ceram. Soc. **68**, 500 (1985).

[161] H. Yan, C. F. Blanford, B. T. Holland, W. H. Smyrl, and A. Stein, *General Synthesis of Periodic Macroporous Solids by Templated Salt Precipitation and Chemical Conversion*, Chem. Mater. **12**, 1134 (2000).

[162] Q. F. Zhou, S. H. Wu, Q. Q. Zhang, Z. J. X., J. Chen, and W. H. Zhang, *Structure and Raman Spectroscopy of Nanocrystalline TiO_2 Powder Derived by Sol-Gel Process*, Chin. Phys. Lett. **14**, 306 (1997).

[163] G. Colón, M. A. Avilés, J. A. Navío, and P. J. Sánchez-Soto, *Thermal Behaviour of a TiO_2-ZrO_2 Microcomposite Prepared by Chemical Coating*, J. Therm. Anal. Cal. **67**, 229 (2002).

[164] Y. A. Vlasov, A. V. Astratov, V. N. Baryshev, A. A. Kaplyanskii, O. Z. Karimov, and M. F. Limonov, *Manifestation of Intrinsic Defects in Optical Properties of Self-Organized Opal Photonic Crystals*, Phys. Rev. E **61**, 5784 (2000).

[165] G. Subramania, K. Constant, R. Biswas, M. M. Sigalas, and K. M. Ho, *Optical Photonic Crystals Fabricated from Colloidal Systems*, Appl. Phys. Lett. **74**, 3933 (1999).

[166] A. Richel, N. P. Johnson, and D. W. McComb, *Observation of Bragg Reflection in Photonic Crystals Synthesized from Air Spheres in a Titania Matrix*, Appl. Phys. Lett. **76**, 1816 (2000).

[167] H. M. van Driel and W. L. Vos, *Multiple Bragg Wave Coupling in Photonic Band-Gap Crystals*, Phys. Rev. B **62**, 9872 (2000).

[168] W. L. Vos and H. M. van Driel, *Higher Order Bragg Diffraction by Strongly Photonic Fcc Crystals: Onset of a Photonic Bandgap*, Phys. Lett. A **272**, 101 (2000).

[169] M. S. Thijssen, R. Sprik, J. E. G. J. Wijnhoven, M. Megens, T. Narayanan, A. Lagendijk, and W. L. Vos, *Inhibited Light Propagation and Broadband Reflection in Photonic Air-Sphere Crystals*, Phys. Rev. Lett. **83**, 2730 (1999).

[170] J. Galisteo Lòpez and W. L. Vos, *Angle Resolved Reflectivity of Single-Domain Photonic Crystals, Effects of Disorder*, Phys. Rev. E **66**, 036616 (2002).

[171] G. Subramania, R. Biswas, K. Constant, M. M. Sigalas, and K. M. Ho, *Structural characterization of thin film photonic crystals*, Phys. Rev. B **63**, 235111 (2001).

[172] R. C. Schroden, M. Al-Daous, C. F. Blanford, and A. Stein, *Optical properties of inverse opal photonic crystals*, Chem. Mater. **14**, 3305 (2002).

[173] G. R. Fowles, *Introduction to Modern Optics* (Dover Publications, New York, 1968).

[174] Private communication from Prof. Dr. W. L. Vos, University of Twente.

[175] J. F. Bertone, P. Jiang, K. S. Hwang, D. M. Mittleman, and V. L. Colvin, *Thickness Dependence of the Optical Properties of Ordered Silica-Air and Air-Polymer Photonic Crystals*, Phys. Rev. Lett. **83**, 300 (1999).

[176] R. J. Spry and D. J. Kosan, *Theoretical Analysis of the Crystalline Colloidal Array Filter*, Appl. Spectrocopy **40**, 782 (1986).

[177] P. Jiang, J. F. Bertone, and V. L. Colvin, *A Lost-wax Approach to Monodis-*

perse Colloids and Their Crystals, Science **291**, 453 (2001).

[178] R. Rengarajan, P. Jiang, P. Colvin, and D. Mittleman, *Optical Properties of a Photonic Crystal of Hollow Spherical Shells*, Appl. Phys. Lett. **77**, 3522 (2000).

[179] Z. Z. Gu, S. Kubo, W. Qian, Y. Einaga, D. Tryk, A. Fujishima, and O. Sato, *Varying the Optical Stop Band of a Three-Dimensional Photonic Crystal by Refractive Index Control*, Langmuir **17**, 6751 (2001).

[180] W. T. Dong, H. J. Bongard, and F. Marlow, *New Type of Inverse Opals: Titania with Skeleton Structure*, Chem. Mater. **15**, 568 (2003).

[181] S. J. B. Reed, *Electron Microprobe Analysis* (Cambridge University Press, New York, 1975), p. 228.

[182] V. N. Bogomolov, S. V. Gaponenko, I. N. Germanenko, A. M. Kapitonov, E. P. Petrov, N. V. Gaponenko, A. V. Prokofiev, A. N. Ponyavina, N. I. Silvanovich, and S. M. Samoilovich, *Photonic Band Gap Phenomenon and Optical Properties of Artificial Opals*, Phys. Rev. A **55**, 7619 (1997).

[183] S. G. Romanov, T. Maka, C. M. S. Torres, M. Muller, and R. Zentel, *Photonic Band-Gap Effects Upon the Light Emission from a Dye-Polymer-Opal Composite*, Appl. Phys. Lett. **75**, 1057 (1999).

[184] S. V. Gaponenko, V. N. Bogomolov, E. P. Petrov, A. M. Kapitonov, A. A. Eychmueller, A. L. Rogach, I. I. Kalosha, F. Gindele, and U. Woggon, *Spontaneous Emission of Organic Molecules and Semiconductor Nanocrystals in a Photonic Crystal*, J. Lumines. **87-89**, 152 (2000).

[185] S. V. Gaponenko, V. N. Bogomolov, E. P. Petrov, A. M. Kapitonov, D. A. Yarotsky, I. I. Kalosha, A. A. Eychmueller, A. L. Rogach, J. McGilp, U. Woggon, and F. Gindele, *Spontaneous Emission of Dye Molecules, Semiconductor Nanocrystals, and Rare-Earth Ions in Opal-Based Photonic Crystals*, J. Lightwave Technol. **17**, 2128 (1999).

[186] E. P. Petrov, V. N. Bogomolov, I. I. Kalosha, and S. V. Gaponenko, *Modification of the Spontaneous Emission of Dye Molecules in Photonic Crystals*, Acta Phys. Pol. A **94**, 761 (1998).

[187] E. P. Petrov, V. N. Bogomolov, I. I. Kalosha, and S. V. Gaponenko, *Spontaneous Emission of Organic Molecules Embedded in a Photonic Crystal*, Phys. Rev. Lett. **81**, 77 (1998).

[188] T. Yamasaki and T. Tsutsui, *Spontaneous Emission from Fluorescent Molecules Embedded in Photonic Crystals Consisting of Polystyrene Microspheres*, Appl. Phys. Lett. **72**, 1957 (1998).

[189] K. Yoshino, S. B. Lee, S. Tatsuhara, Y. Kawagishi, M. Ozaki, and A. A. Zakhidov, *Observation of Inhibited Spontaneous Emission and Stimulated*

Emission of Rhodamine 6G in Polymer Replica of Synthetic Opal, Appl. Phys. Lett. **73**, 3506 (1998).

[190] W. L. Vos, H. M. van Driel, M. Megens, A. F. Koenderink, and A. Imhof, in *Photonic Crystals and Light Localization in the 21st Century*, edited by C. M. Soukoulis (Kluwer, Dordrecht, 2001), pages 191-218.

[191] A. F. Koenderink, M. Megens, G. van Soest, W. L. Vos, and A. Lagendijk, *Enhanced Backscattering from Photonic Crystals*, Phys. Lett. A **268**, 104 (2000).

[192] M. Megens, J. E. G. J. Wijnhoven, A. Lagendijk, and W. L. Vos, *Fluorescence Lifetimes and Linewidths of Dye in Photonic Crystals*, Phys. Rev. A **59**, 4727 (1999).

[193] A. G. Galstyan, M. E. Raikh, and Z. V. Vardeny, *Emission Spectrum of a Dipole in a Semi-Infinite Periodic Dielectric Structure: Effect of the Boundary*, Phys. Rev. B **62**, 1780 (2000).

[194] A. F. Koenderink and W. L. Vos, *Anomalous Diffuse Transmission of Photonic Crystals*, (2002), submitted to Phys. Rev. E.

[195] D. Labilloy, H. Benisty, C. Weisbuch, T. F. Krauss, D. Cassagne, C. Jouanin, R. Houdre, U. Oesterle, and V. Bardinal, *Diffraction Efficiency and Guided Light Control by Two-Dimensional Photonic Bandgap Lattices*, IEEE J. Quantum Electron. **35**, 1045 (1999).

[196] A. F. Koenderink and W. L. Vos, *Light Exiting from Photonic Band Gap Crystals is Diffuse and Strongly Directional*, Phys. Rev. Lett. **91**, (2003), in print.

[197] J. Martorell and N. M. Lawandy, *Observation of Inhibited Spontaneous Emission in a Periodic Dielectric Structure*, Phys. Rev. Lett. **65**, 1877 (1990).

[198] B. Y. Tong, P. K. John, Y. Zhu, Y. S. Liu, S. K. Wong, and W. R. Ware, *Fluorescence-lifetime Measurements in Monodispersed Suspensions of Polystyrene Particles*, J. Opt. Soc. Am. B **10**, 356 (1993).

[199] Z. Y. Li and Z. Q. Zhang, *Weak Photonic Band Gap Effect on the Fluorescence Lifetime in Three-Dimensional Colloidal Photonic Crystals*, Phys. Rev. B **63**, 125106 (2001).

[200] M. Megens, H. P. Schriemer, A. Lagendijk, and W. L. Vos, *Comment on "Spontaneous Emission of Organic Molecules Embedded in a Photonic Crystal"*, Phys. Rev. Lett. **83**, 5401 (1999).

[201] X.-H. Wang, R. Wang, B.-Y. Gu, and G.-Y. Yang, *Decay Distribution of Spontaneous Emission from and Assembly of Atoms in Photonic Crystals with Pseudogaps*, Phys. Rev. Lett. **88**, 093902 (2002).

[202] J. Zhou, Y. Zhou, S. Buddhudu, S. L. Ng, Y. L. Lam, and C. H. Kam, *Photoluminescence of ZnS:Mn Embedded in Three-Dimensional Photonic Crystals of Submicron Polymer Spheres*, Appl. Phys. Lett. **76**, 3513 (2000).

[203] M. J. A. de Dood, A. Polman, and J. G. Fleming, *Modified Spontaneous Emission from Erbium-doped Photonic Layer-by-layer Crystals*, Phys. Rev. B **67**, 115106 (2003).

[204] T. Förster, *Experimentelle und theoretische Untersuching des Zwischenmolekularen Übergangs von Elektronenanregungsenergie*, Zeitschrift fur Naturforschung **4a**, 321 (1949).

[205] S. Astilean and W. L. Barnes, *Quantum Efficiency and the Photonic Control of Molecular Fluorescence in the Solid State*, Appl. Phys. B **75**, 591 (2002).

[206] M. De Dood, *Silicon Photonic Crystals and Spontaneous Emission*, Ph.D. thesis, Utrecht University, 2002.

Summary

Photonic crystals are three-dimensional dielectric structures with a periodicity comparable to the wavelength of light. Due to the periodic variation of refractive index, the crystals possess unusual optical properties that affect the propagation and the emission of light. The "holy grail" of the field is the achievement of a photonic band gap: a frequency range for which light will not propagate in any direction because of Bragg diffraction. In the exciting case of a photonic band gap the emission by light sources in photonic crystals is strongly modified, resulting in inhibited emission. If emission can be controlled this way new applications can be thought of, like thresholdless miniature lasers. Interesting chemical applications are also suggested here, such as uses in solar cells and photon-induced conversion reactions. Efficiency of dye-sensitized solar cells and reaction rates of photon-induced conversions could possibly be controlled in this way. Likewise macroporous materials are interesting from a catalytic and separation chemistry point of view; the macroporous photonic crystals can act as zeolites for large molecules.

In this thesis the preparation and characterization of opal-based photonic crystals are described with the aim to control the properties of internal light sources. We also study the fluorescence of light sources embedded in such photonic crystals. Our macroporous structures, also called air-sphere crystals, are carefully synthesized and of high quality. With fluorescence measurements on these photonic crystals we probe the optical properties that lead up to the photonic band gap. The concept of the photonic band gap was already described in the late 1980s and since then many people have explored the development of photonic crystals consisting of varying structures and materials. The structure and long range order of the fabricated photonic crystals are usually characterized by means of electron microscopy. Optical experiments, such as reflectivity, transmission and emission experiments,

are performed to learn more about the interaction strength of the structure with light. Modifications in reflectivity, transmission and emission spectra result from Bragg diffraction and appear as a stop band in respectively the reflected, transmitted and emitted spectrum. Since the stop gaps are the building blocks of the photonic band gap their properties are essential.

The probability of an emission source to spontaneously decay is described by Fermi's golden rule. Fermi's golden rule can be written in a part related to the light source itself and a part related to the position dependent field. Exactly this position dependent field part, also called the local density of states (LDOS) or averaged over volume, total density of states (DOS), is strongly influenced in a photonic crystal structure (see chapter 1). In the case of a photonic band gap the DOS goes to zero. A exciting way to investigate the modified DOS, is to measure the lifetime of an embedded light source. Since the lifetime is inversely proportional to the available DOS, a change in lifetime will indicate a change in the DOS. The modification in DOS can be measured with either continuous wave (cw) or time-resolved experiments. Cw measurements were previously performed and a decrease in the total emitted power was observed which corresponded to a decrease in the DOS. A requirement to observe a DOS change with these cw measurements was a low quantum efficiency of the light source (see section 6.1).

In this thesis we want to measure the modified DOS in a dynamic way. For these time-resolved measurements, however, a high quantum efficiency is required and therefore the properties of the light source and the backbone material of the crystal should be carefully chosen. In chapter 2 we considered several emission sources and we have chosen the well-known laser dye Rhodamine 6G (R6G) as a light source. R6G exhibits a high quantum efficiency, a broad inhomogeneous and narrow homogeneous emission spectrum and is "bleachable". From previous experiments air-sphere crystals made of the semiconductor titania, turned out to be very effective photonic crystals, due to its high refractive index contrast and optical transparency. With these titania air-sphere crystals it was already demonstrated with cw measurements that the R6G emission, and subsequently the DOS, was strongly reduced by the photonic crystal structure. The quantum efficiency of the dye on titania in these experiments, however, was very low and therefore an observation of a lifetime effect was impossible. Titania exhibits a large electronic band gap and the adsorbed R6G dye shows electron transfer from its excited state to the conduction band of titania, which reduces the quantum efficiency drastically. This is a general feature of fluorescent light sources on semiconductor surfaces. In our research we tried to coat the titania surface with an insulating silica layer in order to preclude the electron transfer. For coated titania powders, we have demonstrated that a deposited thin silica layer indeed prevented the electron transfer, but because of the confined geometry of the air-sphere crystal itself, it was not possible to de-

posit a layer of silica on the titania surface of the air-sphere crystal. Therefore we explored the possibility to measure lifetimes of R6G adsorbed on other materials, as alumina, zirconia and polystyrene. When photonic crystals are made of these pure insulating materials, time-resolved measurements will provide information about the DOS since the quantum efficiency of the dye on these materials remains high. We demonstrated that R6G dye adsorbed on polystyrene does not show electron transfer and therefore this combination turned out to be an excellent candidate for time-resolved emission measurements on polystyrene opals.

In chapter 3 we have described the synthesis and characterization of air-sphere crystals, also called inverse opals, one of the most effective photonic crystals. The general synthesis of our air-sphere crystals consists of three steps. First a template is formed via a self-organizing system consisting of colloidal particles. This template is also called artificial opal because of its beautiful opalescence. Second the interstitial holes in the template are infiltrated with a liquid precursor of a metaloxide, which reacts to yield solid material. In the final step the infiltrated template is heated during which the template is calcined and the infiltrated material, the metaloxide, becomes crystalline. The resulting obtained air-sphere crystal is a replica of the artificial opal and therefore often called inverse opal. We have synthesized air-sphere crystals consisting of several backbone materials. The best known material used for air-sphere crystals in the visible range is titania, which has a high refractive index, and is transparent at optical wavelengths. The air-sphere crystals, as well as the templates, were well-characterized by optical and electron microscopy. To characterize the optical properties we performed reflectivity measurements. The relative width of the reflectivity peak, or the stop band, was investigated since it is a building block for the photonic band gap. We concluded from the characterization that our air-sphere crystals are of high quality and exhibit long range order. Since the photonic band gap is expected to occur at the second order Bragg diffraction, and this second order Bragg is much more sensitive to disorder, a long range order is essential.

In chapter 4 we take a closer look at the process of air-sphere crystal formation. By applying two different materials during the synthesis of the air-sphere crystal, the distribution of both materials in the structure can be investigated. The homogeneity was examined from mm to 100 nm scale by means of energy dispersive X-ray spectroscopy and by examination with the naked eye. To our knowledge we are the first that report on spatial distributions in air-sphere crystals. We observed extreme spatial compositional inhomogeneities on mm, 100 μm and 100 nm scale. The technique of successive infiltrations was originally developed for spherically layered air-sphere crystals, in order to create an environment with a shielded semiconductor surface to prevent electron transfer. The inhomogeneous infiltration discussed in chapter 4, however, explains why this technique will not result

in air-sphere crystals with a homogeneous layer of insulating material on the inner surface. Another important consequence of the inhomogeneous distribution of the oxides can be the spatial variation of the average refractive index, which might be important for optical applications. When applying only one material, however, this seems to be no issue since the inhomogeneities average out.

In chapter 3 the stop band was already measured in reflectivity experiments and the relative width of the stop band was analyzed. In chapter 5 the stop band was investigated with emission experiments. In these emission experiments the light is probed from inside instead of externally as is done in reflectivity experiments. We measured directional fluorescence spectra of R6G dye in polystyrene opals and alumina air-sphere crystals and investigated quantities as spectral position, spectral width and amount of attenuation. The measured stop bands were compared with calculated stop gaps and they showed good agreement. Since both direct (opals) and indirect (inverse opals) structures were measured, attenuations observed in the spectra were compared with each other. The attenuations were explained in terms of mean free paths and Bragg lengths. We observed, as expected, that the alumina inverse opal exhibits a longer mean free path and a shorter Bragg attenuation length compared to the mean free path and the attenuation length of polystyrene opals. An intriguing feature that happens at both the direct and indirect structures is an enhancement of emission at the blue side of the stop band. We explained this enhancement with a model of the so-called escape function of diffuse light. Emission that is limited to propagate in certain directions due to internal Bragg diffraction, escapes in other existing angles and appears as enhanced emission. Since the enhancements at the blue side of the stop band are both present for the direct and the indirect structure, the explanation of the enhancement with standing wave effects was ruled out. In chapter 5 we reported on the first emission measurements on photonic crystals with second order Bragg diffraction. A strong attenuation of R6G emission was observed and although the shape and the position of the second order stop band is much more complicated than the first order stop band, we were able to compare the second order stop band with reflectivity measurements on a similar sample. The positions and the intensity of the features agreed very well. Since the DOS at this second order Bragg is expected to vary much more our pioneering research is of utmost importance and stresses the need for further theoretical interpretation.

Since the spectra measurements in chapter 5 demonstrated that the polystyrene opals strongly influence the angle-dependent emission of R6G, we performed in chapter 6 time-resolved angle-independent measurements; a lifetime change will be independent on angle. From chapter 2 we already learned that R6G dye on polystyrene does not exhibit electron transfer but remains its high efficiency and therefore the polystyrene opals are very promising to use in time-resolved mea-

surements. Due to large variations in the DOS of photonic crystals, it was expected to see enhanced or inhibited spontaneous emission, appearing in shorter or longer lifetimes. From the angle-independent lifetime measurements discussed in chapter 6 we conclude, however, that it is very difficult to observe a lifetime change caused by the photonic structure, as is discussed below.

We have measured lifetimes as a function of wavelength and although a λ^3 behavior should be expected (from Fermi's golden rule), a wavelength independent behavior was observed. This was explained in terms of the homogeneous linewidth. Formerly it was assumed, based on literature, that the homogeneous linewidth was as small as 5 % of the complete emission spectrum. It turned out that the homogeneous linewidth of dye molecules adsorbed on polystyrene however, is much broader, possibly as wide as the emission spectrum. If the homogeneous linewidth of the dye is broader than the width of the stop gap, the spontaneous emission can not be modified and therefore no changes in lifetime will be observed.

We also observed that reabsorption of dye emission is a major issue in photonic crystals. Due to multiple scattering of the light by defects in the photonic crystal, the light path of emitted light is strongly folded up and has typical length scales of ~ 1 cm. This light path is clearly much longer than the sample thickness, and therefore the chance for reabsorption by dye molecules, especially at high dye-concentrations, can be increased. As a consequence the lifetime is considerably lengthened but not as a result of the photonic structure. We have calculated for our samples that it is very likely that 10^{-5} Molar R6G doped samples exhibit reabsorption and indeed these samples show longer lifetimes compared to samples doped with 10^{-6} Molar R6G.

Both effects, the unexpected broad homogeneous linewidth of the dye and an increasing chance for reabsorption with increasing dye concentration, are very important since many groups nowadays try to investigate modified spontaneous emission with the use of fluorescent dyes. The effects discussed in this thesis, possibly precludes people to observe any lifetime change with dyes and should be carefully considered in the future.

A very remarkable feature that was observed in the lifetime data in chapter 6, was a radius dependent lifetime behavior. For R6G in opals with smaller sphere radii a shorter lifetime was obtained while opals with larger sphere radii displayed a longer lifetime. We proposed a hypothesis that describes a relation between the lifetime and the local DOS at the sphere surface of single spheres. The remnants of this single sphere behavior, i.e., an increased LDOS nearby the sphere surface are proposed to account for the variations observed in the lifetimes.

This thesis clearly demonstrated that photonic crystals, opals as well as inverse opals, are in many ways an interesting subject of research. While chemists put a lot of effort in synthesizing photonic crystals, like varying crystal structures and

materials, physicists concentrate more on optical and fundamental properties such as photonic band gaps. This thesis was written from a chemist point of view, but a lot of physics was involved. Exactly this combination makes this thesis interesting for both disciplines, and in the future this will probably become visible in applications in both fields; macroporous materials in optical chips as well as in for instance catalysis.

Samenvatting

Licht en kleur

Wat hebben licht en kleur met elkaar te maken? Alles!

Licht kan beschreven worden als een golf, vergelijkbaar met bijvoorbeeld een watergolf, alleen is de periodiciteit niet enkele meters zoals bij watergolven in de zee, maar honderden nanometers, 0.0000001 meter of een miljoenste meter. Deze periodiciteit noemen we een golflengte, met een latijns symbool aangegeven als λ. Een golf is niets anders dan een verplaatsing van energie. Licht is een electromagnetische golf die zowel electrische als magnetische energie bevat. Blauw licht heeft een golflengte van $\sim$ 450 nanometer en rood licht een golflengte van $\sim$ 650 nanometer. Ultraviolet licht heeft een nog veel kortere golflengte, $\lambda < 400$ nanometer.

Wit licht bestaat uit een mengsel van alle kleuren bij elkaar: in feite bevat wit licht alle kleuren van de regenboog, maar omdat deze kleuren met elkaar mengen zien we een witte kleur. Wit licht bevat alle golflengtes van 400-700 nanometer, we noemen dit het spectrum van wit licht. We kunnen aan wit licht dan ook niet een enkele golflengte toekennen.

Een kleurverschijning kan ontstaan door verschillende processen. De belangrijkste daarvan zijn absorptie, weerkaatsing, uitzending en verstrooiing. Deze processen hebben alles met licht te maken, ze vinden allen plaats door wisselwerking tussen licht en materie.

Absorptie: een veel voorkomende vorm van kleurverschijning is absorptie van licht. Wanneer een voorwerp met wit licht wordt beschenen, kunnen kleuren met bepaalde golflengtes geabsorbeerd (=opgenomen) worden door het materiaal. Juist

de golflengtes die niet geabsorbeerd worden bepalen de kleur. Wanneer een voorwerp alle kleuren van het witte licht behalve rood absorbeert, zal het voorwerp rood kleuren. Een materiaal dat alle kleuren absorbeert zal een zwarte kleurverschijning hebben.

Uitzending: niet alleen het materiaal zelf, maar ook kleurstoffen aanwezig in het materiaal kunnen de kleur bepalen. Bijvoorbeeld ranja en fluorescerende merkstiften die een felle kleurverschijning hebben omdat de aanwezige kleurstof licht uitzendt. Andere voorbeelden van uitzending zijn pigmenten die in verf worden gebruikt.

Verstrooiing: een andere vorm dat de kleurverschijning kan beïnvloeden is verstrooiing. Wanneer deeltjes kleiner dan de golflengte van licht zijn worden ze verstrooid, dat wil zeggen dat het licht in alle willekeurige richtingen verspreid wordt. De lucht is bijvoorbeeld blauw omdat de kleine deeltjes in de hemel het licht met kortere golflengtes (=blauw) meer verstrooien dan licht met langere golflengtes (=rood). Melk is niet transparant maar wit omdat deeltjes in de melk alle kleuren van het witte spectrum evenveel verstrooien.

Weerkaatsing: een verschijnsel dat wij in ons onderzoek echter het meest interessant vinden is de weerkaatsing van het licht door de structuur van een object. De structuur kan bijvoorbeeld bestaan uit laagjes gaten of bolletjes, gerangschikt in een bepaald patroon: de kristalstructuur. Het verschijnsel waarbij het licht weerkaatst wordt aan de regelmatige structuur van het object wordt veroorzaakt door interferentie. De kleurverschijning die daarmee gepaard gaat wordt ook wel regenboogkleuring genoemd. Bij beschijning van zulke structuren met wit licht worden alle kleuren weerkaatst. Maar omdat elke kleur van het witte licht anders wordt gereflecteerd, d.w.z. onder een andere hoek weerkaatst wordt en dus als het ware "opgesplitst" wordt, nemen we een regenboogkleuring waar. Dit vindt bijvoorbeeld plaats als je de onderkant van een compact disc beschijnt met licht. Alle kleuren van de regenboog zijn zichtbaar en bij beweging zie je de kleuren verspringen. Wanneer er naast dit soort weerkaatsing ook wit licht verstrooiing plaatsvindt, zoals in melk, noemt men de verschijning opalescentie. Voorbeelden van opalescentie zijn de paarlemoeren verschijning in schelpen. De schelp bestaat uit een gelaagde structuur van organisch en anorganische materiaal, die het witte licht opsplitst in zijn kleuren; een regenboogkleuring. Maar doordat er ook wit licht verstrooiing plaatsvindt door kleine oneffenheden, nemen we een paarlemoeren kleur waar.

Interferentie

Om te kunnen begrijpen hoe regenboogkleuring en opalescentie plaats kunnen vinden is in figuur 1 het begrip interferentie weergegeven. Wanneer een dun laagje olie drijft op water, weten we uit ervaring dat er van bovenaf allerlei kleuren worden waargenomen. Wanneer een lichtgolf van het ene materiaal naar het andere reist, treedt er breking en terugkaatsing op: een gedeelte van de golf wordt weerkaatst, afhankelijk van het materiaal en de golflengte van het licht en een gedeelte reist na breking verder. In figuur 1 wordt het inkomende licht met golflengte λ teruggekaatst aan zowel het olie-oppervlak, resulterend in golf a, als aan de overgang olie/water, resulterend in golf b. Deze weerkaatste lichtgolven zullen met elkaar wisselwerken oftewel interfereren, en afhankelijk van de onderlinge positie van de toppen en dalen, zal er versterking of uitdoving plaatsvinden. Wanneer de toppen en dalen gelijk vallen zoals in figuur 1 is weergegeven, dan zijn de golven in fase en zullen de golven a en b elkaar versterken: ze worden als het ware bij elkaar opgeteld. In de figuur zijn er stippellijnen aangebracht die de top en het dal van beide golven markeren. De golven zijn in fase omdat de golflengte λ van het inkomende licht exact één keer in het laagje past; een halve golflengte reist heen (de gestreepte curve) en een halve goflengte reist terug naar het oppervlak. De resulterende golf a+b heeft dezelfde golflengte λ als het inkomende en het weerkaatste licht. De intensiteit is echter wel verschillend. De amplitude A van een golf (de hoogte en diepte van respectievelijk de toppen en dalen) is een maat voor de intensiteit van

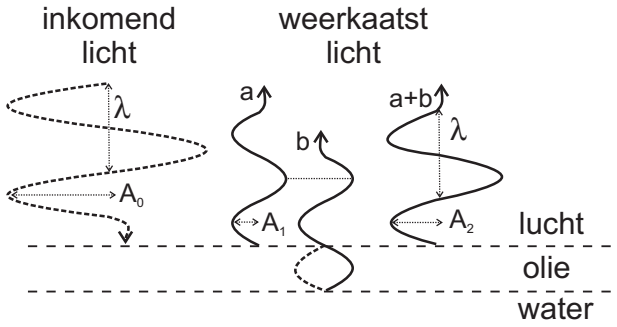

FIGUUR 1: *Het inkomende licht met golflengte λ wordt (gedeeltelijk) weerkaatst aan zowel de lucht/olie als aan de olie/water overgang, resulterend in respectievelijk golf a en b. Omdat de dikte van het olielaagje net zo dik is als een halve golflengte, is golf b t.o.v. golf a precies een golflengte verschoven. De golven zijn nu in fase; hun toppen en dalen vallen samen (aangegeven met een stippellijn), en versterken elkaar. De golf a+b heeft een grotere amplitude A_2 dan de weerkaatste golven a en b afzonderlijk (A_1), en golf a+b verschijnt als een felle weerkaatsing.*

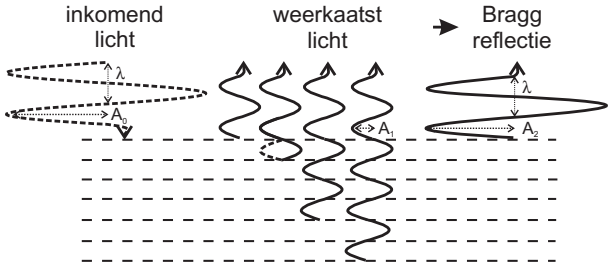

FIGUUR 2: *Het principe van Bragg-reflectie. Door een periodieke stapeling van twee materialen die steeds met een half golflengte verschil alterneren, wordt het inkomende licht aan meerdere vlakken weerkaatst. Nu interfereren niet twee, maar veel meer golven met elkaar. Omdat de golven in fase lopen, versterken ze elkaar, hetgeen resulteert in een Bragg reflectie; een felle weerkaatsing. De Bragg reflectie heeft een grotere amplitude A_2 dan de weerkaatste golven afzonderlijk (A_1) en kan bijna net zo groot zijn als de amplitude van het inkomende licht (A_0). Merk op dat de golflengte van het inkomende en het weerkaatste licht hetzelfde zijn (λ).*

de golf. De amplitude van het inkomende licht A_0 is groter dan de amplitude van de weerkaatste golven A_1 omdat slechts een deel van het licht weerkaatst wordt, het andere deel reist verder door het materiaal. De twee weerkaatste golven a+b samen hebben een hogere intensiteit dan de golven a en b afzonderlijk omdat hun amplitudes bij elkaar zijn opgeteld.

Wanneer het inkomende licht niet uit een enkele golflengte bestaat, maar uit bijvoorbeeld wit licht, dan wordt alleen de golflengte die past in de dikte van het olielaagje weerkaatst. Deze golflengte wordt beter weerkaatst dan de andere golflengtes.

Tot nu toe hebben we alleen interferentie besproken voor licht dat loodrecht op het oppervlak valt. Wanneer licht onder een hoek het oppervlak beschijnt zal een andere weglengte en dus een andere golflengte versterkt worden. Dit resulteert in een regenboogkleuring: onder verschillende hoeken verschijnen er verschillende kleuren.

Een olielaagje op water is een voorbeeld waar slechts één laagje het licht doet weerkaatsen. Maar stel je eens voor dat een materiaal uit veel meer laagjes bestaat die precies de dikte hebben van een halve golflengte van licht; dan versterken niet twee, maar veel meer golven elkaar. Dit verschijnsel wordt ook wel Bragg weerkaatsing of Bragg reflectie genoemd en is essentieel in ons onderzoek aan fotonische kristallen. In figuur 2 is deze situatie geschetst. Niet twee, maar veel meer golven versterken elkaar. Het resultaat is een weerkaatsing met een amplitude A_2 die vele malen groter is dan de amplitude van het weerkaatste licht A_1. Doordat

de laagjes, aangegeven met stippellijnen, steeds met een half golflengte verschil alterneren, wordt het inkomende licht aan elk laagje weerkaatst. De weerkaatste golven zijn in fase en versterken elkaar; een Bragg reflectie. Bij Bragg reflectie is de intensiteit of de amplitude van de weerkaatste lichtgolf zo groot dat hij (bijna) net zo groot kan zijn als de intensiteit van het inkomende licht (A_0).

Een belangrijke grootheid voor fotonische kristallen is de brekingsindex van de materialen die aanwezig zijn in het fotonisch kristal. Een brekingsindex van een materiaal zegt iets over hoe snel licht zich door dat materiaal verplaatst. In materialen met een brekingsindex $n = 1$, bijvoorbeeld lucht, beweegt licht zich voort met de lichtsnelheid $c = 300000$ km/s (naar de maan in ruim in één seconde!). In materialen met een hogere brekingsindex, bijvoorbeeld diamant met $n = 2.4$, beweegt licht zich langzamer voort. De naam brekingsindex komt van het feit dat het licht "gebroken" wordt als het van het ene naar het andere medium gaat. De lichtgolf zal niet rechtlijnig maar met een knik het materiaal met de andere brekingsindex betreden. Een grote verhouding (een hoog contrast) in brekingsindex voor de materialen in onze fotonische kristallen is erg belangrijk. Hoe hoger het contrast hoe meer licht weerkaatst wordt en dus hoe sterker de Bragg reflectie is. Het contrast tussen diamant en lucht is ongeveer 2.4. Voor fotonische kristallen worden liefst materialen gebruikt die een nog hogere brekingsindex hebben. De maximale brekingsindex die voor zichtbaar licht te gebruiken is, is ongeveer 3.

Fotonische kristallen

Wat zijn fotonische kristallen nu eigenlijk? Fotonische kristallen zijn structuren die regelmatig geordend zijn en een periodiciteit in brekingsindex hebben die van de zelfde orde van grootte is als de golflengte van licht. Doordat ze deze structurele regelmaat hebben zullen lichtgolven weerkaatst worden aan de kristalvlakken: het licht wordt Bragg gereflecteerd. Wanneer Bragg reflectie plaatsvindt onder verschillende hoeken nemen we regenboogkleurige verschijningen waar, net zoals bij een compact disc. Door de periodiciteit te kiezen, kunnen we licht met bepaalde golflengtes buiten het kristal sluiten. Een kleinere periodiciteit ($\sim$ 400 nanometer) zal blauwe golflengtes weerkaatsen en een grotere periodiciteit ($\sim$ 600 nanometer) zal rode golflengtes weerkaatsen. Op deze manier kunnen wij bepalen welke golflengtes wel of niet het kristal in mogen; we manipuleren zogezegd het licht. Licht dat van binnenuit het kristal komt kan er dan ook niet uit. Sterker nog, het licht kan dan zelfs niet bestaan!

Wanneer licht van een bepaalde golflengte een kristal niet in of uit kan, in alle drie de dimensies (in de hoogte, in de breedte en in de diepte), noemen we dit een fotonische bandkloof. In het Engels wordt deze bandkloof "photonic band gap" genoemd (vanwaar www.photonicbandgaps.com). Als een fotonische bandkloof

aanwezig is in een kristal, veranderen de eigenschappen zodanig dat soms het licht helemaal niet aan kan gaan: het blijft donker in het kristal.

Luchtbolkristallen

Uit berekeningen is gebleken dat in fotonische kristallen die voor meer dan 80% uit lucht bestaan en een brekingsindex contrast hebben dat hoog genoeg is, een fotonische bandkloof daadwerkelijk gevormd kan worden. Daarom zijn nu wereldwijd chemici bezig kristallen te maken die aan deze eisen voldoen. De bekendste fotonische kristallen tot nu toe zijn de zogenoemde luchtbolkristallen: een kristal dat bestaat uit een rangschikking van luchtbolletjes in een materiaal met een hoge brekingsindex. Doordat het kristal bestaat uit luchtbolletjes is het duidelijk dat het kristal inderdaad voor een groot gedeelte uit lucht bestaat. In ons onderzoek hebben we zulke luchtbolkristallen gemaakt van verschillende materialen. Deze materialen moeten een hoge brekingsindex hebben en mogen geen licht absorberen. Wanneer de materialen (zichtbaar) licht absorberen, is het namelijk onmogelijk om het licht op te sluiten. Je raakt het licht dan juist kwijt doordat het wordt omgezet in warmte.

Hoe maak je zulke luchtbolkristallen? In zekere zin bootsen we in de eerste stap van de synthese van de luchtbolkristallen de natuur na: we maken een kunstmatig opaal. Een opaal in de natuur bestaat uit een gerangschikte structuur van glasbolletjes. Wij maken net zo een structuur, maar gebruiken dan plastic latex bolletjes in plaats van glasbolletjes. De bolletjes hebben een afmeting van ongeveer 500 nanometer in doorsnede. Een mengsel van zulke plastic bolletjes met water, doen we in een plat glazen buisje en we laten dit een paar weken staan. De bolletjes zinken dan en stapelen zich spontaan in een geordende structuur: een kristalstructuur. Vervolgens laten we het water verdampen en ontstaat er een kunstmatig opaal. Dit opaal bevat net zulke mooie kleurschakeringen als opalen in de natuur; door de geordende structuur in de bolletjes treedt er Bragg reflectie op. Maar een fotonische bandkloof zullen deze kunstmatige opalen niet bezitten, want fotonische kristallen zouden voor meer dan 80% uit lucht moeten bestaan, terwijl een structuur met gestapelde bolletjes grotendeels uit vast materiaal bestaat. Om toch een fotonische bandkloof te kunnen creëren, hebben we de structuur omgekeerd, we gebruiken de kunstmatige opaal als een mal, zie ook figuur 3. We vullen de luchtruimte tussen de bolletjes op met een materiaal dat een hoge brekingsindex heeft en verwijderen vervolgens de bolletjes. Het verwijderen van de bolletjes gebeurt door vernietiging, de plastic bolletjes worden verbrand bij temperaturen boven de 400 graden. Na verbranding blijft er op de plek waar de bolletjes gezeten hebben lucht achter; het luchtbolkristal is gevormd.

Voorbeelden van de mal (het kunstmatig opaal) en het uiteindelijke luchtbolkristal zijn afgebeeld in figuur 4. Deze foto's zijn gemaakt met een electronenmi-

croscoop. Met deze microscoop kunnen objecten zichtbaar worden gemaakt die zo klein zijn als 1 nanometer. Afbeelding 4(a) toont een opaal dat bestaat uit bolletjes met een doorsnede van 500 nanometer. De bolletjes zijn mooi gerangschikt in een hexagonale kristalstructuur, in het midden zie je zelfs de bolletjes die een rij lager liggen, omdat het bovenliggende bolletje eruit is gevallen. Met het blote oog ziet dit kunstmatige opaal er net zo uit als een echt opaal; mooie regenboogkleuren, zoals ook te zien in hoofdstuk 3, figuur 3.4. In afbeelding 4(b) is een luchtbolkristal, oftewel een inverse opaal, gemaakt van titaandioxide weergegeven. Op de plek waar de bolletjes zaten zit nu lucht; luchtbolletjes. De zwarte plekjes in de foto noemen we ook wel raampjes en zijn de plaatsen waar de polystyreen bolletjes elkaar raakten; hier is geen materiaal afgezet. De diameter van de luchtbolletjes is hier ongeveer 600 nanometer. Het luchtbolkristal in figuur 4(b) is gemaakt van een andere mal dan in figuur 4(a) is afgebeeld. Hoewel het luchtbolkristal mooi regelmatig geordend is, zien we ook een aantal scheurtjes en losse brokjes materiaal liggen. Deze kleine oneffenheden ontstaan tijdens het fabricageproces en zijn bijna niet te vermijden. Mooie kleurenfoto's van soortgelijke luchtbolkristallen zijn te vinden in hoofdstuk 3, waar ook nog veel meer mooie electronenmicroscoop foto's zijn afgebeeld.

Het luchtbolkristal dat in figuur 4 getoond wordt, is gemaakt van titaandioxide, een materiaal dat transparant is voor zichtbare golflengtes. Wij kennen titaandioxide veelal van de toepassing in tandpasta of witte verf, waar het gebruikt wordt voor

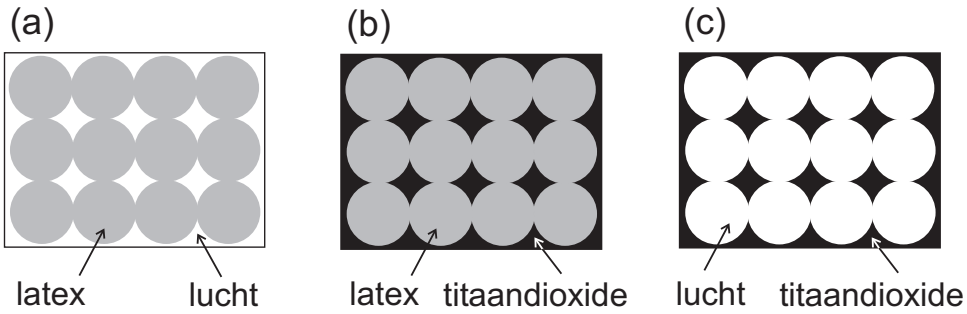

FIGUUR 3: *Schematische weergave van de synthese van een luchtbolkristal. (a) Een driedimensionale mal, een kunstmatig opaal, bestaat uit plastic latex bolletjes die gerangschikt zijn in een hexagonaal patroon. De opaal is gevormd door zelf-organisatie van de bolletjes vanuit een suspensie in water. (b) De luchtruimte tussen de plastic bolletjes wordt opgevuld met titaandioxide, een materiaal met een hoge brekingsindex (2.7). (c) In de laatste stap van de synthese worden de plastic bolletjes verbrand. Na verbranding blijft er een luchtbolkristal van titaandioxide over. Wat in figuur (a) plastic was is nu lucht, wat in figuur (a) lucht was is nu titaandioxide; de structuur is geïnverteerd.*

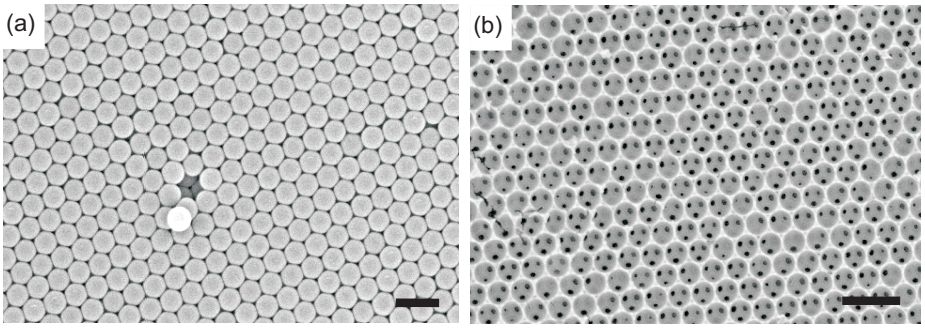

FIGUUR 4: *Electronenmicroscoop afbeelding van een polystyreen opaal (de mal) en een luchtbolkristal. (a) Een kunstmatig opaal opgebouwd uit bolletjes met een doorsnede van 500 nanometer (schaalbalk is 500 nanometer). De bolletjes zijn mooi gerangschikt in een hexagonaal patroon. De structuur is drie-dimensionaal, zoals te zien aan het gat in het midden; hier mist een bolletje en zijn de beneden liggende bolletjes te zien. (b) Een luchtbolkristal van titaandioxide, de replica van een kunstmatig opaal. De diameter van de luchtbollen is 600 nanometer (de schaalbalk is 1500 nanometer) en zijn ook gerangschikt in hexagonaal patroon. De zwarte plekjes noemen we "raampjes"; het zijn de plaatsen waar de bolletjes in de mal elkaar aanraakten en geen titaandioxide is afgezet.*

zijn witte kleur. Het titaandioxide heeft een hoge brekingsindex, $n = 2.7$, hoger dan diamant en is dus erg interessant om te gebruiken voor fotonische kristallen. We hebben ook luchtbolkristallen gemaakt van andere materialen zoals siliciumdiodixe (glas), aluminiumoxide (dezelfde stof waaruit saffier bestaat) en zirconiumdioxide (een mineraal). Maar ook van gemengde materialen zoals titaandioxide/aluminiumoxide en titaandioxide/zirconiumdioxide. Hoewel deze materialen een iets lagere brekingsindex bezitten dan titaandioxide zijn ze zeer nuttig geweest voor ons onderzoek. We hebben bijvoorbeeld geleerd dat het opvullen van de mal niet homogeen verloopt, wat erg belangrijk is om te weten wanneer we luchtbolkristallen maken van meer dan één materiaal (zie hoofdstuk 4).

Een groot gedeelte van dit proefschrift gaat over het maken en karakteriseren van fotonische luchtbolkristallen. Maar als je ze maakt wil je er natuurlijk ook iets mee doen. Kunnen ze daadwerkelijk licht buitensluiten en licht binnen in het luchtbolkristal verbieden?

Lichtbronnen

De wisselwerking tussen de fotonische kristallen en licht noemen we fotonische interactie. We meten deze fotonische interactie door de samples met licht te beschijnen, bijvoorbeeld met een felle witte lamp, en te kijken hoeveel licht er daadwerkelijk buiten het kristal blijft, dus weerkaatst wordt. Dit soort experimenten zijn in het verleden al regelmatig gedaan, maar een nieuwe benadering is om het licht niet van buiten te laten komen maar van binnen. Vervolgens meten we of het licht inderdaad niet uit het kristal komt. Omdat een lichtbron zoals wij die kennen, bijvoorbeeld een gloeilamp, niet in een fotonisch kristal past, gebruiken we andere lichtbronnen. Een goede kandidaat hiervoor is een kleurstof. Een kleurstofmolecuul is een verbinding die licht met een bepaalde golflengte opneemt en vervolgens licht met een andere golflengte uitzendt. Wanneer dit kleurstofmolecuul licht (=energie) absorbeert en het in een hoger gelegen energieniveau raakt, noemen we hem aangeslagen. De stof blijft hier maar een hele korte tijd, ongeveer een paar nanosecondes (0.000000001 seconde), voordat hij weer terugvalt naar de grondtoestand; het laagste energieniveau in een molecuul. Deze "terugvaltijd" noemen we de levensduur en is karakteristiek voor elke kleurstof. De wet van behoud van energie beschrijft dat energie niet zomaar verloren kan gaan en dus komt bij deze overgang van een hoog energetisch naar een laag energetisch niveau, energie vrij in de vorm van licht. Elk kleurstofmolecuul heeft zijn eigen energieniveaus en zendt dus ook licht uit van verschillende golflengtes. Zo kennen we blauwe kleurstoffen, b.v. indigo waar onze spijkerbroeken mee gekleurd worden, of (fluorescente) gele kleurstoffen gebruikt in neonreclames.

De kleurstof die wij gebruikt hebben heet Rhodamine, en zendt rood licht uit. Het rode licht dat uitgezonden wordt is niet een enkele golflengte, maar een gebiedje aan golflengtes, ongeveer van 560-650 nanometer: dit is het spectrum van Rhodamine. We plaatsen deze Rhodamine moleculen in onze fotonische kristallen door de kristallen in een alcoholische oplossing van de kleurstof te dopen.

Experiment

In hoofdstuk 5 zijn experimenten beschreven waar gekeken wordt naar de uitzending van Rhodamine moleculen die in een fotonisch kristal zitten. In deze experimenten zien we dat er inderdaad licht van een bepaalde golflengte wordt uitgesloten. Dit komt tot uiting in de vorm van een "deuk" in het spectrum van de kleurstof. Door het gemeten spectrum te vergelijken met het spectrum van de kleurstof onder normale omstandigheden, bijvoorbeeld opgelost in een vloeistof, kunnen we precies zien wat de effecten zijn van het fotonisch kristal. We hebben

metingen gedaan van kleurstofmoleculen in luchtbolkristallen, maar ook metingen van kleurstofmoleculen in de mal. Uit berekeningen is gebleken dat deze mallen namelijk ook al een sterke fotonische interactie vertonen. We hebben in beide systemen, zowel in de luchtbolkristallen als in de kunstmatige opalen, gemeten dat het licht uitgezonden door de kleurstof voor meer dan 50% weerkaatst werd en niet uit het kristal kwam! We hebben het licht dus daadwerkelijk kunnen opsluiten!

Maar iemand kan dan vragen: is dat nu zo bijzonder? Als ik een doos bouw met aan de binnenkant spiegels kan ik dat ook. En dat is niet waar, want spiegels blijken een niet onaanzienlijk deel van licht te absorberen! Het interessante aan een fotonische bandkloof is echter dat er naast weerkaatsing ook een ander fenomeen kan plaatsvinden; lichtbronnen die in een kristal geplaatst zijn kunnen helemaal niet aangaan. Een voorbeeld; een aangeslagen kleurstofmolecuul wil licht uitzenden met een bepaalde energie maar de energie "past" niet in het kristal. Het kleurstofmolecuul blijft in de aangeslagen toestand, veel langer dan de verwachte nanoseconde. Zijn levensduur wordt dus verlengd. Als je op deze manier het licht kan manipuleren, dus "uit" en "aan" kunt zetten, liggen toepassingen als optische chips en miniatuurlasers in het verschiet.

In hoofdstuk 6 hebben we experimenten uitgevoerd om te zien of we de levensduur van de kleurstofmoleculen inderdaad konden zien veranderen. Door de levensduren in de fotonische kristallen te vergelijken met de levensduur in een standaard systeem, hoopten we een verschil te zien. Inderdaad hebben we in onze metingen voor het eerst verschillen gevonden in levensduren tussen kleurstofmoleculen in een fotonisch kristal en in een standaard systeem. Bovendien hebben we geleerd dat veel andere factoren een belangrijke rol spelen, bijvoorbeeld de concentratie van de kleurstofmoleculen in het kristal. Bij hogere concentraties zien we dat er langere levensduren zijn dan bij lagere concentraties. Dit komt omdat bij hogere concentraties het uitgezonden licht door één kleurstofmolecuul weer opgenomen kan worden door een ander kleurstofmolecuul, waardoor het lijkt alsof de kleurstof langer in de aangeslagen toestand blijft. Ook is de breedte van het spectrum van de kleurstof erg belangrijk. Wanneer het spectrum van een kleurstof te breed is, zal het moeilijk zijn om een levensduureffect waar te nemen. De fotonische bandkloof moet dan namelijk breder zijn dan het spectrum en dat is meestal moeilijk te realiseren. Een andere belangrijke factor bleek de diameter van de bolletjes. Hoewel het te verwachten is dat de diameter van de bolletjes de voortplanting van licht beïnvloedt (dit hangt immers samen met de periodiciteit in het kristal en dus de golflengte van weerkaatst licht), verwachtten we niet dat de bolletjes afzonderlijk de levensduur van het licht zouden beïnvloeden. Ons vermoeden is dat ieder bolletje op zich, dus niet per se gerangschikt in een rooster, de levensduur kan beïnvloeden. Omdat dit slechts een vermoeden is, zullen er in de toekomst nog vele berekingen en experimenten uitgevoerd moeten worden.

Tot nu toe is het niemand nog gelukt, ook ons niet, om een fotonische bandkloof te creëren. Oorzaken waarom dit nog niet gelukt is, zijn onder andere dat de kristallen vaak niet groot genoeg zijn en nooit helemaal perfect zijn; ze bevatten veelal kleine scheurtjes of misvormde luchtbollen die ontstaan zijn tijdens het fabricageproces. Hoewel de fotonische bandkloof er in praktijk nog niet is, leren we van onze experimenten heel veel; de oplossingen van de problemen die we nu tegenkomen zijn zeer nuttig voor toekomstig onderzoek. Bovendien lijken onze resultaten nu al interessant voor industriële onderzoekers.

Dit boekje is geschreven vanuit een chemisch perspectief. De nadruk ligt op het synthetiseren en karakteriseren van de fotonische kristallen. Hoewel synthese doen erg leuk is, is het minstens even leuk om te meten (=weten) of datgene wat je gemaakt hebt daadwerkelijk doet wat je ervan verwacht had. Reflectiviteit, emissie en levensduurmetingen aan de gesynthetiseerde kristallen, allemaal (optisch) fysische experimenten, zijn in dit boekje beschreven op een manier hoe ik dit ervaren heb en hopelijk daardoor ook voor veel chemici begrijpelijk.

Dankwoord

Iedereen die heeft bijgedragen aan de totstandkoming van dit boekje, op wat voor wijze dan ook, ben ik zeer erkentelijk. Toch wil ik een aantal mensen in het bijzonder noemen.

Allereerst Willem Vos (Zorro). Mijn dagelijkse begeleider met de altijd open deur. Hoewel ik in het begin de drempel om die deur door te gaan (onterecht) te hoog vond, en dus veel te weinig langs kwam, heb ik dat de laatste maanden dubbel en dwars ingehaald. Ik heb ontzettend veel van je geleerd, je wees me vaak op het bechgerisme (dat denk ik nooit uit me te slaan zal zijn), en ik zal jouw wijze lessen zeker (kunnen) gebruiken in de toekomst. Ook wil ik Ad Lagendijk bedanken. Aan je inspirerende geest, zowel op wetenschappelijk als sociaal niveau, heb ik veel gehad. Ad en Willem ben ik beide erkentelijk voor het gestelde vertrouwen en de mogelijkheid om te kunnen promoveren.

Femius, zowel op persoonlijk vlak als op de werkvloer hebben we veel aan elkaar gehad. Misschien ik wel meer aan jou, vooral wat de LaTeX belevenissen betreft. We hadden allebei een partner in Amsterdam (?!) en dat geeft toch een soort band... Desalniettemin ben ik blij dat we ons eigen flatje hadden gevonden (en niet zijn gaan "hokken" in Hengelo om daar een gestoffeerde w.c. bril te delen). Veel succes in Zwitserland en ik kom snel logeren! Martijn ook bedankt voor de gezelligheid en de laatste technische proefschrift kwesties. Wij genoten het laatste jaar nog regelmatig van heerlijke broodjes van Ed Rooth. Binnenkort zullen we deze echter beide moeten missen. Veel succes in het buitenland.

Mijn onderzoek is gestart in de WICM groep aan het WZI in Amsterdam. Alle groepsleden aldaar bedankt: Jaime, Gijs, Tom H., Mischa, Frank S., Arnout, Dirk, Juan, Manu, Denis, Yuri (muchas gracias para los opalos), Frank P., Dau, Henry, Henk, Rudolf en Gerard, ik ben jaloers op jullie nieuwe chemielab...

Zonder (technische) hulp van anderen ben je nergens: Wim bedankt voor de technische ondersteuning en je gastvrijheid voor een plekje op jouw kamer in Amsterdam. Bert en Eddy (glasblazerij), Hugo en Ton (o.a. optische microscoop), Bert en Willem (Röntgen experimenten), Derk en Marc (computer ondersteuning), Mariet, Ineke, Ina, Roos, Rita (administratieve ondersteuning), mede-asbestslachtoffers Dennis, Jeroen, Joost en vele anderen. Allemaal bedankt!

In mijn tijd in Amsterdam heb ik met verschillende mensen buiten het instituut samengewerkt. Ik denk met veel plezier terug aan de SEM-sessies bij biologie in de Watergraafsmeer. Zonder de hulp van Wijnand Takkenberg stond mijn boekje nu niet vol met mooie foto's! In Leiden wil ik Ton Gortenmulder en John Mydosh bedanken voor de gastvrijheid en de hulp bij de EDS-experimenten. Uit Utrecht bedank ik de collega's van het Debye-instituut waarmee we op allerlei verschillende locaties, een toch altijd productieve werkbespreking konden houden: John Kelly, Daniel Vanmaekelbergh, Bert, Michel, Stefan, Floris en Rint (leuk dat je nu bij COPS zit). Mijn voorganger Judith Wijnhoven (nu in Utrecht) bedank ik o.a. voor de hulp bij de colloïdsynthese en de onophoudelijke interessse in de avonturen met Bill en Joe. In St. Louis I would like to thank Bill Buhro and Joe Farthing for our collaboration and I wish you both good luck.

En toen kwam de boodschap dat onze hele groep naar de andere kant van Nederland zou gaan verhuizen. Wat nu? Na veel wikken en wegen heb ik toch besloten om mee te gaan. In Enschede ontstond zo al snel de groep Complex Photonic Systems (COPS). "Regelneef" Raymond bedankt voor de soepele verloop van de verhuizing. Wim ook bedankt voor alle hulp vòòr en tijdens het verhuizen, inclusief ons ritje met de bus vol fotonische schatten. De Universiteit Twente in het algemeen wil ik bedanken voor de hartelijke ontvangst.

Hoewel de verhuizing van Amsterdam naar Enschede op het persoonlijk vlak niet makkelijk was, waren er ook positieve dingen. Naast een mooi chemielab, een gloednieuw kantoor, ook een zwembad en een sintelbaan op de campus. Bata- en watervrienden: Tijmen, Martijn, Léon (mèt streepje!), Peter, Willem, Frans, Eric, bedankt voor de leuke trainingen en/of "zwemlunches". Volgend jaar ren ik zeker weer mee met de Batavierenrace! KaMu (Karen Munnink), KaMo (Karen van der Molen) en KaO (Karin Overgaag), al was het prima vertoeven als enige vrouw in de groep, nu met jullie erbij is het toch ook wel erg gezellig. Al snel groeide COPS tot een bloeiend geheel, nu maar liefst al bestaande uit meer dan twintig man & vrouw! Peter, Martijn, Tom, Tijmen, Rint, Ivan, Philip, Boris, Cock, Bas, Léon, Raymond, Willem, Allard, Ad, Karen, Karen, Karin, Arie, Ivo, Timo, allemaal bedankt voor de gezellige sfeer en veel succes toegewenst in de toekomst. Ik zal de filmavonden en andere groepsactiviteiten (die òòk blijven groeien) missen. Léon bedankt voor de assistentie bij de EDS experimenten en vele andere praktische klusjes. Ik hoop de trucjes van de fotonische kristallen fabricage goed overgebracht te hebben.

De OT groep op de tiende verdieping ook bedankt voor alle hulp en samenwerking: o.a. Eliane (voor de reflectiviteitsmeting), Kobus, Erik, Frans en Jeroen (voor de assistentie bij de “spikes”).

I would like to thank all members of the thesis committee for reading the manuscript and giving their approval to defend my thesis.

Stichting FOM wil ik bedanken voor de financiële bijdrage in de kosten van een tweede huishouding.

Hoewel werk een belangrijk deel van je leven is, is het leven naast het werk minstens zo belangrijk. Juist het laatste anderhalf jaar heb ik dat leven, met familie en vrienden, enorm gemist. Hoewel ik weinig tijd met jullie heb mogen doorbrengen waren jullie in gedachten altijd bij me. Bedankt voor alle getoonde belangstelling.

Papa en mama, ondanks jullie eigen zorgen altijd klaar staan voor anderen. Jullie hebben mij, en mijn zusjes, de mogelijkheid gegeven om te studeren en daar ben ik jullie erg dankbaar voor. Door jullie steun heb ik het zo ver weten te schoppen.

Als laatste bedank ik Mies (Michael). Jij was, bent en zal voor altijd mijn steun en toeverlaat zijn. Toen ik vertelde dat de groep naar Enschede zou verhuizen zei je zonder na te denken dat ik vooral mee moest gaan. Hoewel dit goed bedoeld was weet ik niet of ik dat wel leuk vond (“ga je me niet missen dan?”). Maar het is goed dat we het gedaan hebben, want het is me gelukt, het boekje is klaar! Van nu af aan weer lekker sàmen dansen, zwemmen, fietsen, uit eten gaan en nog veel meer!